5-2015

A Study of the Dayside High-Lattitude Ionospheric Electrodynamics During Extended Solar Minimum

Janelle V. Jenniges
Utah State University

A STUDY OF THE DAYSIDE HIGH-LATITUDE IONOSPHERIC ELECTRODYNAMICS DURING EXTENDED SOLAR MINIMUM

by

Janelle V. Jenniges

A dissertation submitted in partial fulfillment
of the requirements for the degree

of

DOCTOR OF PHILOSOPHY

in

Physics

Approved:

Dr. Jan J. Sojka Major Professor	Dr. Charles G. Torre Committee Member
Dr. Bela G. Fejer Committee Member	Dr. Ludger Scherliess Committee Member
Dr. Anthony R. Lowry Committee Member	Dr. Mark R. McLellan Vice President for Research and Dean of the School of Graduate Studies

UTAH STATE UNIVERSITY
Logan, Utah

2015

The views expressed in this article are those of the author and do not reflect the official policy or position of the United States Air Force, Department of Defense, or the U.S. Government.

ABSTRACT

A Study of the Dayside High-Latitude Ionospheric Electrodynamics
During Extended Solar Minimum

by

Janelle V. Jenniges, Doctor of Philosophy
Utah State University, 2015

Major Professor: Dr. Jan J. Sojka
Department: Physics

The high-latitude electric field fall-off region connects convection in the polar cap to the region where ring currents modify the penetration electric field equatorward of the polar cap boundary. This region is often overlooked because it falls between the limits of low-latitude and high-latitude ionospheric models. However, penetrating electric fields cause large changes in ion composition; and therefore, correctly modeling the electric fields and plasma drift in this region aids in correctly specifying the ionosphere. Many ionospheric models use the Kp index as a physical driver, and so the latitude dependence of the plasma drift in the fall-off region was investigated as a function of Kp using Defense Meteorological Satellite Program ion drift data from the 2007–2010 solar minimum. Both the dusk and dawn sectors were analyzed and fit to analytical functions describing the fall-off with decreasing latitude. The latitude dependencies were found to differ in the dusk and dawn sectors with a factor of two increase in the expansion of the duskside polar cap radius and auroral region over the dawnside. Additionally, the low-Kp polar cap radius was found to be five degrees smaller than the radius currently used in simple ionospheric models.

(172 pages)

PUBLIC ABSTRACT

A Study of the Dayside High-Latitude Ionospheric Electrodynamics
During Extended Solar Minimum

Janelle V. Jenniges

This research investigated how electric fields, currents, and charged particles in Earth's high-latitude ionosphere respond to changing input from the sun. The ionosphere surrounds the entire Earth, makes radio communication possible, and can significantly degrade satellite communications and geo-positioning (navigation) capabilities. Many satellites fly within the ionosphere where a solar storm can cause increased satellite drag or destroy onboard electronics. Therefore, understanding and correctly predicting the behavior of this environment is important, and the results from this research will be used to improve current ionospheric models.

A relationship between the level of magnetic activity on Earth due to changes in the solar wind on and the response of Earth's high-latitude ionosphere was determined by examining ion and electron flow patterns in the polar cap and auroral regions. The data was obtained from a sun-synchronous polar-orbiting Defense Meteorological Satellite Program (DMSP) satellite during a time of quiet solar activity. Using this data, averaged patterns of the high-latitude ion and electron flow were created to examine the behavior of the polar cap. For very low geomagnetic activity, the polar cap radius was found to be five degrees smaller than the polar cap radius currently used in simple ionospheric models.

Additionally, each orbit was considered individually to obtain an analytic representation of the velocity profile. This was done separately in both the dawn and dusk regions to study how the rapidly decreasing ion and electron flows are related to the geomagnetic activity. A much larger than expected asymmetry was found between the dusk and dawn sectors with the dawn sector flows decreasing twice as fast as the dusk sector flows.

ACKNOWLEDGMENTS

Many people along the way have made this dissertation achievable. My time at Utah State University would not have been possible without the sponsorship and support of the United States Air Force and the Air Force Institute of Technology. I would never have even considered going back to school for a Ph.D. had it not been for the encouragement of Dr. Ariel Acebal who insisted this was the next best step for me. He has become a trusted mentor and good friend.

The guidance and supervision of my advisor, Dr. Jan Sojka, was instrumental in this work. His eagerness to work with me and his enthusiasm for this research kept me going even when the way forward was not clear. Not only did he guide me professionally, but he and his wife, Susan, found time to include me in their personal lives, with many dinners and evening strolls along the river with their grandchildren. I am happy to call them both friends.

The USU faculty and staff all contributed to my learning experience and I am particularly thankful to the front office ladies—Karalee, Shawna, Sharon, and Melanie—for their assistance in making my grad school experience a smooth one. I also want to thank my committee for their inputs and the time spent making sure this dissertation was the best it could be. Furthermore, Dr. Roderick Heelis was vital to this research and aided in understanding all the complexities in working with raw data.

I am grateful for all the other graduate students who helped me realize I wasn't the only one struggling, and for the friends I made in Utah for providing much needed breaks from my studies. Finally, I want to thank my family, especially my mom and dad, for supporting me and always believing in me. I am proud to be your daughter and will always look up to your daily commitment to hard work in accomplishing your goals.

Janelle V. Jenniges

CONTENTS

LIST OF TABLES

LIST OF FIGURES

CHAPTER 1
INTRODUCTION

1.1. Motivation

The ionosphere is the region in the Earth's atmosphere that consists of a weakly ionized plasma and is a very dynamic medium where both long-term, global-scale patterns and short-term, small-scale perturbations exist. The primary physical drivers for the ionosphere include electric and magnetic fields, current systems, and neutral winds that vary depending on solar cycle, season, time of day, location, and geomagnetic activity. Models are used to predict how changes in these drivers change the structure and characteristics of the ionosphere. Realistic output from these ionospheric models can only be obtained by accurately specifying the physical drivers.

Electric fields are the primary driving force for high-latitude ionospheric plasmas, but a complete description of the evolving global ionospheric electric field is still not available. Therefore, accurate measurements of the electric fields and the resulting plasma drift are critical in understanding and creating models of the ionospheric processes. Electric fields are also important in ionosphere-magnetosphere coupling at mid and high latitudes; creating a dynamic model of this connection depends on a thorough understanding of the convection electric fields.

Understanding and being able to predict the structure and dynamics of the ionosphere is important because the characteristics and dynamics of the ionosphere affect radio frequency propagation used for communication. Systems such as surveying and navigation systems that use global positioning system satellites, over-the-horizon radars, high-frequency communications, and the Federal Aviation Administration's Wide Area Augmentation System are thus affected by changes in the ionosphere [*Schunk et al.*, 2004].

The high-latitude convection pattern has been extensively studied and modeled by *Volland* [1978], *Heppner and Maynard* [1987], *Heelis et al.* [1982], *Weimer* [1995], and many others. Recent work using the Super Dual Auroral Radar Network (SuperDARN) and Incoherent Scatter Radars (ISR) has resulted in large-scale statistical ionospheric con-

vection patterns [*Cousins and Shepherd*, 2010], a technique to estimate the reconnection electric field as a function of local time [*Cowley and Lockwood*, 1992], and the observation of large-scale ionospheric flows in the nightside ionosphere during relatively quiet geomagnetic conditions [*Senior and Blanc*, 1984]. Another state-of-the-art model is the Assimilative Mapping of Ionospheric Electrodynamics (AMIE) model that can be run in a real-time mode and synthesizes various direct and indirect observations to estimate the time-varying distributions of electric fields, currents, and conductivities over the entire polar ionosphere [*Richmond*, 1992]. While all of these models have contributed to the understanding of the high-latitude convection pattern, there is still much to be learned.

The convection pattern is highly dependent on geomagnetic activity and the orientation of the interplanetary magnetic field (IMF), but less is understood about the dependencies of the midlatitude fall-off region. This region connects the high-latitude polar cap convection to the region where the ring currents modify the low-latitude penetration electric field equatorward of the polar cap boundary. The electric field in this midlatitude region is typically modeled in a simple manner, but magnetosphere-ionosphere dynamics may create structure in this region that has previously been neglected by ionospheric models.

The goal of this dissertation is to examine the plasma drift in the midlatitude fall-off region and to classify the fall-off using the geomagnetic index. This classification will enable ionospheric models such as the Time Dependent Ionospheric Model (TDIM) that use the Kp index as a primary driver to use the best representation of the high-latitude convection pattern. Fine tuning the dayside electrodynamics in ionospheric models should result in a more accurate representation of ionospheric conditions and thus, a more reliable prediction of ionospheric impacts on communication and navigation systems.

1.2. Method

This study uses satellite measurements of the high-latitude plasma drift obtained from the Defense Meteorological Satellite Program (DMSP) during the 2007–2010 solar minimum period to examine the high-latitude convection pattern. The temporal and spatial resolution of the DMSP data, approximately 14 daily polar passes with a 101-minute orbital period

spread across a swath of magnetic latitudes and local times due to the satellite's sun-synchrony, requires that a climatological evolution of the convection pattern with IMF, Kp, and season be studied versus instantaneous changes in the convection pattern.

In a method similar to *Weimer* [1995], average convection patterns are obtained for different solar and geomagnetic conditions. The velocity profile in the fall-off region from these convection patterns is compared against other empirical models and is used to distinguish patterns associated with the solar and geomagnetic conditions. Following this, a completely different approach is used where each individual orbit is fit to a function, and the free parameters are determined by the fit, which are investigated for trends with Kp.

In this dissertation, Chapter 2 provides an overview of the ionosphere, the plasmasphere, and the high-latitude electric field and plasma convection. DMSP instrumentation for ion drift measurements are also described, and shortfalls in the data collection are outlined. Finally, various polar cap convection models are described. The processes used to prepare the data for analysis and to transform the coordinate system from the satellite frame of reference to a flat Earth Cartesian frame are discussed in Chapter 3. Chapters 4–6 discuss the results of the dissertation. In Chapter 4, the data is binned based on solar and geomagnetic conditions and then averaged to obtain convection patterns. These averaged convection patterns are then compared to other empirical models and are used to obtain a relationship between the geomagnetic index and the polar cap radius. Chapter 5 shows the results of fitting three different functions to the duskside fall-off velocity profiles, while Chapter 6 shows the classification of the orbits in the dawnside fall-off region. Both Chapters 5 and 6 show Kp trends computed by analyzing various parameters against Kp for each function. Finally, Chapter 7 summarizes the results and outlines future work to be accomplished.

CHAPTER 2
BACKGROUND

2.1. Overview

The upper ionosphere is a very dynamic medium where both regular global patterns and short-term, small-scale perturbations exist. Identifying the energy sources and processes that generate these motions is tightly coupled to the determination of the plasma velocities and electric fields. It is desirable to obtain electric field and plasma drift measurements from a satellite because the geographic and temporal resolution is significantly better than any similar ground-based measurement, and many correlative measurements can be made simultaneously on the same satellite. These measurements can then be used to create electric field and polar cap convection models that can be used to describe the $\mathbf{E} \times \mathbf{B}$ driver for ionosphere dynamics. A short summary of the ionosphere and plasmasphere is given in section 2.2, while the processes that create the high-latitude electric fields and plasma convection are described in section 2.3. Section 2.4 covers DMSP and the onboard instruments used to measure ion drift. Finally, a variety of polar cap convection models are outlined in section 2.5.

2.2. The Ionosphere and Plasmasphere

The ionosphere is a quasi-neutral ionized plasma that is created by photoionization of the neutral atoms and molecules in Earth's atmosphere by solar ultraviolet radiation and extends from about 50 km to beyond 2000 km [*Schunk and Nagy*, 2009]. The plasmasphere is the region between the ionosphere and the magnetosphere consisting of low energy (≤ 1 eV), relatively dense (10 to 10^3 cm^{-3}) plasma that begins where H^+ becomes the dominant ion and ends at 3–6 Earth radii, depending on geomagnetic activity [*Tascione*, 1994]. In general, the plasmasphere lies beneath the magnetic field line that maps to $\pm 60^\circ$ magnetic latitude at the surface. Both the ionosphere and plasmasphere are characterized by the vertical structure of the ion and electron densities. The structure and characteristics of the ionospheric regions are highly dependent on solar cycle, season, time of day, geographic

location, and geomagnetic activity. Figure 2.1 shows typical ion density profiles in the ionosphere and plasmasphere as measured by the incoherent scatter radar at Arecibo, Puerto Rico (18° N, 67° W). The top panel is during the day at 1436 local time (LT) and the bottom panel is at night (2230 LT). The transition height from O^+ to H^+ changes from day to night and also changes with season and geomagnetic activity. At night and during winter, the light ions become the dominant species at much lower altitudes. As will be discussed in section 2.4, this significantly influences the ability to measure the ion drift.

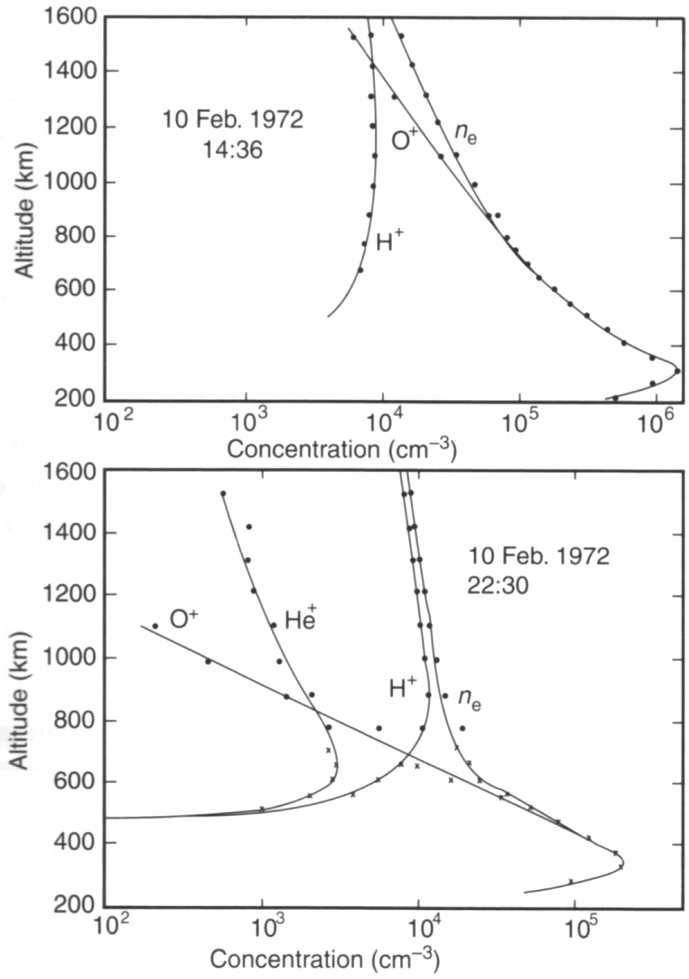

Figure 2.1. Altitude profile of typical ion densities. Daytime (1436 LT) densities are shown on the top and nighttime (2230 LT) densities are shown on the bottom. Measurements were taken with the incoherent scatter radar at Arecibo, Puerto Rico. Used with permission from *Hagen and Hsu* [1974].

Production, loss, and transport control the ion and electron density distributions in the ionosphere and plasmasphere. These three processes can be described and modeled using the ion and electron continuity and momentum equations (equations 2.1 and 2.2, respectively). The continuity equation equates the time rate of change of the density (dn_s/dt) to the combined effects of transport ($-\boldsymbol{\nabla} \cdot n_s \mathbf{V}_s$), production ($P_s$), and loss ($L_s$) of a species, s. The continuity equation is

$$\frac{dn_s}{dt} = -\left(\boldsymbol{\nabla} \cdot n_s \mathbf{V}_s\right) + \left(P_s - L_s\right), \tag{2.1}$$

where n_s is the density of the species and $\mathbf{V}_s$ is the velocity of the species. When thermal diffusion, Coriolis force, and centripetal force are all assumed to be negligible, the general momentum equation is given as

$$\rho_s \frac{D_s \mathbf{V}_s}{Dt} = -\boldsymbol{\nabla} p_s - \boldsymbol{\nabla} \cdot \boldsymbol{\tau}_s + \rho_s \mathbf{g} + n_s q_s \left[\mathbf{E} + \mathbf{V}_s \times \mathbf{B}\right] + \sum_t \rho_s \nu_{st} \left(\mathbf{V}_t - \mathbf{V}_s\right), \tag{2.2}$$

where the subscripts denote the species, s, and the target, t, ρ_s is the mass density, D_s/Dt is the convective derivative, p_s is the pressure, $\boldsymbol{\tau}_s$ is the stress tensor, $\boldsymbol{g}$ is gravity, q_s is the charge, $\boldsymbol{E}$ and $\boldsymbol{B}$ are the electric and magnetic fields, respectively, and ν_{st} is the collision frequency.

In general, transport is negligible below 200 km and the change in ion concentration is described only by production and loss mechanisms and the ionosphere is in a state of photochemical equilibrium [*Schunk and Nagy*, 2009]. Above 200 km production and loss no longer dominate the continuity equation and transport must be included. In the top-side ionosphere (above 300 km) and plasmasphere, production and loss are negligible and transport is the dominant process that controls ion and electron concentrations.

The ion transport can be simplified into two cases; motion parallel to (along) the magnetic field, and motion perpendicular to (across) the magnetic field. The overall plasma motion is a combination of these two motions and can be described by looking at the approximations, simplifying assumptions, and solutions to equation 2.2.

For motion along the magnetic field, the diffusion approximation (steady state and subsonic), charge neutrality ($n_e = n_i$), and zero current ($n_e \boldsymbol{V}_e = n_i \boldsymbol{V}_i$) assumptions are made, resulting in the ambipolar diffusion equation

$$\boldsymbol{V}_{i||} = -D_a \left[\frac{1}{n_i} \boldsymbol{\nabla}_{||} n_i + \frac{1}{T_p} \boldsymbol{\nabla}_{||} T_p - \frac{m_i \boldsymbol{g}_{||}}{2 k_b T_p} + \frac{(\boldsymbol{\nabla} \cdot \boldsymbol{\tau}_i)_{||}}{2 n_i k_b T_p} - \frac{m_i}{2 k_b T_p} \nu_{in} \boldsymbol{V}_{n||} \right], \tag{2.3}$$

where k_b is Boltzmann's constant, the subscript n is for the neutral gas, and $||$ denotes flow parallel to the magnetic field. The ambipolar diffusion coefficient (D_a) and plasma temperature (T_p) are given as

$$D_a = \frac{2 k_b T_p}{m_i \nu_{in}} \tag{2.4}$$

$$T_p = \frac{T_e + T_i}{2}. \tag{2.5}$$

Equation 2.3 shows the ions move along the magnetic field with the neutral wind subject to density gradients, temperature gradients, gravity, and stress forces.

The two dominant forces in this equation are the parallel density gradient ($\boldsymbol{\nabla}_{||} n_i$) and the thermospheric neutral winds ($\boldsymbol{V}_{n||}$) [*Schunk and Nagy*, 2009]. The density gradient points from low to high densities. For O^+ below the ionization peak, the gradient is in the upward direction because O^+ is not present in the lowest portions of the ionosphere. However, the diffusion coefficient is proceeded by a negative and the resulting motion due to diffusion is down the field lines (toward the Earth). In the upper ionosphere, the density gradient is downward during the day toward the ionization peak and upward at night due to the decay of the peak. The resulting flow due to diffusion in the upper ionosphere is then upward during the day and downward at night.

In the high-latitude ionosphere, where the Earth's magnetic field is open (or the field lines extend far into the magnetotail), upward diffusion of the light ions (H^+ and He^+) essentially leads to an escape of the light ions from the ionosphere. This is known as the polar wind with light ion velocities parallel to the magnetic field reaching several kilometers per second [*Kelley*, 1989]. This typically leaves the heavier O^+ ion as the dominant ion

below 1000 km in the polar ionosphere. One feature related to the polar wind is the light-ion trough; this is a region at a fixed altitude where the densities of the light ions decrease with increasing latitude. An example is shown in Figure 2.2 where the top panel shows the total density and the bottom panel shows the fractions of O^+, H^+, and He^+ measured by DMSP in the northern hemisphere in September 2007. An abrupt decrease in the light ion density marks the equatorward boundary of the trough and is typically between 55° and 65° magnetic latitude [*Kelley*, 1989]. The trough is created when plasma in the outer plasmasphere is convected away due to enhanced magnetospheric electric fields during geomagnetic storms and substorms. Upward ionospheric diffusion then occurs both day and night in an attempt to replace the lost plasma. The low-latitude plasmasphere refills quickly due to the small volume within closed magnetic field lines while the upper ionosphere at high latitudes is always in a partially depleted state due to the open field lines [*Schunk and Nagy*, 2009].

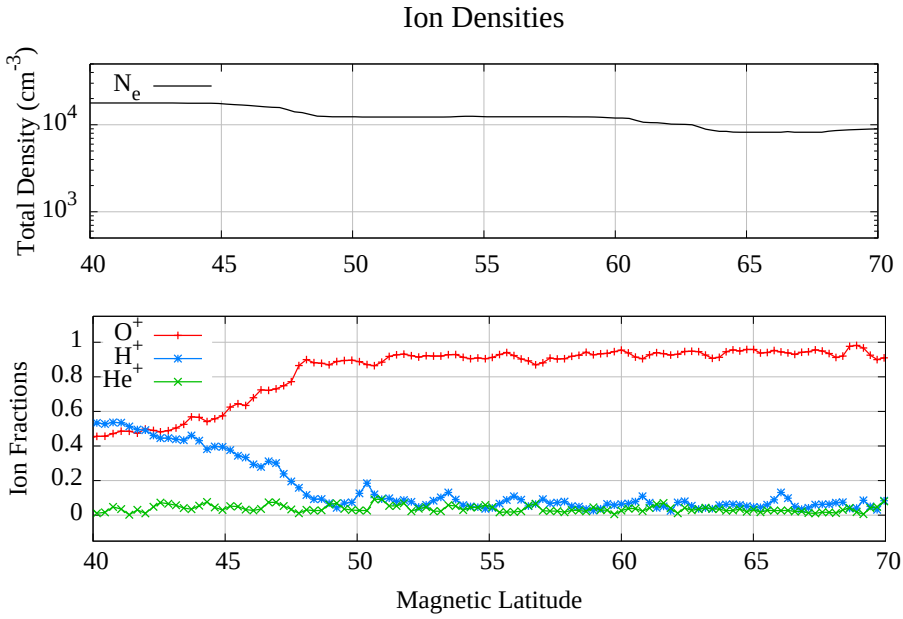

Figure 2.2. Example of the light ion trough. Ion densities were measured by DMSP in September 2007. The top panel shows the total ion density and the bottom panel shows the relative contributions of O^+, H^+, and He^+.

The thermospheric neutral winds are primarily controlled by solar heating. In general, the thermospheric winds are directed radially away from the subsolar point with daytime meridional winds blowing toward the poles and nighttime meridional winds blowing toward the equator. The winds are weak near the subsolar point and increase in magnitude as the distance from the subsolar point increases. Weak daytime winds are due to higher ion concentrations creating increased ion drag on the neutrals. In the midlatitude region where the field lines are tilted with respect to the Earth's surface, the neutral winds push the plasma down the field lines to lower altitudes during the day (poleward flow) and up the field lines to higher altitudes at night (equatorward flow). The movement to different altitudes and latitudes can significantly change the ion concentration.

Motion across the magnetic field can be looked at in a manner similar to motion along the magnetic field. After transforming to a reference frame moving with the neutral wind, the plasma flow across the magnetic field (indicated by the $\perp$ symbol) is given by the following equation:

$$\boldsymbol{V}_{s\perp} = \frac{1}{1+K^2}\left[\frac{-D_s}{p_s}\boldsymbol{\nabla}_\perp p_s + \frac{1}{\nu_{sn}}\boldsymbol{g}_\perp + \mu_s \boldsymbol{E}_\perp\right] + \frac{1}{1+1/K^2}\left[\boldsymbol{V}_p + \boldsymbol{V}_g + \boldsymbol{V}_E\right], \tag{2.6}$$

where

$$K = \frac{\omega_{cs}}{\nu_{sn}} \quad \text{is the gyrofrequency to collision frequency ratio,} \tag{2.7}$$

$$D_s = \frac{k_b T_s}{m_s \nu_{sn}} \quad \text{is the diffusion coefficient,} \tag{2.8}$$

$$\mu_s = \frac{q_s}{m_s \nu_{sn}} \quad \text{is the mobility,} \tag{2.9}$$

and

$$\boldsymbol{V}_p = \frac{-1}{n_s q_s}\frac{(\boldsymbol{\nabla}_\perp p_s \times \boldsymbol{B})}{B^2} \quad \text{is the gradient drift,} \tag{2.10}$$

$$\boldsymbol{V}_g = \frac{m_s}{q_s}\frac{(\boldsymbol{g}_\perp \times \boldsymbol{B})}{B^2} \quad \text{is the gravitational drift,} \tag{2.11}$$

$$\boldsymbol{V}_E = \frac{(\boldsymbol{E}_\perp \times \boldsymbol{B})}{B^2} \quad \text{is the electrodynamic drift.} \tag{2.12}$$

The particle charge, q_s, in Equations 2.10 and 2.11 indicates electrons and ions drift across the magnetic field in opposite directions in the presence of pressure gradients and gravity, while the lack of the particle charge in equation 2.12 requires they drift together in the presence of an electric field that is perpendicular to the magnetic field.

At low altitudes the magnetic field strength is small compared to the collision frequency, $K \to 0$, and the second term in equation 2.6 becomes negligible. This occurs because of the high concentration of neutrals in the lower atmosphere. The resulting plasma motion is perpendicular to the magnetic field, but in the same direction as the force causing the motion. At intermediate locations where $K \approx 1$, the plasma motion is a combination of the motion perpendicular to the magnetic field and parallel to the force [*Kelley*, 1989].

At high altitudes where collisions are negligible, $K \to \infty$, and the first term in equation 2.6 drops out leaving only motion perpendicular to both the magnetic field and the force; that is,

$$\boldsymbol{V}_{s\perp} = \boldsymbol{V}_p + \boldsymbol{V}_g + \boldsymbol{V}_E. \tag{2.13}$$

Typically the drifts due to pressure gradients and gravity are small at altitudes above 150 km and the electrodynamic drift dominates [*Schunk and Nagy*, 2009]. Therefore, in this regime, we can approximate the motion of the ions perpendicular to Earth's magnetic field with the simple relation

$$\boldsymbol{V}_\perp = \frac{(\boldsymbol{E} \times \boldsymbol{B})}{B^2}. \tag{2.14}$$

At low latitudes, the electrodynamic drift is caused by the dynamo electric field created in the E region of the ionosphere and transmitted along the highly conductive dipole field lines to the F region. This electric field is generated by the thermospheric winds as the ions are dragged across the magnetic field. The dynamo electric field is eastward during the day with a resulting upward $\boldsymbol{E} \times \boldsymbol{B}$ drift; the opposite occurs at night with a westward electric field and a downward drift [*Schunk and Nagy*, 2009]. The daytime combination of upward drifts and downward diffusion is responsible for the ionization peaks on both sides of the geomagnetic equator known as the equatorial fountain or anomaly (Figure 2.3).

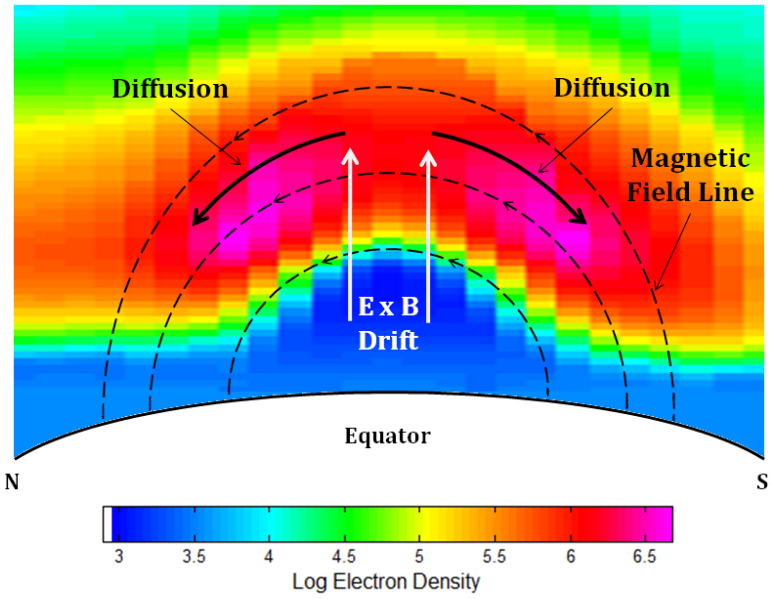

Figure 2.3. Formation of the equatorial anomaly. The high electron density is a result of an upward electrodynamic drift and diffusion down the magnetic field lines.

At high latitudes the electric field that drives the electrodynamic drift is created by the interaction of the solar wind and the Earth's geomagnetic field. In general, a two-cell convection pattern is created at high latitudes with the dawn-to-dusk electric field driving the plasma sunward across the polar cap with a return flow (antisunward) equatorward of the polar cap. This process will be discussed in more detail in the following section.

In addition to the continuity and momentum equations, the temperature of each species due to heat transport is required to accurately describe the true nature of the ionosphere. This temperature change is described by the energy equation:

$$\frac{D_s}{Dt}\frac{3p_s}{2} = -\frac{5}{2}p_s\left(\boldsymbol{\nabla}\cdot\boldsymbol{u}_s\right) - \boldsymbol{\nabla}\cdot\boldsymbol{q}_s + Q_s - L_s + \sum_t \frac{\rho_s \nu_{st}}{m_s + m_t} 3k_b\left(T_t - T_s\right), \tag{2.15}$$

where $\boldsymbol{q}_s$ is the heat flow, Q_s is the local heating rate, and L_s is the local cooling rate (other variables described previously). The left side of the energy equation shows the change in energy due to both time and transport. The right side is a combination of compressional heating, divergence of heat flow, local heating and cooling, and kinetic energy transfer during elastic collisions.

Ion-neutral collisions are a significant source of ion heating at high latitudes. These collisions can modify the thermosphere circulation, temperature, and composition, which in turn affects the ionosphere. The amount of energy exchanged is dependent on the relative velocity between the ion and neutral particles, which can be large due to the electrodynamic drift of the ions. Ion drag on the neutrals will eventually set the neutral gas in motion as well, resulting in an equalization of the ion and neutral velocities in steady state. Therefore, significant ion frictional heating typically occurs at high latitudes just after the plasma convection pattern changes. Elevated ion temperatures alter the ion composition through temperature-dependent chemical reaction rates. According to *Schunk and Nagy* [2009], this indicates that in regions where the ion drift is large, the associated frictional heating should lead to a rapid conversion of O^+ into NO^+. Additional information on ionospheric processes can be found in Appendix A.

2.3. High-Latitude Electric Fields and Plasma Convection

Electric fields are one of the primary driving forces for plasmas in the upper ionosphere. In the Earth's high-latitude ionosphere, ion and electron motion is dominated by the electrodynamic drift as shown in section 2.2. A dynamo electric field is created in the magnetosphere by the movement of the solar wind across the Earth's open magnetic field lines (Figure 2.4) and is governed by the relation $\boldsymbol{E}_d = -\boldsymbol{V}_{sw} \times \boldsymbol{B}$ where $\boldsymbol{E}_d$ is the dynamo electric field, $\boldsymbol{V}_{sw}$ is the velocity of the solar wind, and $\boldsymbol{B}$ is the Earth's magnetic field.

This dawn-to-dusk electric field maps down along geomagnetic field lines into the Earth's polar cap region where it interacts with ionospheric plasma. The existence of a convection electric field across the polar cap indicates there is a charge buildup on the boundary between open and closed geomagnetic field lines. The charge is positive on the dawnside and negative on the duskside. These charges act to induce electric fields on nearby closed field lines that are opposite in direction to the convection electric field [*Schunk and Nagy*, 2009]. These electric fields are located in the auroral zone and act to move the plasma in a sunward direction. Figure 2.5 is an idealized diagram of the high-latitude electric fields and the resulting plasma drift. Note the electric fields are always directed perpendicular

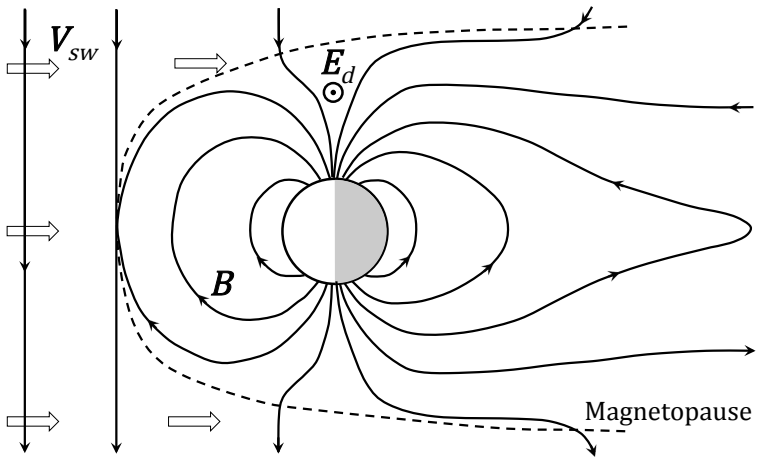

Figure 2.4. Schematic diagram of the dynamo electric field ($\boldsymbol{E}_d$). The dynamo electric field is created by the solar wind dynamo, maps down to ionospheric altitudes along the highly conducting geomagnetic field lines, and causes the plasma to drift in an antisunward direction.

to the slightly tilted magnetic field lines in the polar regions. The absence of electric fields parallel to the magnetic field indicates very high conductivity along the field lines so they may be considered conducting wires or equipotential lines.

When the electrodynamic drift is the dominant force on the ions, the lines of equipotential in the high-latitude ionosphere also correspond to streamlines of plasma drift. In the most ideal representation, and with a southward directed IMF, the flow pattern exhibits a two-cell pattern, with antisunward flow over the polar cap and return (sunward) flow in the polar oval. Therefore, the dashed lines in Figure 2.5 represent not only lines of equipotential, but also the plasma drift. When the IMF is northward, the connection between the Earth's magnetic field and the solar wind is drastically different. Since B_z is northward roughly half of the time, many of the resulting flow patterns are very different from the idealized two-cell pattern (see section 2.5.)

The field lines that separate the oppositely directed electric fields in the polar cap and polar oval contain field-aligned currents (FACs) that flow between the ionosphere and magnetosphere. The current is downward into the ionosphere on the dawnside, across the polar cap from dawn to dusk, and then up the magnetic field lines away from the ionosphere on the duskside. The currents close in the magnetosheath and the entire system is analogous

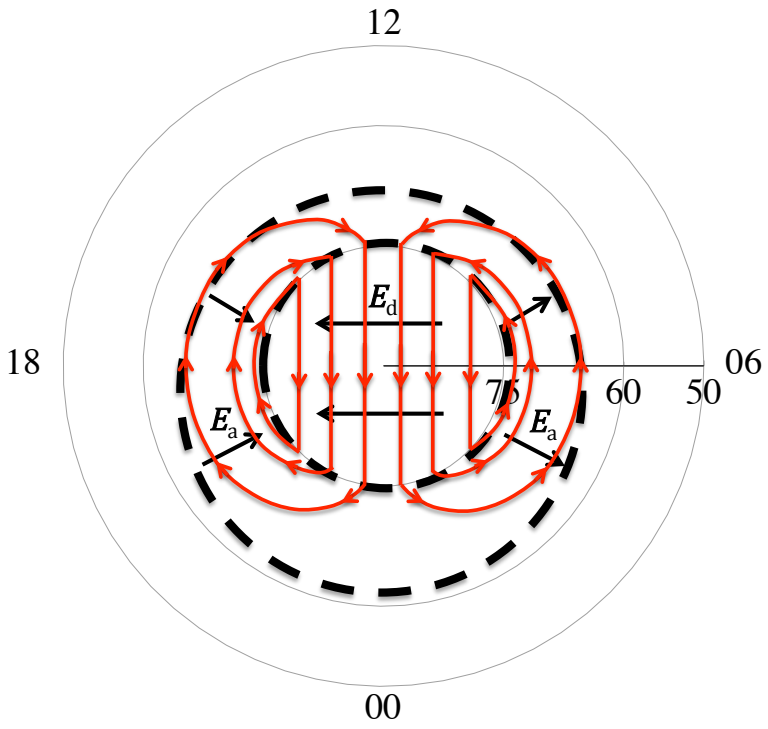

Figure 2.5. Idealized diagram of the high-latitude ionospheric electric fields ($\boldsymbol{E}_d$ and $\boldsymbol{E}_a$) and the resulting plasma drift (red flowlines). In the most ideal case a two-cell pattern exists with antisunward flow in the polar cap and return (sunward) flow in the polar oval.

to a magnetohydrodynamic generator, where the solar wind is the conductor connected by the FACs to the ionosphere, which is the load [*Kelley*, 1989].

Typical field strengths during quiet times are on the order of 10 mV/m in the polar cap and 30 mV/m in the polar oval [*Prölss*, 2004]. The electric field is integrated across the polar cap along a line from 0600 magnetic local time (MLT) to 1800 MLT to yield a cross-cap potential; quiet-time electric fields yield a cross-cap potential of more than 30 kV while the cross-cap potential during a strong geomagnetic storm can reach as high as 120 kV [*Weimer*, 1995]. Typical drift velocities associated with these quiet time field strengths are nearly 200 m/s in the polar cap and 600 m/s in the polar oval. Storm time drift velocities can reach over 1500 m/s.

At latitudes equatorward of the oval, the electric field strength is usually quite small (< 5 mV/m) due to the shielding of the inner magnetosphere. In the outer magnetosphere, a cross-tail convection electric field directed oppositely to the general dawn-to-dusk electric

field is produced by pressure gradients associated with the inner edge of the plasmasheet and the region-2 Birkeland currents. The region-2 currents, which are generally downward into the ionosphere on the dusk side and upward on the dawn side, form a closed loop between the ionosphere and magnetosphere. Far from Earth, the cross-tail convection electric field is dominant, but in the inner magnetosphere where the Birkeland currents are strong, the cross-tail convection electric field and the dynamo electric field nearly cancel each other, leaving the inner magnetospheric electric field much weaker than the outer field.

One exception to this is during the initial phase of a geomagnetic storm, which can cause variations in the region-2 currents and allow penetration electric fields to reach the low to midlatitudes at up to 10 mV/m, which is twice their normal amplitude [*Fejer*, 2003]. Even during quiet times, small-scale structure within the FACs can decrease the shielding effect and allow penetration of electric fields to lower latitudes. These penetration electric fields generate low-latitude zonal plasma drifts and can significantly alter the ion composition.

Magnetospheric plasma flowing toward the Earth encounters an increasing magnetic field strength. Gradient and curvature drifts are important in this region [*Prölss*, 2004] and depend on the charge of the particle, so a zonal charge separation occurs with positive charges at dusk and negative charges at dawn. This creates a dusk-to-dawn electric field in the inner magnetosphere, which tends to cancel out the convection electric field. The inner magnetosphere is, therefore, shielded from the magnetospheric electric field, and the plasma flows around this region. This shielding only operates on long timescales, and fluctuations of the convection electric field with periods shorter than several hours (as with geomagnetic storms) can penetrate to low latitudes [*Kelley*, 1989].

Since the convection electric field is reduced to almost zero at low latitudes, the electric field, due to the rotation of the Earth, becomes comparable to the convection field equatorward of the oval. Including corotation causes plasma drift trajectories that are significantly different from the two-cell pattern. The most significant difference is on the duskside near 60° where the corotation and convection electric fields oppose each other and create complex drift trajectories. Figure 2.6 shows drift trajectories for a typical two-cell pattern with

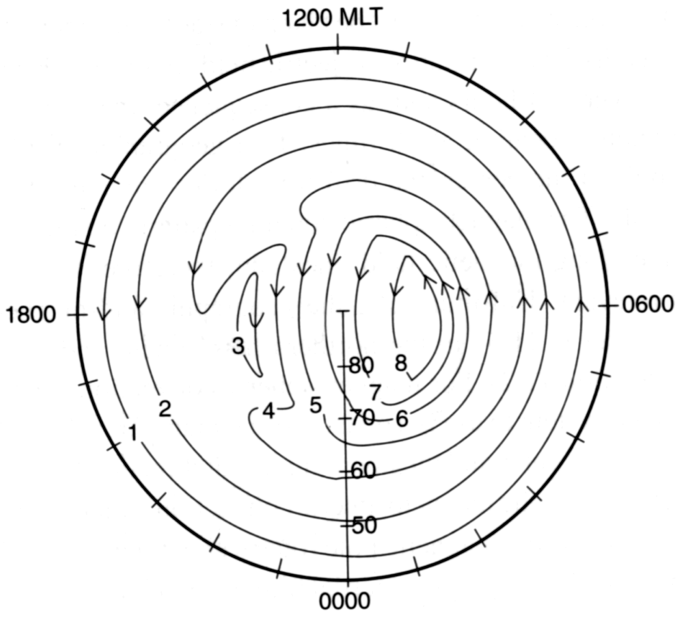

Label	1	2	3	4	5	6	7	8
Circulation period (day)	1.00	1.01	0.10	1.34	0.50	0.31	0.18	0.11

Figure 2.6. Plasma drift trajectories with corotation and convection electric fields. The trajectories are for a symmetric two-cell convection pattern; the circulation times for each trajectory are shown at the bottom. Used with permission from *Sojka et al.* [1979].

a cross-cap potential of 64 kV. Plasma flowing on trajectories 1 and 2 essentially corotate with the Earth. Just poleward of this, a stagnation region exists where the corotation and convection electric fields are opposed. Plasma in this region (trajectory 4) can take more than a day to completely circulate the Earth. Plasma that is completely contained within the polar cap (trajectory 3, 5–8) has short circulation times because the trajectories are short and the electrodynamic drift speeds are high. Corotation is removed from the ion drift before constructing the polar cap convection patterns.

Coupled with the location of the solar terminator, the varying plasma drift in different regions of the high-latitude ionosphere causes various ionospheric features. Typically, anti-sunward flow acts to carry high-density day side plasma into the polar cap. During winter a large portion of the polar cap is in darkness. When the plasma drift is slow, after the plasma

convects across the solar terminator it has ample time to decay due to lack of sunlight and recombination processes. A polar hole is formed just poleward of the night side auroral oval due to this significant decay. As the plasma enters the oval, densities increase because of impact ionization due to precipitating electrons. When the antisunward plasma drift is high, the plasma moves quickly across the polar cap only decaying slightly and a tongue of ionization is formed that extends across the polar cap form the day side to the night side. Another interesting winter feature is the midlatitude electron density trough. This feature occurs just equatorward of the night side auroral oval and is a region of low electron density that has a narrow latitudinal extent, but is extended in longitude [*Schunk and Nagy*, 2009]. Plasma trapped in the stagnation region is in darkness for extended periods of time and leads to very low electron densities.

The convection electric field is much more complicated than a simple two-cell convection pattern. With the significant influence of the plasma drift on ion concentration, it is important to understand the dynamic nature of the polar cap convection pattern for all variations of solar cycle, season, MLT, and geomagnetic activity. The convection electric field is strongly correlated with geomagnetic activity, K_p, and it depends on the solar wind dynamic pressure and orientation of the IMF (B_x, B_y, B_z) [*Schunk and Nagy*, 2009]. During the last 30 years, a concerted effort has been made to develop empirical and statistical patterns of the polar cap convection pattern for a wide range of conditions. Both electric field and ion drift measurements made from ground-based radars and satellite-borne instruments have been synthesized, binned, averaged, and fit with analytical expressions in an attempt to represent these patterns. The following section will discuss how in situ ion drift measurements are made via polar orbiting satellites and section 2.5 will describe some of the initial and more recent convection models.

2.4. Ion Drift Measurements

There are many different methods available to measure the high-latitude electric fields and plasma convection. Direct measurement of the electric fields is possible with electric field probes on polar orbiting satellites [e.g., *Aggson and Heppner*, 1964; *Dolezalek*, 1964;

Kavadas and Johnson, 1964; *Pfaff et al.*, 2010; *Wygant et al.*, 2013]. The ionospheric plasma convection can then be inferred from the electric field measurements. Alternatively, the drift velocity of the ions can be obtained directly using ion traps [e.g., *Hairston et al.*, 2010; *Hanson and Heelis*, 1975; *Hanson et al.*, 1981, 1993; *Klenzing et al.*, 2008; *Knudsen*, 1966]. Additionally, ground-based radars, both coherent and incoherent scatter radars, can be used to measure the drift velocity using the Doppler shift of reflected radio signals [e.g., *Alcayde et al.*, 1986; *Cousins and Shepherd*, 2010; *Heinselman and Nicolls*, 2008; *Hysell et al.*, 2009; *Lester*, 2013; *Peymirat and Fontaine*, 1997]. Ion drift measurements from the retarding potential analyzer (RPA) and ion drift meter (IDM) onboard the DMSP are utilized in this study. The following sections discuss these ion traps including some of the advantages and disadvantages of each.

2.4.1. Retarding Potential Analyzer

The planar retarding potential analyzer measures ion currents to determine the ion drift velocity parallel to the satellite ram direction. The term planar refers to the configuration of the grids within the sensor and to the aperture plane of the sensor face. Given an aperture with area A that is perpendicular to the $\hat{\mathbf{x}}$ direction, the current flowing thru the area is

$$I = ANq \int_{-\infty}^{\infty} dV_y \int_{-\infty}^{\infty} dV_z \int_{0}^{\infty} dV_x \, F(\mathbf{V}) \, V_x, \tag{2.16}$$

where N is the total particle density, q is the fundamental charge, $F(\mathbf{V})$ is the ambient plasma velocity distribution, and V_x is the particle velocity normal to the aperture. If the ion velocity distribution is assumed to be Maxwellian, the one-dimensional distribution function is

$$F(\mathbf{V}) = \sqrt{\frac{m}{2\pi kT}} exp\left[-\frac{mV_x^2}{2kT}\right]. \tag{2.17}$$

Because $F(\mathbf{V})$ is independent of V_y and V_z, the expression for the current diverges to

$$I = ANq \int_{0}^{\infty} V_x \, F(\mathbf{V}) \, dV_x. \tag{2.18}$$

The RPA utilizes an energy filter behind the aperture so only a specific subset of energies will contribute to the measured current. In practice, this energy filter is a set of wire mesh grids that are positively biased relative to the instrument ground. A diagram of a typical RPA is shown in Figure 2.7. The number of grids may vary from instrument to instrument, but in general the order of the biasing is the same.

The first grid, G1, is the aperture grid and is grounded to shield the external plasma from potentials applied inside the sensor. G2 is the energy filter and for ion collection is typically swept through a retarding voltage (RV) from 0 up to 32 volts. A pair of grids are used instead of a single grid to provide a more uniform potential in the grid plane [*Klenzing et al.*, 2008]. The suppressor grid, G3, and the shield grid, G4, are both negatively biased (G3 ≈ -15 V) to repel any incoming electrons and to prevent secondary photoemission from the collector, respectively.

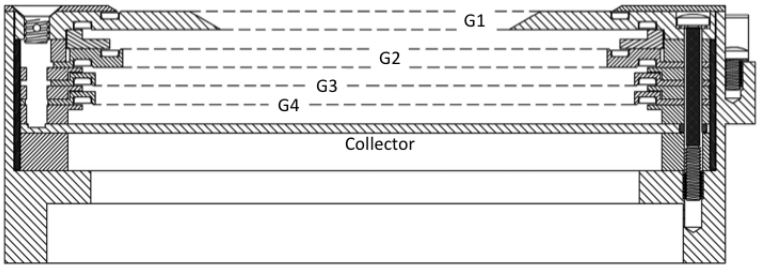

Figure 2.7. Diagram of the retarding potential analyzer.

Only ions with sufficient kinetic energy will penetrate the retarding voltage grids. Ions must have a kinetic energy $\left(\mathcal{E}_x = mV_x^2/2\right)$ greater than the stopping potential of the retarding voltage ($\mathcal{E}_{st} = q\Phi_{RV}$) to pass the energy filter. Additionally, the ions must overcome the spacecraft potential Φ_s, which will typically be negative. Therefore, the required ram energy is $\mathcal{E}_x = mV_x^2/2 - q\Phi_s$. This means the required velocity is

$$V_x \geq \sqrt{\frac{2q}{m}\left(\Phi_s + \Phi_{RV}\right)}. \tag{2.19}$$

In the simplest case where this is the only factor determining what fraction of ions reach the collector, the transmission function is a step function with

$$\chi(\mathbf{V}, \Phi_s, \Phi_{RV}) = \begin{cases} 0, & V_x < \sqrt{\dfrac{2q}{m}\left(\Phi_s + \Phi_{RV}\right)}, \\ \chi_0, & V_x \geq \sqrt{\dfrac{2q}{m}\left(\Phi_s + \Phi_{RV}\right)} \end{cases} . \tag{2.20}$$

The transmission function maps the flux outside the instrument to the flux seen by the collector and is included in the current equation integral:

$$I = ANq \int_0^\infty \chi(\mathbf{V}, \Phi_{RV})\, V_x\, F(\mathbf{V})\, dV_x. \tag{2.21}$$

Integration of equation 2.21 leads to the analytic form used by *Whipple* [1959]

$$I = \frac{ANq\,\chi_0\,V_x}{2}\left[1 + \mathrm{erf}(\beta f) + \frac{1}{\beta\sqrt{\pi}V_x} e^{\left(-\beta^2 f^2\right)}\right], \tag{2.22}$$

where

$$\beta = \sqrt{\frac{m}{2kT}}, \tag{2.23}$$

$$f = V_x - \sqrt{2q\Phi_{RV}/m}. \tag{2.24}$$

Sweeping the applied retarding voltage allows a current–voltage (I–V) curve to be constructed. For typical orbital velocities in the upper ionosphere, all ions crossing the aperture plane will reach the collector when no retarding voltage is applied, while a retarding voltage of 30 volts will restrict collection to ions with mass greater than 60 amu [*Heelis and Hanson*, 2013]. This voltage range effectively spans the energy range of all major planetary ion species. In theory, the velocity parallel to the sensor normal, V_x, is then determined by using a least squares technique to fit the I–V curve to equation 2.22. The measured current is the linear sum over all ion species described by equation 2.22. In addition to V_x, the ion temperature and concentrations are also found using this technique. In practice it can be difficult to obtain accurate ion concentrations; the error can be reduced if a high-resolution ion-mass spectrometer is used to determine the relative amounts of ions with nearly the

same mass (e.g. N_2^+, NO^+, and O^+). The RPA is used to determine the absolute total concentration for each of the widely separated ion mass groups [*Hanson and Heelis*, 1975].

If the spacecraft potential, Φ_s, is not known or measured independently, it will also need to be derived using the least squares fit. If only a single ion or ion mass group is present, it is difficult to separate the effect of a change in Φ_s from a change in V_x. For spacecraft velocities of 8 km/s, an uncertainty of 0.1 V in Φ_s results in an error of approximately 40 m/s for NO^+ ions and nearly 80 m/s for O^+ ions [*Hanson and Heelis*, 1975].

In reality, many simplifying assumptions are made in order to relate the I–V curve to the velocity distribution function. Some of these include treating the planes of the grids as equipotential surfaces; assuming the transparency of the grids is neither a function of retarding potential nor of angle; simplifying the sheath boundary as plane and parallel to the RPA face; assuming all ions collected originate in the undisturbed plasma; and approximating the grids and collector as being infinite in extent [*Knudsen*, 1966].

In general, the transmission function χ and optical transparency depend on the grid geometry and the applied potential. If the potential across a grid is not uniform, excess ions will leak through the filter and increase the current. Additionally, ions with energies slightly greater than $\mathcal{E}_{st}$ may be lensed around the grid wire, increasing the transmission for these particular energies to a value greater than the optical transparency. These errors are significantly reduced by using a pair of retarding grids instead of just a single retarding grid [*Klenzing et al.*, 2008]. However, the addition of an additional grid may cause high-energy particles lensed around wires in the first grid to be collected by wires in subsequent grids, leading to a decrease in the expected current.

A plasma sheath on the order of λ_D will form around the spacecraft body and adjacent to the sensor. Curvature of the sheath boundary (i.e. not plane and parallel to the RPA aperture) will cause two related effects. First, the area of ion collection becomes larger, and second, the ions collected over the opening will have a range of angles of attack. For typical cylindrical sensor configurations, these effects need to be taken into account unless the sheath thickness (λ_D) is relatively small compared to the dimensions of the plane front of

the sensor [*Knudsen*, 1966]. This is usually not an issue in the ionosphere; e.g. $\lambda_D \approx 2.5$ cm while the flat ground plane of the RPA is 40 cm in diameter.

Typical I–V curves obtained from the RPA on Atmosphere Explorer-C (AE-C) are shown in Figure 2.8. The top three panels show I–V curves obtained when at least two ion mass groups are present in sufficient quantities to allow both the spacecraft potential and the ion drift velocity to be determined. The greater ram energy of the heavier ions in the vehicle frame of reference cause the ion current at high positive retarding potentials (> 10 V) to be almost entirely due to heavier molecular ions (N_2^+, NO^+, O_2^+). At typical orbital satellite velocities the ram energy is approximately 0.3 eV per amu so molecular ions have approximately 4 to 5 eV more energy on average than the O^+ ions [*Hanson et al.*, 1970]. At low retarding potentials (< 3 V) the current is due to the sum of all constituent ions. It is typical that the heavier ion currents are saturated before the light ions can produce a recognizable current and so the light ions (H^+, He^+) can still be determined from the I–V curve. This is true if the concentration of the light ions is more than 5% of the total ion concentration. The O^+ and N^+ current maxima can also clearly be seen in the top three panels of Figure 2.8.

Panels 4 and 5 of Figure 2.8 show cases where large drift velocities toward and away from the sensor face distort the natural shape of the I–V curve. If the drift velocity is large enough, the maximum retarding voltage may not be enough to repel the ions; panel 6 shows the I–V curve for which the observed ion drift velocity was 3015 m/s. The 32 V maximum retarding potential was just able to produce an adequate I–V curve for computation.

Ions with large thermal velocities will disperse within the sensor and not all ions will reach the collector. For O^+ and heavier ions the errors introduced rarely exceed a few percent and even for the lighter ions the increase in normal velocity due to the vehicle potential tends to minimize the effects. However, corrections as large as 20% or more may be applicable for H^+ ions [*Hanson et al.*, 1970].

Both photoemission from solar illumination of the sensor and energetic particle fluxes must be considered as sources of error in the determination of the ion drift velocity. Current

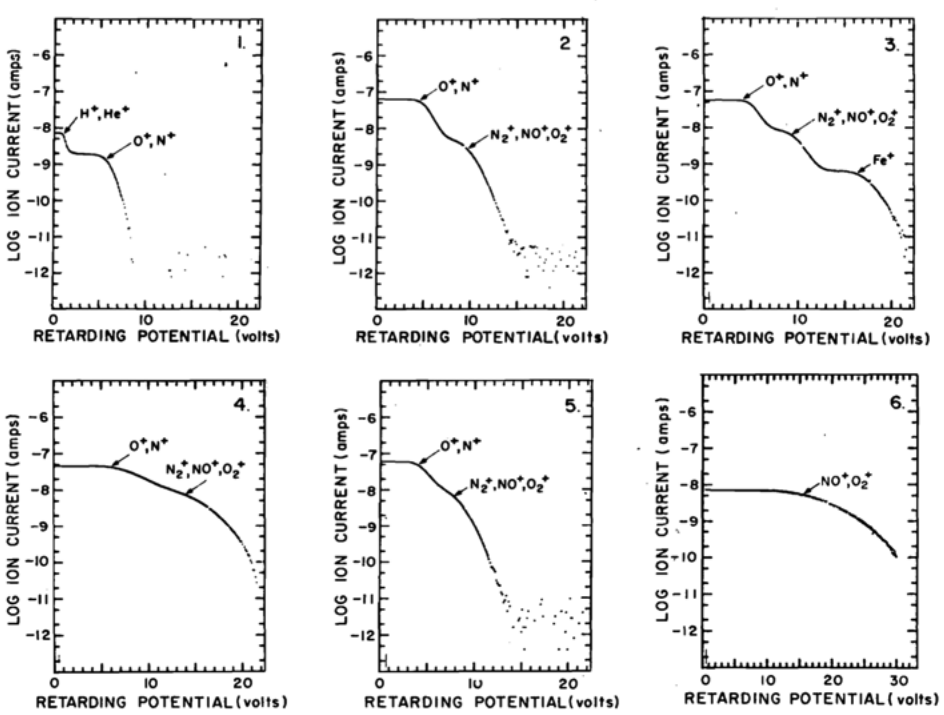

Figure 2.8. I–V characteristic curves obtained from the RPA on AE-C. The observed mass groups are indicated on the curves. Used with permission from *Hanson and Heelis* [1975].

due to photoelectrons from solar illumination of the suppressor grid is directly related to solar zenith angle and can be subtracted. Energetic particles will typically be repelled by the suppressor grid and, therefore, only very-high-energy electrons will reduce the measured current. This can occur in the auroral region where large anisotropic, non-uniform, time dependent electron fluxes exist. Fortunately these effects are confined to small spatial regions and the contaminated data can easily be recognized. An additional complication associated with energetic particle fluxes is the large ion concentration and composition gradients that accompany them. This type of error is most likely to occur at night at low altitudes where the ion concentration is small [*Hanson and Heelis*, 1975].

Spatial or temporal ion density irregularities can introduce large errors in the determination of V_x. As noted by *Hanson and Heelis* [1975], the total retarding potential sweep time for AE-C is 750 ms, whereas it is possible for the ion density to change by a factor greater than two in 200 ms under disturbed conditions. A final consideration involves the limits of the detectors. The lower limit for current detection of modern electrometers is

about 2 x 10^{-11} A. This places a lower limit of about 100 cm^{-3} on the ion concentration for which the ion temperature and drift velocity can be derived.

2.4.2. Ion Drift Meter

The Ion Drift Meter is also an ion trap that uses biased grids to propel ions to the collector plate and repel electrons. Instead of measuring the energy (velocity) distribution, the IDM measures the asymmetry in the amount of current collected on segmented collector plates. This current asymmetry can be directly related to the arrival angle of the ions, and since the parallel velocity is already known from the RPA, the ion drift velocity perpendicular to the sensor plane can be found using simple geometry.

A side view schematic of the IDM is shown in Figure 2.9; the sensor is mounted in the same manner as the RPA with the sensor aperture perpendicular to the satellite velocity. When the satellite is moving supersonically with respect to a hot plasma, the sensor aperture will produce a collimated ion beam within the sensor. The aperture grids (G3) and the shield grids (G4 and G5) are all grounded to the sensor/spacecraft potential. Immediately preceding the collector is a suppressor grid (G6) that is negatively biased to prevent electrons from accessing the collector and to suppress photoelectrons emitted from the collector. The grid just outside the aperture (G2) may be set to either the sensor ground or be positively biased to repel H^+ ions that have thermal velocities comparable to the satellite velocity and will degrade the measurement. Because the retarding grid is external to the aperture, it does not have an effect on the arrival angle of the ions in the collimated beam.

Figure 2.10 shows the face of the sensor plane (bottom) and the geometry of the sensor relative to the incoming ion beam (top). The collector is sectioned into four segments so that pairing segments AB and CD allow the determination of the vertical angle of arrival (and thus the vertical velocity, V_z), while pairing segments AC and BD gives the horizontal component, V_y. The other horizontal component of the velocity, V_x, which is in the ram direction of the satellite, is determined solely by the RPA (section 2.4.1). Figure 2.11 shows the sensor coordinates in relation to the satellite body and direction of flight, $\mathbf{V_s}$. If the ion beam is perpendicular to the sensor plane, the arrival angle will be zero and both pairs of

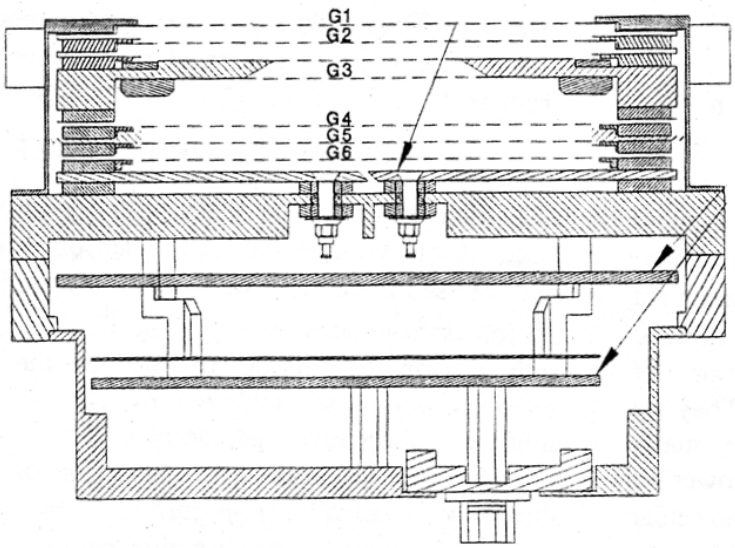

Figure 2.9. Cross section of a planar ion drift meter. Used with permission from *Heelis and Hanson* [2013].

collector plates will receive the same current. When the entry velocity is not perpendicular, the current distribution will not be equal and will increase as the arrival angle increases.

The perpendicular velocity is calculated by taking a ratio of the current difference, $\Delta I = I_{AC} - I_{BD}$ to the total current $I = I_{AC} + I_{BD}$. The currents are defined as

$$I_{AC} = kW\left(\frac{W}{2} + D\tan\alpha\right), \tag{2.25}$$

$$I_{BD} = kW\left(\frac{W}{2} - D\tan\alpha\right), \tag{2.26}$$

where k is a number that depends on the ion density, charge, and transmission properties of the sensor, W is the width of the aperture, D is the depth of the sensor, and α is the ion arrival angle. Because

$$\tan\alpha = \mathbf{V}\cdot\hat{\mathbf{Y}}/\mathbf{V}\cdot\hat{\mathbf{X}}, \tag{2.27}$$

taking the ratio of ΔI and I gives

$$\mathbf{V}\cdot\hat{\mathbf{Y}} = \frac{\Delta I}{I}\frac{W}{2D}\mathbf{V}\cdot\hat{\mathbf{X}}. \tag{2.28}$$

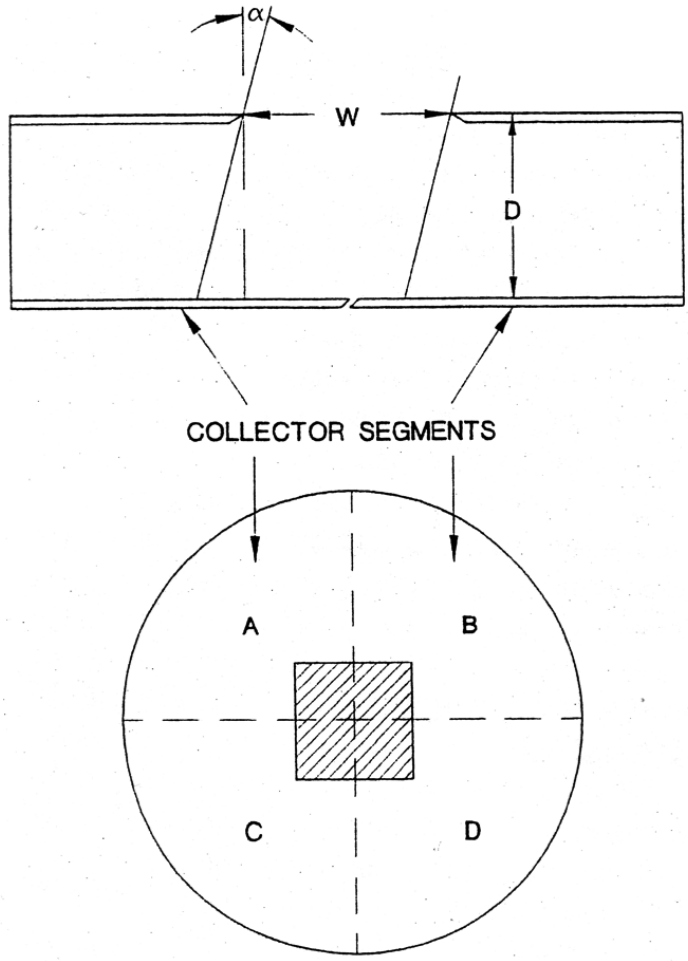

Figure 2.10. The ion arrival angle, α, as measured by the IDM. The asymmetry in the current collected from two halves of a segmented collector determines the arrival angle. Used with permission from *Heelis and Hanson* [2013].

Everything on the right side is either known from the sensor configuration (W, D) or is measured (ΔI and I by the IDM and $\mathbf{V} \cdot \hat{\mathbf{X}}$ by the RPA). $\mathbf{V} \cdot \hat{\mathbf{Z}}$ is obtained in a similar fashion when the segment pairs are switched.

IDM measurement errors originate in many of the same sources as the RPA. Photoemission causes spurious currents and high thermal velocities affect the measured arrival angle. Photoemission can cause significant errors when the resulting current is not constant across the sensor plates. This is especially a problem when the spacecraft is illuminated just after emerging from eclipse and the zenith angle is high. Not only is the resulting current anisotropic, but the suppressor grid holder may also be illuminated and, depending on the

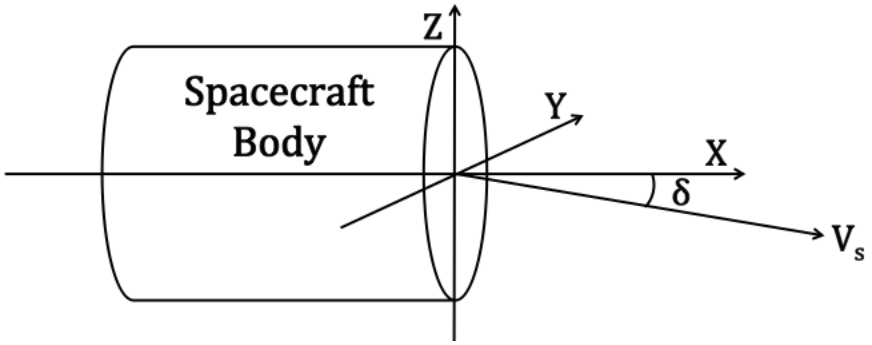

Figure 2.11. Schematic of satellite velocity vector in relation to sensor axes.

instrument design, could significantly add to the extraneous current [*Hanson and Heelis*, 1975]. If the photocurrent magnitude is known as a function of solar zenith angle, this error can be calibrated out. Ions with high thermal velocities can also significantly affect the calculation of the drift velocities. These ions will readily enter the sensor aperture, but the collimated beam will disperse due to the significant thermal velocity resulting in loss of accuracy in the true ion arrival angle. If the sensor contains a retarding grid (G2 as described above) it can be positively biased to aid in the exclusion of lighter ions. This error is greatest when the ion composition contains a significant portion of H^+, resulting in an error classified as the H^+ anomaly. Acceleration of the ions due to the plasma sheath and the resulting negative spacecraft potential will also change the ambient ion arrival angle. This effect can change the derived perpendicular velocity by up to 10%.

Uncertainty in spacecraft attitude can also have a significant effect in the determination of the perpendicular ion drift velocity, much more so than in the calculation of the parallel component. If the angle, δ, between the satellite velocity and the sensor look direction is small (Figure 2.11), then the parallel ion drift velocity is given by

$$\mathbf{V_x} = \mathbf{V_s} \cos \delta. \tag{2.29}$$

This is a weak function of δ, and for small angles the error imposed by using an uncorrected $\mathbf{V_s}$ or from the specification of δ is quite small. The error in the perpendicular drift velocity

($\Delta\mathbf{V_p}$) due to an error in the offset angle ($\Delta\delta$), is given by

$$\Delta\mathbf{V_p} = \mathbf{V_s} \sin\Delta\delta \approx \mathbf{V_s}\,\Delta\delta. \tag{2.30}$$

For a satellite velocity of 7.5 km/s, an error of 1° in δ corresponds to a 150 m/s error in the perpendicular velocity [*Heelis and Hanson*, 2013]. Therefore, knowledge of the satellite attitude is very important in correctly specifying the perpendicular ion drift velocity. Table 2.1 summarizes error sources and mitigation techniques for both the RPA and IDM.

2.4.3. Defense Meteorological Satellite Program

The mission of the Defense Meteorological Satellite Program is to provide global visible, infrared, and passive microwave data, as well as other specialized meteorological, oceanographic, and solar-geophysical data in support of worldwide Department of Defense operations. DMSP satellites are in low-Earth, near-circular, sun-synchronous polar orbits near 840 km altitude with an inclination near 98°. This results in keeping the spacecraft's orbit roughly fixed in geographic local time throughout the year. The orbital period is 101 minutes resulting in just over 14 orbits per day.

The first DMSP satellites were launched in 1965, but it was not until 1976 that the payload included space weather sensors. Of the five space environment sensors flying on DMSP, the Special Sensor Ion and Electron Scintillation Monitor (SSIES) package built at the Center for Space Sciences at the University of Texas at Dallas contains the thermal plasma instruments (RPA and IDM) that measure ion drifts. DMSP launched the first satellite with RPA and IDM sensors in 1987 and they have been on every DMSP spacecraft since. The flight-15 (F15) spacecraft, launched into a 2100 MLT orbit in December 1999, is in a suitable location to study the dawn–dusk convection patterns.

2.4.4. DMSP Measurement Errors

When direct particle detection is employed to make velocity measurements, it is important to consider which gas species are involved and the precise nature of the interaction between the satellite and the ambient gas being detected. The dominant constituents of

Table 2.1. RPA and IDM Error Sources and Mitigation Techniques

Problem	**Effect**	**Mitigation**
RPA		
Unknown spacecraft potential	For $\Delta\Phi_s = 0.1$ V, $\Delta V_x = 40$ m/s	Apply voltage to spacecraft
Single ion / ion mass group	Changes in Φ_s vs. V_x unclear	High resolution mass spectrometer
High-energy ion lensing	Increases transmission	Use pair of retarding grids
Plasma sheath curvature	Increased collection area/modified incident angle	Sensor plane dimension $> \lambda_D$
Large drift velocity	Unable to repel ions; distorted I–V curve	Increase retarding voltage
Large thermal velocity	Ions disperse in sensor; H^+ errors up to 20%	Data uncertain when $H^+ > 20\%$
Solar illumination of sensor	Photoemission causes erroneous current	Remove using solar zenith angle
Energetic particles	Photoemission reduces actual current	Spatially confined, easily recognized
Ion density irregularities	Large errors in V_x determination	Decrease RV sweep time
IDM		
Spacecraft attitude uncertainty	If $\mathbf{V_s} = 7.5$ km/s and $\Delta\delta = 1°$, $\Delta V_y = 150$ m/s	Remove errors during data processing
Solar illumination	Photoemission causes spurious currents	Remove using solar zenith angle
Large thermal velocity	Erroneous ion arrival angle	Positively bias retarding grid
Plasma sheath / negative Φ_s	Ion acceleration changes arrival angle by 10%	Sensor plane dimension $> \lambda_D$

the upper atmosphere below 500 km have average thermal velocities that are small compared to satellite velocities. In the high-altitude region, which is populated with hot hydrogen and helium ions, the mean thermal ion velocities can be comparable to or greater than the satellite velocity. When the ions have large thermal velocities, the ion beam disperses within the sensor altering the measured arrival angle and current ratios. Atomic oxygen is normally the dominant ion in the 250–500 km altitude range with mean thermal velocities around 1 km/s at 1000 K, which is less than the typical satellite velocity of approximately 8 km/s. Due to their smaller mass, H^+ ions have thermal velocities around 4.4 km/s; the H^+ anomaly occurs when the ratio of H^+ to O^+ exceeds 20% and the high thermal velocities of the hydrogen ions become comparable to the spacecraft velocity causing error in the velocity determination. Electrons have a very large thermal velocity around 190 km/s and cannot be used to determine the plasma drift velocity [*Schunk and Nagy*, 2009].

The DMSP ion drift velocity data suffer from two main sources of error. The first is due to satellite attitude knowledge and the second occurs when there is a large percentage of light ions (H^+ and He^+). The high thermal velocity of the light ions causes significant errors in the IDM data. As mentioned previously, this is because these ions cause the collimated beam to disperse resulting in an incorrect arrival angle measurement. For DMSP, this typically becomes a problem when the light ion concentration reaches 20 to 25% of the total ion density [*Hairston and Heelis*, 1993]. This environment occurs primarily at night in the winter hemisphere and both the horizontal and vertical velocity show anomalously large values ($>$ 1.9 km/s) and large scatter ($\sim$0.4 km/s) as seen in Figure 2.12. The main correction for the H^+ anomaly is done in the ground processing.

The second source of error is in the attitude determination of the spacecraft. The DMSP spacecraft is spin stabilized and uses a horizon scanner and momentum wheels to maintain its orientation. If the orientation is not precisely known, a direct current offset appears in the data that typically varies with season [*Berg et al.*, 2013]. This offset accumulates across the orbit and is observed as nonzero zonal velocities at low latitudes (after corotation has been removed). The drift data are typically converted to an electric field and then integrated

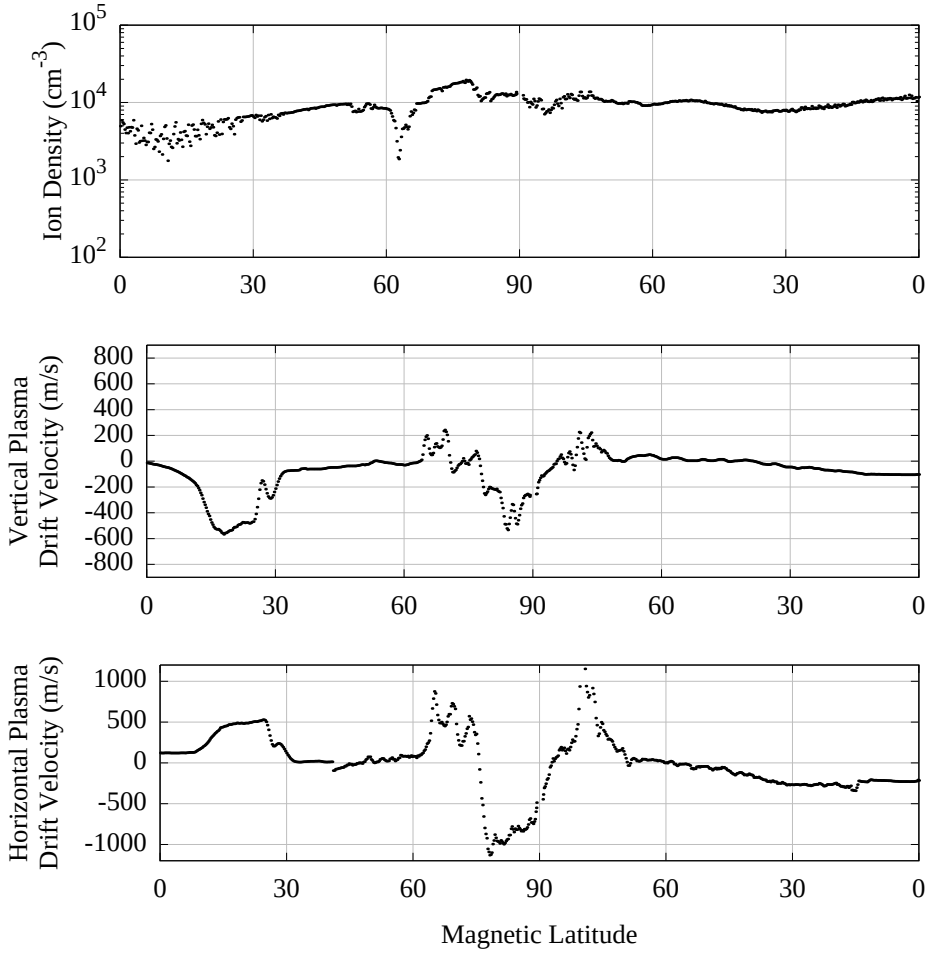

Figure 2.12. DMSP ion density and drift velocities in the northern hemisphere. The plot starts at the equator and goes over the northern polar region. The H+ anomaly is apparent as the large nonzero velocities in both the horizontal and vertical flows on prior to the northern polar region. Errors due to the satellite attitude can be seen in the offset from zero of the horizontal drift velocity.

to obtain the potential. The integrated potential is then calibrated so it goes to zero at low latitudes [*Hairston and Heelis*, 1993]. Figure 2.13 shows both the original integrated potential (red line) and the adjusted potential with the direct current offset removed (black line). The same process for removing the direct current offset from the potential can be applied directly to the plasma drift velocities.

Although accurate measurements are critical in understanding and creating models of the ionospheric processes, no matter the method used to obtain either ion drift or electric field measurements in the polar cap, the data is limited both spatially and temporally. Addi-

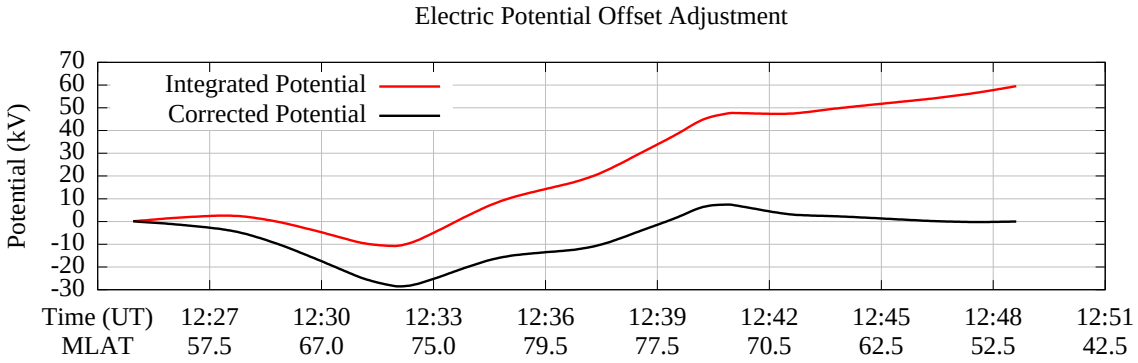

Figure 2.13. Integrated and corrected electric potential for a polar orbit. The red line is the original integrated electric field data that includes the spacecraft attitude error. The black line is the data recalibrated to return to zero at low latitudes.

tionally, the real-time assimilation of this data into physical models is still being developed. Therefore, the need exists for a comprehensive description of the entire polar cap convection pattern. The following section describes the various empirical polar cap convection models that are typically used as drivers for ionospheric models.

2.5. Polar Cap Convection Models

Many polar cap convection and electric field models have been developed including empirical, statistical, theoretical, and physical models. Most are climatological models with the weather features of the polar cap convection being difficult to capture as the polar cap field distributions can shift on a time scale of minutes in response to changes in the IMF configuration [*Heppner and Maynard*, 1987]. *Kamide et al.* [1982] captured the full convection pattern using seventy magnetometer stations to deduce patterns of electric fields and currents for a three day period in March 1978. A five minute time resolution allows the growth and decay of the high-latitude three-dimensional current system during individual magnetospheric substorms to be studied.

Volland [1975] and *Heppner* [1977] were two of the first to create models of the high-latitude electric fields for different solar and geomagnetic conditions. The analytical model of *Volland* [1975] provides a simple parameterization of the electric potential. Self-consistent calculations have shown the electric field intensity outside the polar cap decreases rapidly

with decreasing latitude due to the effect of ring current ions and the coupling of the ionosphere and magnetosphere with FACs, which tends to shield the internal magnetosphere and the midlatitude ionosphere from the magnetospheric convection field. The simplest form of the *Volland* [1975] electric field potential is a function of only two parameters: the total potential drop across the polar cap (Φ_0), and the attenuation exponent (γ). The analytical expression is given as

$$\Phi = \frac{1}{2}\Phi_0 \left(\frac{\sin\Theta_0}{\sin\Theta} \right)^{2\gamma} \sin\phi, \tag{2.31}$$

where the electrostatic potential at ionospheric heights is given as a function of the magnetic local time, ϕ, and of the invariant colatitude, Θ, for all colatitudes equatorward of the colatitude, Θ_0, of the polar cap/auroral zone boundary. A uniform electric field is obtained with $\gamma = 1$. The inverse power sine wave was chosen as the best analytical representation of the middle- and low-latitude electric potential decay. The two regions considered by this model included one within the polar cap and another for middle and low latitudes. A simplistic representation of the two-cell convection pattern as obtained by modeling these two regions (see Figure 2.5) with a region of positive electric potential on the dawnside and a region of negative potential on the duskside. The plasma flows antisunward within the polar cap and sunward at lower latitudes. Although this simplistic model was updated [*Volland*, 1978] to include a third region in the auroral zones to better approximate the transition region of the meridional electric field, equation 2.31 is still valid in the polar cap and the midlatitude fall-off region and is still being used today in ionospheric models such as the Utah State University (USU) TDIM as a simple representation for the convection electric field. In the USU TDIM model, the total potential drop, Φ_0, depends on Kp while the attenuation exponent is fixed at $\gamma = 2$.

The *Volland* [1978] model is still being used primarily because it is one of the few simple analytical models. The *Heppner and Maynard* [1987] empirical model was hand fit to data from many satellite passes and takes into account IMF conditions with the three different convection electric field models shown in Figure 2.14. Models A and DE represent pattern distributions encountered under northern hemisphere negative IMF B_y conditions,

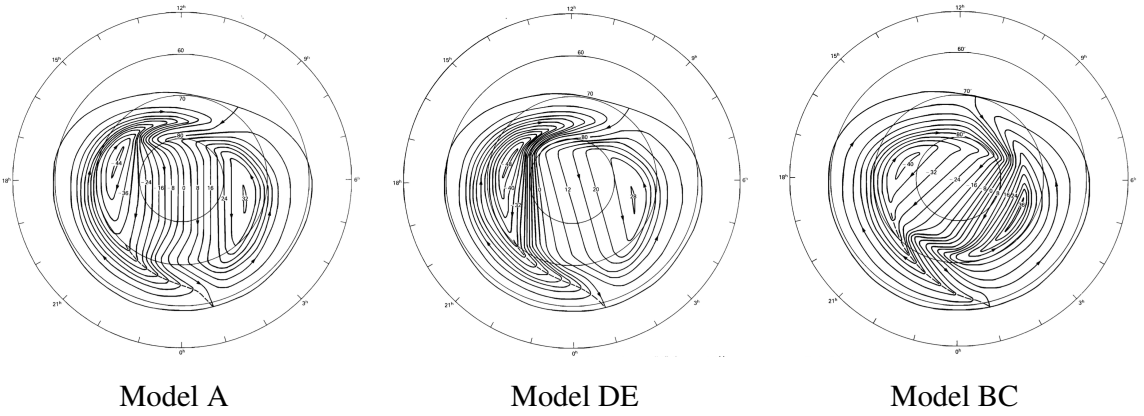

Figure 2.14. *Heppner and Maynard* [1987] convection patterns. Three different IMF conditions are shown with all three models correlating to $-B_z$ IMF. Model A represents IMF $0 > B_y > -10$ nT in the northern hemisphere. Model DE represents $B_y < -10$ nT IMF conditions in the northern hemisphere. Model BC represents $+B_y$ IMF conditions in the northern hemisphere. All contours are plotted in 4-kV intervals. Used with permission from *Heppner and Maynard* [1987].

while model BC represents positive IMF B_y conditions in the northern hemisphere. Model A best represents IMF B_y close to zero (but still negative), while model DE represents conditions with a largely negative B_y component. All three models represent negative IMF B_z conditions. The models also take into account the fact that the signatures in the southern hemisphere for negative IMF B_y conditions are the same as those in the northern hemisphere for positive IMF B_y conditions, and vice versa, analogous to the hemispherical reversal of the dawn–dusk polar cap electric field [*Heppner*, 1972, 1973, 1977]. To represent B_z positive, the BC and DE models are distorted by stretching the evening cell towards noon and rotationally twisting the foci clockwise. The pictorial results of *Heppner and Maynard* [1987] were later converted into a more useful numerical representation by *Rich and Maynard* [1989] using spherical harmonics.

One of the more widely used empirical models is that of *Weimer* [2001]. This model uses the electric field data available from Dynamics Explorer-2 to construct a global statistical representation of the high-latitude convection pattern as a function of magnetic local time and geomagnetic latitude. It shows the dependence of the convection pattern on the IMF clock angle and magnitude, the dipole tilt angle, the solar wind velocity and density, and the

AL index. The data was divided into different groups based on the geophysical conditions and a least square fitting technique using spherical harmonics was used to obtain a global map of the electric potential for each group. The *Weimer* [2001] model is an updated version of the *Weimer* [1995] and *Weimer* [1996] models. An example of the statistical patterns is shown in Figure 2.15. An update in 2005 combined the electric potential model with a model for FACs in order to obtain more accurate electric field values and boundary locations [*Weimer*, 2005]. The addition of the FAC model allows the calculation of the total Poynting flux and Joule heating in the ionosphere.

While many other empirical and mathematical models [e.g., *Hairston and Heelis*, 1990; *Papitashvili and Rich*, 2002; *Rich and Hairston*, 1994; *Sojka et al.*, 1986] have been developed in an attempt to more accurately describe the global distribution of the high-latitude convection pattern, satellite data is not the only source for high-latitude ionospheric convection models. Ground-based magnetometers [e.g., *Friis-Christensen et al.*, 1985; *Kamide et al.*, 1982; *Papitashvili et al.*, 1994], as well as ground-based radars, have been used to develop empirical models of the high-latitude ionospheric convection. *Foster et al.* [1986] used ISR data from Millstone Hill, United States and Sondre Stromfjord, Greenland to derive a pattern very similar to *Heppner and Maynard* [1987]. The Millstone Hill ISR data was also used by *Holt et al.* [1987] to develop an empirical convection model while *Alcayde et al.* [1986] and *Peymirat and Fontaine* [1997] used the European incoherent scatter (EISCAT) radar to develop their model. The most recent iterations of observationally based statistical models come from SuperDARN [e.g., *Cousins and Shepherd*, 2010; *Grocott et al.*, 2012; *Lester*, 2013; *Pettigrew et al.*, 2010], which at the end of 2012 consisted of a network of 31 operational high-frequency coherent scatter radars.

SuperDARN has been used extensively in the past decade as a source for the electric field and ion drift data used in constructing high-latitude convection models. The radars use the doppler shift of the signal imposed by the motion of ionospheric particles to determine the vector velocities perpendicular to the magnetic field [*Lester*, 2013]. With radars located at both high and midlatitudes the entire convection pattern can be mapped to in-

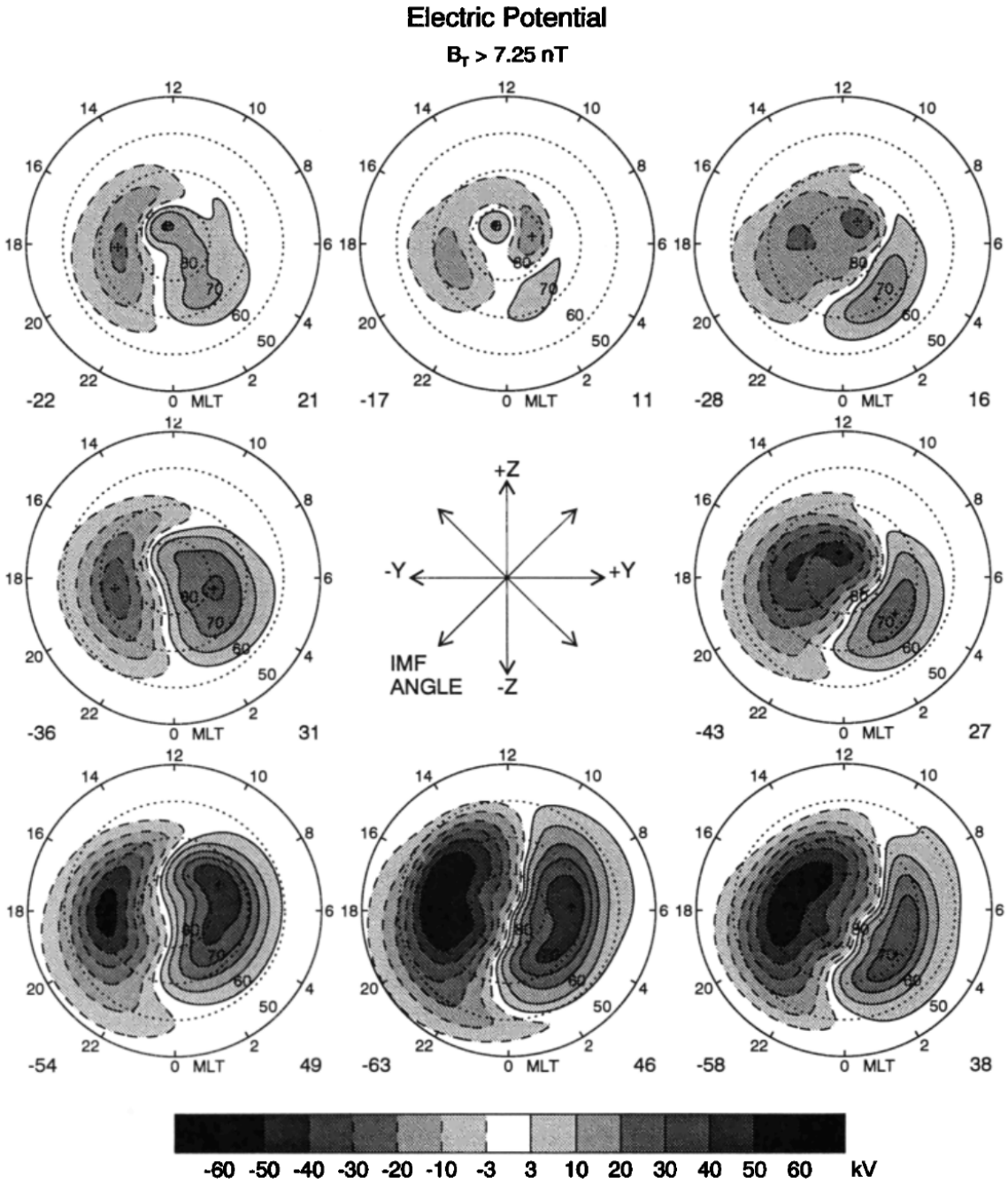

Figure 2.15. *Weimer* [1995] convection patterns for $B_T > 7.25$ nT. The positive and negative potentials are indicated by solid and dashed lines, respectively. The numbers in the lower left and right corners of each graph show the values of the smallest and largest potentials in each pattern, while plus symbols mark the locations of these points. Used with permission from *Weimer* [1995].

clude periods when strong magnetic storms occur. A discrete set of statistical convection patterns was obtained by *Pettigrew et al.* [2010] using an averaging and fitting technique applied to the plasma drift data obtained from SuperDARN backscatter measurements. Taking into account the dipole tilt angle, separate patterns for the northern and southern hemisphere were calculated and it was shown the dipole tilt has significant impacts on the convection patterns that were not symmetric between hemispheres. *Cousins and Shepherd* [2010] extended the work of *Pettigrew et al.* [2010] by modifying the binning and averaging methods and adding in a dependence on the solar wind velocity, which has been shown to be effective in driving ionospheric convection. In addition, the model has increased functionality that allows the results to be used as a dynamical, rather than discrete, model for high-latitude convection [*Cousins and Shepherd*, 2010]. The basis functions of the spherical harmonic expansion of the ionospheric electric potential to the radar measurements are examined in detail by *Grocott et al.* [2012] to describe the different characteristic elements of the ionospheric convection pattern. This examination shows approximately two-thirds of the voltage associated with the typical convection pattern is described by a simple twin vortex basis function while the remaining one-third is associated with deviations from the twin vortex, namely the IMF B_y dawn–dusk asymmetries and high-latitude sunward convection cells associated with IMF $B_z > 0$. A recent major discovery with SuperDARN is the observation of large-scale ionospheric flows in the nightside ionosphere during relatively quiet magnetic conditions [*Lester*, 2013].

The Assimilative Mapping of Ionospheric Electrodynamics procedure is different from all other high-latitude convection models in that it was devised to estimate the time-varying distributions of electric fields, currents, conductivities, and related quantities over the entire polar ionosphere by the mutually consistent synthesis of a variety of direct and indirect observations [*Richmond*, 1992]. The AMIE model has been used in a wide range of studies where several different data sources have been assimilated; some of these sources include electric fields from radars and satellites, electric currents from satellites, magnetic perturbations from satellites, and ground-based magnetometers [*Richmond and Kamide*, 1988].

However, in its real-time mode, only the ground-based magnetometer data is assimilated with convection patterns produced in one-minute increments. *Bekerat et al.* [2005] showed these real-time specifications of the convection pattern adequately represent the DMSP observations about 32% of the time, which is a significant improvement over statistical convection patterns [*Bekerat et al.*, 2003].

Several kinetic and magneto hydrodynamic (MHD) models that use fluid equations to describe the particle populations are also in use. The Rice Convection Model is one of these kinetic models and treats the large range of particle energies within the inner magnetosphere as approximately 100 different fluids [*Toffoletto et al.*, 2003]. The kinetic equations and numerical methods chosen provide an accurate treatment of the inner magnetosphere and include the flow of electric currents along magnetic field lines to and from the conducting ionosphere. The currents and associated electric fields are self-consistently computed, where perfectly conducting field lines are assumed. Induction electric fields associated with a time-dependent magnetic field are also used [*Toffoletto et al.*, 2003]. Coupling the kinetic model to an ionospheric convection model allows a self-consistent solution for the solar wind–magnetosphere–ionosphere system. Significant MHD models in use include the Lyon–Fedder–Mobarry (LFM) model [*Lyon et al.*, 2004], the Space Weather Modeling Framework (SWMF) [*Toth et al.*, 2005], which is built around the BATS-R-US MHD core [*Powell et al.*, 1999], the Open General Geospace Circulation Model (OpenGGCM) [*Raeder et al.*, 2008], and the Grand Unified Magnetosphere–Ionosphere Coupling Simulation (GUMICS).

The MHD and kinetic models are based on first-principals physics and take into consideration physical properties such as joule/frictional heating through the Poynting flux. The empirical models of *Heppner and Maynard* [1987], *Weimer* [2005], and *Foster et al.* [1986] use various parameterizations to characterize the high-latitude plasma convection pattern. The *Volland* [1978] model solution falls between these two regimes with a parameterized solution based on physical properties. Most current models can reproduce the climatological structure of the high-latitude convection pattern, but few are designed to capture the instantaneous features needed in space weather applications.

CHAPTER 3
METHODOLOGY

3.1. Overview

This chapter discusses the data used in this study and how it is prepared for use. The first section discusses the method used to calibrate and smooth the data. Section 3.3 outlines the coordinate system used for the data and the transformations applied to each orbit. The last section discusses the method used to bin the data according to the solar wind configuration and geomagnetic activity.

3.2. Data Preparation

In this study, ion drift velocities obtained from DMSP during the low solar activity period from January 2007 through December 2010 are investigated. DMSP satellites are in polar orbits that are sun synchronous at an altitude of 830 km with an orbital period of 101 minutes. Along with all three velocity components for the ion drift, the SSIES instrument suite onboard the DMSP satellite measures the total ion density, ion composition, ion and electron temperatures, and calculates the corotation velocity components and spacecraft and sensor potentials. The RPA and IDM data is binned into 4-second averages, which translates into approximately 30 km of spatial coverage, so root mean square errors and standard deviation values are also available. The data file includes positioning information, such as the date and time, altitude, magnetic latitude and local time, geographic latitude and longitude, solar zenith angle, and spacecraft mean velocity. The F15 satellite is used because the orbits are primarily on the dayside in an approximately dusk to dawn path in the northern hemisphere. The southern hemisphere passes are primarily on the nightside and will not be used in this study. Additionally, a large swath of coverage in magnetic coordinates is available due to the offset of the Earth's dipole from its spin axis. Figure 3.1 shows the orbit paths in magnetic coordinates for three days throughout the study period. As time progresses, the satellite slowly precesses westward; by 2010 the ascending node has shifted to 1600 MLT, while the descending node has shifted to 0500 MLT.

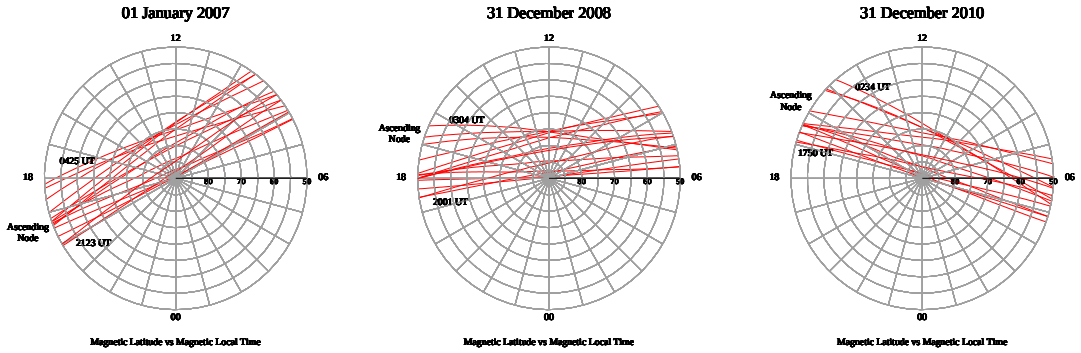

Figure 3.1. DMSP F15 orbit paths. Three different days spread across the study period are shown. The offset of the Earth's dipole from its spin axis causes the sun synchronous orbits to create a swath of coverage in magnetic coordinates. The satellite is also slowly precessing westward such that the ascending node shifts from 1900 MLT in 2007 to 1600 MLT in 2010.

Before an analysis of the data is possible, it must first be calibrated and smoothed. Calibrating the data will remove any instrument inaccuracies, while smoothing the data removes the smallest scale perturbations. These small-scale perturbations represent phenomena on the order of 50 km or less, including gravity waves and traveling ionospheric disturbances. Though interesting, these phenomena are too small to be captured by the DMSP instruments that have just a 30 km resolution. The instrumentation is able to capture the medium and large-scale features of the ionosphere, including atmospheric tides and gravity waves that are on the order of 50 to 500 km, respectively. The methods used to prepare the data for analysis were done in collaboration with Dr. Roderick Heelis, the Principal Investigator for the IDM and RPA instruments on DMSP.

As discussed in section 2.4, the two main sources for instrument error are satellite attitude errors and the H^+ anomaly. Errors in satellite attitude create an offset that must be consistently removed from the data while the H^+ anomaly (regions where the percentage of H^+ is large) results in inaccurate ion drift measurements. Errors due to the H^+ anomaly are removed by setting four specific filters. First, any data point with an ion density less than 1.5×10^4 cm^{-3} or greater than 8% of an 11-point median is removed. Second, if the fraction of oxygen ions is less than 80% (or greater than 100%), the data is ignored.

Next, any data point with an ion or electron temperature greater than 12,000 K is removed. Finally, any velocity with an absolute value greater than 4,000 m/s is removed. After these three tests have been applied, the velocity data is smoothed using a 5-point running boxcar filter to remove the small-scale perturbations. While small perturbations in the data may represent actual physical features, this study is to investigate medium-to-large-scale features, so the smallest perturbations in the data will be ignored.

Next, the satellite attitude error is addressed. The error due to the direct current offset is removed from the x and y velocity components in a manner similar to the calibration of the electric potential shown in Figure 2.13. The velocity is used instead of the potential or the electric field because it is the quantity being directly measured. More approximations and assumptions are required in the calculation and integration of the electric field to obtain the electric potential. As many simplifying assumptions are already being made, it was decided to adjust the velocity directly, instead of propagating the error into the electric potential before removing it. Even so, it is possible the adjustments made to the velocity components may contaminate the fall-off gradients that are of interest.

To correct the velocity profiles, the low-latitude velocity is assumed to go to zero after corotation is removed; this assumption arises from the fact the low-latitude equipotential is also assumed to be zero due to the shielding by Birkeland currents. If the measured low-latitude velocity is not zero, an offset is calculated for both the ascending and descending nodes of the orbit. The entire orbit is shifted equally by the ascending node offset, but the descending node offset is distributed linearly across the polar region.

As recommended by Dr. Heelis, instead of calibrating each orbit individually, the offset is determined on a monthly basis, and this monthly offset is then applied to each individual orbit. The calibration is done this way because the attitude error should have a seasonal or monthly trend making the day-to-day error consistent [*Berg et al.*, 2013]. The offset is determined by first finding the latitude between 40° and 60° where the standard deviation of an entire month's worth of velocity data is the smallest. The calibration is done separately for each velocity component. Once the offset latitudes for both the ascending and descending

nodes are chosen, the monthly mean is calculated at each location—these are the offsets. First the entire orbit is shifted by the ascending node offset; this shift is also added to the descending node offset. The descending node offset is then removed from the orbit. The full adjustment is taken at the descending node offset latitude and the amount of the adjustment is decreased linearly back over the polar region so no additional change is applied at the ascending node offset latitude. Figure 3.2 shows the original and adjusted horizontal velocity components both before and after the offset has been applied for the month of June 2009, and Figure 3.3 shows the monthly offsets applied to the V_y velocity component for a single orbit in June 2009. Data equatorward of the offset latitude is not used for any further analysis.

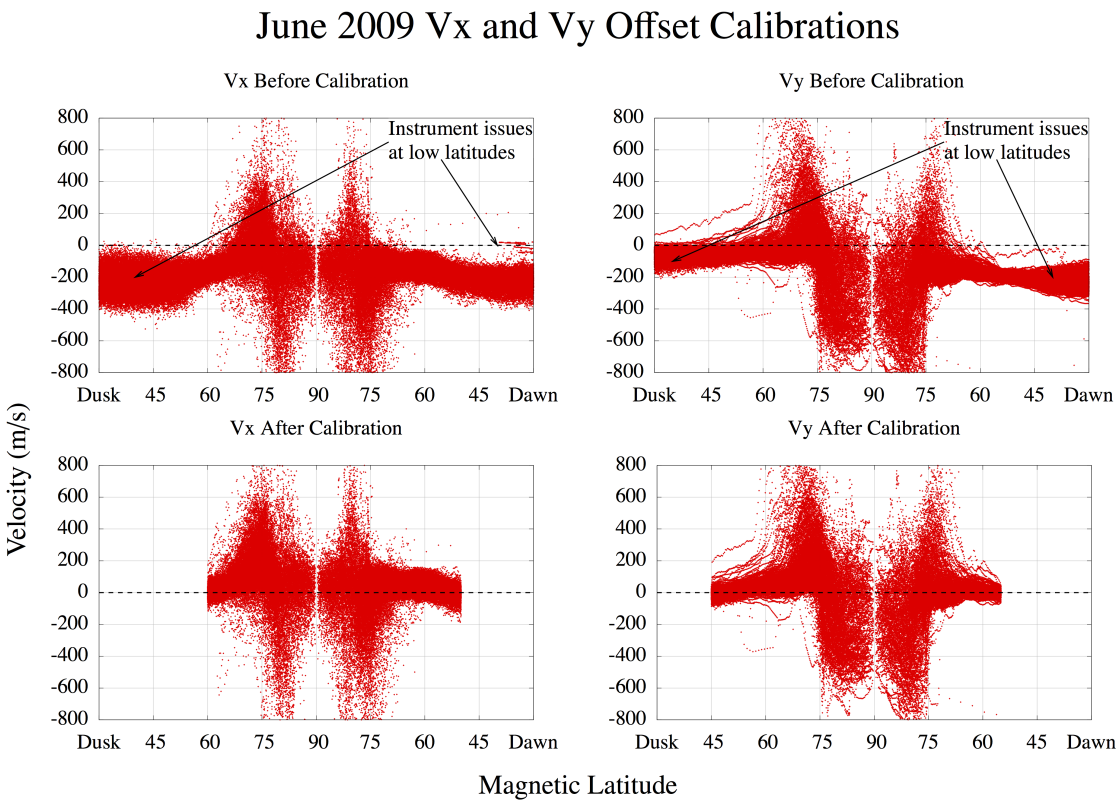

Figure 3.2. Original (top) and adjusted (bottom) velocities for June 2009. The offset was determined at the latitude with the smallest standard deviation and was subtracted linearly across the orbit.

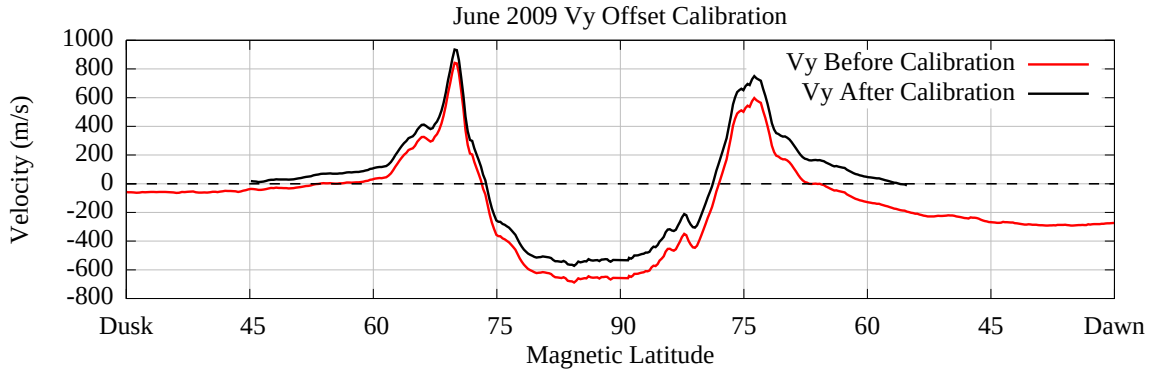

Figure 3.3. Original (red) and adjusted (black) V_y for a single orbit in June 2009. The offset latitudes and values were determined using Figure 3.2.

3.3. Coordinate Transformation

The satellite data is given in a reference frame based on the satellite's current position. The z direction is vertically upward, the x direction is the satellite ram direction, and the y direction is perpendicular to the x direction to complete a right-handed coordinate system. Because the ram direction for each orbit is oriented differently to the dusk–dawn line, the data must be transformed from the satellite reference frame to a general reference frame. This new reference frame is a Cartesian coordinate frame with the z direction remaining vertically upward, but the positive y direction becomes sunward. The positive x direction is perpendicular to y to complete the right-hand coordinate frame. Figure 3.4 shows an example of both the original satellite coordinates and the new Cartesian coordinates for two locations on a typical DMSP F15 orbit. The coordinates in the satellite reference frame are indicated with a prime (i.e., V_x' and V_y'); the new coordinates used for the remainder of this research are the unprimed variables. To complete this transformation, first the Cartesian location of each data point on the satellite path (C_x and C_y) are found by converting the magnetic latitude (MLAT) to magnetic colatitude (90 - MLAT) and magnetic longitude (MLON: MLT converted to degrees) and taking

$$C_x = (90 - MLAT) \times \cos\left(MLON \times \frac{\pi}{180}\right) \tag{3.1}$$

$$C_y = (90 - MLAT) \times \sin\left(MLON \times \frac{\pi}{180}\right). \tag{3.2}$$

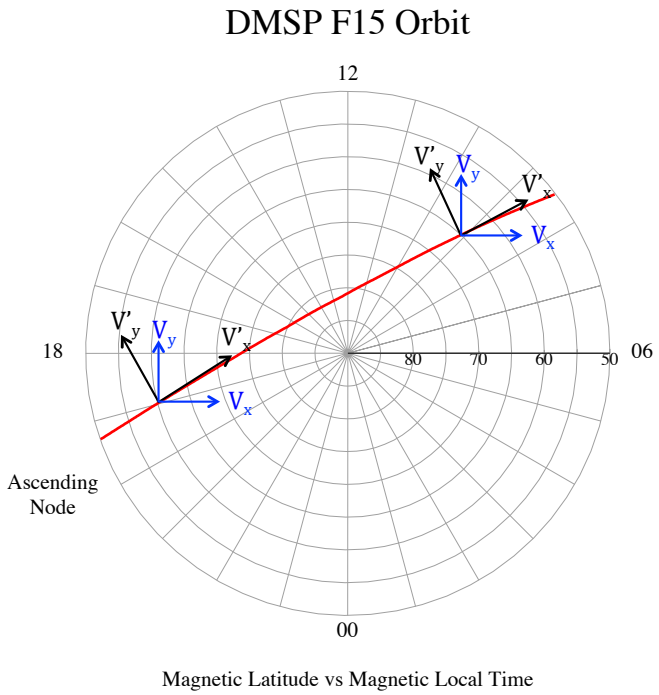

Figure 3.4. Coordinate transformation from satellite to general reference frame. V_x' and V_y' are the original velocity magnitudes, while V_x and V_y are the velocities rotated into the Cartesian coordinate system.

Once the location of the data point is found in the Cartesian system, the angle between the satellite's current trajectory and the dusk–dawn line is found by taking the inverse tangent of the current trajectory's slope by calculating

$$\theta = \arctan\left[\frac{C_y(j+1) - C_y(j)}{C_x(j+1) - C_x(j)}\right], \tag{3.3}$$

where the index, j, indicates the data point in the orbit. Finally, a rotation matrix (equation 3.4) is used to find the new velocity components: V_x, V_y, and V_z. The x and y velocities are rotated by an angle of θ while the z direction velocity is unchanged.

$$\begin{pmatrix} V_x \\ V_y \\ V_z \end{pmatrix} = \begin{pmatrix} \cos\theta & -\sin\theta & 0 \\ \sin\theta & \cos\theta & 0 \\ 0 & 0 & 1 \end{pmatrix} \begin{pmatrix} V_x' \\ V_y' \\ V_z' \end{pmatrix}. \tag{3.4}$$

3.4. Data Binning

To obtain coherent convection patterns, the data must be categorized. Some typical categories are based on solar cycle, season, geomagnetic index, and the IMF configuration. The data used is all from the solar minimum period of 2007 to 2010. Figure 3.5 shows the geomagnetic 3-hour Kp index and the F10.7 solar radio flux measured during this solar minimum. The geomagnetic index remains almost exclusively below six, and the F10.7 ranges between 67 and 93 solar flux units (sfu) with an extended period in late 2008 through early 2009 when it barely topped 70 sfu. Although a solar minimum, all configurations of the IMF were present. Different IMF configurations result in significantly different convection patterns, while an increase in the geomagnetic index is typically correlated to an increase in the polar cap radius. To capture both relations we first bin the data by IMF clock angle and IMF magnitude (IMF Bins) and then by IMF clock angle and Kp value (Kp Bins).

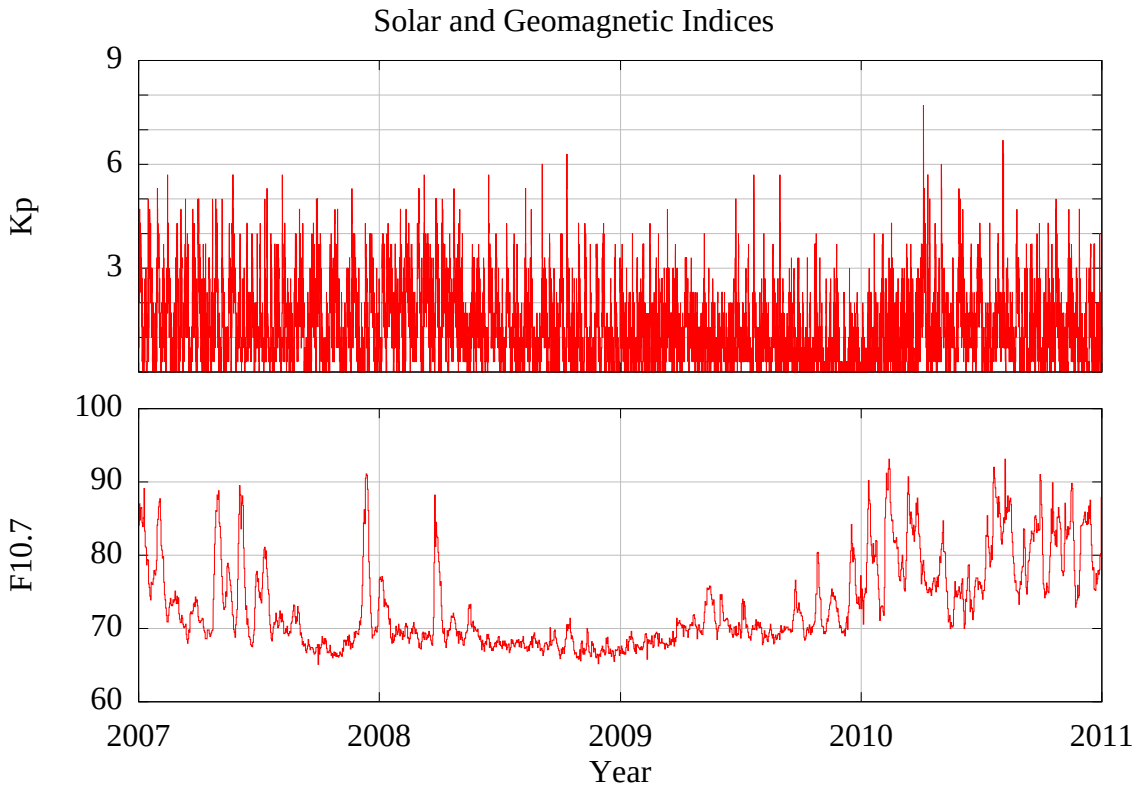

Figure 3.5. Solar and geomagnetic indices for 2007–2010. The top plot shows the 3-hour Kp geomagnetic index and the bottom plot shows the F10.7 solar radio flux.

3.4.1. IMF Average and Delay

Each orbit is put into one of 32 IMF bins based on the polarity (positive or negative) of the B_y and B_z component and the total magnitude of the IMF (B_T). The IMF data used is from the Advanced Composition Explorer (ACE) satellite 64-second data obtained from the Magnetic Field Experiment/Solar Wind Electron, Proton, and Alpha Monitor (MAG/SWEPAM) 64-Second Level 2 Data Server at www.srl.caltech.edu. The level 2 data have been verified by the instrument team and include calibration data and transformation into appropriate coordinate systems. The data do not account for the time it takes for the solar wind to transit to the magnetopause or the delayed response time of the Earth's magnetosphere. Adding a delay to the timing of the measurements accounts for the transit time, while taking an average of the measurements helps take into account the structure of the IMF just before and throughout the polar pass. Averaging the data is done before delaying because it is possible (and occurred in a few instances) that the adjusted times become out of order due to variable solar wind speeds. By averaging first, the problem of dealing with disordered timestamps is avoided.

A 40-minute average of the 64-second ACE data was calculated starting from 30 minutes prior to the start of the polar pass through 10 minutes past the start of the pass. Using 30 minutes prior to the start of the orbit was done to account for the fact that the convection pattern does not change instantly with changes in the IMF, but is influenced by the prior configuration of the IMF [*Weimer*, 1995]. Small IMF changes during the orbit are accounted for by including in the average ten minutes of data within the orbit. The standard deviation of the IMF data used in the averaging was also looked at and if the standard deviation for B_y, B_z, or B_T was larger than a set threshold the orbit was rejected due to the variable IMF configuration during the orbit. Figure 3.6 shows a histogram of the standard deviations for the IMF B_z component average and the thresholds set for each magnitude bin.

The ACE data need to be delayed because the satellite is at the L1 Lagrangian point, which is 1.5 million km away from the Earth—about 235 Earth radii (R_E) away—while the magnetopause is located near an average of 10 R_E from the Earth. However, there has been

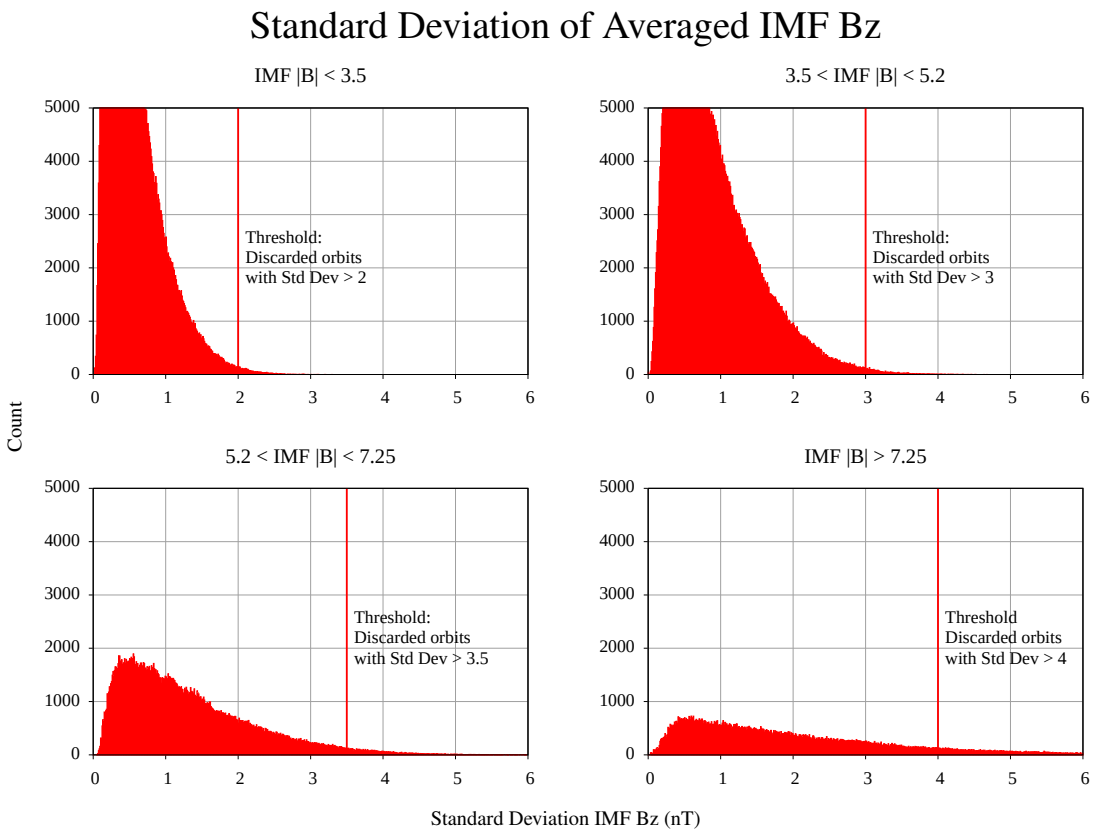

Figure 3.6. Standard deviation of IMF B_z 40-minute average. The data is separated by IMF magnitude and a threshold is set for each magnitude bin. Orbits with a standard deviation larger than the threshold value are discarded.

controversy over the best method to delay the data. Two different variables exist that can be adjusted: the first is the point to which the data is delayed, i.e., the magnetopause, the top of the ionosphere, the Earth's surface, etc., and the second is which speed to use for the delay: the actual measured speed, or a typical solar wind speed value. On top of the delay, the polar cap convection pattern can take an additional 15–45 minutes to respond to the IMF [*Hairston and Heelis*, 1995]. We briefly investigate five different delay methods.

The first method was to delay the measurements from L1 to the magnetopause at approximately 10 R_E using the measured solar wind speed. The second method was to again delay the measurements to the magnetopause, but this time using the average solar wind speed of 450 km/s. The third method was to delay the measurements from L1 to the Earth's surface using the measured solar wind speed. The fourth method was to again delay

the measurements to the Earth's surface, but this time using the average solar wind speed of 450 km/s. The final method was to delay the measurements from L1 to the magnetopause using the measured solar wind speed and then adding 20 additional minutes to the delay to account for the polar cap response time. The methods are summarized in Table 3.1.

Table 3.1. Methods Used to Calculate the IMF Delay*

Method	Delay Location	Wind Speed	Adjustment
1	Magnetopause (10 R_E)	Measured	None
2	Magnetopause (10 R_E)	450 km/s	None
3	Earth's Surface	Measured	None
4	Earth's Surface	450 km/s	None
5	Magnetopause (10 R_E)	Measured	+20 min

*Five different methods were used to calculate the delay in solar wind measurements from ACE for the IMF data. The location indicates the distance the measurement was delayed, while the speed used is either the value measured by the ACE satellite or an average solar wind speed value. The last column indicates if any additional adjustments were made after the calculation.

The timestamps for each measurement were adjusted by adding a delay time calculated by taking distance between L1 and the delay location and dividing by the solar wind speed for that same reading. For the methods where the measured solar wind speed is used, if no solar wind measurement is available, the delay for the previous measurement is used.

$$\text{Delay Time} = \frac{\text{L1} - \text{Delay Location}}{\text{Wind Speed}} + \text{Adjustment}. \tag{3.5}$$

Each orbit is binned according to the averaged and delayed IMF conditions at the time the satellite crosses 50° on its ascending node. Only northern hemisphere passes are used for this study because the inclination of the DMSP orbit steers the southern hemisphere pass into the nightside. For the years 2007–2010, there are 20,455 total orbits; no matter which method is used, each IMF bin contains at least 100 orbits with a maximum bin size of over 1400 orbits for the $B_y = 0$, $B_z > 0$, $B_T < 3.5$ nT bin. The bin obtained for each orbit using the five different methods are then compared to each other (Table 3.2).

Table 3.2. Bin Comparison Using Different Delay Methods*

Methods Compared	Percent of Orbits with Same Bin
1 vs. 2	65%
1 vs. 3	91%
1 vs. 5	49%
2 vs. 4	91%
3 vs. 4	65%
3 vs. 5	53%

*Percentage of orbits that were assigned to the same bin for the two methods indicated.

Two significant results stand out; the first shows the location to which the data is delayed is unimportant. This is seen in the comparison between methods one and three and between two and four where the location was changed from the magnetopause to the Earth's surface. In both of these comparisons, the orbits were placed in the same bin 91% of the time. Therefore a distance of 10 R_E appears negligible, which is important because the magnetopause only varies between 6 and 12 R_E for a large and small solar wind dynamic pressure, respectively.

The second result shows it is important to include the wind speed in the delay calculation. For methods two and four in this study a typical average solar wind speed of 450 km/s was used to calculate the delay and resulted in the same bin as the methods using the measured solar wind speed only 65% of the time. This indicates it is important to use the measured wind speed. However, since all the data was taken during solar minimum, the typical average solar wind speed of 450 km/s is most likely too high. To check this result, the wind speed was changed in methods two and four to 350 km/s. The delay time difference between using 350 km/s and 450 km/s is around 15 minutes, but the percentage of orbits that received the same bin changed by less than one percent. This indicates an average solar wind speed of 450 km/s is an acceptable value to use for this study.

The comparison of methods one and three to method five also showed the IMF configuration does not change significantly within a 20 minute period in approximately half of the orbits. This is good because it means that for these orbits, the IMF configuration

can be considered fixed while the satellite passes over the northern hemisphere polar cap. One last note is that even though we are discussing the delay method, the data was also averaged. There are just as many (or more) ways to average the IMF data, which were not investigated. Based on the results of this study, method one, which is using the measured solar wind speed delayed to the magnetopause at 10 R_E, was chosen as the preferred binning method and is the method employed throughout this analysis.

3.4.2. IMF Binning

After all the IMF data are averaged and delayed, the orbit files are read and the time that the satellite passes 50° on its ascending node is used to indicate the start of the polar pass (first measurement point for magnetic latitude greater than 50). For this study, only northern hemisphere polar passes were used. This orbit time is then compared to the delayed timestamps for the IMF data. The averaged IMF B_y, B_z, and B_T for first delayed IMF timestamp past the orbit time is then saved as the IMF configuration for that pass. These three values are then used to place the orbit into one of the 32 IMF bins. The magnitude is separated into four levels with separations at 3.5, 5.2, and 7.25 nT. Eight B_y/B_z configurations are used such that there are categories where B_y is close to zero for large values of B_z and vice versa. These categories are the same as used by *Weimer* [1995] and are shown in Figure 3.7; each red cross represents an orbit. Figure 3.8 shows the number of orbits that fall into each IMF bin.

3.4.3. Kp Binning

For the Kp bins the Kp index is used instead of the magnitude of the IMF for categorizing each orbit. To retain the cases where the Kp influence is most clear, only four IMF clock angle bins were used: $B_y = 0, B_z > 0; B_y = 0, B_z < 0; B_y > 0, B_z = 0; B_y < 0, B_z = 0$. After the orbits were separated into these four categories, they were further separated based on integer Kp values for a total of 20 bins. The bins and number of orbits that fall into each Kp bin are shown in Figure 3.9. As can easily be seen, very few orbits have Kp > 4, and these bins are not used in the final analysis.

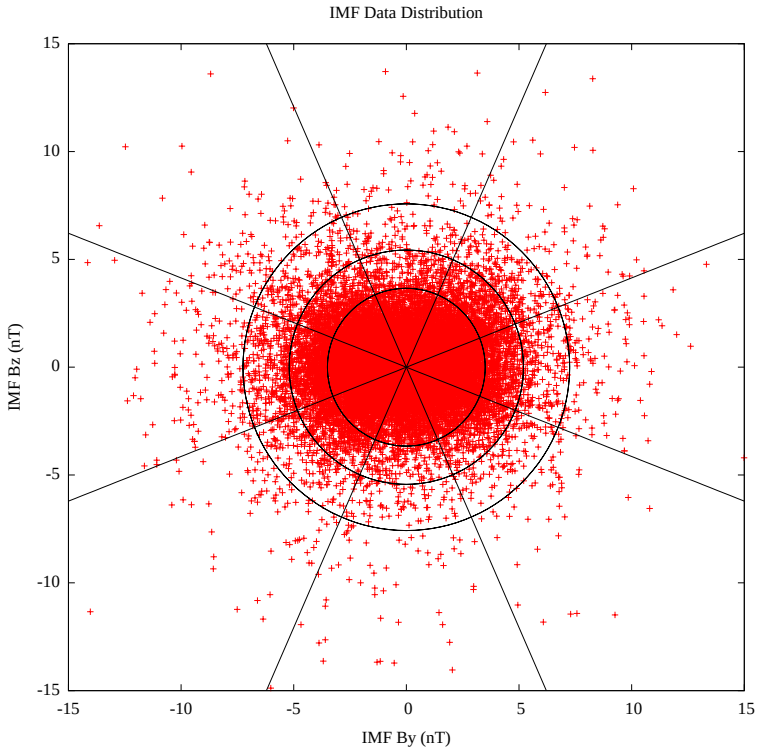

Figure 3.7. Interplanetary magnetic field data distribution. This graph shows the IMF B_y and B_z values for each of the 20,455 DMSP passes. The concentric circles at 3.5, 5.2, and 7.25 nT show dividing lines sorted by total magnitude of the IMF. The radial lines show the division of the data according to the angle of the IMF vector in the y-z plane. There are eight angular bins, each 45° wide.

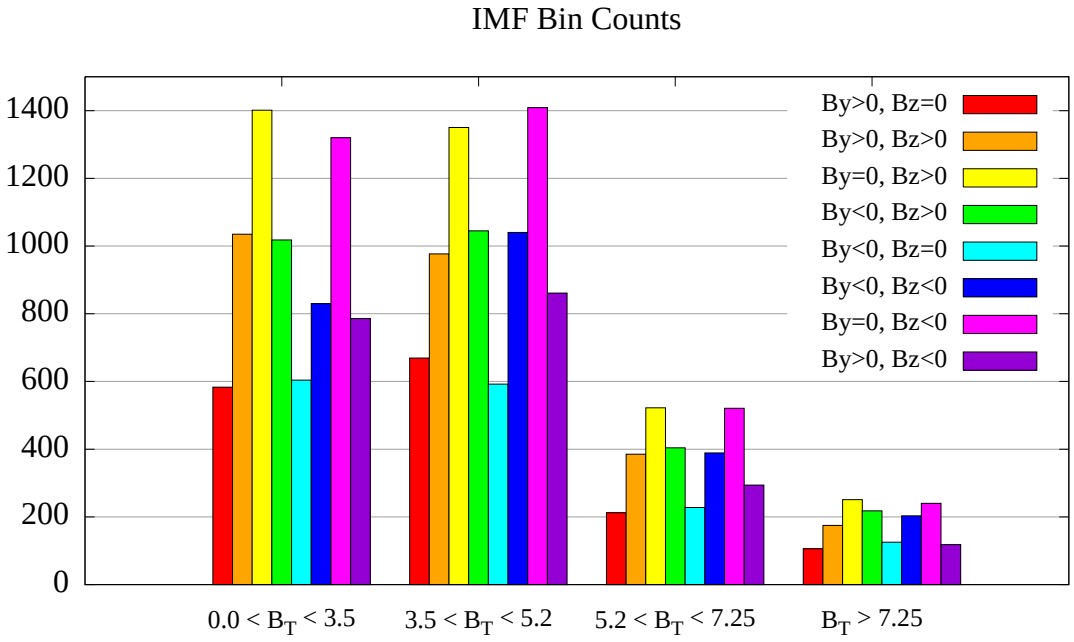

Figure 3.8. Number of orbits in each IMF bin. There are four magnitude bins and eight clock angle bins. The number of orbits in the largest magnitude bins never falls below 100.

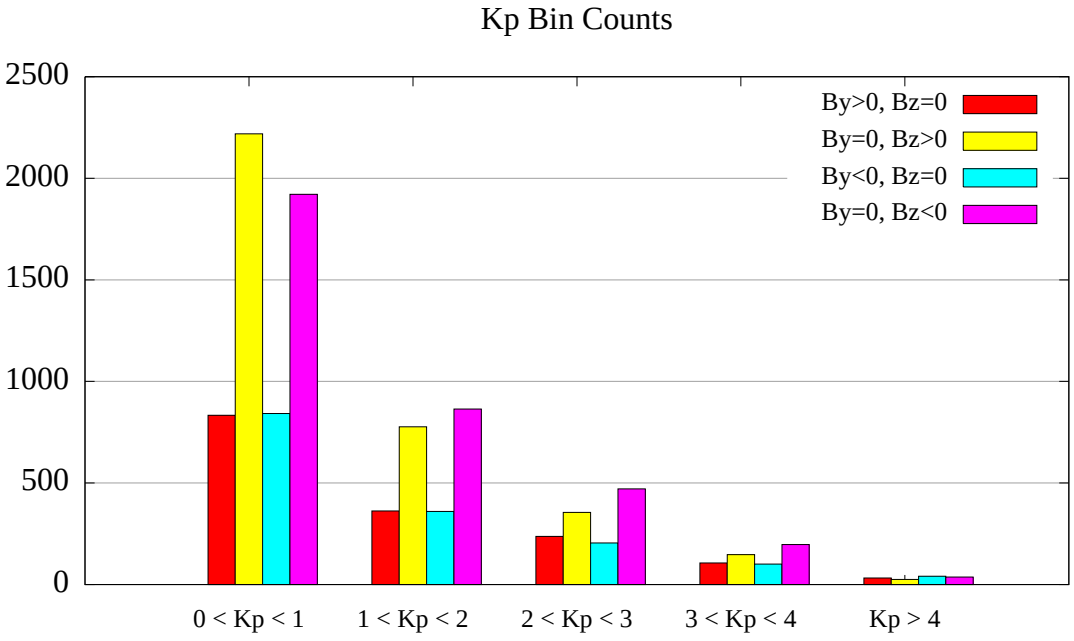

Figure 3.9. Number of orbits in each Kp bin. There are four IMF clock angle bins and five Kp bins. Very few orbits have a Kp > 4.

CHAPTER 4
COMPARISON OF DATA TO CURRENT MODELS

4.1. Introduction

As described in Chapter 2, multiple models currently exist that attempt to describe the polar cap convection pattern. The degree to which the models account for solar and geomagnetic conditions varies, but all use these conditions as the primary model drivers. The data used in this study was obtained during conditions of low solar activity, when the Kp index was low. In this chapter, we investigate averaged convection patterns obtained from DMSP data and compare these patterns to established empirical models. Because averaged data is used, the patterns represent a climatological pattern and not the short-term dynamics of the high-latitude region. Comparisons to the *Sojka et al.* [1986] model, which is based on *Volland* [1978] and used in the USU TDIM, *Weimer* [2005] model, and *Heppner and Maynard* [1987] (H-M) model are made, and the relationship of the polar cap radius to the geomagnetic index is investigated.

4.2. Methodology

For this portion of the study, an averaged convection pattern is calculated separately for each IMF and Kp bin. The data is first filtered and smoothed and then the offset is removed as described in Chapter 3. Each velocity data point is gridded using a 41 $\times$ 41 square grid covering all magnetic latitudes greater than 50 degrees. The average and standard deviation for each velocity component is then calculated for each grid box. A single vector is plotted in the center of each grid box using the V_x and V_y velocity components. Figure 4.1 shows the resulting velocity vectors (panel a) and standard deviation (panel c) for the IMF bin with $B_y = 0, -5.2 < B_z < -3.5$. Also shown in this figure is the number of points in each bin used to calculate the average velocity (panel b) and the standard deviation as a percentage of the magnitude of the velocity (panel d).

A coherent convection pattern is obtained for all 20 Kp bins and 32 IMF bins with narrow bands of strong sunward flow surrounding a widespread area of antisunward flow

across the polar cap. The largest standard deviations occur in the region encompassing the convection reversal boundary due to the rapid change in both magnitude and direction of the flow. In particular, it can be seen in panel d) that the standard deviation percentage is significantly lower on the duskside near 70°, which corresponds to the region of the strongest sunward flow in panel a). The largest values of the standard deviation and the standard deviation percentage occur in the polar cap boundary region where the flow velocities turn from sunward to antisunward and vice versa. The number of points used for calculating the average is typically smaller at lower latitudes due to the precession of the DMSP orbit over the four-year period studied. The number of points is particularly low on the dawnside due to the filtering done previously for erroneous data. The late afternoon sector on the duskside has a particularly large number of data points in each bin as most of this data was taken during daylight, which significantly reduces the occurrence of the H^+ anomaly. These trends are consistent for all IMF and Kp bins with the exception that the number of points decreases steadily as IMF magnitude and Kp increase. The unique characteristics of the convection patterns for each IMF and Kp bin are discussed in detail in section 4.3.

The averaged convection patterns were used to determine a polar cap boundary. First a cubic spline function was calculated for each horizontal grid row of the averaged DMSP data, and then the roots of the spline function were found using the secant method [*Burden and Faires*, 2005]. After plotting these roots on a polar plot, a circle was hand fit to approximate the polar cap boundary. An elliptical polar cap was considered, but was discarded due to lack of data in the noon and midnight sectors to aid in fitting the ellipse to the roots.

Figure 4.2 shows examples of how the polar cap boundary was determined. The averaged velocity vectors in the background serve as the starting point; the red stars indicate where the roots are located and the red circle is the final polar cap boundary. Many plots have roots at low latitudes ($< 65°$ MLAT), which were considered to be erroneous and mainly due to averaged velocities near zero. Of interest is the cluster of roots in the cusp region, typically around 65–75° MLAT and 1000–1100 MLT; this locus of roots indicates a much more complicated pattern than a simple circular polar cap. However, as the cusp

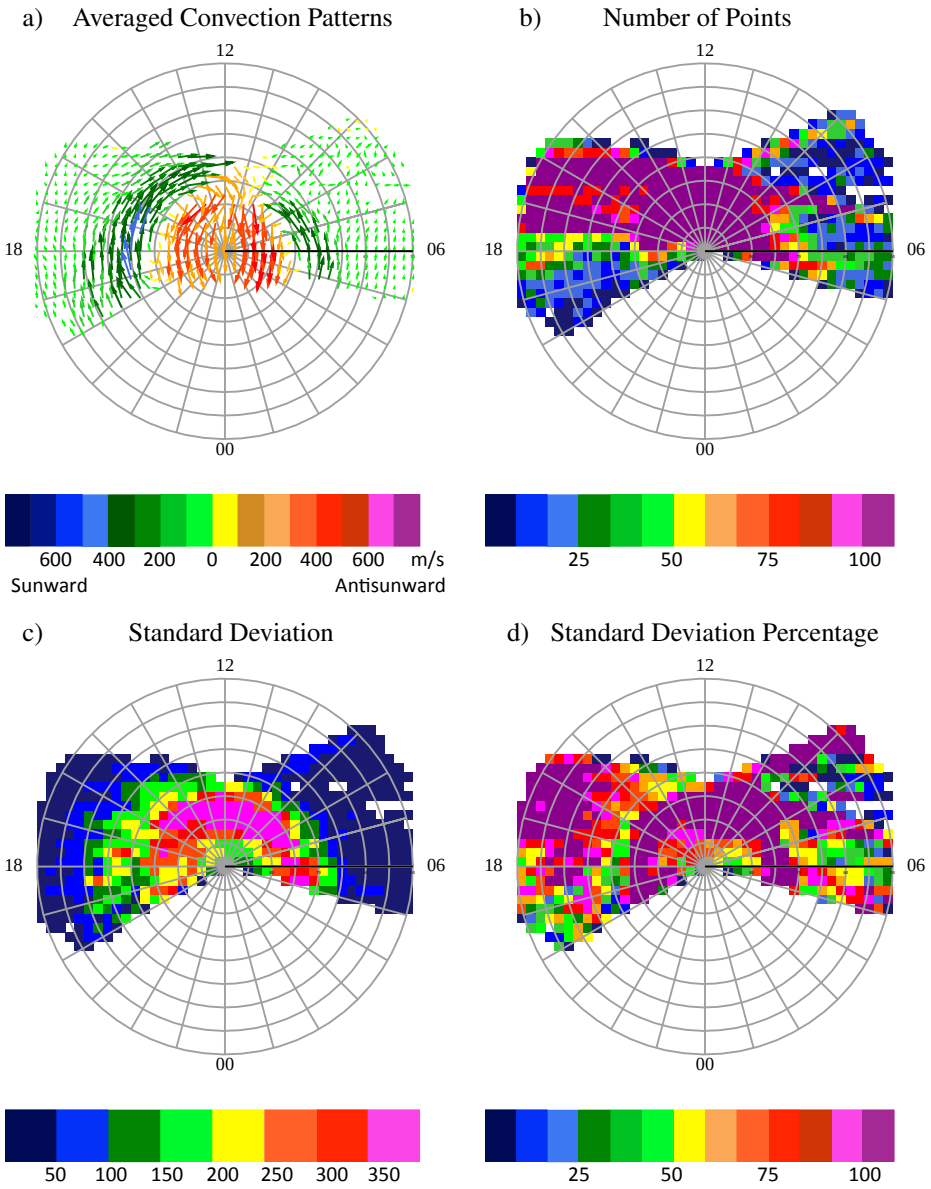

Figure 4.1. Averaged convection pattern statistics. All four panels are for IMF $B_y = 0, -5.2 < B_z < -3.5$. Panel a) shows the velocity vectors; panel b) shows the number of data points available for each bin; c) shows the standard deviation for each bin; and d) shows the standard deviation as a percentage of the velocity magnitude.

is in a region where the data begins to become sparse, further analysis was not possible. From the polar cap boundary, both a polar cap radius (PCR) and offset were computed. The offset was computed for both the dawn–dusk and noon–midnight directions; however, as mentioned previously, the lack of noon–midnight data makes this offset somewhat unreliable. These results will be discussed in the following section.

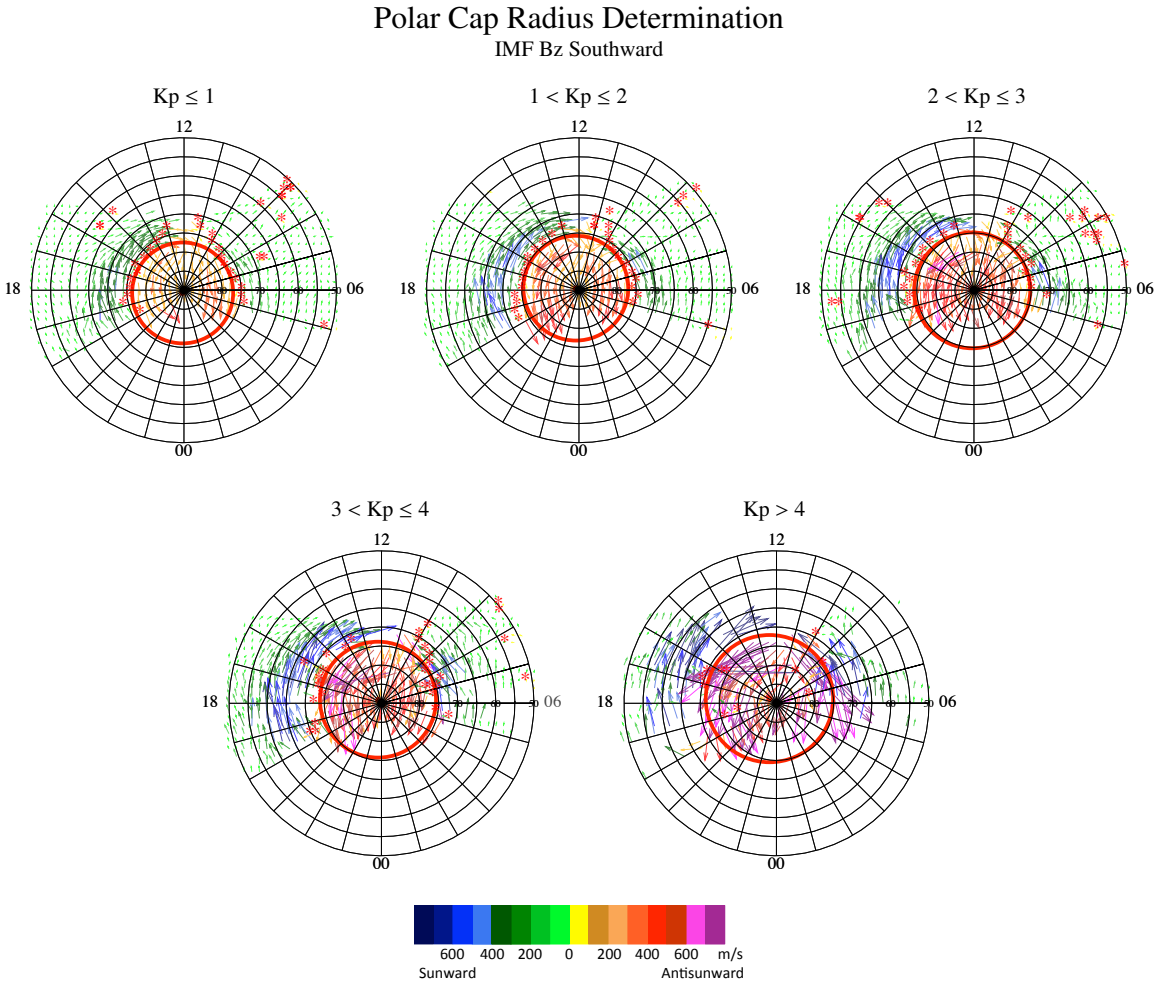

Figure 4.2. Method used to determine polar cap boundary. Velocity vectors represent the magnitude of averaged values of the V_x and V_y components of the ion drift measured by DMSP. A cubic spline was calculated for each horizontal row of the averaged DMSP data. The polar cap boundary was then determined by hand fitting a circle (red) to the roots (red stars) of the cubic spline function. The radius of the hand-fit circle and the offset of the center of the circle from the magnetic pole were then computed. This was done for all 20 Kp bins and 32 IMF bins; shown here are the five Kp bins for IMF $B_y = 0, B_z < 0$.

Finally, the sunward/antisunward flow in a dusk-to-dawn cross section is analyzed for each Kp and IMF bin. The cross section was obtained from the V_y velocity component from 1800 and 0600 MLT. This analysis was done to compare the velocity profiles of the averaged data to various empirical convection models. The three models that were chosen for comparison are the USU TDIM, *Weimer* [2005], and H-M models. The *Sojka et al.* [1986] model uses only Kp as a driver while both *Weimer* [2005] and H-M use IMF conditions. *Heppner and Maynard* [1987] uses Kp to scale the size of the polar cap while *Weimer* [2005] requires the tilt, solar wind velocity, and solar wind density. For this study, a tilt of zero was used along with typical values of 450 km/s for the velocity and 1 cm^{-3} were used. Slight variations on these values were investigated, but the change to the velocity profile was negligible compared to difference in the averaged data. The *Sojka et al.* [1986] and H-M models were run to cover geomagnetic conditions up to Kp = 5 with $By = 0, B_z = -10$ nT; *Weimer* [2005] was run for four IMF configurations: $B_y = 0, B_z < 0$; $B_y = 0, B_z > 0$; $B_y < 0, B_z = 0$; and $B_y > 0, B_z = 0$. All three of these models are designed to output electric potential. The velocities are determined by first finding the electric field by taking the gradient of the potential, $\mathbf{E} = -\nabla\Phi$, and then using the International Geomagnetic Reference Field to calculate $\mathbf{V} = \mathbf{E} \times \mathbf{B}/B^2$.

4.3. Results

The averaged polar cap convection pattern plots show surprisingly coherent flow patterns. For comparison with accepted electric potential patterns, the IMF binned patterns are plotted in a fashion similar to *Weimer* [1995] in Figures 4.3–4.6. Both the arrow length and color indicate the vector magnitude; warm colors indicate antisunward flow while cool colors indicate sunward flow. The IMF magnitude and angle for the IMF binned plots and the IMF configuration and Kp range for the Kp binned plots are indicated in each figure. As noted in the previous section, the data behind these averages often have large standard deviations and/or very limited number of data points used in the calculation. These limitations leave some unphysical velocity vectors that are still plotted, but do not detract from the overall flow pattern.

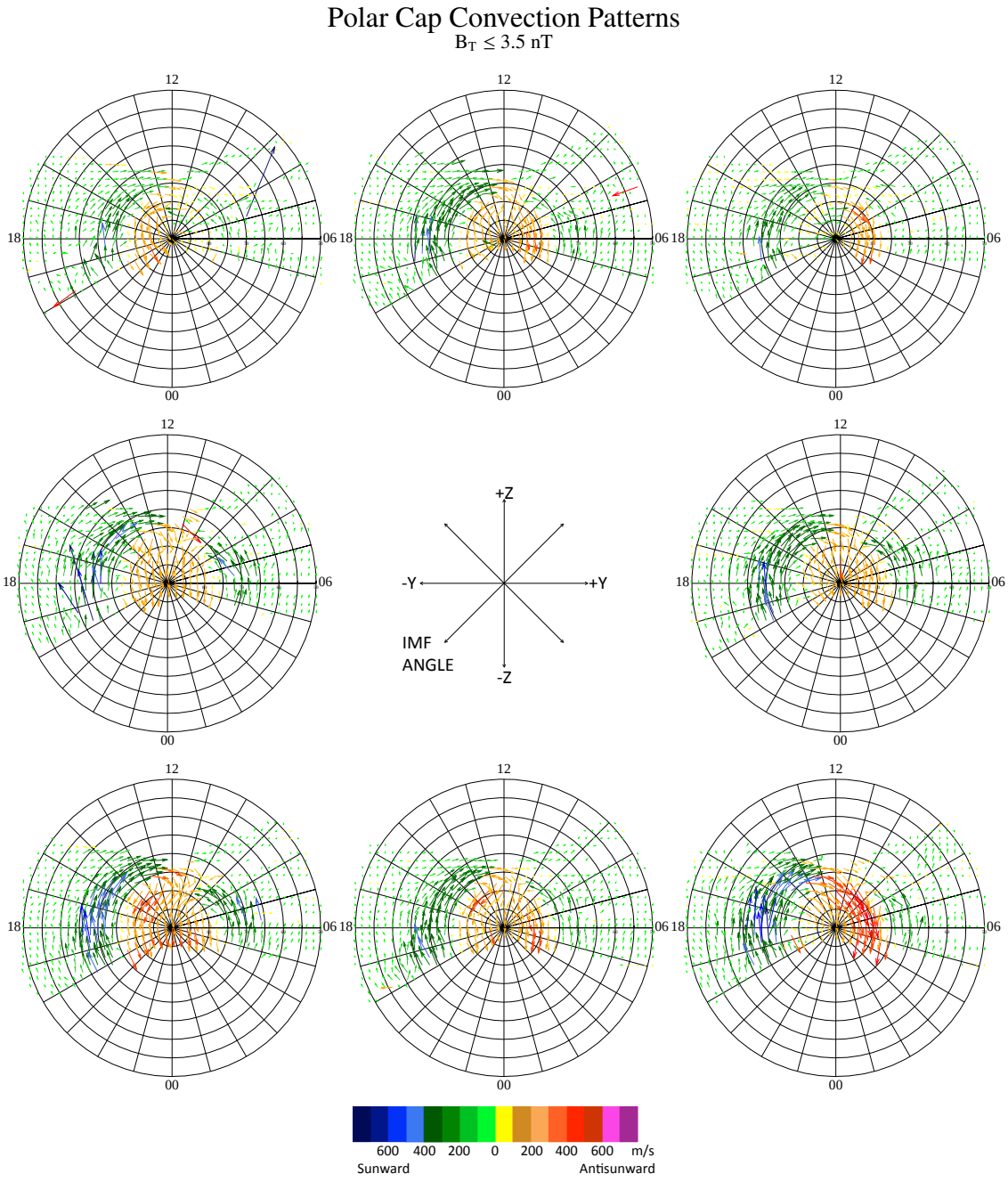

Figure 4.3. Polar cap convection patterns binned by IMF for $B_T \leq 3.5$ nT. Vectors represent the magnitude of averaged values of the V_x and V_y components of the ion drift measured by DMSP for each IMF configuration. Sunward and antisunward flow are indicated by cool and warm colors, respectively; vector length is also proportional to magnitude.

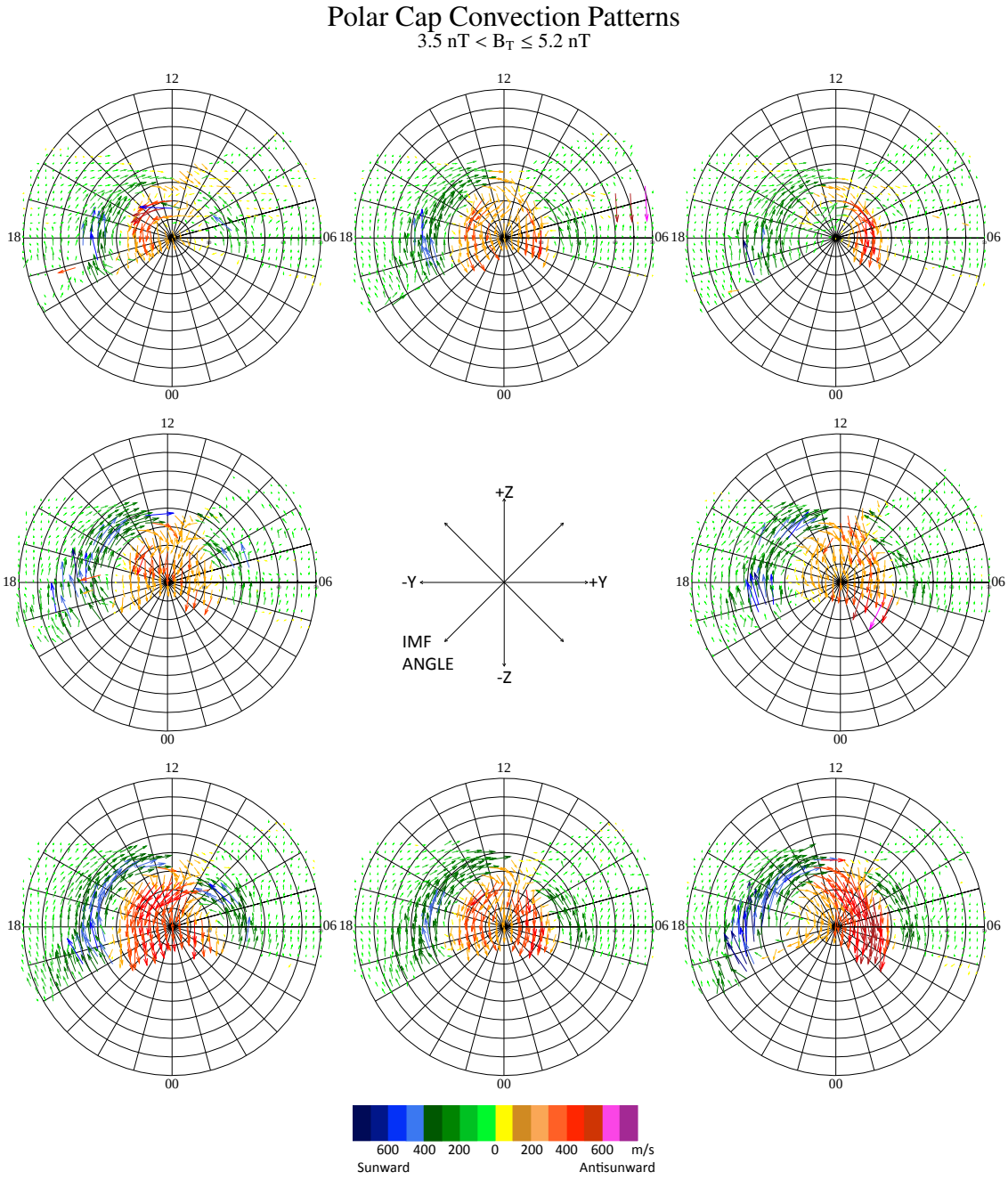

Figure 4.4. Polar cap convection patterns binned by IMF for $3.5 < B_T \leq 5.2$ nT. Plot convention is the same as Figure 4.3.

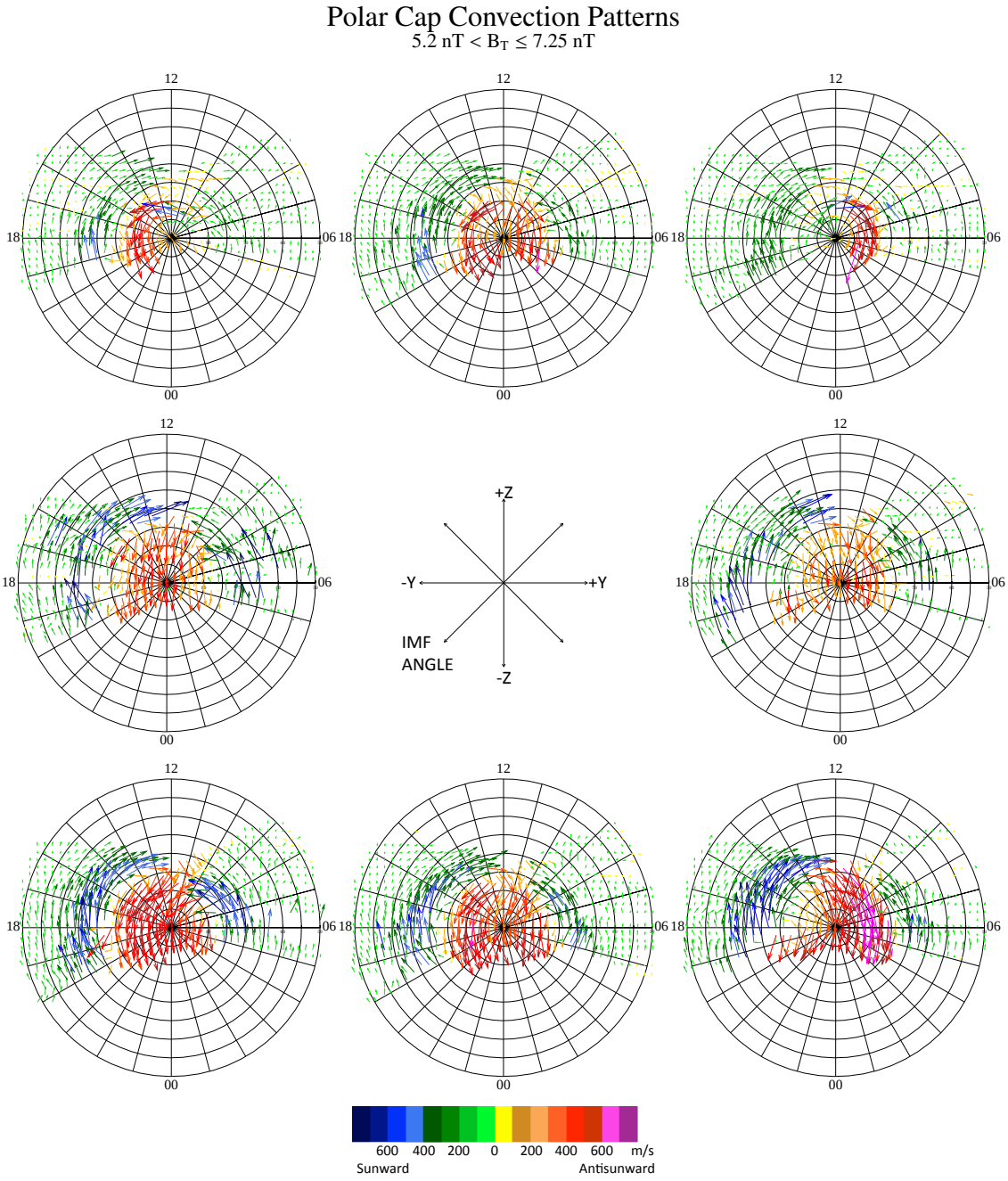

Figure 4.5. Polar cap convection patterns binned by IMF for $5.2 < B_T \leq 7.25$ nT. Plot convention is the same as Figure 4.3.

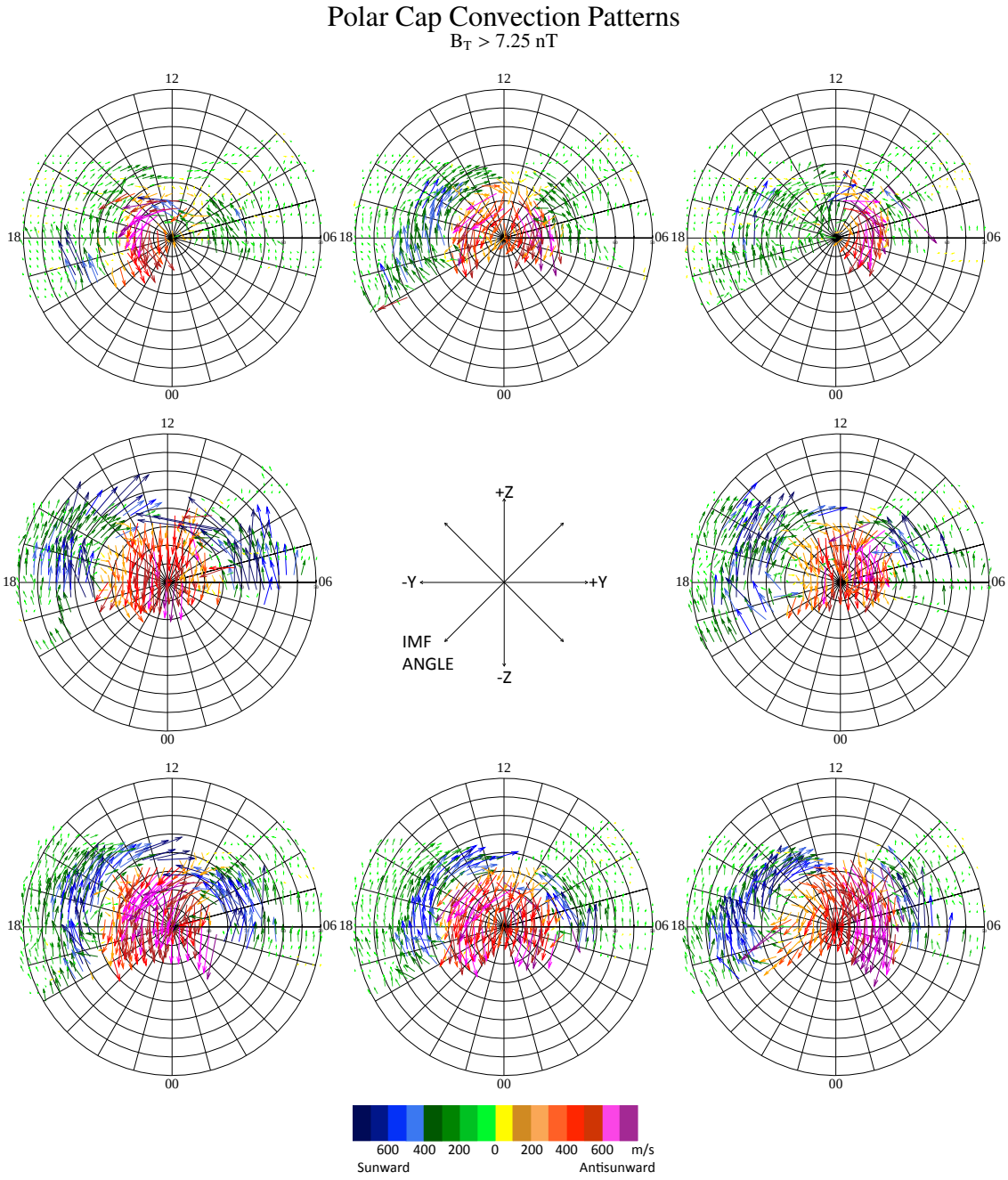

Figure 4.6. Polar cap convection patterns binned by IMF for $B_T > 7.25$ nT. Plot convention is the same as Figure 4.3.

Two results are immediately obvious from the IMF binned patterns: first, the flow velocities increase significantly as IMF magnitudes increase for both the antisunward flow within the polar cap and the sunward flow within the auroral regions. $B_z < 0$ polar cap velocities range from 100–200 m/s for small B_T to more than 700 m/s for large B_T. Second, the asymmetry of the two-cell pattern is pronounced for $B_y \neq 0$ and $B_z < 0$, especially for larger magnitudes, with a larger dusk cell for $B_y > 0$ and a larger dawn cell for $B_y < 0$. For almost all cases, the sunward flow on the duskside slightly enhanced over the dawnside flow. This is consistent with a stronger duskside cell as shown in *Weimer* [1995].

When $B_y = 0$ is zero, the obtained convection patterns do not support a multi-cell pattern for B_z positive. For the $B_y = 0$ cases, the flow also tends to diverge around the pole with the lowest velocities in the polar cap centered over the pole. It is unclear whether this is an artifact of a coordinate transformation or is actually a characteristic of the data. However, this type of flow pattern is reminiscent of the crescent shaped *Heelis et al.* [1982] electric potential patterns.

For the cases where B_z is zero and B_y is either purely positive or negative, the convection patterns support the asymmetry shown by *Weimer* [1995]. For cases with B_y positive, although the tilt in the convection cells is not very apparent, the dusk cell is larger than the dawn cell, especially for lower B_T, and the strongest polar cap flows are on the dawnside in the same location as where *Weimer* [1995] shows the strongest gradient in the electric potential. For B_y negative, the patterns show strong antisunward flow distributed evenly across the polar cap. Of interest in Figure 4.6 is the middle right plot ($B_y > 0$, $B_z = 0$); this plot shows sunward flow near 83° MLAT and 1400 MLT in what should be a strong dusk–dawn flow. This region corresponds with the elongation of the dusk cell maximum in the *Weimer* [1995] pattern and could indicate a double electric potential maximum instead of just an elongation.

Both the asymmetry and the tilt in the polar cap flows are seen with the mixed IMF conditions ($B_y \neq 0, B_z < 0$). The strongest flows are seen when B_z is negative and $B_T >$ 7.25 nT for both B_y positive and negative as shown in the bottom right and left plots in

Figure 4.6, respectively. These plots show both sunward and antisunward flow velocities over 600 m/s, the convection cell vortices line up well with the location of the maximum and minimum electric potential, and the maximum flow speeds align with the strongest gradients in the electric potential when compared to *Weimer* [1995].

The averaged DMSP data is plotted for the Kp bins just as was done for the IMF bins in Figures 4.7–4.10. Some of the conclusions remain the same: the velocities increase with higher Kp; there is no multi-cell pattern for $B_z > 0$; duskside sunward flow is stronger for all cases; antisunward flows diverge and/or weaken around the pole. Additionally, it was found the cusp is more apparent in the Kp bins, especially for the $1 < \text{Kp} \leq 2$ and $2 < \text{Kp} \leq 3$ bins. Also the areal coverage for the region of antisunward flow increases with increasing Kp; this observation led to the analysis of the polar cap boundary to be discussed later. Finally, the $\text{Kp} > 4$ bin does not have many data points, and so the results may not be statistically significant. However, even though the data is sparse, strong antisunward flow extends to almost 50° MLAT for $\text{Kp} > 4, B_y < 0, B_z = 0$ (Figure 4.9).

Both IMF and Kp bins were used to analyze the dependency of the polar cap radius. The top four panels in Figure 4.11 and both panels in Figure 4.12 show the radius values obtained from the polar cap boundary determintion method described in section 4.2. A least square fit of the data points versus Kp is shown for each of the four IMF configurations; all trends are fairly similar (panels a–d in Figure 4.11) and combining all 20 of the data points indicates the relation for the polar cap is

$$PCR = 12.2 + 1.1 \times \text{Kp} \tag{4.1}$$

with a goodness of fit value of $R^2 = 0.87$ (where $R^2 = 1.0$ is a perfect fit). The smallest radius observed is approximately 12° for $\text{Kp} < 1$, and it reaches a maximum of 19° for $\text{Kp} > 4$. This relation is significantly different in both the starting radius and change with Kp than the relation used by the USU TDIM. The default electric potential model in the TDIM is a simplified *Volland* [1978] approximation with a polar cap radius equal to $17.0 + 0.3 \times \text{Kp}$. This relation is shown by the green line in panel e) of Figure 4.11. Also

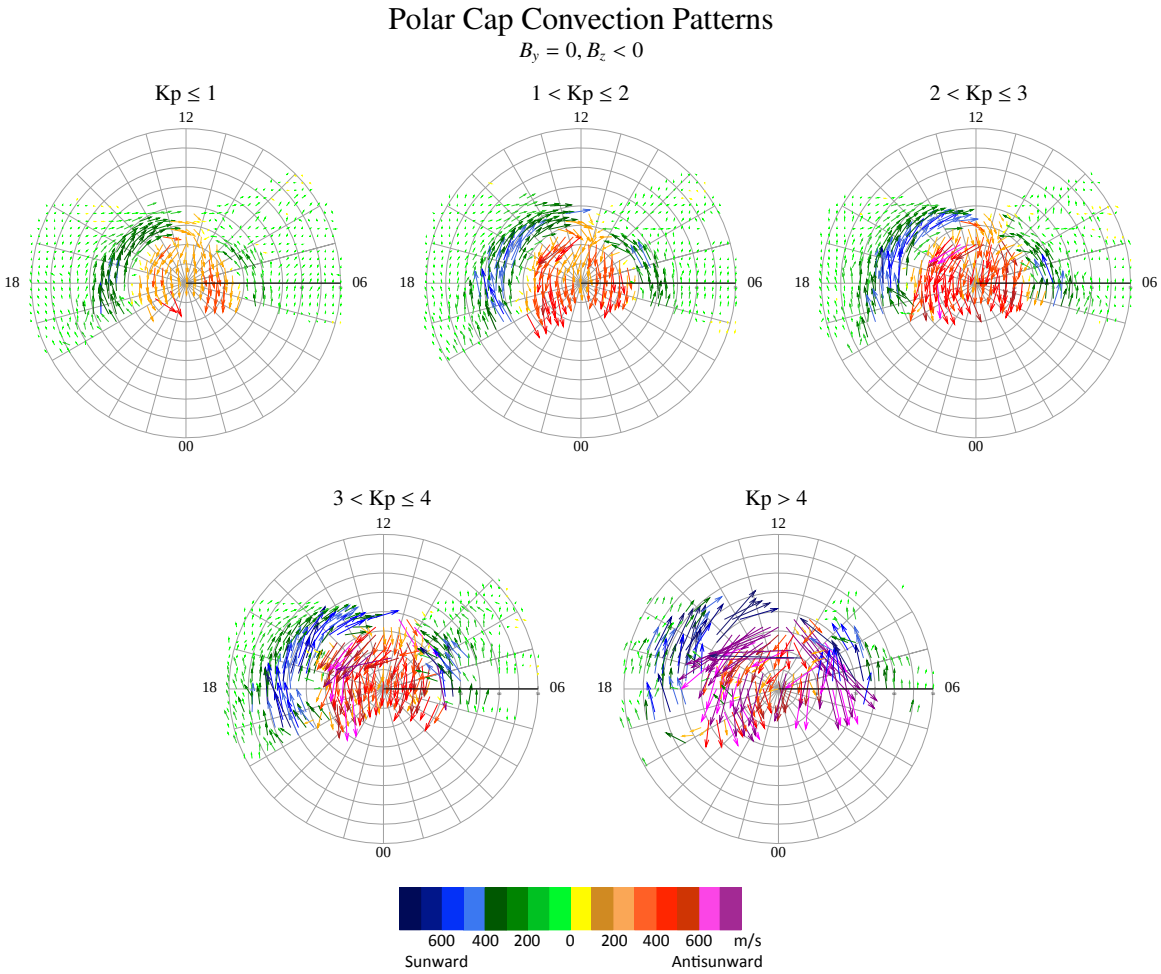

Figure 4.7. Polar cap convection patterns binned by Kp for $B_y = 0, B_z < 0$. Vectors represent the magnitude of averaged values of the V_x and V_y components of the ion drift measured by DMSP for each Kp range. Sunward and antisunward flow are indicated by cool and warm colors, respectively; vector length is also in proportion to its magnitude.

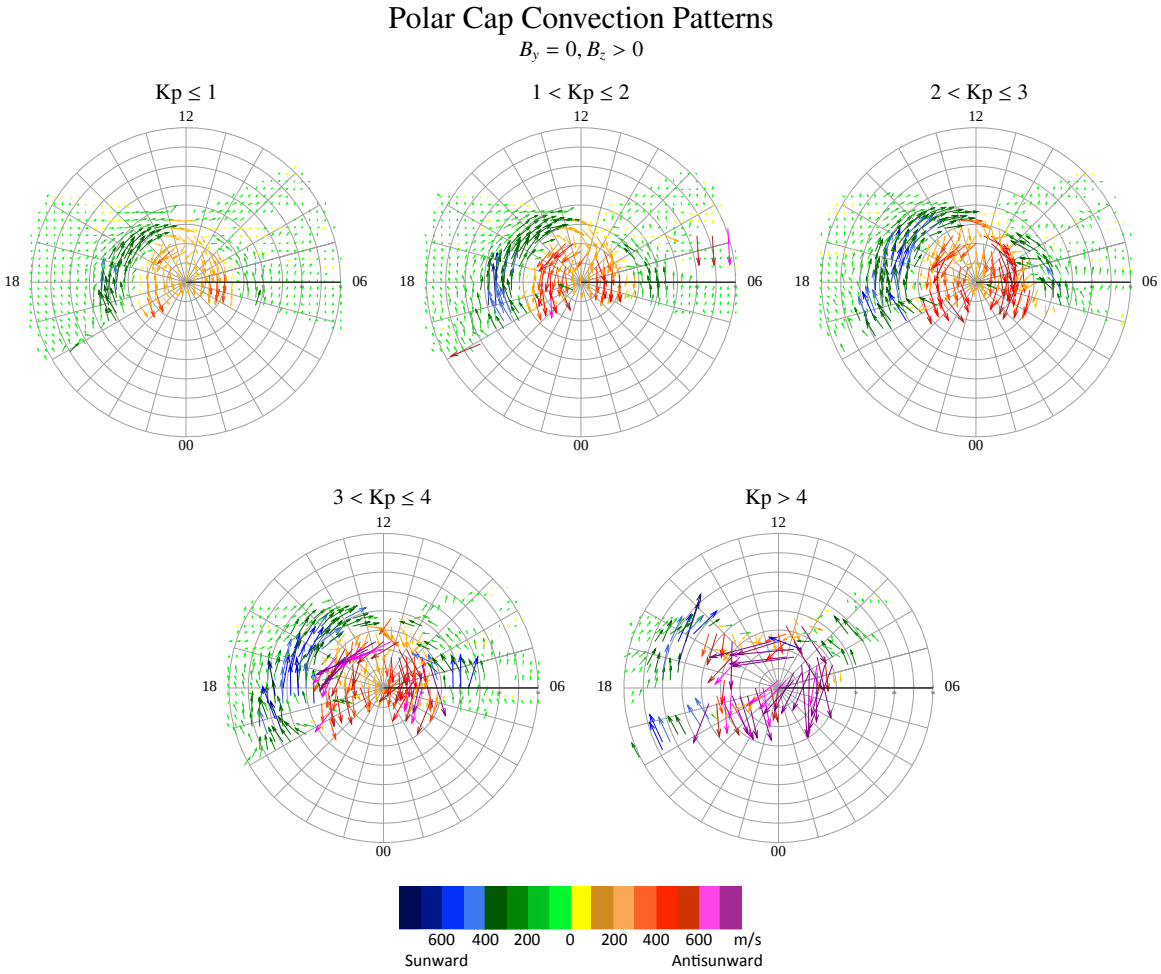

Figure 4.8. Polar cap convection patterns binned by Kp for $B_y = 0, B_z > 0$. Plot convention is the same as Figure 4.7.

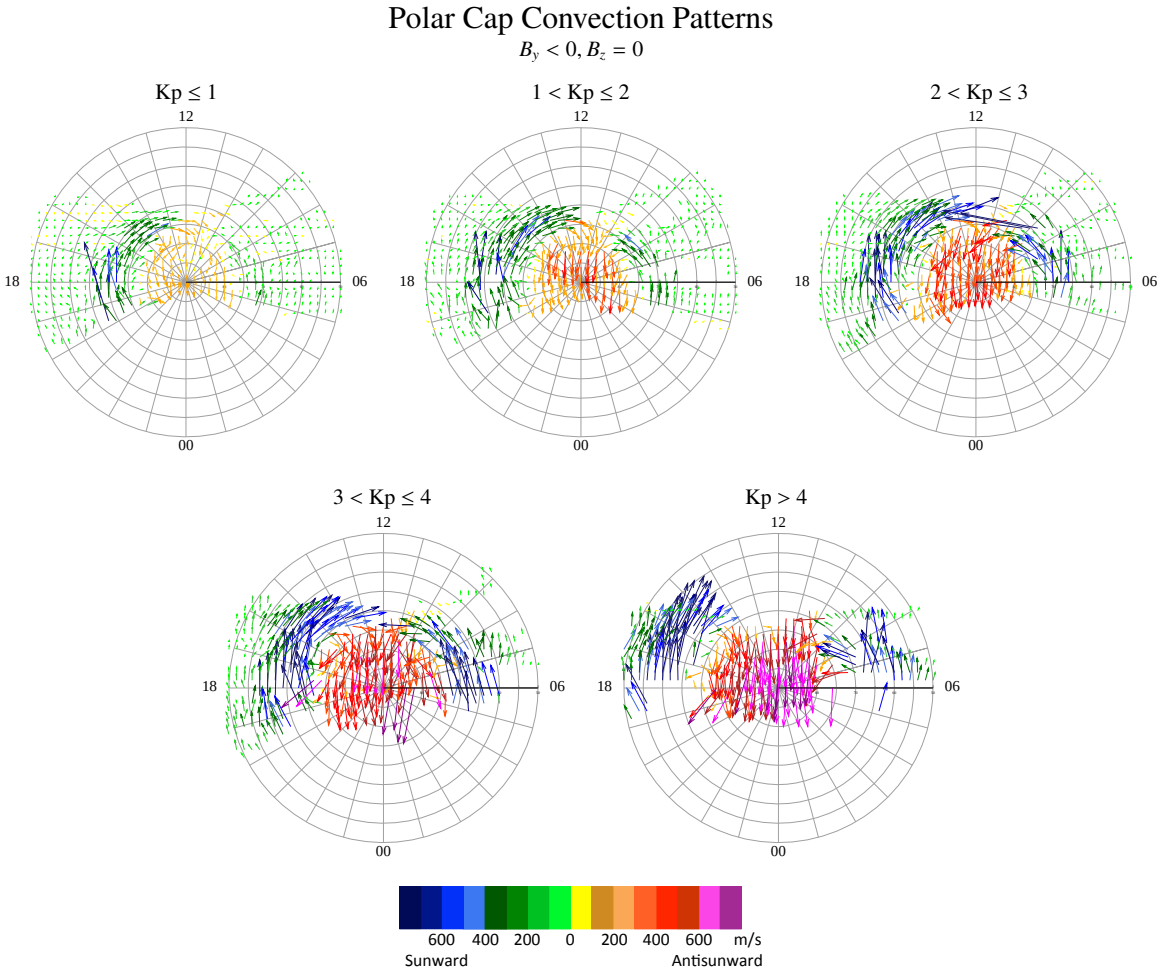

Figure 4.9. Polar cap convection patterns binned by Kp for $B_y < 0, B_z = 0$. Plot convention is the same as Figure 4.7.

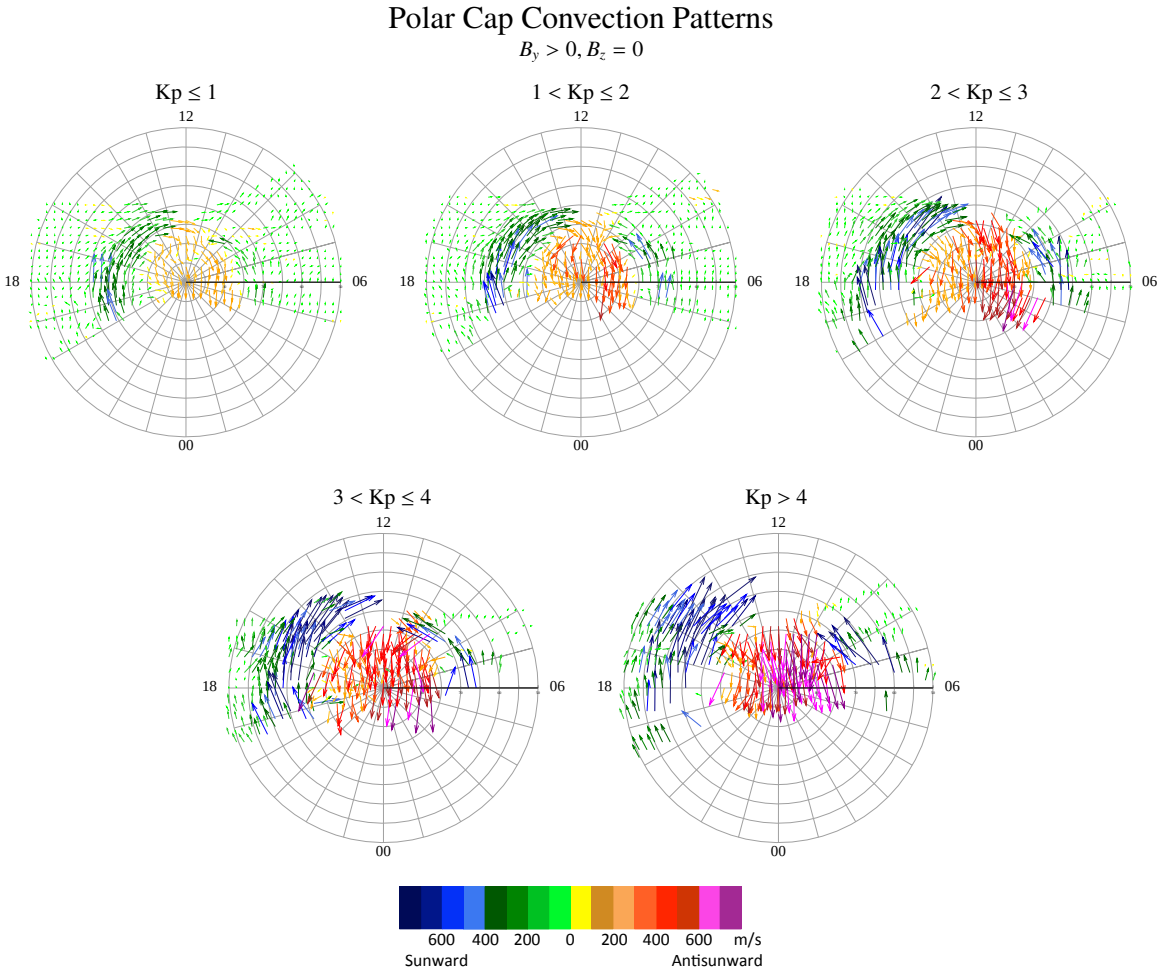

Figure 4.10. Polar cap convection patterns binned by Kp for $B_y > 0, B_z = 0$. Plot convention is the same as Figure 4.7.

shown in this panel are the results of *Xiong and Lühr* [2014] (blue line) which used FACs to deduce the poleward boundary of the auroral oval using ten years of magnetic field data (August 2000–August 2010). An elliptical description was used to describe the polar cap boundary for three Kp ranges. The elliptical dusk–dawn semi-major axis parameter is used for comparison here as it comes from a similar region as our calculated radius values. If a least square fit were to be drawn to the *Xiong and Lühr* [2014] dusk–dawn semi-major axis values, the result would be $PCR = 10.1 + 1.2 \times \text{Kp}$ with $R^2 = 1.0$. Even though the starting radius is two degrees smaller, the slope is nearly identical to that derived in this study. One possibility for the discrepancy is the polar cap radius in the TDIM was most likely calculated using active geomagnetic conditions, while equation 4.1 was calculated using only data from quiet geomagnetic conditions.

Figure 4.12 shows trends in the polar cap radius based on IMF magnitude and clock angle. The smallest polar cap radius is again just over 12° and increases to almost 17° for $B_T < -7.25$ nT but increases only to 14° for $B_T > 7.25$ nT. This is the case regardless of the dominant component of the IMF. The average trend for negative IMF values (B_y or B_z) is $PCR = 11.8 - 0.5 \times \text{IMF}$ with $R^2 = 0.97$ and the average trend for positive values is $PCR = 12.5 + 0.2 \times \text{IMF}$ with $R^2 = 0.48$. The relation for the positive values is not as statistically significant as for the negative trend. This analysis shows an increasing polar cap radius with increasing IMF magnitude, but positive values of both B_y and B_z have smaller radii than negative values of the same magnitude.

In addition to the radius, the offset of the center of the polar cap in both the dawn–dusk and noon–midnight directions were computed. The values are plotted in Figures 4.13 and 4.14 in a manner similar to the polar cap radius plots. Trendlines are shown for the four IMF configurations, but the goodness of fit values are low, ranging from $R^2 = 0.11$ for the noon–midnight trend (blue line) in panel d) to $R^2 = 0.83$ for the noon–midnight trend in panel a). All of the data is consistent, however, and shows a tendency for the polar cap to move from dawn to dusk (positive offset to negative offset) as Kp increases, while at the same time moving from midnight to noon. The equation for these relations are given in

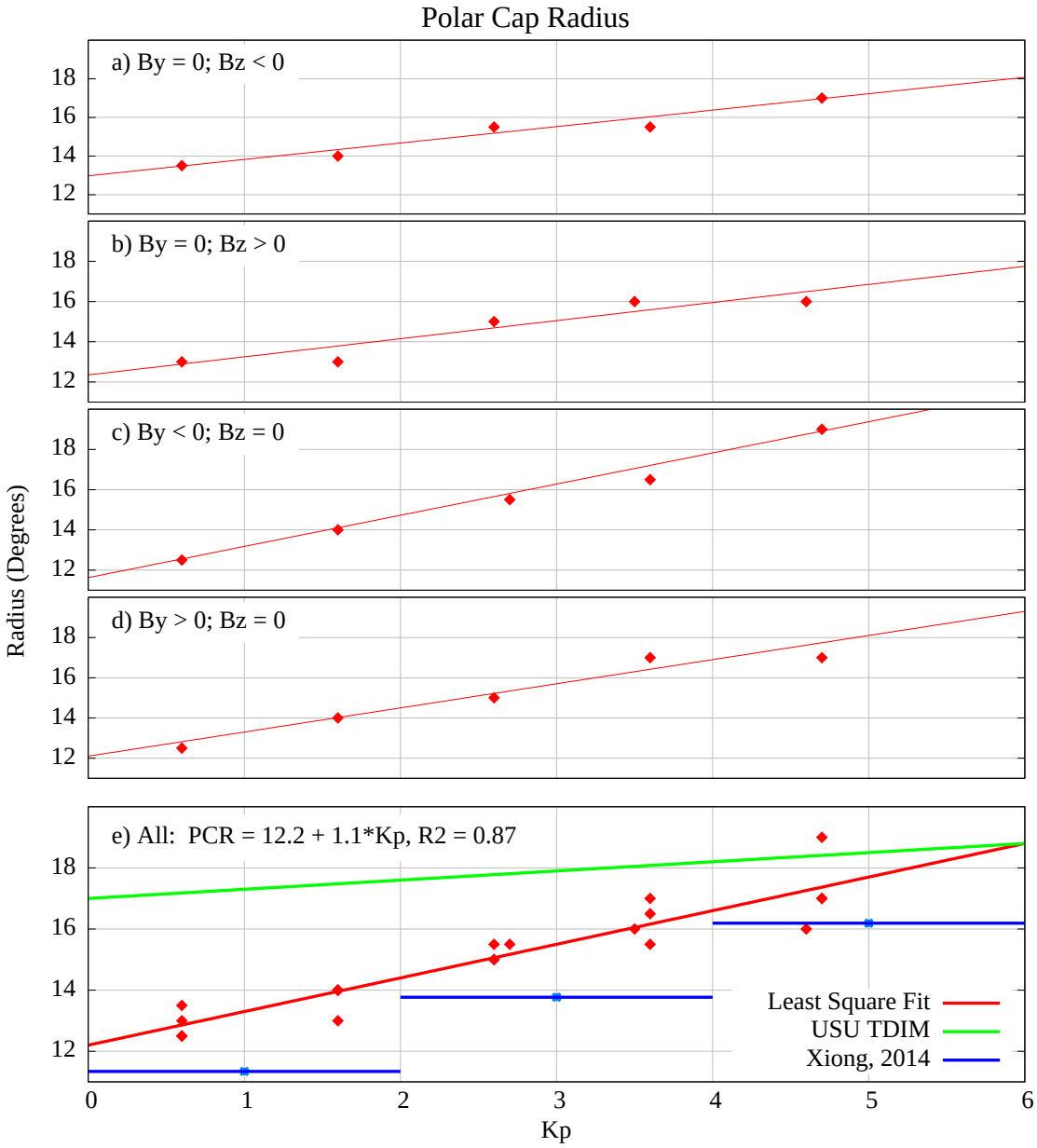

Figure 4.11. Polar cap radius trends based on averaged Kp convection patterns. Each panel shows data points for different IMF configurations: panel a) shows $By = 0, B_z < 0$; b) shows $By = 0, B_z > 0$; c) shows $By < 0, B_z = 0$; panel d) shows $By > 0, B_z = 0$; and panel e) shows radius values for all four IMF configurations in addition to a least square fit line (red). Panel e) also shows polar cap radius relations used in the USU TDIM model (green) and recent findings by *Xiong and Lühr* [2014] (blue).

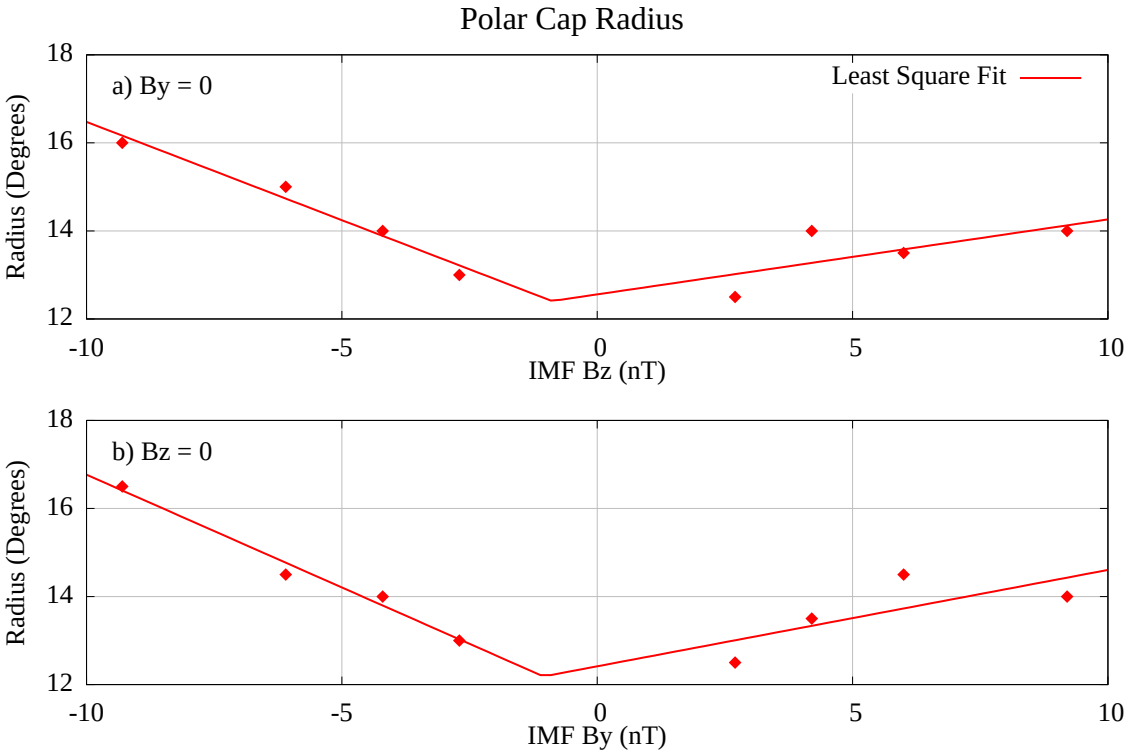

Figure 4.12. Polar cap radius trends based on averaged IMF convection patterns. Trends for when IMF $B_y = 0$ are shown in panel a) while trends for IMF $B_z = 0$ are shown in panel b). The least square fit was done separately for positive and negative IMF values.

panel e) with the dawn–dusk offset going as

$$\text{Dawn–Dusk Offset } = 0.37 - 0.4 \times \text{Kp}, \tag{4.2}$$

and the noon–midnight offset as

$$\text{Noon–Midnight Offset } = -1.02 + 0.4 \times \text{Kp}. \tag{4.3}$$

Both equations have low goodness of fit values with $R^2 = 0.42$ for the dawn–dusk offset and $R^2 = 0.48$ for the noon–midnight offset.

Offsets were also calculated using the IMF bins and are shown in Figure 4.14. This method did not produce any significant trends with all R^2 values below 0.80 except for the noon–midnight offset for $B_z = 0$ (blue line in panel b). However, while the dawn–dusk

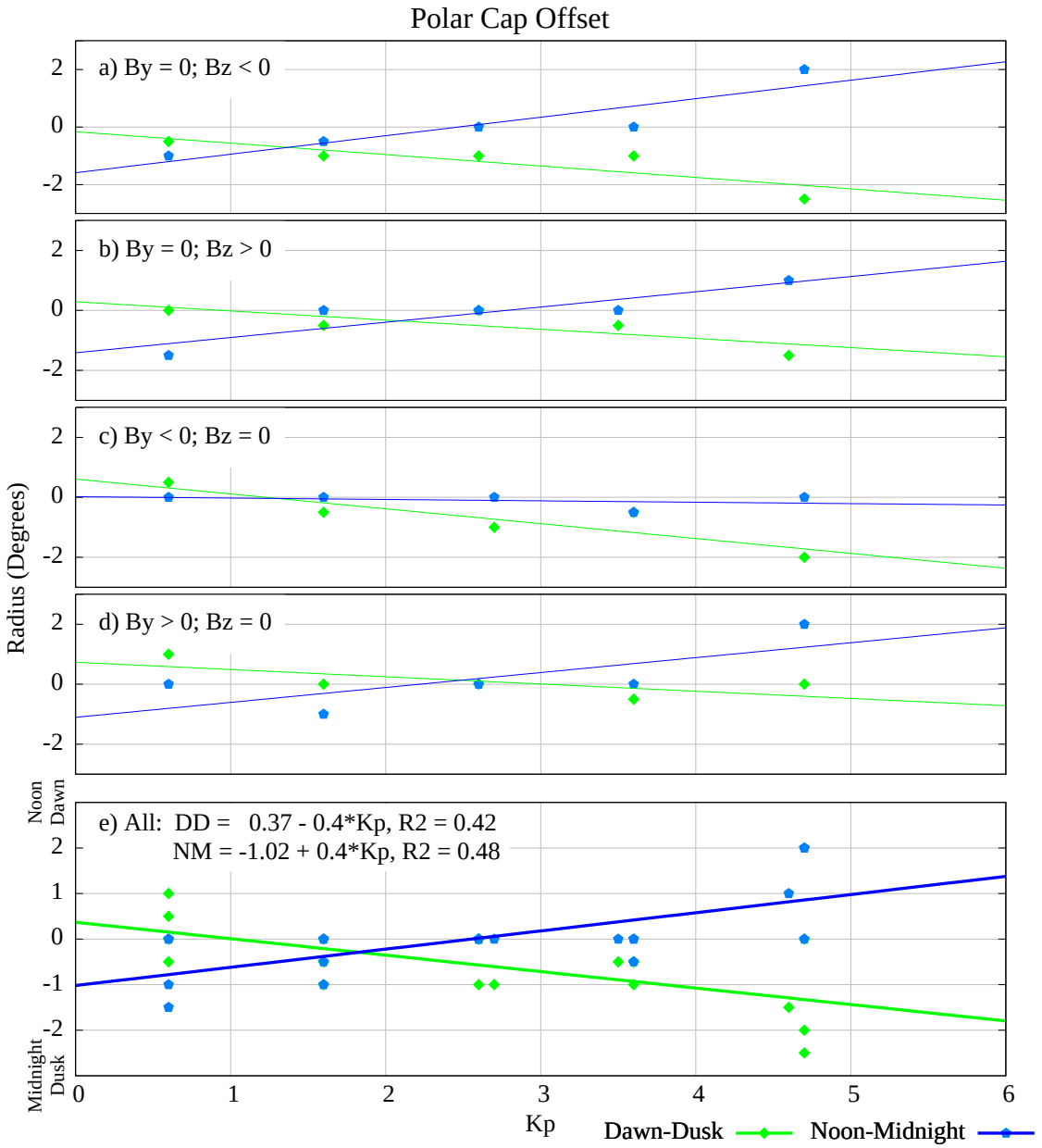

Figure 4.13. Polar cap offset trends based on averaged Kp convection patterns. Each panel shows data points and least square fit lines for different IMF configurations: panel a) shows $By = 0, Bz < 0$; b) shows $By = 0, Bz > 0$; c) shows $By < 0, Bz = 0$; panel d) shows $By > 0, Bz = 0$; and panel e) shows offset values for all four IMF configurations. Dawn–dusk (noon–midnight) offsets are represented by green (blue) data points and lines. Positive values indicate an offset toward dawn/noon, while negative values are offsets toward dusk/midnight.

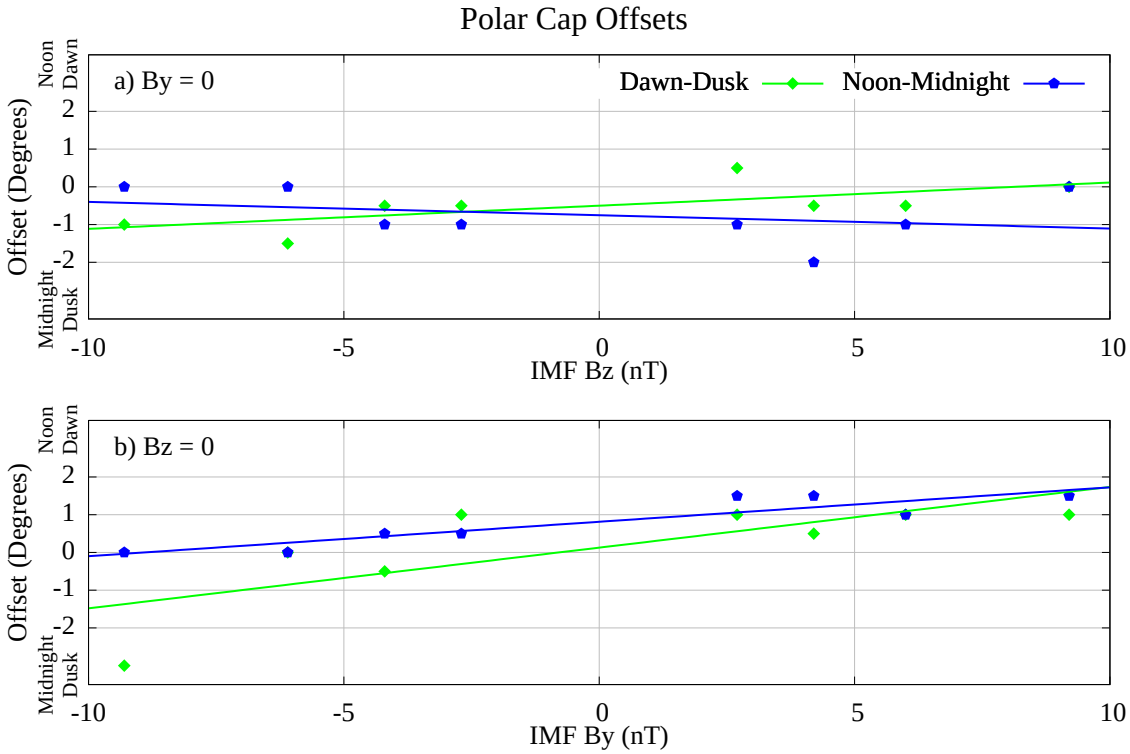

Figure 4.14. Polar cap offset trends based on averaged IMF convection patterns. Trends for when IMF $B_y = 0$ are shown in panel a), while trends for IMF $B_z = 0$ are shown in panel b). The y-axis and color scheme are the same as in Figure 4.13.

offsets are backed by fairly robust data as discussed previously and shown in Figure 4.1, the lack of data in the noon and midnight sectors leads to an incomplete picture of the entire polar cap region.

Arguably, one of the only data-dense cross sections for the time period studied is the dusk–dawn cross section. Therefore, this cross section was chosen for further investigation. Additionally, the near-polar orbit of the DMSP satellite means some orbits do indeed make a pass across the magnetic north pole from dusk to dawn. This cross section is used to look at the two-dimensional slice of sunward/antisunward velocities derived from the DMSP data and compared to empirical model output.

The dusk–dawn cross sections were initially compared to the USU TDIM output. The TDIM requires as input Kp, a dawn–dusk offset, a noon–midnight offset, and a skew value. For this study, the Kp values were varied, while the other three parameters were kept at zero.

This model output was then compared to the averaged velocity data for the Kp bins with $B_y = 0, B_z < 0$. Figure 4.15 shows these cross sections; only the V_y component is plotted and the solid lines are the averaged DMSP data, while the lines with the cross symbol are the TDIM output. The Kp > 4 bin is not shown because it did not contain enough data to result in a physically realistic profile. The TDIM computes the electric potential fall-off from the auroral zones to the midlatitudes using a $1/\sin^4 \Lambda$ function (where Λ is the magnetic colatitude) as recommended by *Volland* [1978]. This fall-off and the relation to Kp is quite obvious with the peak sunward (positive) velocity around 70° MLAT increasing from just over 500 m/s for Kp ≤ 1 to almost 1500 m/s for $3 <$ Kp ≤ 4. Neither a sharp reversal in the flow nor such a drastic increase in sunward velocity is apparent in the data. In fact, the data shows a much more gradual change from the negative, antisunward flow in the polar cap to the positive, sunward flow in the auroral zone. The latitude at which the reversal occurs follows the expected trend for both, starting at a higher latitude for low Kp and extending the antisunward flow to lower latitudes as Kp increases. The model is symmetrical about the pole, while there are clear asymmetries in the averaged data. The peak velocity for averaged data sunward flow is slightly higher on the duskside than the dawnside with values ranging from 400–600 m/s in the dusk peak and from 200–500 m/s in the dawn peak. Antisunward velocities in the polar cap are constant for the TDIM output with values increasing by approximately 75 m/s for every integer increase in Kp. The DMSP velocities are fairly consistent across the polar cap, but a slight decrease near the pole occurs for all Kp ranges.

The next dusk–dawn cross section comparison was done to compare the data to the *Weimer* [2005] model output. This empirical model is driven by solar wind and IMF conditions and so the Kp bins were not relevant to this comparison. As mentioned in section 4.2, the model was run using a solar wind velocity of 450 km/s, a solar wind density of 1.0 cm^{-3}, and a dipole tilt of zero degrees. Four IMF clock angles were run with the nonzero IMF component stepped through the eight different magnitude ranges indicated in Figure 4.16. Each panel in this figure is for a different IMF clock angle, and the line color

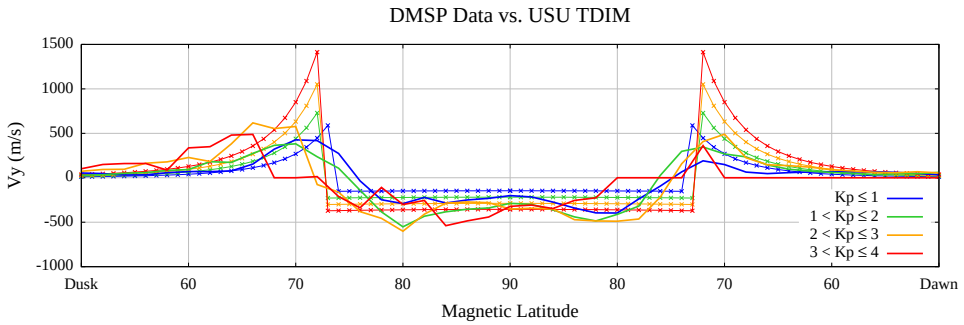

Figure 4.15. Comparison of *Volland* [1978] sunward/antisunward flow velocities to averaged DMSP data for a dusk-to-dawn cross section. Different colors indicate four different Kp bins for both model (lines with the cross symbol) output and averaged DMSP data (solid lines). Positive values indicate sunward flow.

indicates the magnitude range. The model output is shown as lines with the cross symbol and the averaged DMSP data is shown as solid lines. With the exception of $B_y < -7.25$ in panel c), all of the data profiles have lower peak velocities than the model output.

The top panel represents a typical two-cell convection pattern with no B_y influence and an open IMF with B_z southward. In this scenario, the auroral zone peaks for the model output are 2–4 times greater than the data, but polar cap velocities are quite similar, especially on the duskside. On the dawnside, the model output again reaches much larger magnitudes than the data reaches. The model shows more symmetric flow across the pole than the significantly asymmetric flow velocities in the model output. However, there is a significant dip towards zero near the pole for both the model and averaged data; this was noted earlier in the averaged convection pattern plots. The reversal latitudes for the data are almost all poleward of the model output latitudes, which supports the previous finding for a smaller polar cap radius than is typically used.

Although the *Weimer* [2005] output clearly shows sunward flow across the center of the polar cap for the B_z northward (panel b), the data does not reflect this; instead there are fairly constant velocities across the polar cap. The dawnside reversal of the averaged data is closer to the pole than the model output, but the peak velocities of the data and model are the most similar of all the cases. The duskside peak latitude is equatorward of model peaks with the resulting fall-off extending further equatorward, as well.

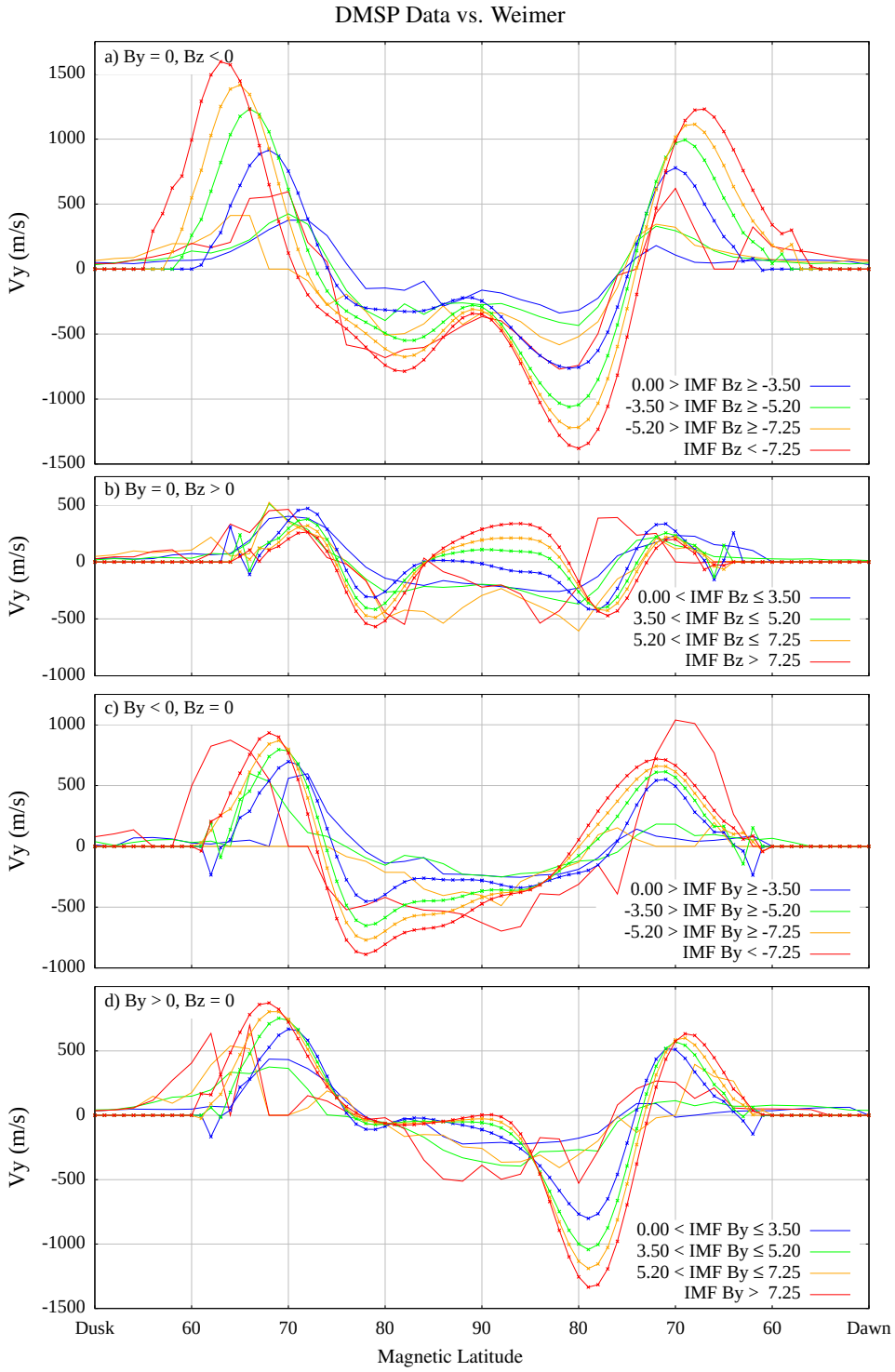

Figure 4.16. Comparison of *Weimer* [2005] sunward/antisunward flow velocities to averaged DMSP data for a dusk-to-dawn cross section. Each panel contains both model (lines with the cross symbol) output and averaged DMSP data (solid lines) for different IMF conditions. Positive values indicate sunward flow, and the IMF clock angle is indicated in the top left corner of each panel. Each color indicates a different magnitude of B_y and B_z.

For the $B_y < 0, B_z = 0$ IMF conditions shown in panel c), both the model output and the averaged data show larger peak velocities on the duskside than on the dawnside; this is consistent with negative B_y values. However, $B_y < -7.25$ is the only magnitude bin in this case that has significant peak on the dawnside; all other bins have peaks less than 250 m/s while the model indicates peak velocities from 500–700 m/s. The only IMF magnitude where the data shows a larger peak velocity than the model is when $B_y < -7.25$; this occurs on the dawnside with a model peak of 700 m/s and a data peak of approximately 1050 m/s. The location of the peaks are also separated by two degrees in latitude with the data peak velocity equatorward of the model peak velocity. The expected asymmetry across the polar cap is not present in the data cross sections.

The bottom panel also does not show the asymmetry expected across the polar cap for positive B_y. The model output shows a large asymmetry across the polar cap with all of the antisunward flow on the dawnside of the pole, but the averaged data show a constant magnitude of antisunward flow within the polar cap. There is, however, a slight asymmetry in the magnitude of the peak velocities in the auroral regions, but the peak velocities for the data profiles are still much lower than the model output.

The differences between a dusk–dawn cross section of the averaged data and the H-M model output were also examined and are shown in Figure 4.17. In this case, four specific IMF conditions were used (shown at the top left of each panel), and the changes driven by geomagnetic activity were studied. There appears to be a slight interpolation error in the model output at the pole, but this does not significantly detract from the analysis. Additionally, some of the cases may not have enough data in the $3 < \mathrm{Kp} \leq 4$ range to produce a reliable cross section; this is especially true for $B_y \neq 0$. The gradual reversal from sunward to antisunward flow is similar to *Weimer* [2005], but the peak velocity magnitudes are much lower. This results in a much better agreement between the data cross sections and the H-M model output for the three IMF conditions in panels b–d. For the B_z southward conditions in panel a) the peak model velocities in the auroral regions are still 200–400 m/s larger than the data. The H-M model does not show sunward flow across the polar cap

region for B_z positive, but the velocities are quite small compared to the data velocities. The model again shows asymmetries for the $B_y \neq 0$ cases, and while the data do not agree for B_y negative, they are quite similar to the model output for B_y positive.

The final comparison shown in Figure 4.18 is of the four empirical models versus the averaged DMSP data for the same four IMF conditions as in Figure 4.17 with $2 < \mathrm{Kp} \leq 3$. It is clear from this plot the USU TDIM output is a very simplified representation of the high-latitude convection. Neither of the other two models nor the data show the same sharp and instantaneous reversal in the flow direction. Instead, the much more realistic pattern is a gradual decrease from the peak sunward flow in the auroral region until the flow reverses direction and then gradually increases to the peak antisunward flow in the polar cap. The decrease from the auroral region peak to a velocity of zero at the polar cap boundary occurs across approximately 3–10 degrees in latitude. With the exception of panel c) the data most closely correlates to the *Heppner and Maynard* [1987] model output.

4.4. Summary

Binning and averaging the data results in surprisingly coherent two-cell convection patterns; however, the data shows no evidence of a multi-cell pattern with sunward flow in the polar cap for B_z northward. When examining dusk–dawn cross sections, the model asymmetries associated with positive B_y are much larger and more pronounced than any asymmetry that shows up in the data. Additionally, the *Weimer* [2005] auroral region velocities can be up to four times larger than the data, and in general, the cross sections of the averaged data are best represented by the H-M model output. When a circular polar cap is fit to the averaged data, a clear relation between the polar cap radius and Kp emerges that is significantly different in both starting radius and change with Kp than what is currently being used to drive the USU TDIM model. The *Volland* [1978] type TDIM should be adjusted for the low Kp values experienced during very low solar minimum conditions to account for a polar cap radius at least four degrees smaller. The significance of such a compression of the polar cap radius in the TDIM model should be investigated.

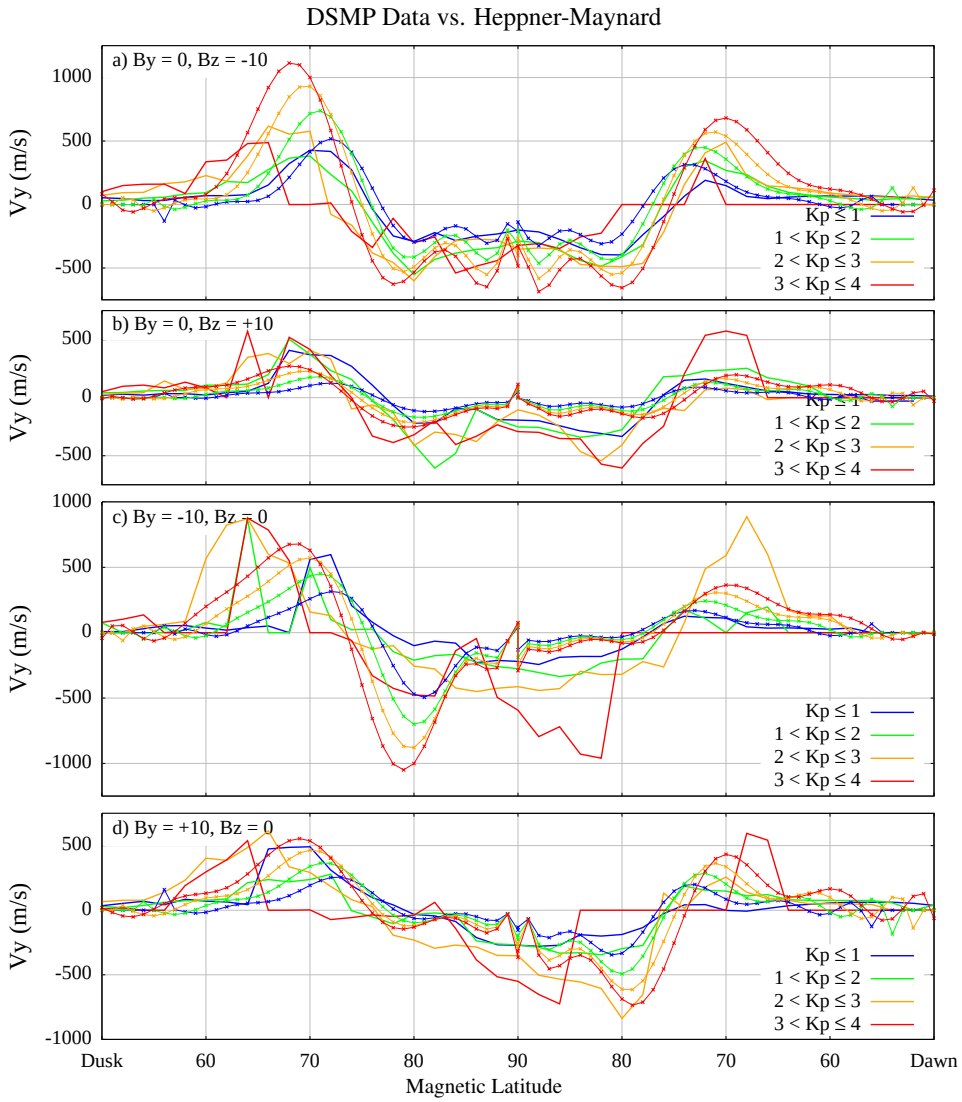

Figure 4.17. Comparison of H-M sunward/antisunward flow velocities to averaged DMSP data for a dusk-to-dawn cross section. Each panel contains both model (lines with the cross symbol) output and averaged DMSP data (solid lines) for different IMF and Kp conditions. Positive values indicate sunward flow. Panel a) shows $By = 0, B_z = -10$, b) shows $By = 0, B_z = +10$, c) shows $By = -10, B_z = 0$, and panel d) shows $By = +10, B_z = 0$. Each color indicates a different magnitude of Kp, as shown in each panel.

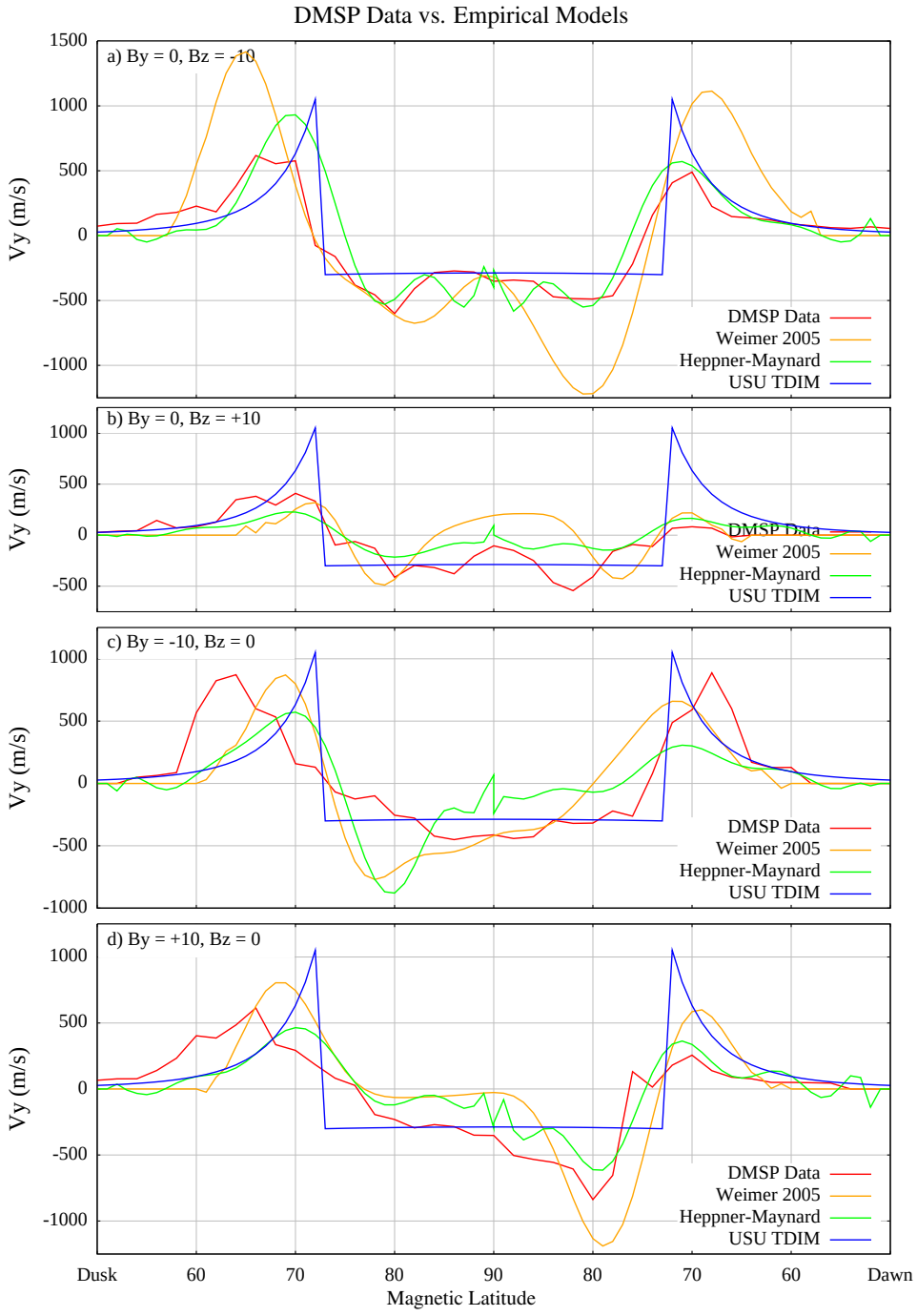

Figure 4.18. Comparison of all three empirical model sunward/antisunward flow velocities to averaged DMSP data for a dusk-to-dawn cross section. Positive values indicate sunward flow. Panel a) shows $By = 0, B_z = -10$, b) shows $By = 0, B_z = +10$, c) shows $By = -10, B_z = 0$, and panel d) shows $By = +10, B_z = 0$. A value of $Kp = 2.5$ was used for all model runs and the data is from the Kp bin with $2 < \text{Kp} \leq 3$.

CHAPTER 5
DUSKSIDE FALL-OFF REGION CLASSIFICATION

5.1. Introduction

Although there are many high-latitude convection models, none are able to capture the instantaneous changes in the polar cap electric field and all have specific advantages and disadvantages. In the previous chapter we examined how a convection pattern obtained from averaging four years of DMSP data compared to different empirical high-latitude convection models. It was noted, although the data was binned according to solar and geomagnetic conditions, the simple fact that multiple orbits were averaged, blended together any orbit-specific features. In this chapter we examine each orbit individually in an attempt to fit different functional forms to the velocity profile of the fall-off region. These fits are first examined individually, then averaged together according to their solar and geomagnetic conditions, and the results are compared to the same empirical models used in the previous chapter.

5.2. Methodology

For this comparison the *Volland* [1975] sine function, along with an exponential and a Gaussian, were used to fit the velocity profile. A single peak followed by a rapid decrease to a platform value typify each of these three functions, which were chosen because they are expected to represent the rapid decrease in the plasma drift velocity outside the polar cap just as the *Volland* [1975] sine function represents the rapid decrease in electric field intensity outside the polar cap with decreasing latitude (section 2.5). The three functions are given as

$$\text{Exponential: } y = y_0 + A \times \exp\left[\frac{(x - x_0)}{B}\right], \tag{5.1}$$

$$\text{Sine: } y = y_0 + \frac{A}{\sin^B(x)}, \tag{5.2}$$

$$\text{Gaussian: } y = y_0 + A \times \exp\left[\frac{-(x - x_0)^2}{2B^2}\right], \tag{5.3}$$

where y_0 is a platform value, x_0 is the latitude of the peak velocity, and A and B are the parameters to be fit. For all three functions, A is related to the magnitude of the peak, while B is related to the gradient of the curve. The portion of the orbit to be fit is constrained between the offset latitude as described in Chapter 3 and x_0, which is the latitude of the peak velocity. An example of these parameters defining the fit region are shown in Figure 5.1.

In order to perform a linear least square fit (LLSF), each expression needs to be transformed into a linear equation. For the exponential, this was done with the following steps:

$$\begin{aligned} y &= y_0 + A\exp\left[\frac{(x-x_0)}{B}\right], && (5.4)\\ y-y_0 &= A\exp\left[\frac{(x-x_0)}{B}\right], && (5.5)\\ \ln(y-y_0) &= \ln\left\{A\exp\left[\frac{(x-x_0)}{B}\right]\right\}, && (5.6)\\ \ln(y-y_0) &= \ln A + \frac{(x-x_0)}{B}, && (5.7)\\ Y &= A' + B'X, && (5.8) \end{aligned}$$

where $Y = \ln(y-y_0)$, $X = (x-x_0)$, $A' = \ln A$, and $B' = 1/B$ to obtain equation 5.8, which is the equation for a line. The LLSF is performed using an automated algorithm and once the A' and B' are returned, the parameters A and B are recovered by taking

$$\begin{aligned} A &= \exp A', && (5.9)\\ B &= \frac{1}{B'}. && (5.10) \end{aligned}$$

Similar transformations are done for the sine and Gaussian functions. For the sine:

$$\begin{aligned} y &= y_0 + \frac{A}{\sin^B(x)}, && (5.11)\\ y-y_0 &= \frac{A}{\sin^B(x)}, && (5.12)\\ \ln(y-y_0) &= \ln\left[\frac{A}{\sin^B(x)}\right], && (5.13) \end{aligned}$$

$$\ln(y - y_0) = \ln A - \ln\left[\sin^B(x)\right], \tag{5.14}$$

$$\ln(y - y_0) = \ln A - B\ln\left[\sin(x)\right], \tag{5.15}$$

$$Y = A' + B'X, \tag{5.16}$$

where in this case, x is the colatitude and $Y = \ln(y - y_0)$, $X = \ln\left[\sin(x)\right]$, $A' = \ln A$, and $B' = -B$, and we take

$$A = \exp A', \tag{5.17}$$

$$B = -B' \tag{5.18}$$

to recover A and B. For the Gaussian:

$$y = y_0 + A\exp\left[\frac{-(x - x_0)^2}{2B^2}\right], \tag{5.19}$$

$$y - y_0 = A\exp\left[\frac{-(x - x_0)^2}{2B^2}\right], \tag{5.20}$$

$$\ln(y - y_0) = \ln\left\{A\exp\left[\frac{-(x - x_0)^2}{2B^2}\right]\right\}, \tag{5.21}$$

$$\ln(y - y_0) = \ln A - \frac{(x - x_0)^2}{2B^2}, \tag{5.22}$$

$$Y = A' + B'X, \tag{5.23}$$

where $Y = \ln(y - y_0)$ and $A' = \ln A$ are still the same, but $X = (x - x_0)^2$ and $B' = -1/2B^2$. To recover A and B we take

$$A = \exp A', \tag{5.24}$$

$$B = \sqrt{-\frac{1}{2B'}}. \tag{5.25}$$

One issue encountered when solving for the LLSF occurred when trying to determine where to set the platform value, y_0. It was initially set to the adjusted velocity at the offset latitude (OL) because, while the velocity of most orbits should be trending towards zero at low latitudes, a penetration event could cause the velocity to level out at some finite

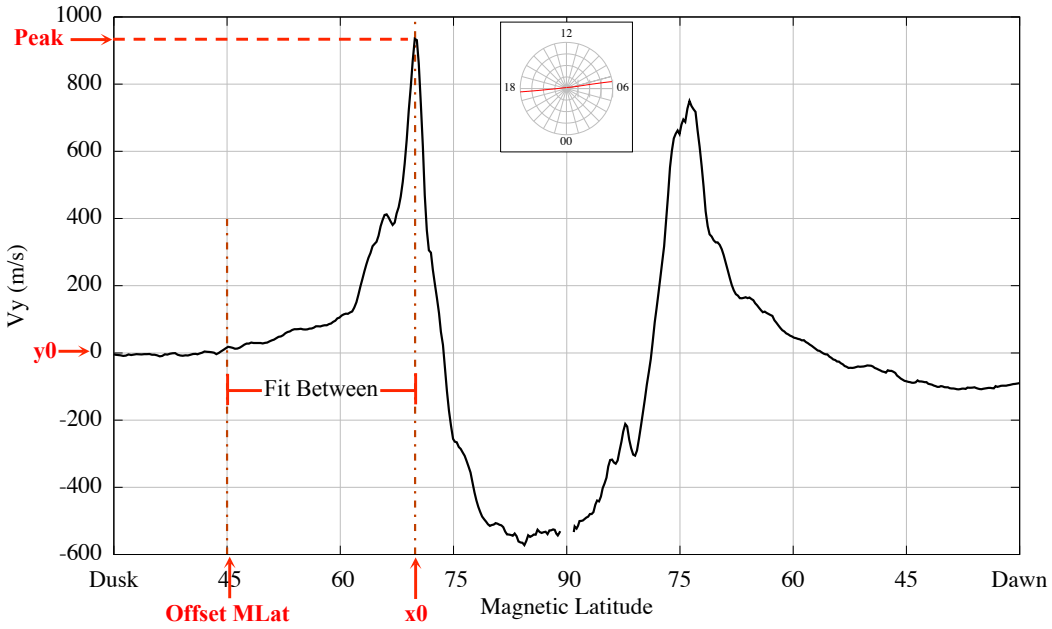

Figure 5.1. Orbit fit parameters for an example orbit. Each function is fit between the offset latitude and the latitude of the peak velocity, x_0. y_0 is the low-latitude velocity limit, typically zero.

value above zero (i.e., a platform). However, because of the small-scale structure within the orbit data, this value often does not represent the low-latitude platform and many instances occur where V_y poleward of the offset latitude is less than y_0. This created a problem in the fitting algorithm because the natural logarithm is undefined for negative numbers.

One solution to this problem is to set y_0 to the minimum value in the region to be fitted. With $y_0 = y_{min}$, the natural logarithm is always defined and all data points are included in the LLSF. However, this solution still may not be, and usually is not, close to the actual platform value. Another solution is to simply set the platform value to zero. While this solution does not explicitly solve either problem, on examination of hundreds of orbits, it was hypothesized it may be the best solution.

Figure 5.2 shows four examples of fits obtained using the three different values for y_0. These plots show only the fall-off region and extend equatorward to 20° to show actual platform value of the velocity data at low latitudes. All plots show exponential fits; the red line uses $y_0 = y_{min}$, the green line is obtained when $y_0 = V_y(OL)$, and the blue line is

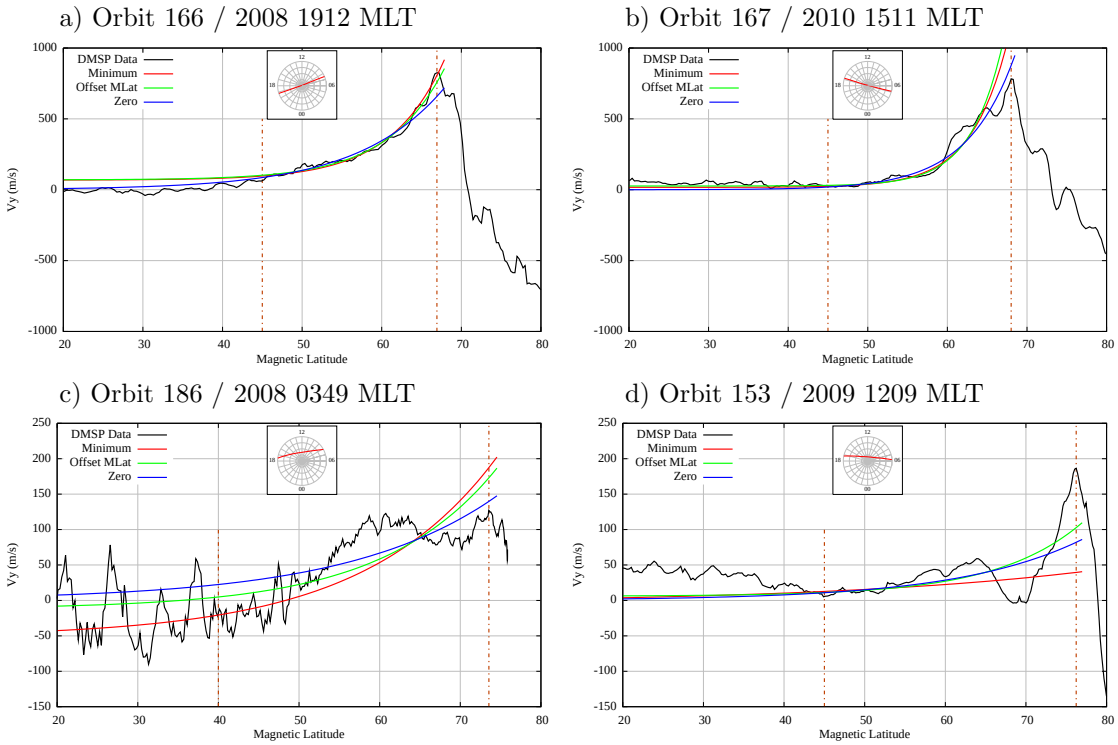

Figure 5.2. Comparison of linear least square fits (LLSF) using different values of y_0. The left vertical brown dashed line indicates the offset latitude while the right vertical brown dashed line indicates the peak latitude. The black line is the orbit data, the red line is the LLSF using $y_0 = y_{min}$, the green line uses $y_0 = V_y(OL)$, and the blue line uses $y_0 = 0$.

for $y_0 = 0$. The left vertical brown dashed line indicates the offset latitude while the right vertical brown dashed line indicates the peak latitude. When the orbit data is well-behaved, there is little difference in the resulting fit (panels a and b); however, when significant structure exists in the velocity data at low-latitudes (panel c) or velocities in the fit region decrease below the velocity at the offset latitude (panel d), then the different values of y_0 can result in different fits either at low latitudes, at the peak latitude, or both. However, it is difficult to say which fit is most correct. Therefore, because for the well-behaved orbits, the fits are all very similar, and in most cases velocities are expected to go to zero at low latitudes, the platform value was chosen as zero. Velocities in the fitted region less than zero were ignored and not included in the fit.

Even with these measures taken to achieve the best fits possible, some orbits still returned unexpected parameters and showed up as outliers in scatterplots of the fit param-

eters. These orbits were examined individually to determine if they represented a class of interesting phenomena or unique set of conditions, or if the unexpected parameters were the result of bad orbit data or poor specifications for the fit parameters. Figure 5.3 shows some of these orbits. Note, the functional fits for all of these orbits have a very high goodness of fit value ($R^2 > 0.80$), but most of the original data is erroneous.

For these plots, the vertical brown dashed lines are the same as in Figure 5.2, but here the red line is the exponential fit, the green line is the sine fit, and the blue line is the Gaussian fit. The left panel shows the entire orbit from 40° in the ascending node on the duskside across the pole, to 40° in the descending node on the dawnside. Missing data in the middle of the plot indicates the orbit did not cross 90° mlat; the small inset shows the orbit path in a polar plot. The right panel shows only the duskside of the orbit from 40° to 75° in order to zoom in on the fitted region. The solar and geomagnetic conditions at the time of each orbit are shown in the upper left corner of each left panel plot.

Panel a) shows a near perfect fit for all three functions, but on closer inspection, the fitted region is only five degrees in latitude and the peak velocity occurs at a low magnetic latitude of 50°. While this technically could be possible, examination of the rest of the orbit and the Kp index give no indication for this low-latitude velocity peak. This is most likely a case where the data is bad due to a high ratio of H^+. Apart from the highly fluctuating velocities from 70–80° on the duskside, the orbit in panel b) appears quite normal. However, velocities of nearly 3 km/s are not typical of quiet solar and geomagnetic conditions with Kp = 0.7 and a slightly negative IMF B_z component. Orbits like this are typical for the winter months of 2007, which was the beginning of the most recent extreme solar minimum. Again the R^2 values are very high, but the resulting fit parameters do not coincide with other orbits that have the same solar and geomagnetic conditions. Because there are so many orbits in 2007 that have this signature, and many of the duskside sectors of the 2007 orbits are in darkness, all orbits from 2007 were discarded for this analysis. The fitted portion of the orbit in panel c) is similar to panel a), but the rest of the orbit data is missing. Therefore, it is difficult to determine if the location and value of the peak velocity is the

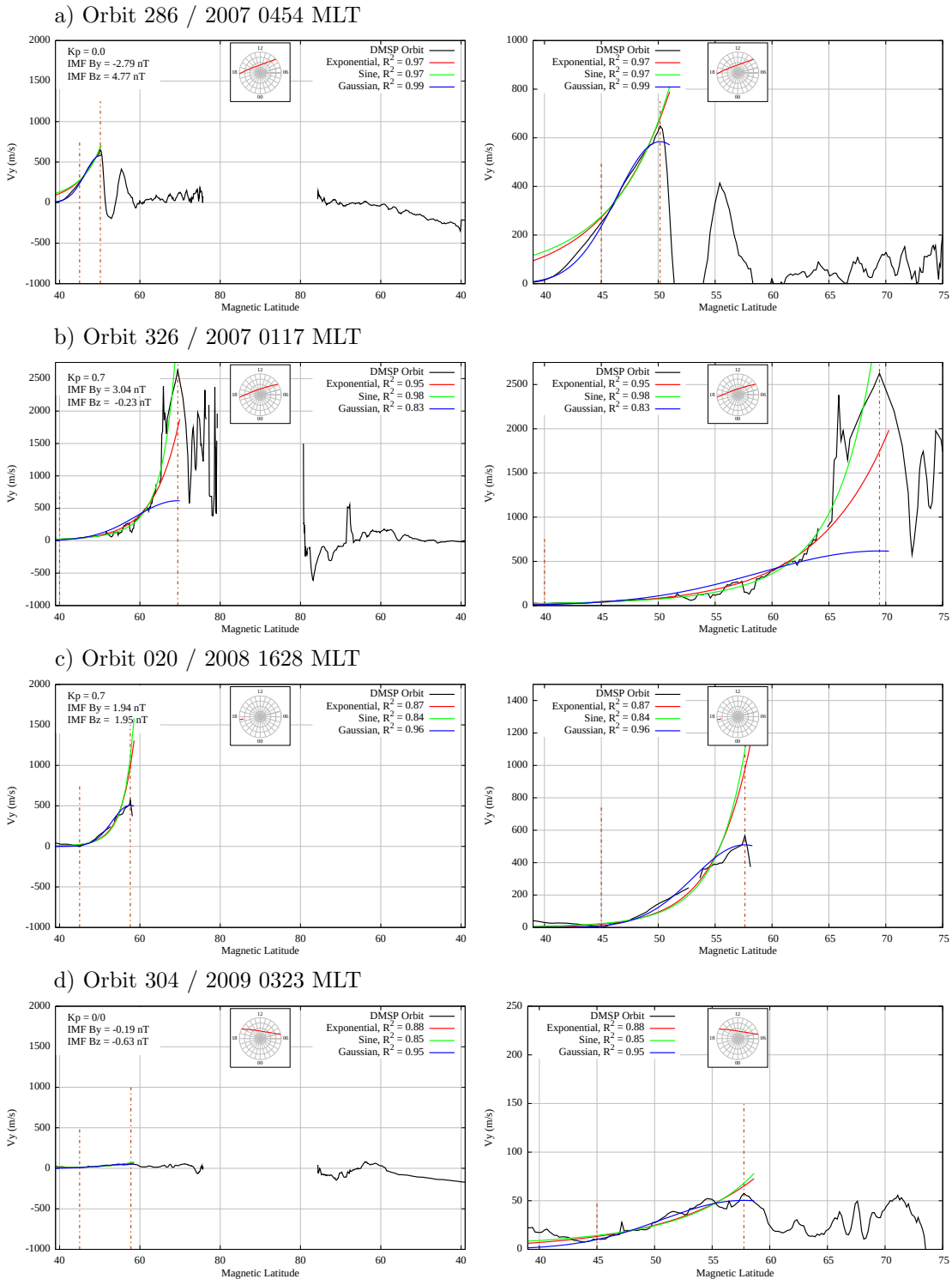

Figure 5.3. Linear least square fits for bad dusk orbit data. The left vertical brown dashed line indicates the offset latitude, while the right vertical brown dashed line indicates the peak latitude. The black line is the orbit data, the red line is the exponential LLSF, the green line is the sine fit, and the blue line is the Gaussian fit.

actual peak or is just where the data cut off. And while panel d) shows perfectly acceptable velocity data for quiet geomagnetic conditions (Kp = 0), the resulting fit parameters are atypical due to the lack of an actual peak in the velocity data in the auroral region.

In an attempt to remove as many bad orbits from the analysis as possible the following parameters were set. All orbits from 2007 were discarded. If the fitted region was less than five degrees, the orbit was discarded. If more than half the data points in the fitted region were missing or negative, the orbit was discarded and was not included in the analysis.

With these stipulations in place, functional fits were performed on 12,592 orbits. The goodness of fit value, R^2, was used to classify which orbits had good fits. Table 5.1 shows the number and percentage of orbits with certain R^2 values for the three functional fits. A perfect fit is $R^2 = 1.0$ and so a very good fit would be an orbit with $R^2 > 0.9$. For both the exponential and sine fits, only 11% of the orbits fall into this category and only 5% for the Gaussian fit. If the criteria for a good fit is extended down to $R^2 > 0.8$, the number of orbits increases to around 31% (about 4,000 orbits) for the exponential and sine fits and to 18.5% for the Gaussian fit (2,300 orbits). Figure 5.4 shows the histograms of R^2 for each functional fit. Both the exponential and the sine are more concentrated at the high R^2 values, while the Gaussian fits are more evenly distributed among the lower R^2 values. In order to evaluate only orbits with good fits but still retain enough orbits for to maintain a statistical significance in the analysis, an R^2 value of 0.8 was chosen as the cutoff.

These restrictions leave us with orbits such as those shown in Figure 5.5 where four examples of orbits with good fits for all three functions are shown. The plot layout is the same as for Figure 5.3. Now that the analysis is restricted to orbits with good functional fits, we can examine the results.

It should be mentioned that the majority of the orbits, nearly 9,000 of them, are not used in this analysis because a good fit was not obtained with the functions chosen. This is evidence that capturing the real structure of the convection pattern is still a problem. These simple models may be adequate in capturing climatological patterns, but the capturing the weather of the ionosphere is needed to model the remaining 70% of the orbits.

Table 5.1. Duskside Goodness of Fit Statistics*

	Exponential Fit		Sine Fit		Gaussian Fit	
	Number	Percent	Number	Percent	Number	Percent
$R^2 > 0.9$	1407	11.2%	1473	11.7%	625	5.0%
$R^2 > 0.8$	3889	30.9%	4015	31.9%	2332	18.5%
$R^2 > 0.7$	5958	47.3%	6264	49.7%	4320	34.3%
$R^2 < 0.6$	4979	39.5%	4653	37.0%	6464	51.3%
$R^2 < 0.4$	2609	20.7%	2303	18.3%	3680	29.2%
$R^2 < 0.2$	1140	9.1%	980	7.8%	1714	13.6%

*Total number and percentage of the 12,592 duskside orbits with goodness of fit R^2 values within the listed categories.

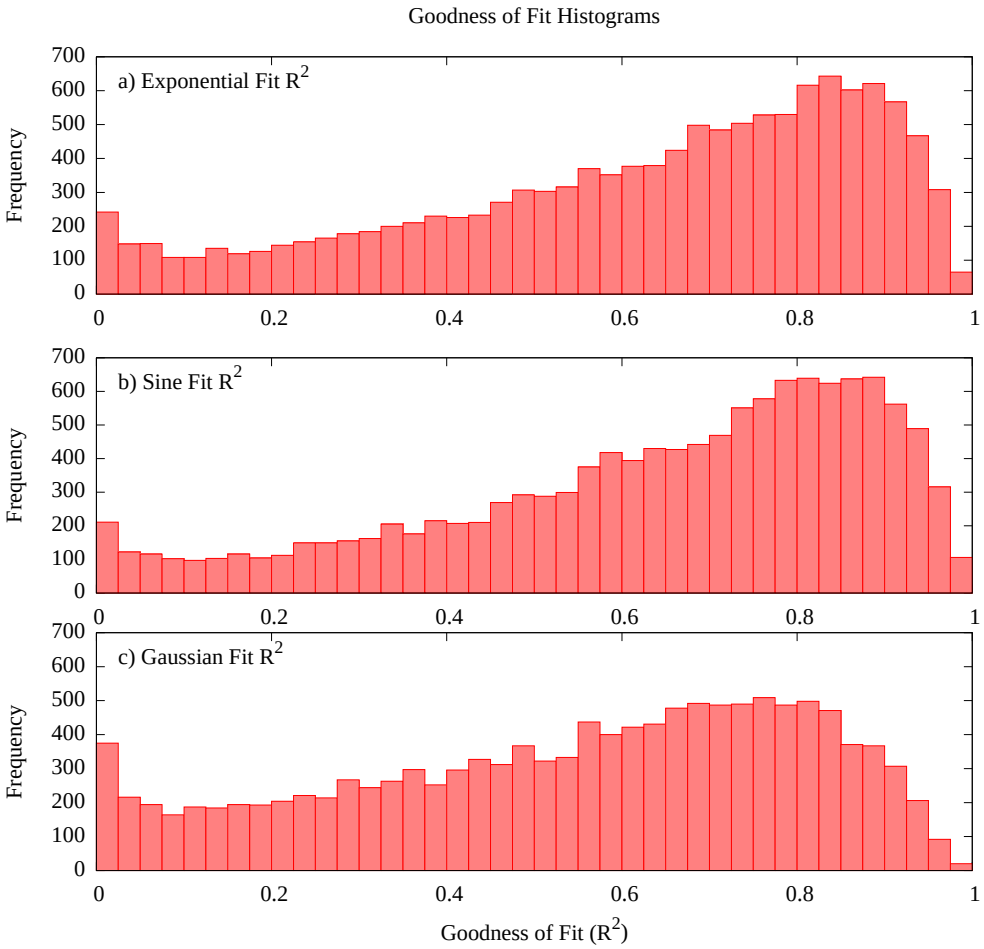

Figure 5.4. Duskside goodness of fit histograms. The top plot is the exponential fit, the middle plot is the sine fit, and the bottom plot is the Gaussian fit.

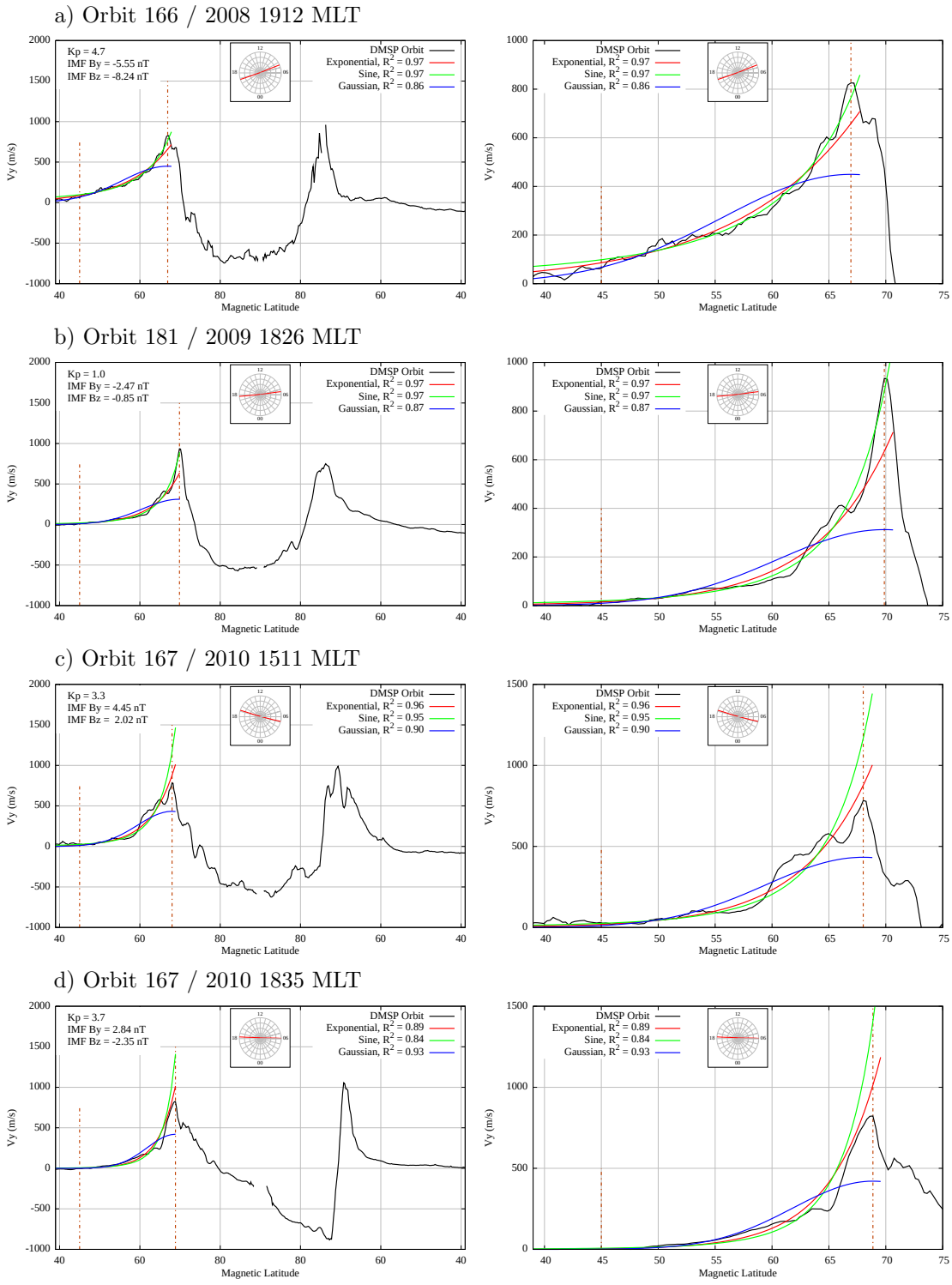

Figure 5.5. Linear least square fits for good dusk orbit data. The left vertical brown dashed line indicates the offset latitude, while the right vertical brown dashed line indicates the peak latitude. The black line is the orbit data, the red line is the exponential LLSF, the green line is the sine fit, and the blue line is the Gaussian fit.

5.3. Results

First, we look at some of the parameters to check the fitted functions are behaving as expected. Figure 5.6 is a plot of the latitude of the peak velocity versus Kp. The red crosses indicate the values for individual orbits, the black dots represent the mean latitude, and the blue squares are the median latitude for each Kp value. The vertical black lines extend to plus/minus one standard deviation from the mean. The angled black line is a LLSF to the mean values, while the blue line was obtained from the TDIM model, and the green line was obtained from the H-M model. The 1800 MLT radian was used to obtain the data for both models.

For low Kp values, the latitude of the peak velocity is around 75° and decreases to 60° for Kp = 6.7; this indicates the polar cap and the auroral zone expand equatorward as Kp increases. The trend obtained from the two models also indicates this expansion, but at a much slower rate than the data. The data follow an expansion of approximately two degrees for every integer increase in Kp, while the TDIM expands only three degrees from Kp = 0 to Kp = 9. The H-M model falls in between with an expansion of just over one degree for every integer increase in Kp. The outlying points in the 50–60° range for low Kp occur because of orbits such as panel a) and c) in Figure 5.3.

Next the velocity at 60° obtained from each of the functional fits is examined as a function of Kp. These plots are shown in Figure 5.7. Panel a) shows the data for the exponential fit, panel b) is for the sine fit, c) is the Gaussian fit, and the bottom plot shows the mean values for all three fits (solid lines) in addition to lines obtained from the two models (dashed). Although there is a large spread in the data, the trend in the mean and median values is very similar for all three fits, as can be seen in the bottom panel. The velocity starts out around 50 m/s for low Kp, and gradually increases up to nearly 500 m/s for Kp = 6. The trend is not linear, as it was with the latitude of the peak velocity, but it indicates a similar expansion. Either the width of the region with strong sunward flow is increasing, or the entire region is moving equatorward. The latter is the most likely since previous analysis indicated both the polar cap and the peak velocity expand equatorward

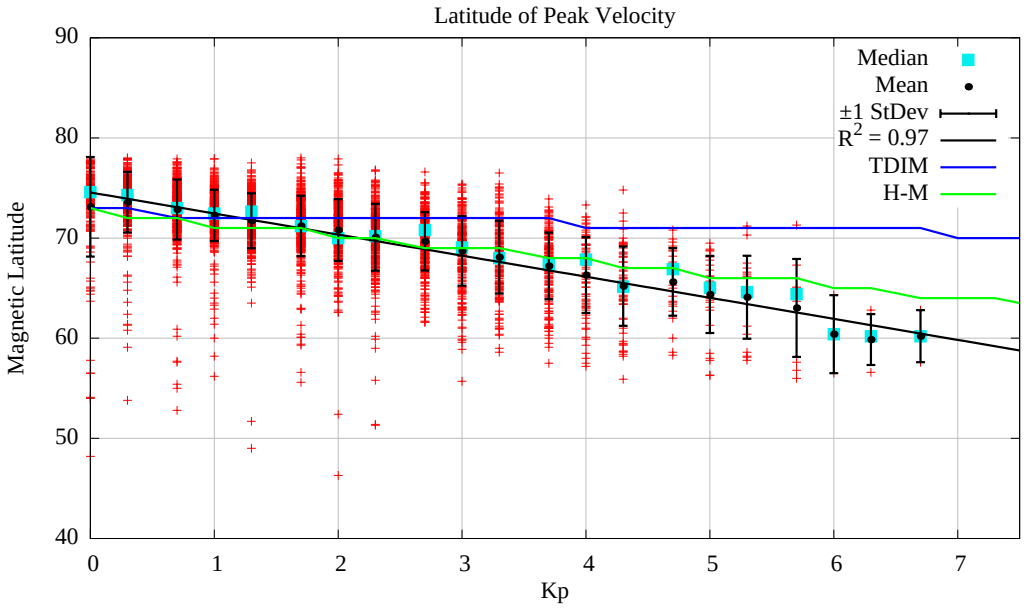

Figure 5.6. Duskside latitude of the peak velocity as a function of Kp. Red crosses indicate values for individual orbits, black dots represent the mean latitude, and blue squares are the median latitude for each Kp value. The vertical black lines extend to plus/minus one standard deviation from the mean. The angled black line is a LLSF to the mean values, while the blue line was obtained from the TDIM model, and the green line was obtained from the H-M model. The 1800 MLT radian was used to obtain the data for both models.

with larger Kp. Although the three fits show a similar trend, it is quite different from the trend obtained from each empirical model. Both models show an increase in the velocity with Kp, but the TDIM increases at a slower, more linear rate, while the H-M model shows a similar trend, but seems to be shifted to the right by 2 Kp.

Similar to the comparison of the velocity at 60°, Figure 5.8 shows the slope of the functional fit at 60° as a function of Kp. The slope was calculated as the change in velocity per degree of latitude; therefore, a small slope represents a flatter line and a large slope indicates a a steeper line. The trend shown by these plots is consistent with the previous two results; as Kp increases, the slope of the line at 60° becomes steeper. Both the exponential and sine fits have similar trends, but the Gaussian in this case more closely resembles the TDIM output. Both show only a small increase in the slope across Kp. For the TDIM this is still consistent with the expansion seen in both Figures 5.6 and 5.7. However, for the Gaussian, this can be explained by the nature of the function. While both the exponential

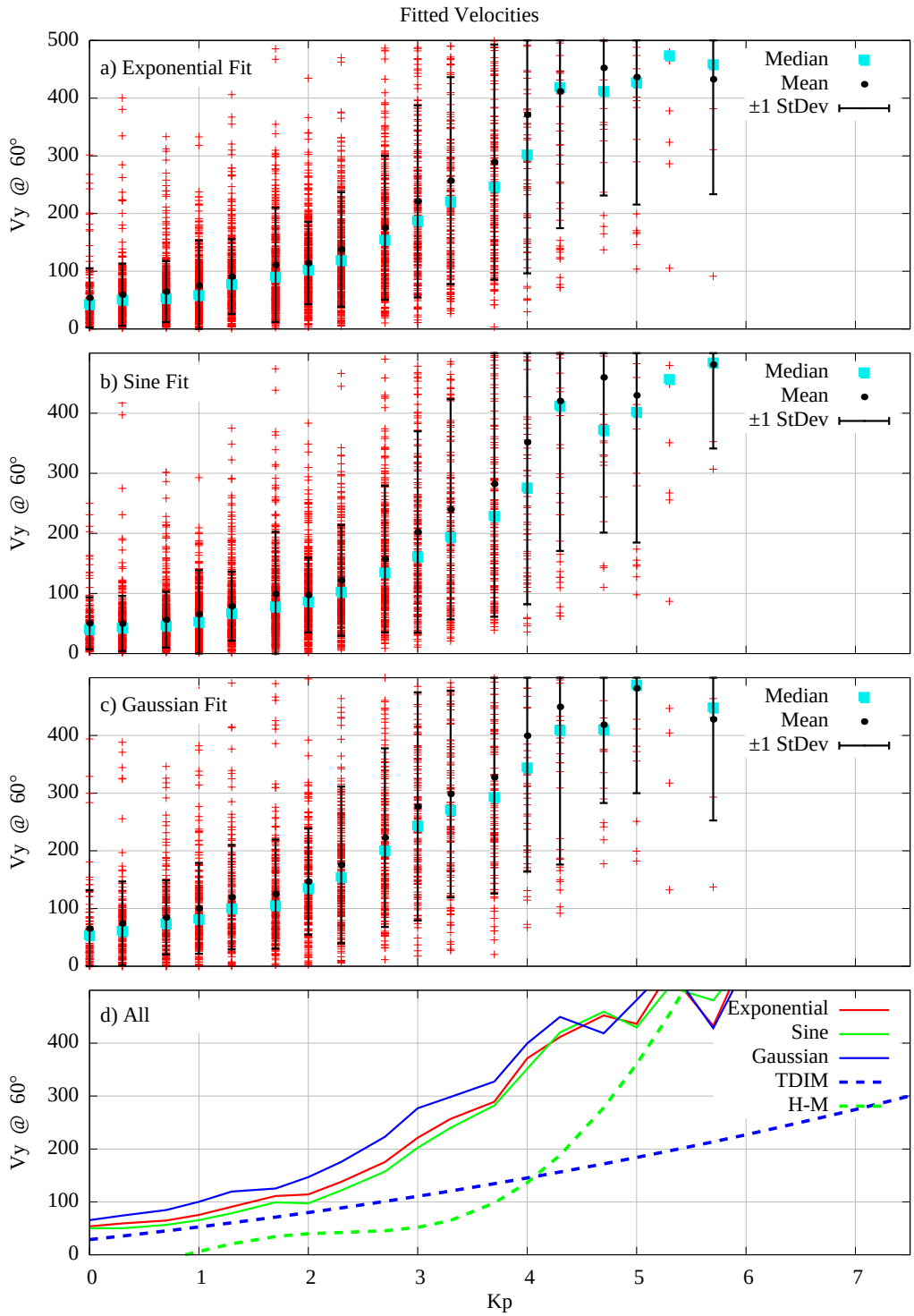

Figure 5.7. Duskside velocity at 60° obtained from functional fits. The top panel is the exponential fit, panel b) is for the sine fit, and panel c) is the Gaussian fit; data is shown in the same manner as the previous figure. Panel d) shows the mean value of the velocity for each fit as solid lines and velocity values at 60° obtained from the TDIM (blue) and H-M model (green) as dashed lines.

and the sine functions continue to increase poleward of the peak velocity latitude, the Gaussian reaches a maximum at the peak velocity latitude. Therefore, as the peak moves closer to 60°, the slope must start to decrease since at the maximum, the slope will be zero. Especially interesting is the output from the H-M model shown by the green dashed line. If Figure 4.17 is examined closely in the fall-off region, it can be seen that the H-M model output has a slight sinusoidal variation, which is most likely due to the interpolation of the convection patterns.

As discussed earlier, each function has two free parameters that are determined using the LLSF algorithm. Parameter A is related to the magnitude of the function and parameter B is related to the slope. Figures 5.9, 5.12, and 5.15 are histograms for the two parameters for the exponential, sine, and Gaussian fits, respectively. The equation for each function is shown at the top of each figure with parameter A in the top panel and parameter B in the bottom panel. This analysis only includes parameters from orbits with a goodness of fit of $R^2 > 0.8$. None of the histograms show a truly normal distribution, especially for parameter A, but the distributions for parameter B are close to normal, but with a positive skew. In addition to the histograms, the parameters are plotted against each other in Figures 5.10, 5.13, and 5.16 to show how A and B are related for each function. Examples of curves plotted using different combinations of A and B are shown in Figures 5.11, 5.14, and 5.17 to show how each parameter affects the curve. In general, as A increases (i.e., larger peak velocities) B decreases.

For the exponential fit parameters shown in Figure 5.9, 67% of the orbits have parameter A below 750; 29% fall between 750 and 2000, and only four percent are larger than 2000. This is not surprising as the data is from a period of low solar activity when velocities are not expected to be large. For the exponential function, the inverse of parameter B represents the exponential decay of the curve; a larger decay constant indicates a steeper gradient. This analysis shows for 67% of the orbits, parameter B is between four and nine. Values less than four account for 15% of the orbits, and the remaining 18% have values greater than nine. Using the median values for parameters A and B, the orbits can be fit

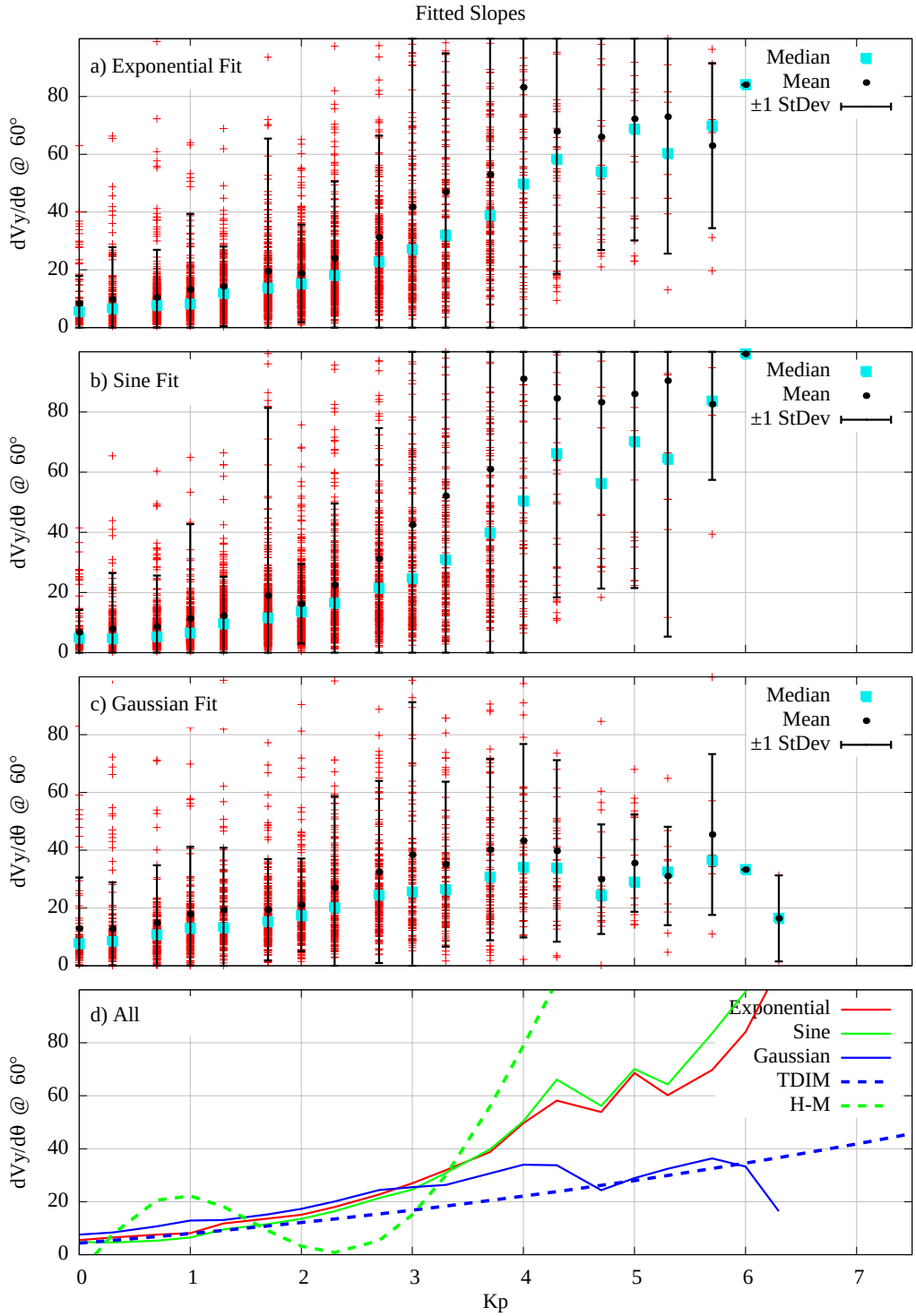

Figure 5.8. Duskside slope at 60° obtained from functional fits. The top panel is the exponential fit, panel b) is for the sine fit, and panel c) is the Gaussian fit; data is shown in the same manner as the previous figure. Panel d) shows the mean value of the velocity for each fit as solid lines, velocity values at 60° obtained from the TDIM (blue), and H-M model (green) as dashed lines.

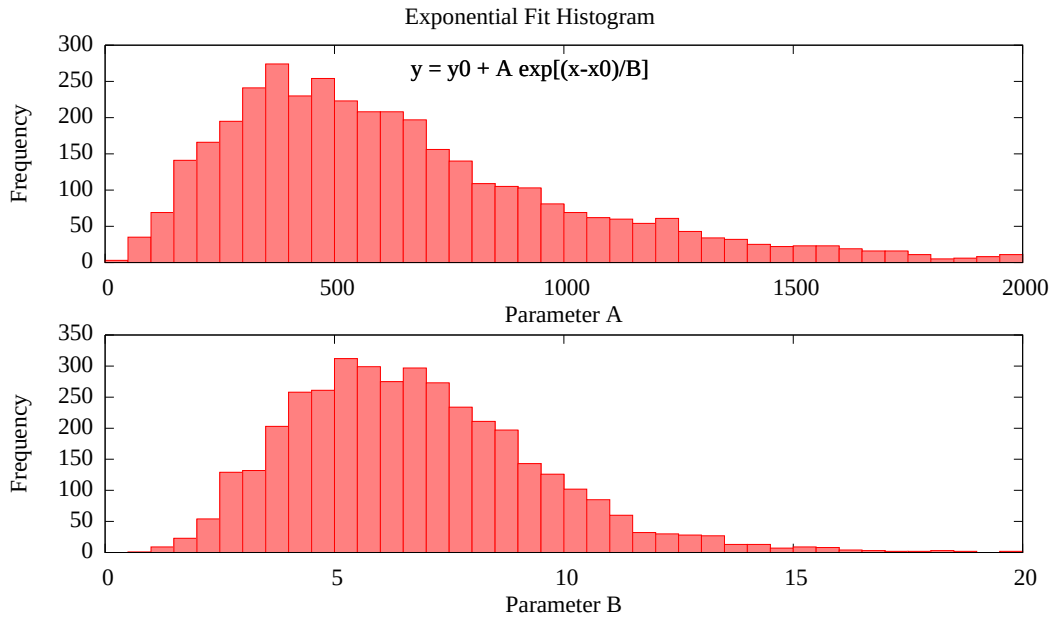

Figure 5.9. Histogram of duskside exponential fit parameters A and B. The function is shown at the top center. Parameter A is in the top panel and parameter B is in the bottom panel.

with an exponential using

$$y = 575 \times \exp\left[\frac{x - x_0}{6.4}\right]. \tag{5.26}$$

In order to understand the gradient, both A and B must be considered. If A remains the same, the function with the smallest B value will have the steepest curve. However, because A can also change, larger values of B do not necessarily mean a flatter curve. In Figure 5.10, the lowest values of B cover all ranges of A. In contrast, only for the lowest values of A do the largest values of B occur. The Roman numerals in Figure 5.10 correspond to the curves shown in Figure 5.11. The curves show exponential functions for three different sets of A and B. The latitude for the peak velocity was held constant at 75° in computing these functions. From this figure, it is clear parameter A also has a large influence on the steepness of the curve. While both the blue and green curves have the same value for B, the blue curve is much steeper because its A value is three times larger. The red and green curves, on the other hand, have the same value for A, but different B values. Because the green curve has a lower B value, it falls off more quickly than the red curve.

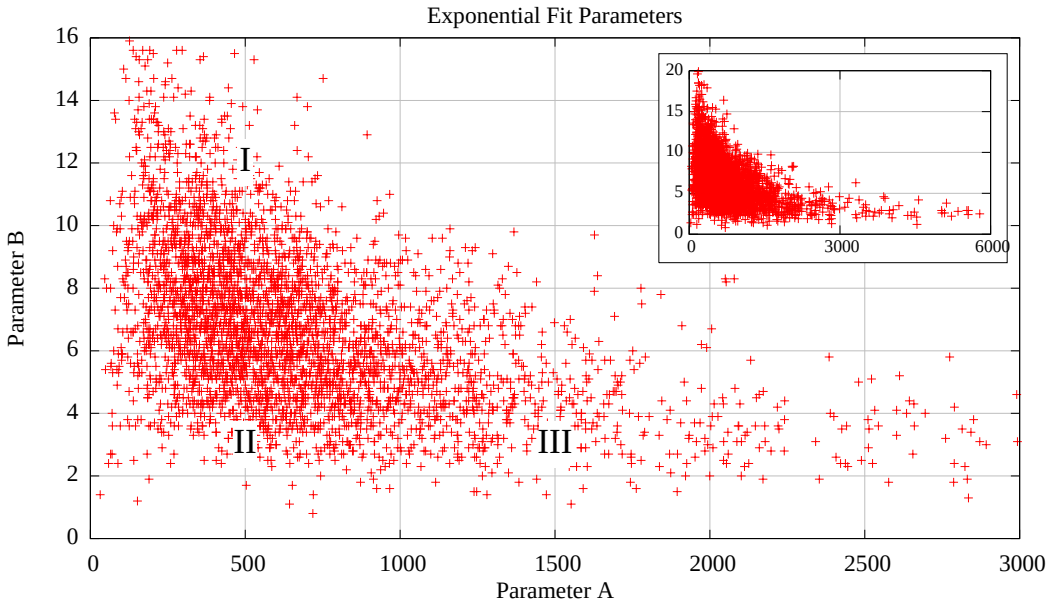

Figure 5.10. Scatterplot of duskside exponential fit parameters A and B. The inset shows the full range of values for A and B, while the main plot shows the region with the largest concentration of points. The Roman numerals correspond to the curves shown in Figure 5.11.

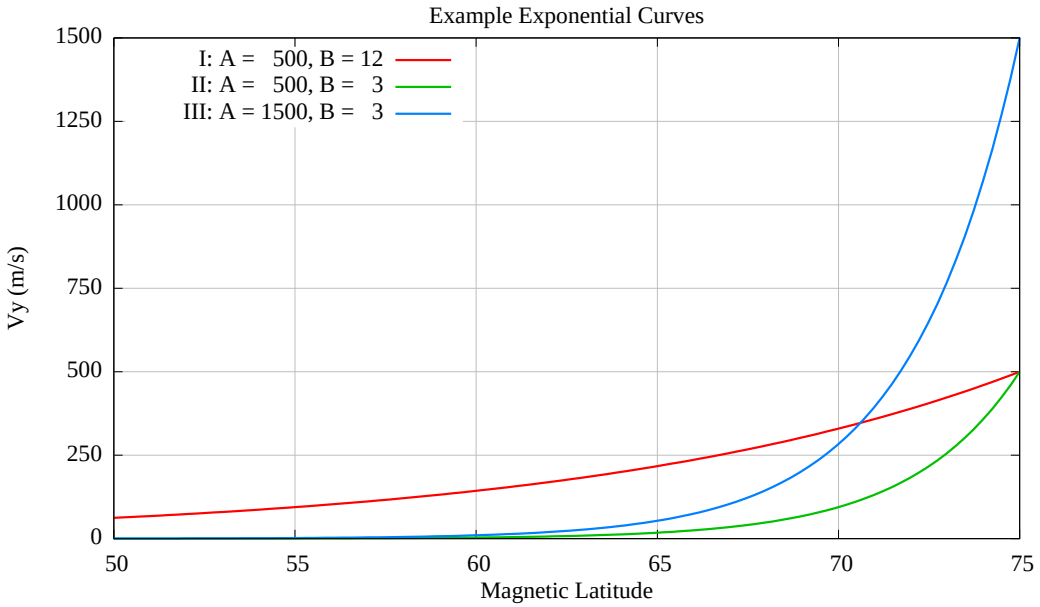

Figure 5.11. Duskside exponential curves using different A and B parameters. The Roman numerals correspond to the locations shown in Figure 5.10.

The sine fit histogram, scatterplot, and example curves are shown in Figures 5.12–5.14, respectively. For the sine function, A does not explicitly give the peak velocity, but is instead a scaling factor of the inverse sine function. In this case the largest concentration of A values falls near zero with 23% of the orbits having $A < 0.5$. Another quarter of the orbits fall in the range of $0.5 < A < 2.5$ and the rest are spread out fairly evenly from $A = 2.5$ to $A = 40$. The largest number of orbits have a B parameter near 4.5, which is nearly identical to the value used by *Volland* [1978]. Using the median values for parameters A and B, the orbits can be fit with a sine using

$$y = \frac{2.3}{\sin(x)^{5.1}}. \tag{5.27}$$

The sine function is different than the exponential in that a larger B parameter means a steeper curve for the same A value. Figure 5.13 shows a scatterplot of all the values for A versus the values for B. While the trend between A and B is similar for the sine, as it was for the exponential with B decreasing for larger values of A, there is not nearly as much spread in the data. For $A > 3$, the spread in the B values is only about four points and is $3 < B < 7$ for $A = 3$ and between $2 < B < 6$ for $A = 10$. For the smallest A values, B ranges from just over four up to nearly 30. The curves with small A and large B are very steep, as can be seen by the red curve in Figure 5.14. Each of the three curves in this figure correspond to the locations marked by Roman numerals in Figure 5.13. The flattest curve (green line) occurs for low values of both A and B and the steepest curve occurs with the largest value of B.

The next set of plots are for the Gaussian fit. The histograms shown in Figure 5.15 are very similar to those returned by the exponential. The A values are concentrated at even lower values with 62% of the orbits falling below $A = 400$. Only five percent of the orbits have $A > 1000$ with the rest of the orbits falling in between these two values. The bottom panel of Figure 5.15 shows the histogram for parameter B for the Gaussian fit. Using the median values for parameters A and B, the orbits can be fit with a Gaussian using

$$y = 332 \times \exp\left[\frac{-(x - x_0)^2}{2 \times 8.6^{\,2}}\right]. \tag{5.28}$$

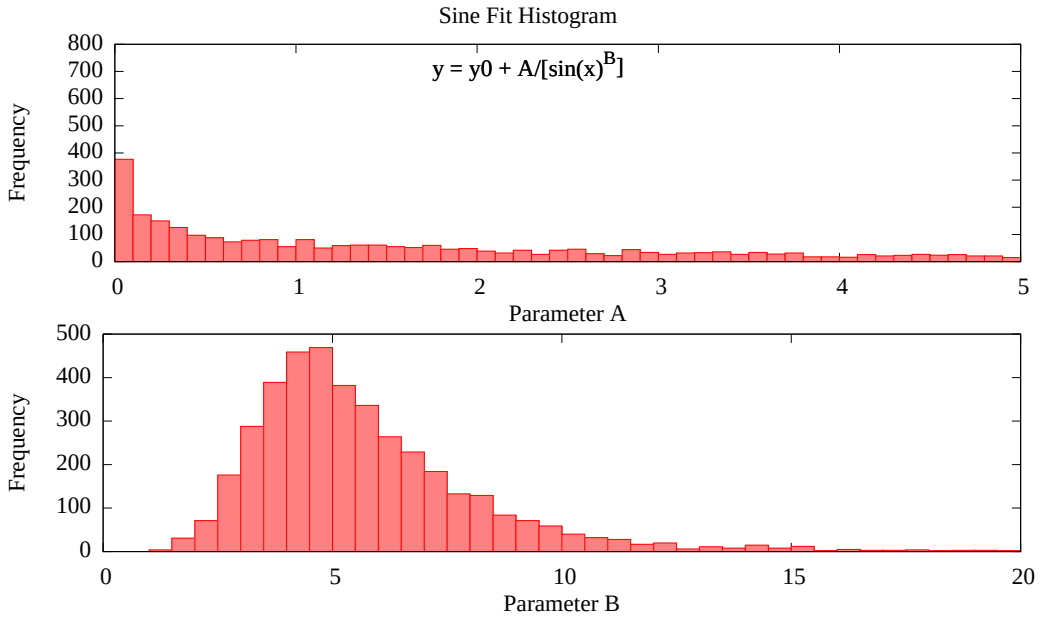

Figure 5.12. Histogram of duskside sine fit parameters A and B. The function is shown at the top center. Parameter A is in the top panel and parameter B is in the bottom panel.

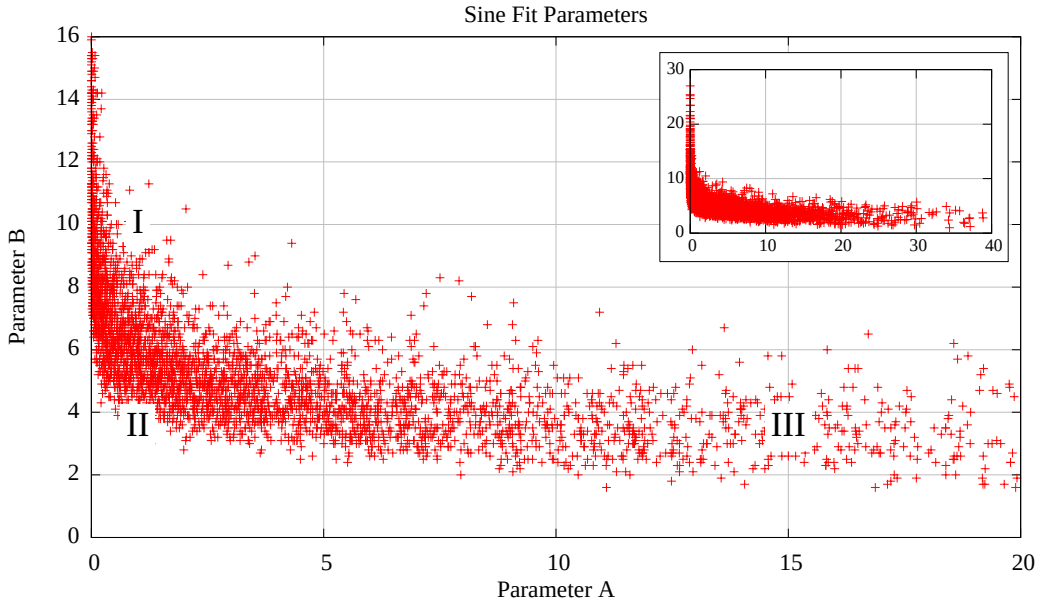

Figure 5.13. Scatterplot of duskside sine fit parameters A and B. The inset shows the full range of values for A and B, while the main plot shows the region with the largest concentration of points. The Roman numerals correspond to the curves shown in Figure 5.14.

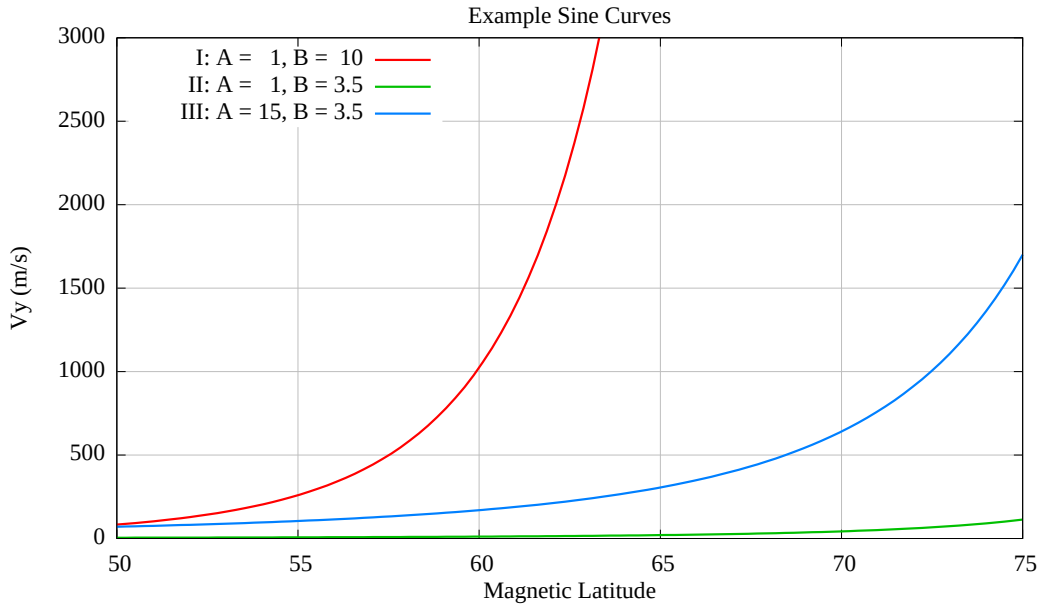

Figure 5.14. Duskside sine curves using different A and B parameters. The Roman numerals correspond to the locations shown in Figure 5.13.

The spread in the value of B is apparent in the wide curve the histogram makes; 63% of the orbits fall in the range $6 < B < 11$ with 20% below $B = 6$ and above $B = 11$. The large spread in B can again be seen in Figure 5.16. This plot is different from the exponential in that the extent of parameter A is much less. In general, this indicates the Gaussian returns a smaller peak than the exponential. For $A < 800$, nearly any value of B is possible; however for $A > 1500$ (seen in the inset plot), the only possible values of B are $3 < B < 6$. Representative curves for different combinations of A and B are shown in Figure 5.17. Just like the exponential, both larger values of A and B create steeper curves. The Gaussian is significantly different from both the exponential and the sine in that the curve reaches its maximum at the latitude of the peak velocity.

Now that A and B have been examined in general for each function, the next step is to investigate how they are related to the geomagnetic index, Kp. As was seen in Figures 5.7 and 5.8, both the velocity and the gradient at a fixed latitude increase with Kp. Therefore, it is logical to assume A should also increase with Kp as it is related to the magnitude of the curve. This is indeed the trend for all three functions as can be seen in Figure 5.18. Each

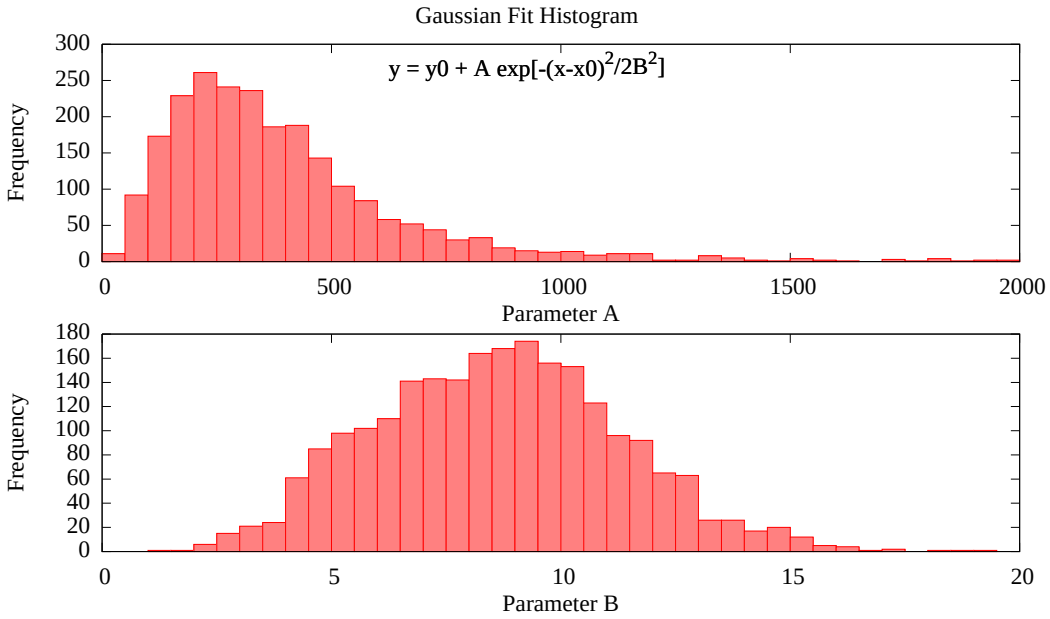

Figure 5.15. Histogram of duskside Gaussian fit parameters A and B. The function is shown at the top center. Parameter A is in the top panel and parameter B is in the bottom panel.

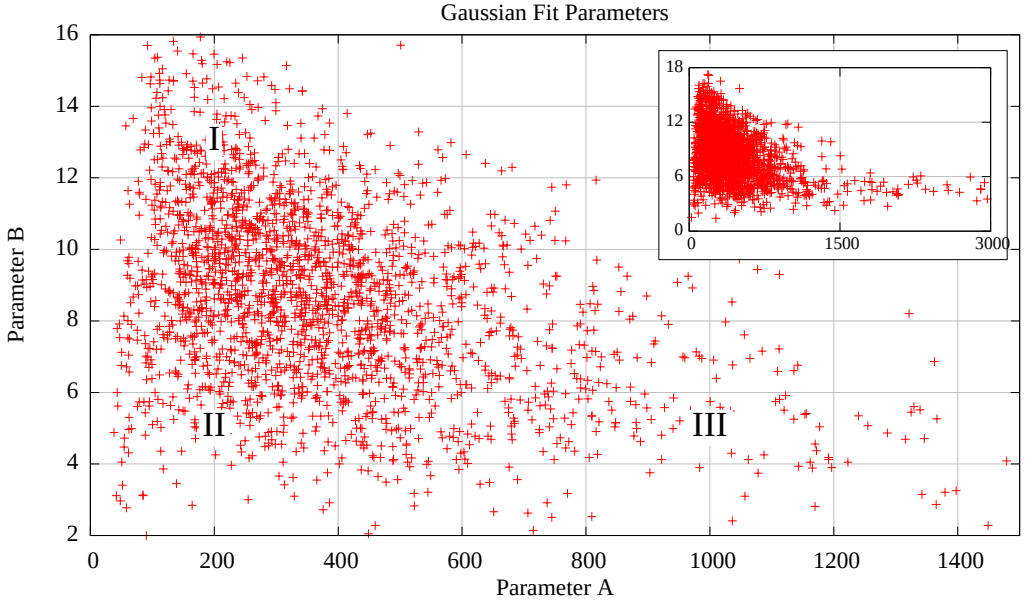

Figure 5.16. Scatterplot of duskside Gaussian fit parameters A and B. The inset shows the full range of values for A and B, while the main plot shows the region with the largest concentration of points. The Roman numerals correspond to the curves shown in Figure 5.17.

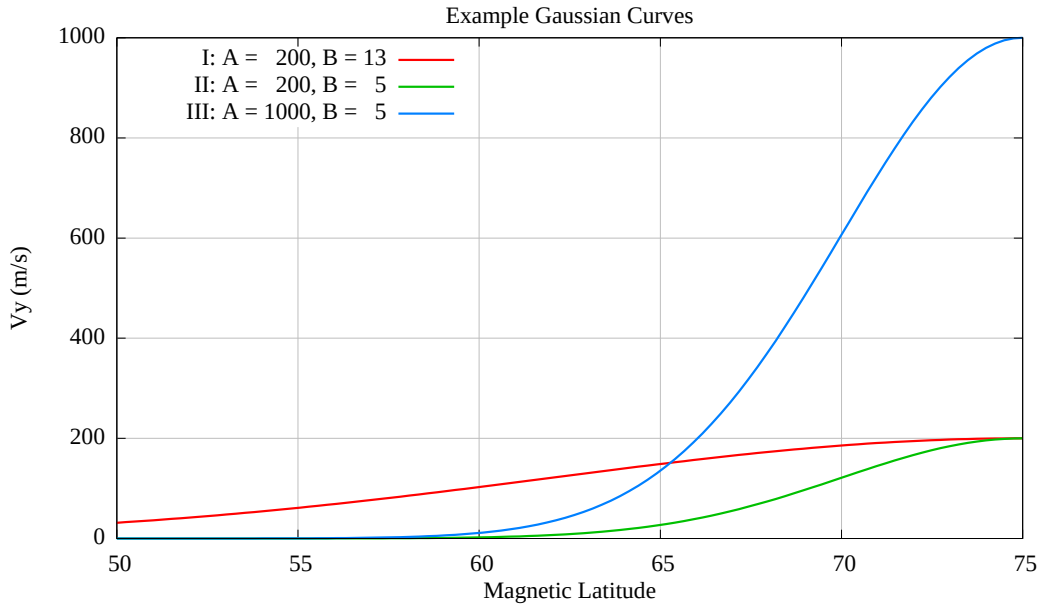

Figure 5.17. Duskside Gaussian curves using different A and B parameters. The Roman numerals correspond to the locations shown in Figure 5.16.

data point is shown by a red cross and the mean and median are shown as black dots and blue squares, respectively. The standard deviation of the mean is plotted with the vertical black bars and a LLSF to the mean is shown by the sloping black line. Only the data with Kp ≤ 4 were used to obtain the LLSF; this was done because the lack of data for Kp > 4 significantly altered the trend and slightly lowered the goodness of fit value.

The y-intercept, slope, and R^2 values for both Kp ranges are shown in Table 5.2. For the exponential, parameter A, which is directly related to the peak velocity, starts near 500 m/s at Kp = 0 and increases by 130 m/s for every integer value in Kp. Following this trend, the average peak velocity of the curve would be 1700 m/s for Kp = 9. The Gaussian (panel c) has a similar relation to parameter A; in this case, the peak velocity starts out at 275 m/s and increases to 945 m/s. Both of these values seem low, especially when compared to values from the TDIM and H-M models. The TDIM has a starting peak velocity of 420 m/s at Kp = 0 and increases to 2500 m/s by Kp = 9. The H-M model is much more conservative, starting at 390 m/s for Kp = 0 and increasing to 1900 m/s by Kp = 9. The results for the sine function follow a similar trend, but because A is not as

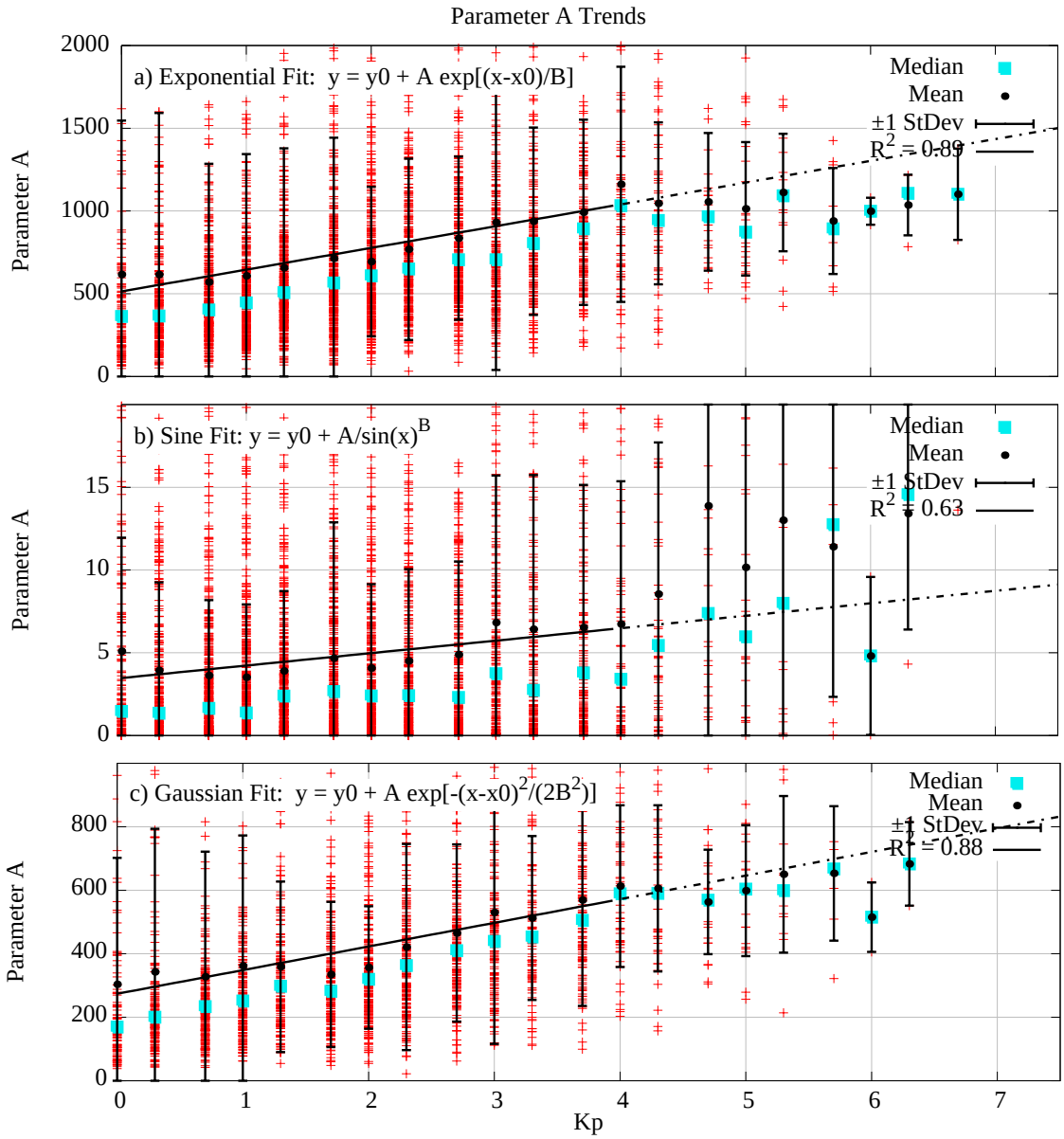

Figure 5.18. Duskside parameter A versus Kp. Data points are shown as red crosses and the mean and median are shown as black dots and blue squares, respectively. The standard deviation of the mean is plotted with the vertical black bars and a LLSF to the mean is shown by the sloping black line. Only the data with Kp ≤ 4 were used to obtain the LLSF.

Table 5.2. Duskside Statistics for A vs. Kp*

		Exponential Fit	Sine Fit	Gaussian Fit
	Y-Intercept	514.12	3.47	273.97
Kp ≤ 4	Slope	131.50	0.75	74.47
	R^2	0.89	0.63	0.88
	Y-Intercept	596.49	1.64	299.50
Kp ≤ 9	Slope	83.97	1.85	59.68
	R^2	0.80	0.58	0.85

*A lack of data for Kp > 4 alters the trend and lowers the goodness of fit value for a linear least square fit.

closely related to the magnitude of the peak velocity, it is difficult to make useful inferences. The results show that parameter A starts at 3.5 and increases by 0.75 for every integer Kp up to 10.25 at Kp $= 9$.

The relationship of Kp to parameter B is examined in Figure 5.19 and Table 5.3. The table again shows the specific values for the y-intercept, slope, and R^2 when a LLSF is done on the mean values of B. The improvement when only data for Kp ≤ 4 is quite substantial here as evidenced by the significant increase in the R^2 values. While parameter B decreases with Kp for both the exponential and Gaussian, it increases for the sine fit. Larger values mean a steeper curve, and so instead of using a static value for this value in the TDIM ($FALLOFF = 4$), the following equation could be used to achieve better results:

$$FALLOFF = 4.86 + 0.52 \times \text{Kp}. \tag{5.29}$$

For the exponential and Gaussian, even though the trend is only slight (-0.21 and -0.15, respectively), a decrease in parameter B indicates the slope of the curve increases for larger Kp which is in line with what is expected.

Most of the analysis so far has been in relation to the peak velocity. Figure 5.20 instead looks at the latitude where the slope of the functional fit is equal to a given value. Typically, a gradient of 15–20 m/s/deg is used to delineate where the midlatitude fall-off region ends [*R. Heelis*, personal communication, February 20, 2014]. Therefore, gradients of 15, 20, and 25 m/s/deg were used as the threshold value. Each functional fit was investigated

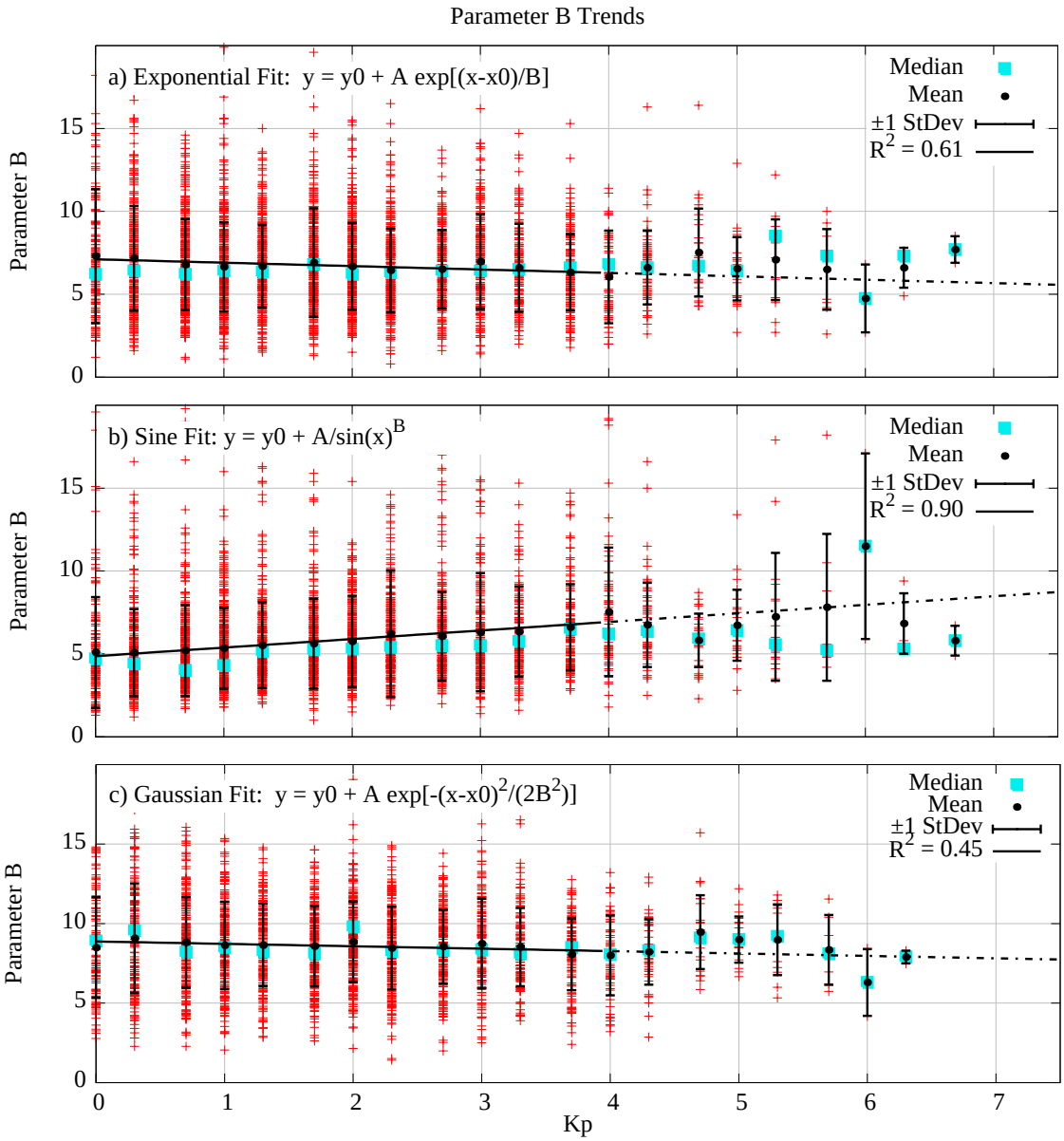

Figure 5.19. Duskside parameter B versus Kp. Data points are shown as red crosses and the mean and median are shown as black dots and blue squares, respectively. The standard deviation of the mean is plotted with the vertical black bars and a LLSF to the mean is shown by the sloping black line. Only the data with Kp ≤ 4 were used to obtain the LLSF.

Table 5.3. Duskside Statistics for B vs. Kp*

		Exponential Fit	Sine Fit	Gaussian Fit
	Y-Intercept	7.11	4.86	8.88
Kp ≤ 4	Slope	-0.21	0.52	-0.15
	R^2	0.61	0.90	0.45
	Y-Intercept	6.89	4.99	8.90
Kp ≤ 9	Slope	-0.06	0.43	-0.13
	R^2	0.05	0.41	0.16

*A lack of data for Kp > 4 alters the trend and lowers the goodness of fit value for a linear least square fit.

to determine at what latitude these threshold gradients were met. Figure 5.20 is a plot of these latitudes versus Kp for a threshold gradient of 20 m/s/deg. Twenty degrees was chosen because the variance in the trend for the three different gradients was less than the variance in the different functional fits. The mean latitude for the three different threshold gradients varied by less than three degrees and the slope of the LLSF to the mean was nearly identical.

All three fits show a distinct trend of decreasing latitude with increasing Kp with the trends for the exponential and sine functions almost identical. For comparison, the Gaussian starts out at a latitude of 62° for Kp = 0, while both the sine and exponential start at 68°. The bottom panel of Figure 5.20 shows all the LLSF to the mean for all three functions as well as values obtained from the TDIM and H-M models. In this plot, it is easy to see the LLSF for the sine and exponential are nearly overlapping; also of note is all three lines converge for larger Kp values. The TDIM (blue line) follows a similar trend, starting at an identical latitude of 68°, but decreasing much more slowly (1.4 versus 3.1) with Kp. The output from the H-M model starts and ends at the same latitude as the TDIM, but again shows fluctuations caused by the interpolation.

Although the geomagnetic index is used in this analysis as the primary indicator of solar and geomagnetic activity, many other indices are available. To be thorough, many of the relationships already discussed were also compared to the index used to describe the symmetric disturbance field in the horizontal direction, SYM-H, obtained from OMNIWeb

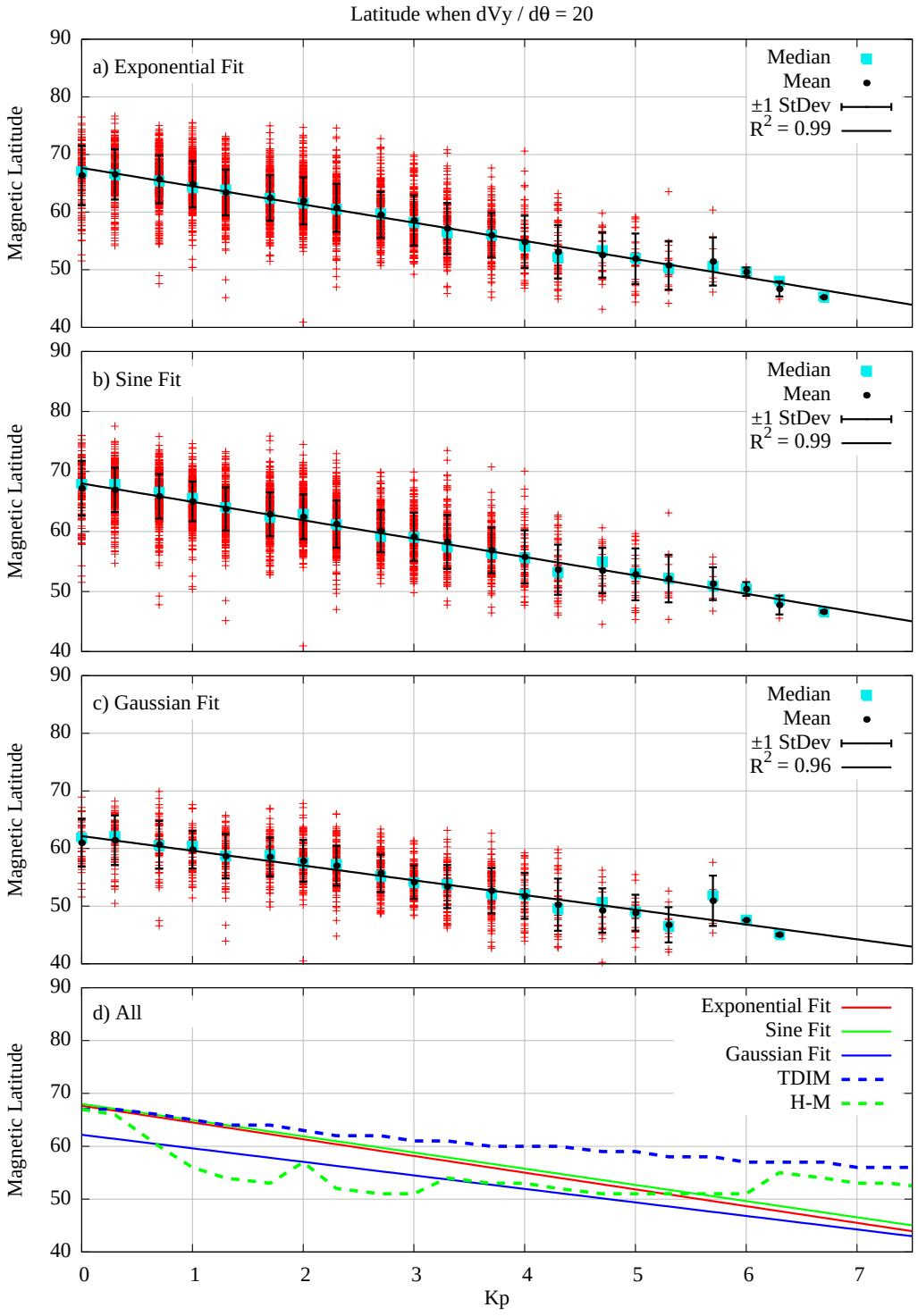

Figure 5.20. Duskside latitude at which $dVy/d\theta = 20$ m/s/deg versus Kp. Plot setup is similar to Figure 5.8.

server run by NASA's Goddard Space Flight Center. The one-minute SYM-H index is essentially the same as the hourly disturbance storm time (Dst) index, except in terms of time resolution [*Lyemori and Rao*, 1996]. SYM-H and Kp are related as can be seen in Figure 5.21. SYM-H is near zero for low Kp and decreases as Kp increases.

Although many different comparisons were completed and examined, the only one that showed a significant trend was for the latitude of the threshold gradient; the result is shown in Figure 5.22. In this plot, the red crosses are data points with Kp ≤ 3, and the green crosses are for Kp > 3. The black line is a LLSF to all the data. A few outliers exist in the lower right portion of the plot with positive SYM-H values and high Kp; it is most likely that the time resolution of the Kp index (three hours) has caused its value to lag behind the SYM-H index. Because the LLSF is to all of the data (and not the mean as in previous plots), the goodness of fit value is quite low ($R^2 = 0.28$). The biggest problem when using this index was the tendency of the data to produce a large blob near SYM-H $= -10$, as seen in this figure. This made determining any kind of relationship between SYM-H and the parameter being investigated impossible.

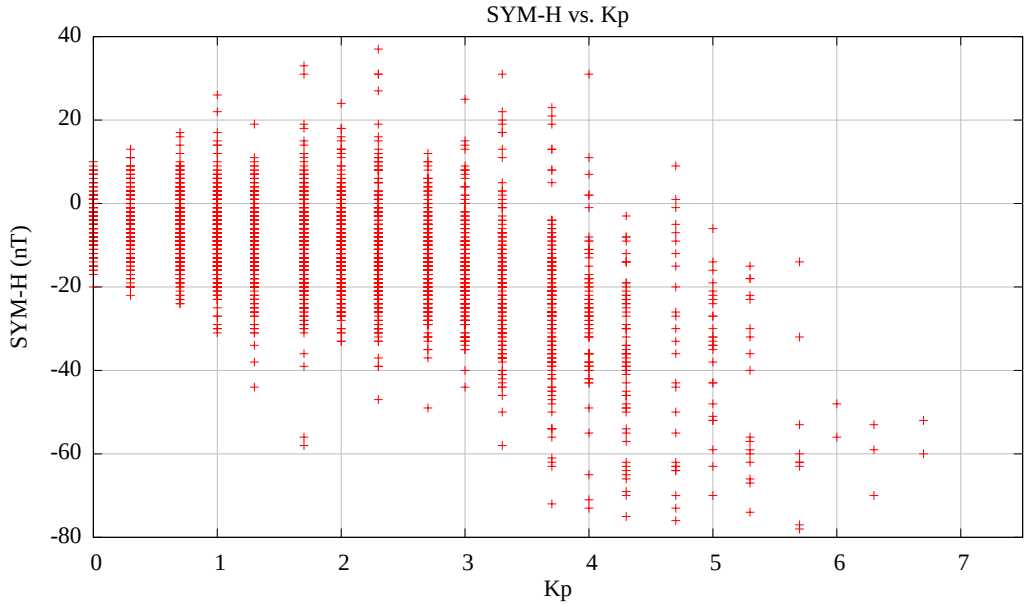

Figure 5.21. Comparison of SYM-H index to Kp index.

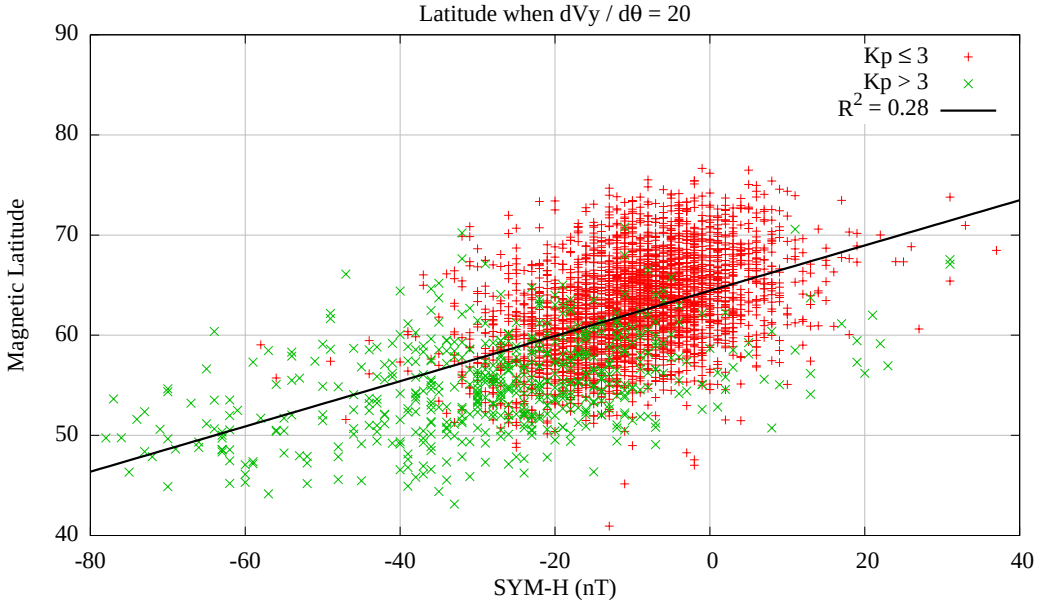

Figure 5.22. Duskside latitude at which $dVy/d\theta = 20$ m/s/deg versus SYM-H. The red crosses are data points with Kp ≤ 3 and the green crosses are for Kp > 3. The black line is a LLSF to all the data.

The final figure in this chapter is a combination of three of the relationships that were examined previously with a new statistical model. Figure 5.23 shows trends for the polar cap radius (solid black line, determined in Chapter 4), the peak latitude (dashed black line), and the latitude of the threshold gradient for each functional fit (red dashed lines). These trends have been overlaid on output from the *Hardy et al.* [1985] auroral oval model. This model uses the Special Sensor–Precipitating Electron and Ion Spectrometer (SSIES) on DMSP to determine the average characteristics of auroral electron precipitation as a function of MLT, magnetic latitude, and geomagnetic activity as measured by Kp [*Hardy et al.*, 1985]. The log of the energy flux is plotted with the highest flux in red. The top panel shows data for the 1700 MLT radian; panel b) is for 1800 MLT, c) for 1900 MLT, and panel d) shows data along the 2000 MLT radian. The *Hardy et al.* [1985] model was run for each MLT, and the trendlines were obtained by sorting the data by year. The precession of DMSP F15 allowed it to start in the 2000 MLT radian in 2007 and move clockwise approximately one hour in local time every year. Although most of the 2007 data

is questionable, the months of May, June, and July contain orbits completely in sunlight above 50°; only the orbits from these three months were used to obtain the trends shown in panel d). Similarly, the 2008 data is a proxy for 1900 MLT, 2009 for 1800 MLT, and 2010 for 1700 MLT (see Figure 3.1). It can easily be seen that the energy flux increases both at larger Kp and in the nightside.

The PCR lines up quite well with the poleward edge of the region with the strongest energy flux, and the latitude of the threshold gradient for each functional fit lines up with the equatorward edge of the flux. The auroral zone should be the region with the largest energy fluxes and therefore, falls between the line for the PCR and the peak velocity latitude; while these two lines do not exactly outline the largest energy fluxes, panel c) at 1900 MLT does a good job. Although a few discrepancies exist, in general the model data and the trendlines shift equatorward from panel a) 1700 MLT to panel d) 2000 MLT.

5.4. Summary

In this chapter, three functions were used to classify the velocity profile in the fall-off region. An exponential, sine, and Gaussian function were fit to the data using a LLSF algorithm. Due to questionable data, the orbits from 2007 were not used for the majority of this analysis. Many orbits displayed realistic structure that was not able to be captured by the functional fit; those orbits were not included in the analysis and only orbits with R^2 values greater than 0.8 were used. Overall, the exponential and sine functions are equivalent within the data variability.

Using the median values for parameters A and B, it was found, in general, the orbits can be fit using the following functional forms:

$$\text{Exponential: } y = 575 \times \exp\left[\frac{x - x_0}{6.4}\right], \tag{5.30}$$

$$\text{Sine: } y = \frac{2.3}{\sin(x)^{5.1}}, \tag{5.31}$$

$$\text{Gaussian: } y = 332 \times \exp\left[\frac{-(x - x_0)^2}{2 \times 8.6^{\,2}}\right]. \tag{5.32}$$

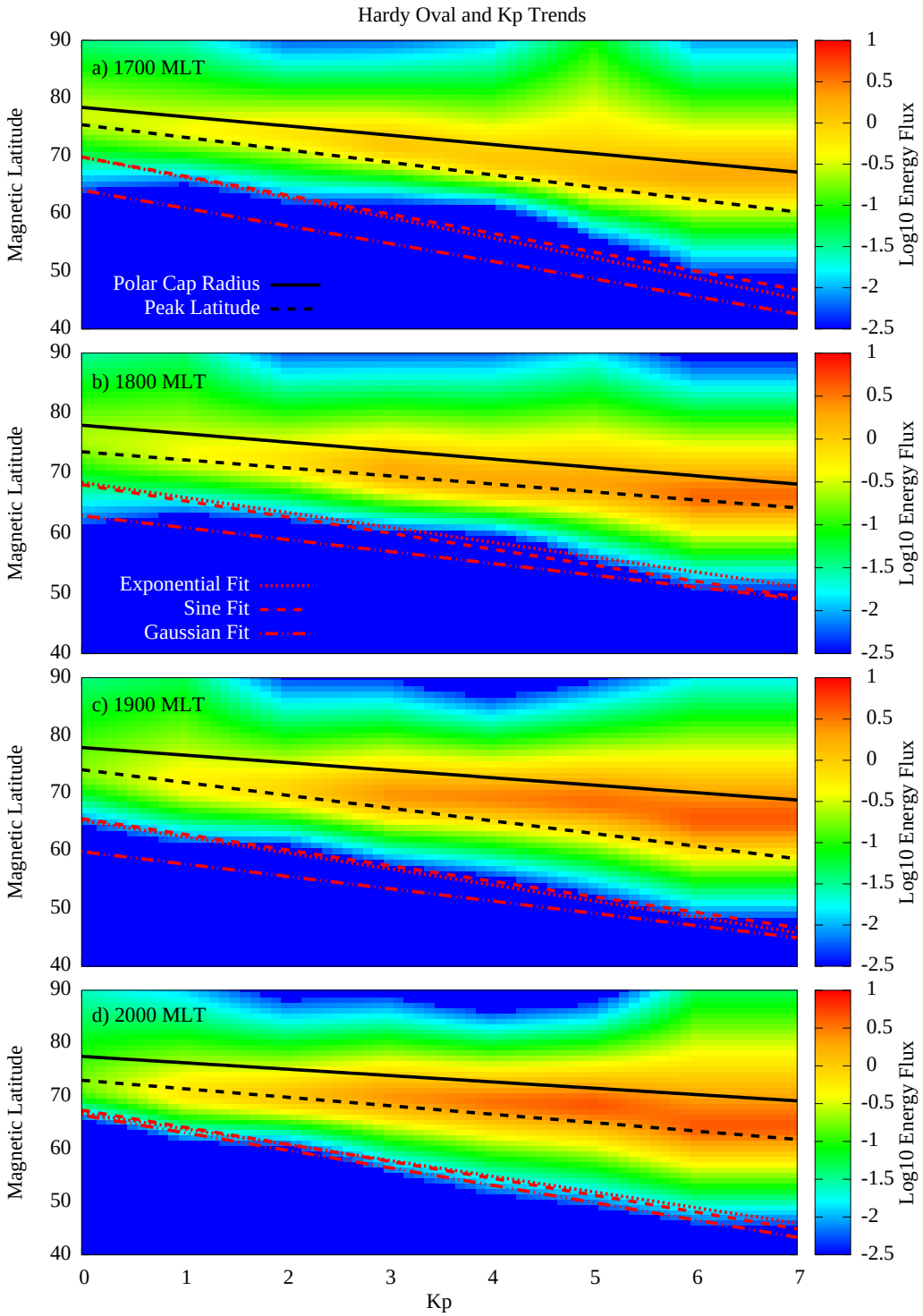

Figure 5.23. Duskside *Hardy et al.* [1985] auroral oval and Kp trends for four MLTs. Kp trends are for the polar cap radius (solid black line), the peak latitude (dashed black line), and the latitude of the threshold gradient for each functional fit (red dashed lines). The background is the log of the energy flux obtained from the *Hardy et al.* [1985] auroral oval model. Each panel is for the MLT indicated in the top left corner.

In an empirical model driven by the Kp index, quiet geomagnetic conditions (Kp < 4) can be recreated using any one of the following sets of functions and Kp-dependent parameters:

$$\text{Exponential Fit: } y = A \times \exp\left[\frac{x - x_0}{B}\right], \tag{5.33}$$

$$A = 514.12 + 131.50 \times \text{Kp}, \tag{5.34}$$

$$B = 7.11 - 0.21 \times \text{Kp}. \tag{5.35}$$

$$\text{Sine Fit: } y = \frac{A}{\sin(x)^B}, \tag{5.36}$$

$$A = 3.47 + 0.75 \times \text{Kp}, \tag{5.37}$$

$$B = 4.86 + 0.52 \times \text{Kp}. \tag{5.38}$$

$$\text{Gaussian Fit: } y = A \times \exp\left[\frac{-(x - x_0)^2}{2B^2}\right], \tag{5.39}$$

$$A = 273.97 + 74.47 \times \text{Kp}, \tag{5.40}$$

$$B = 8.88 - 0.15 \times \text{Kp}. \tag{5.41}$$

A lack of data during active conditions leaves reconstructing velocities in the fall-off region questionable. Equation 5.38 would be especially useful in the TDIM. Additionally, the strong correlation between the analysis done on the functional fits and output from the *Hardy et al.* [1985] auroral oval model gives significance to these results.

CHAPTER 6

DAWNSIDE FALL-OFF REGION CLASSIFICATION

6.1. Introduction

In this chapter, the dawn fall-off region velocities are examined and a common description based on IMF and geomagnetic conditions is attempted using a method similar to the classification of the duskside fall-off region velocity profiles. While the IMF B_y component may introduce an asymmetry in the dawn and dusk convection cells, the fall-off behavior for both regions is typically assumed to be similar. The USU TDIM assumes complete symmetry and uses the same inverse sine function ($\sin^{-4}(\Lambda)$) for both regions. Other models are more complex due to how the model was created (e.g., hand-drawn, spherical harmonics, etc.). The fits are examined individually and are then averaged together according to their solar and geomagnetic conditions, the results are compared to the TDIM and H-M empirical models, and the *Hardy et al.* [1985] statistical auroral oval model.

6.2. Methodology

For the dawnside, only the exponential and sine functions were used to obtain a LLSF to the orbit data. The Gaussian was not used because nearly 10% fewer of the duskside orbits had acceptable goodness of fit values. Also, because the orbits are now being fit from the peak latitude to the offset latitude, a negative must be included in the exponential to indicate a decay of the function. The platform value y_0 is still kept at zero; therefore the two functions used are

$$\text{Exponential: } y = A \times \exp\left[\frac{-(x - x_0)}{B}\right], \tag{6.1}$$

$$\text{Sine: } y = \frac{A}{\sin^B(x)}, \tag{6.2}$$

where x_0 is the latitude of the peak velocity and A and B are the parameters to be fit. The transformation into linear equations is the same as for the duskside (see equation 5.8) with the exception that $X = -(x - x_0)$ for the exponential function. The fit was not completed

if the fall-off region was less than five degrees in latitude or if over half the data points in the fall-off region were missing data or had negative values. To remain consistent with the analysis completed in Chapter 5, only the 2008–2010 DMSP data were used for the majority of this analysis. This left 10,705 orbits to be fit on the dawnside. Of those, 2,399 (22.4%) had a goodness of fit better than 0.80 for the exponential fits and 2,344 (21.9%) for the sine fits. Table 6.1 shows the number and percentage of orbits with different goodness of fit values for the dawnside. From these numbers and the histograms in Figure 6.1 it is easy to see the dawnside orbits are distributed more evenly across all goodness of fit values than on the duskside. Over half the orbits for both the exponential and sine fits have a goodness of fit less than 0.60. Somewhat surprising is the large number of orbits that have goodness of fit values near zero (around 600). A few examples of these orbits are shown in Figure 6.2; the commonality between these orbits is the presence of a region of antisunward flow equatorward of the peak latitude. This antisunward flow results in a very flat fit line and low R^2 values. Most of these orbits do not cross the pole, but instead reach a high latitude of 80° around 1200 MLT and therefore, may be missing the majority of the convection pattern. Only orbits with $R^2 \geq 0.8$ are included in the analysis.

Examples of the orbits included in this investigation are shown in Figure 6.3. The orbits are plotted similar to previous orbit plots with the fitted region between the vertical dashed brown lines. The R^2 values are shown in the top right corner and the IMF B_y and B_z and Kp values are listed in the top left corner. Most of the orbits have specific characteristics that correspond to the solar and geomagnetic conditions. For example, plot a) has asymmetrical antisunward flow in the polar cap with stronger on the dawnside, which is consistent with a positive B_y component. Panel f) shows sunward flow in the polar cap consistent with its low Kp and positive B_z [*Heppner and Maynard*, 1987]. A comparison of panels g) and h) shows the impact of negative IMF B_z on the flow velocities. Both panels show similar velocities even though panel g) has Kp = 5.7, while panel h) only has Kp = 3.7. The difference is in the negative IMF B_z component for panel h) that allows a reconnection between the IMF and geomagnetic field. Panels c) and d) appear to be outliers with very

Table 6.1. Dawnside Goodness of Fit Statistics*

	Exponential Fit		Sine Fit	
	Number	Percent	Number	Percent
$R^2 > 0.9$	811	7.6%	777	7.3%
$R^2 > 0.8$	2399	22.4%	2344	21.9%
$R^2 > 0.7$	3789	35.4%	3828	35.8%
$R^2 < 0.6$	5674	53.0%	5607	52.4%
$R^2 < 0.4$	3758	35.1%	3660	34.2%
$R^2 < 0.2$	2195	20.5%	2131	19.9%

*Total number and percentage of the 10,705 orbits with goodness of fit R^2 values within the listed categories.

low velocities; just like in Figure 6.2, these orbits pass on the dayside of the pole and miss the majority of the convection pattern. Including orbits such as these in the analysis is not ideal as they do not represent a typical fall-off profile. However, they are difficult to discard without visually inspecting every orbit and are therefore included the analysis.

6.3. Results

The latitude of the peak velocity as a function of Kp is plotted in Figure 6.4. The data shows the peak falls between 63° and 78° for low Kp and shifts equatorward by half a degree for every integer increase in Kp. The trend for the data agrees with the output from both the TDIM and H-M models. The goodness of fit for the LLSF to the mean is quite low with $R^2 = 0.34$. This could be the result of the lack of data for Kp > 4 and because of the anomalous behavior of the peak latitude for Kp < 0.7. This sudden decrease at low Kp may be an artifact of the orbits with very low velocities and no distinct peak, which cause the LLSF algorithm to incorrectly identify the peak latitude and the region to be fit.

An analysis of the velocities of the fitted functions at 60° in Figure 6.5 shows a trend similar to the duskside except for the two lowest Kp values. For Kp = 0.0, the velocity is near 100 m/s; it decreases to approximately 75 m/s for Kp = 0.3 before leveling out around 25 m/s at Kp = 0.7. Velocities stay low until Kp = 2.3 when they slowly start increasing with larger Kp. This trend is nearly identical for both the exponential and sine functions. If the lowest Kp values are ignored, the data again are similar to the empirical model output

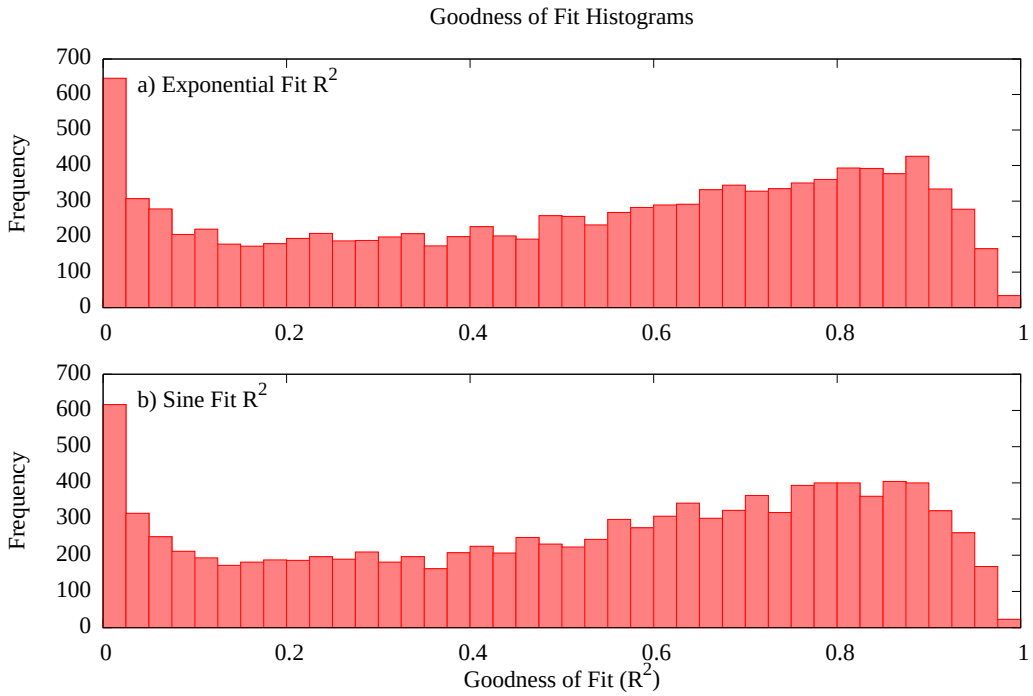

Figure 6.1. Dawnside goodness of fit histograms. The top plot is the exponential fit and the bottom plot is the sine fit.

as shown in panel c). The H-M model shows negative velocities for Kp < 1.5, but this is likely an artifact of the interpolation and fitting of the hand-drawn H-M patterns.

The slope, shown in Figure 6.6, and the velocity at 60° have similar trends. Steep slopes occur at low Kp values before dropping close to zero and then rising gradually with higher Kp. The TDIM output agrees very well with the data, but the H-M output is again influenced by the interpolation of the model. Velocities and gradients increasing with Kp indicate the strongest sunward flows expand equatorward during geomagnetic activity.

Next, A and B are examined for each of the functional fits. Figure 6.7 shows histograms, and Figure 6.8 a scatterplot of parameters A and B for the exponential fit. Parameter A, which controls the magnitude, has a mean value of 1101 and a median value of 624. The majority of the orbits fall below 1000, but 32% have $A > 1000$ with $A > 4000$ occurring in 127 of the orbits. Parameter B is more normally distributed with a mean and median of 5.0 and 4.3, respectively. The population is slightly skewed to the right with 4.5% of the orbits having a value of B greater than two standard deviations from the mean.

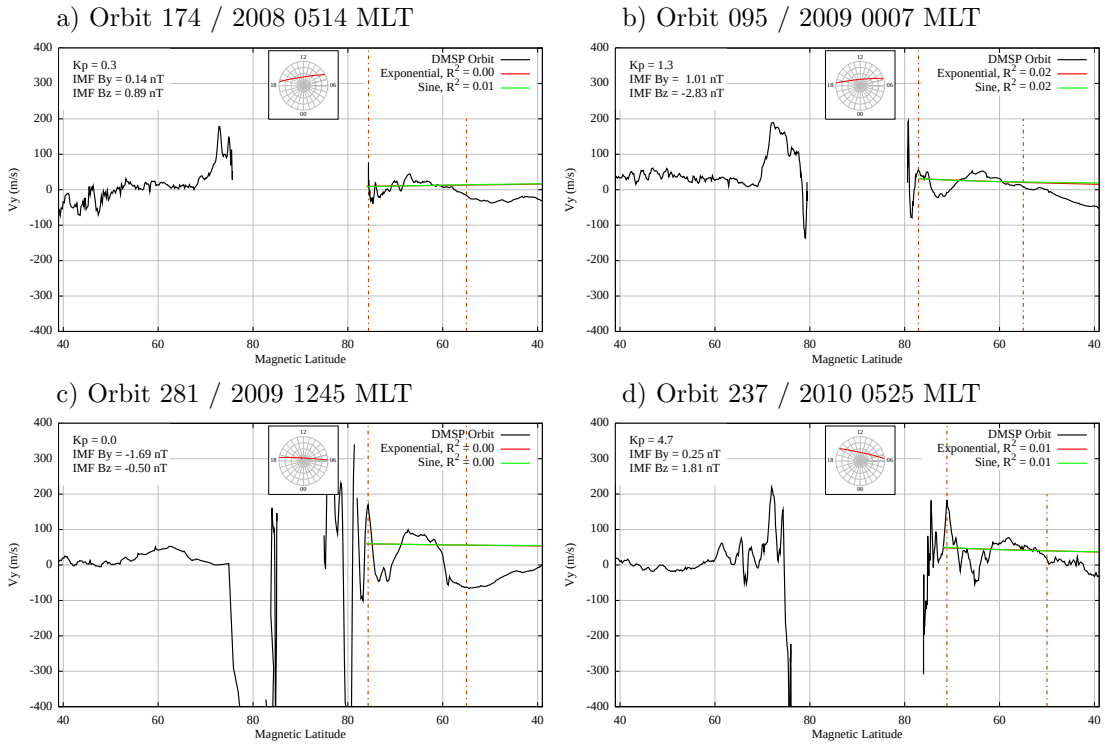

Figure 6.2. Dawn orbits with R^2 near zero. The left vertical brown dashed line indicates the peak latitude, while the right vertical brown dashed line indicates the offset latitude. The black line is the orbit data, the red line is the exponential LLSF, and the green line is the sine fit.

When A and B are plotted together as in Figure 6.8, it is easy to see most of the orbits have low values for both parameters, labeled as region II in the plot. The type of curve generated by these values is shown by the green line in Figure 6.9. The velocity has a reasonable peak value and then falls off to zero fairly quickly (within 10°). The blue curve in this figure corresponds to orbits in region III that have large A values, but small B values. This curve starts with a larger peak velocity, but also falls off to zero within 10–15 degrees. The last type of orbit with lower values of A but high B values, is represented by the red curve in Figure 6.9 and by region I in the scatterplot. These curves will have a peak velocity of less than 1000 m/s, but the large B value means it takes much longer for the velocity to fall off to zero with positive velocities extending 25° equatorward of the peak. These orbits may indicate the presence of a penetration electric field that is required for the velocities at midlatitudes to remain above zero.

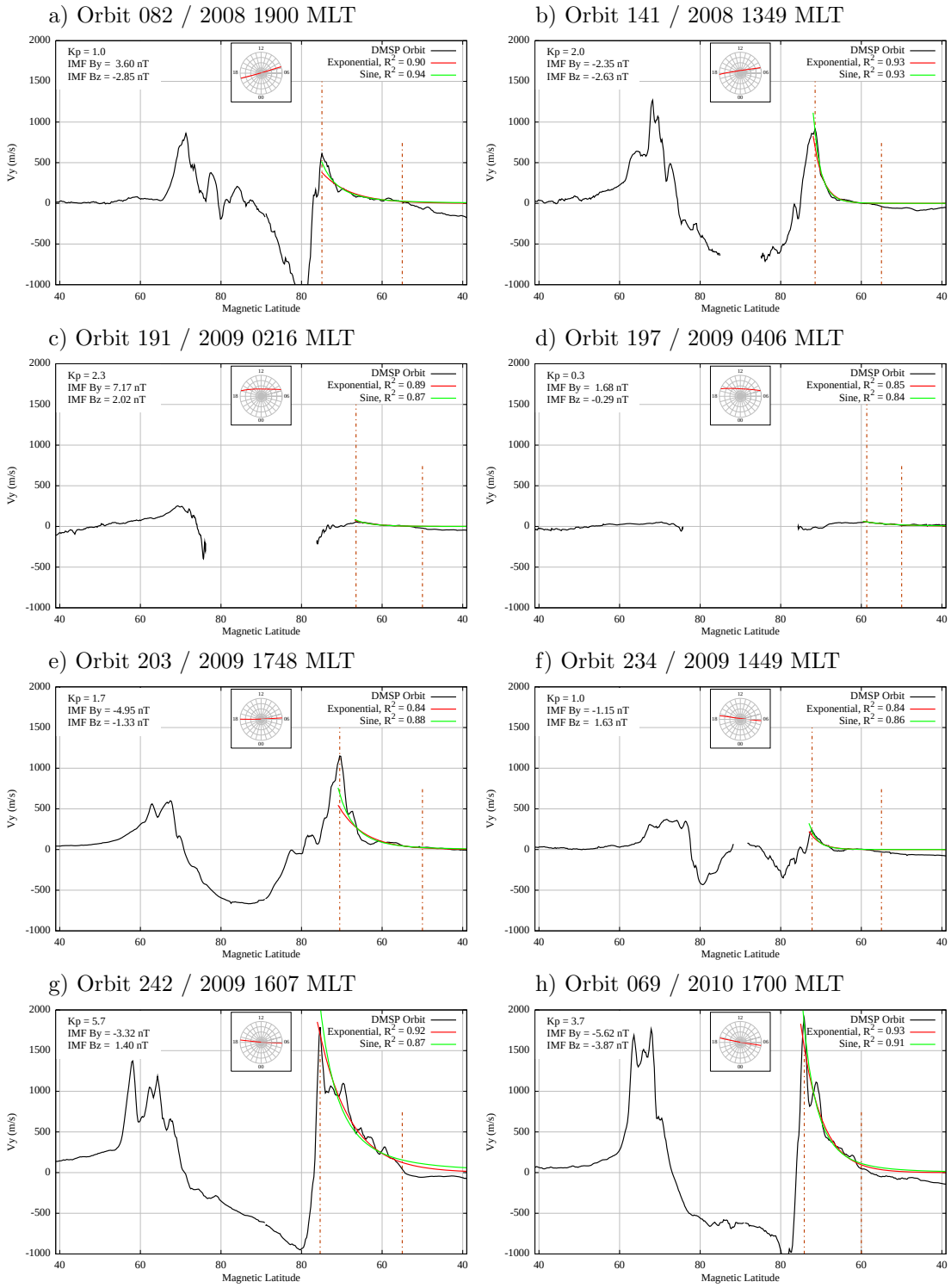

Figure 6.3. Linear least square fits for dawn orbits. The left vertical brown dashed line indicates the peak latitude, while the right vertical brown dashed line indicates the offset latitude. The black line is the orbit data, the red line is the exponential fit, and the green line is the sine fit.

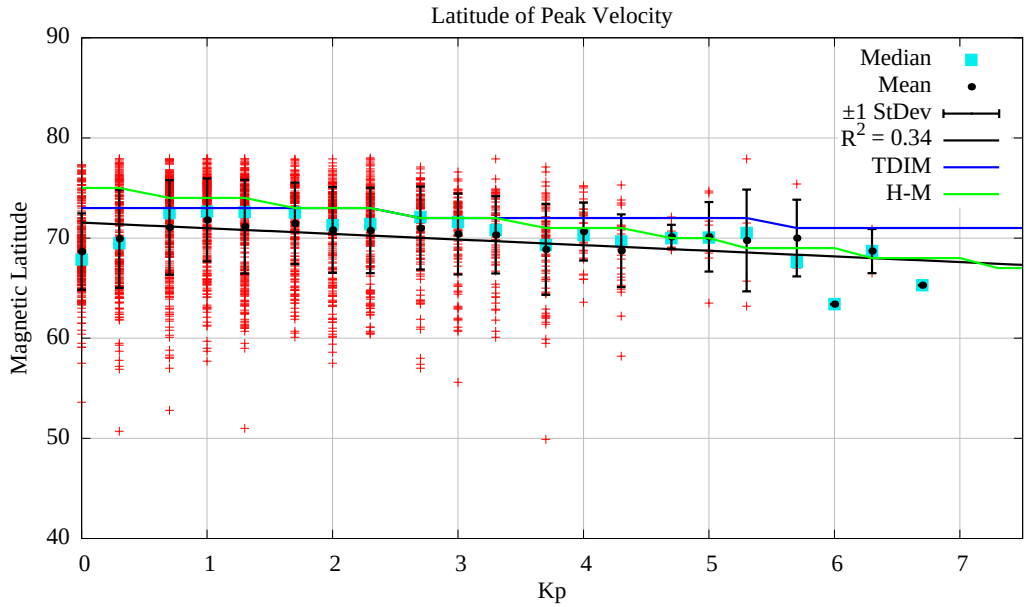

Figure 6.4. Dawnside latitude of the peak velocity as a function of Kp. Red crosses indicate values for individual orbits, black dots represent the mean latitude, and blue squares are the median latitude for each Kp value. The vertical black lines extend to plus/minus one standard deviation from the mean. The angled black line is a LLSF to the mean values, while the blue line was obtained from the TDIM model, and the green line was obtained from the H-M model. The 0700 MLT radian was used to obtain the data for both models.

Similar plots comparing A and B for the sine function are shown in Figures 6.10–6.12. Most of the orbits have a very small A value with a mean and median of 2.9 and 0.9, respectively, but 15% of the orbits have $A > 5$. As shown by the scatterplot in Figure 6.11, orbits with $A > 5$ only correspond to low values of B (region III). This combination of parameters results in a curve similar to the blue line in Figure 6.12. This curve has the slowest fall-off of the three curves shown, and most likely represents a penetration event for the sine function. Parameter B has a mean of 7.8 and a median of 6.6, again indicating a distribution close to normal, but skewed to the right. The most frequently occurring B values are from 4.5–5.5, and only 12% of the orbits have a $B > 12.7$. The bulk of the orbits lie in region II of the scatterplot with low values for both A and B. Curves in this region are represented by the green line in Figure 6.12, which is a very flat curve. For orbits with the same A value but larger B values (region I), the curves are much steeper and reach to much higher magnitudes as shown by the red line in Figure 6.12.

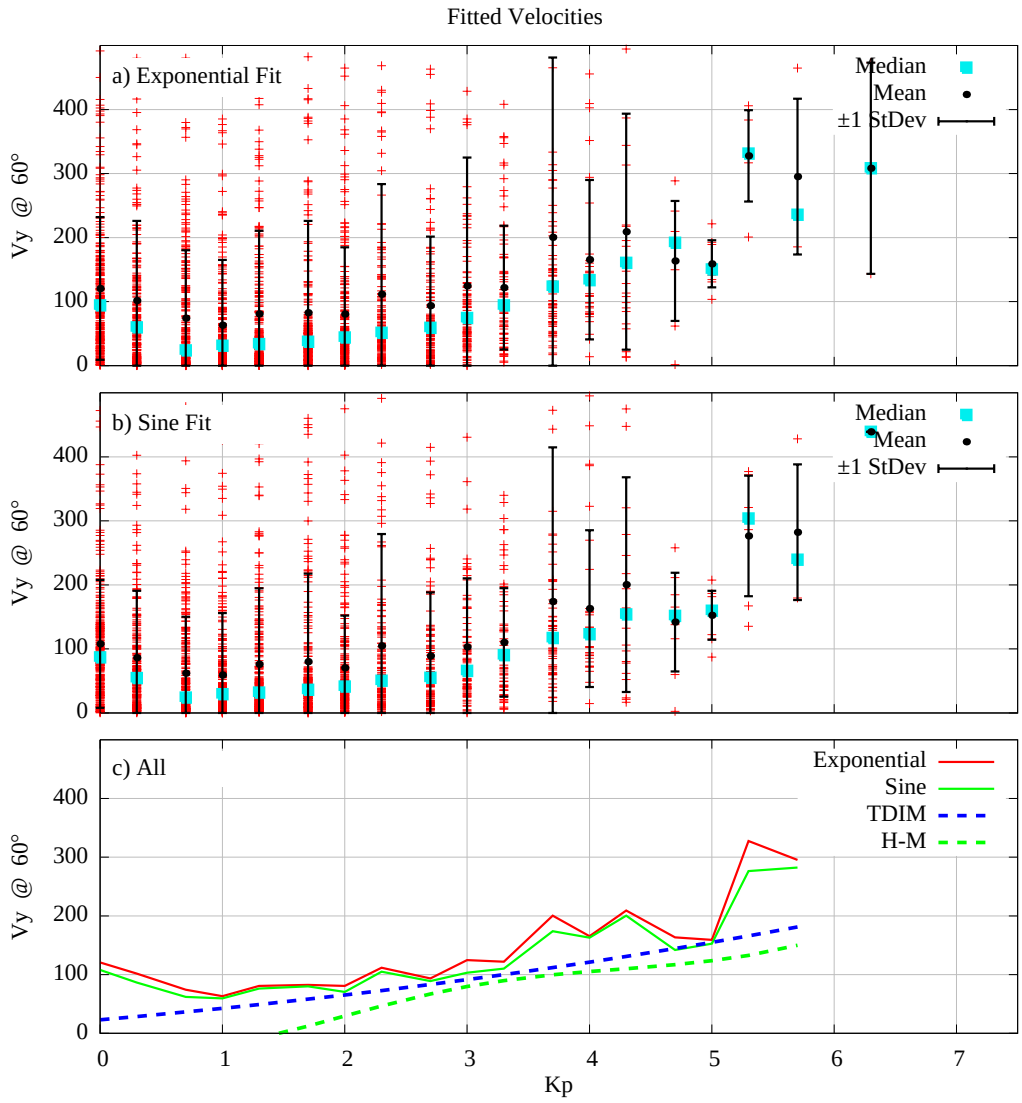

Figure 6.5. Dawnside velocity at 60° obtained from functional fits. The top panel is the exponential fit and panel b) is for the sine fit; data is shown in the same manner as the previous figure. Panel c) shows the mean value of the velocity for each fit as solid lines, velocity values at 60° obtained from the TDIM (blue), and H-M model (green) as dashed lines.

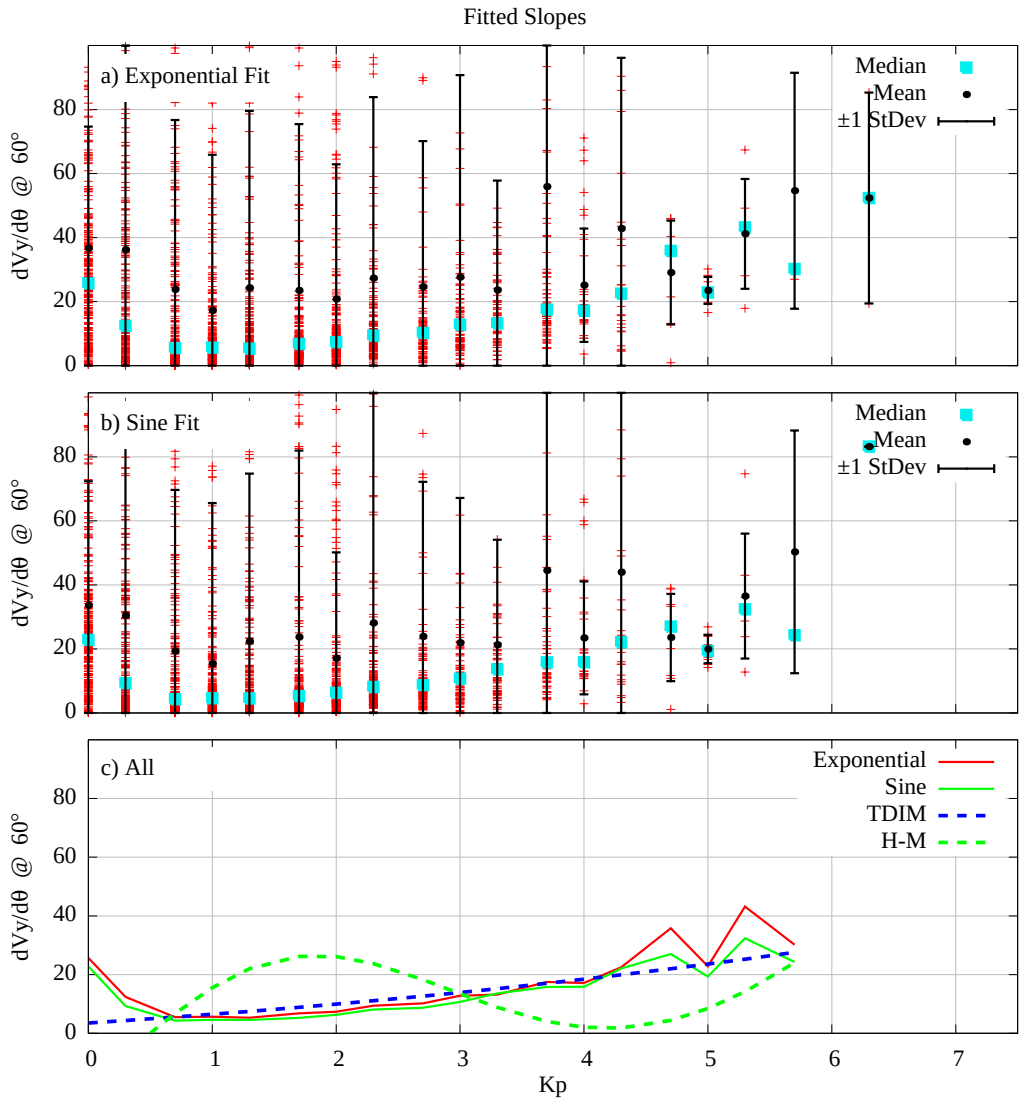

Figure 6.6. Dawnside slope at 60° obtained from functional fits. The top panel is the exponential fit and panel b) is for the sine fit; data is shown in the same manner as the previous figure. Panel c) shows the mean value of the velocity for each fit as solid lines, velocity values at 60° obtained from the TDIM (blue), and H-M model (green) as dashed lines.

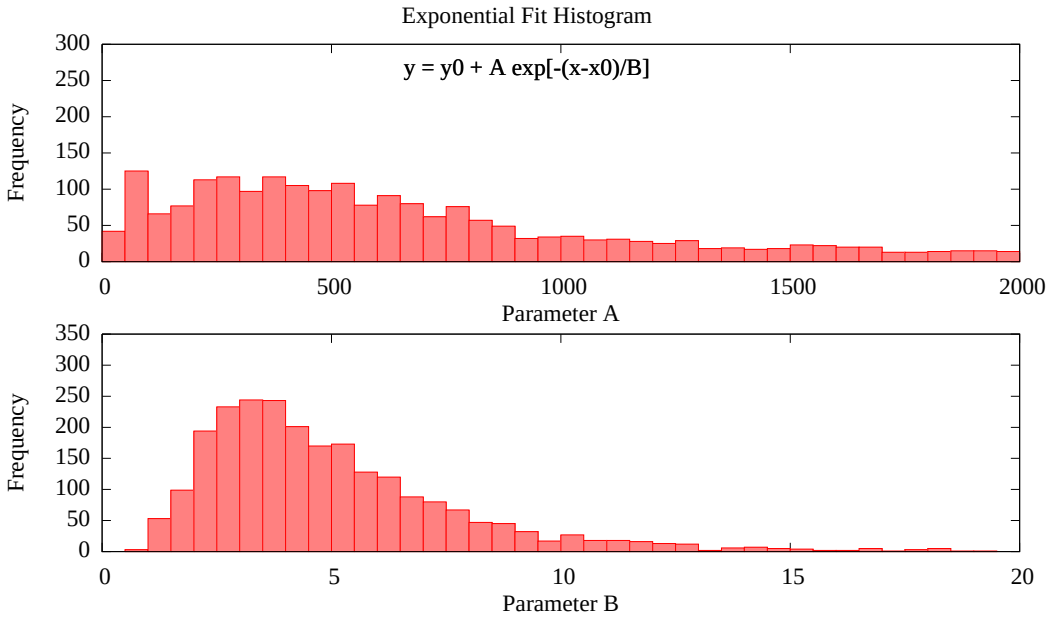

Figure 6.7. Histogram of dawnside exponential fit parameters A and B. The function is shown at the top center. Parameter A is in the top panel and B is in the bottom panel.

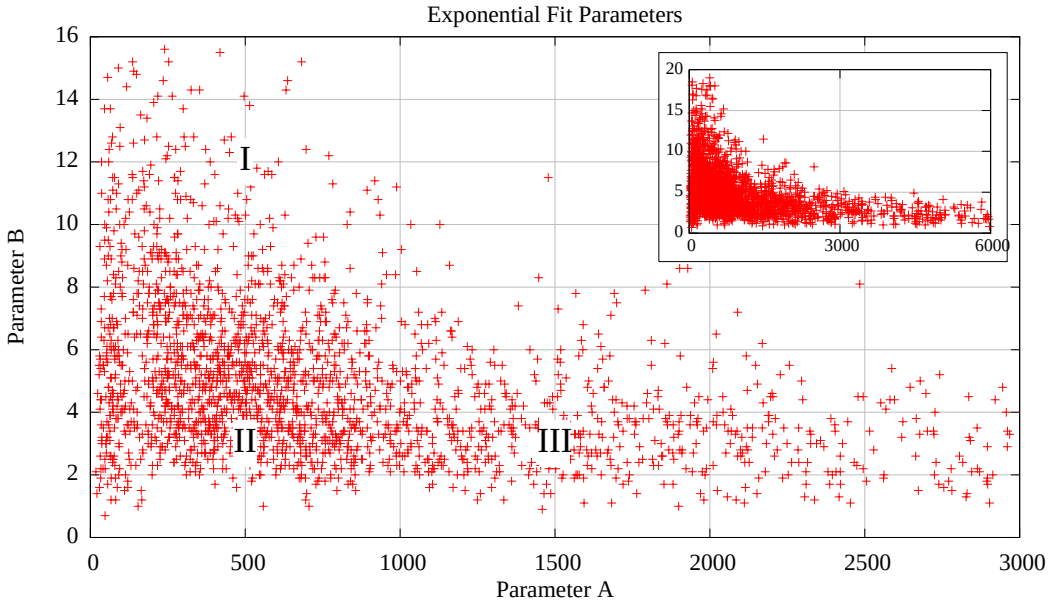

Figure 6.8. Scatterplot of dawnside exponential fit parameters A and B. The inset shows the full range of values for A and B while the main plot shows the region with the largest concentration of points. The Roman numerals correspond to the curves shown in Figure 6.9.

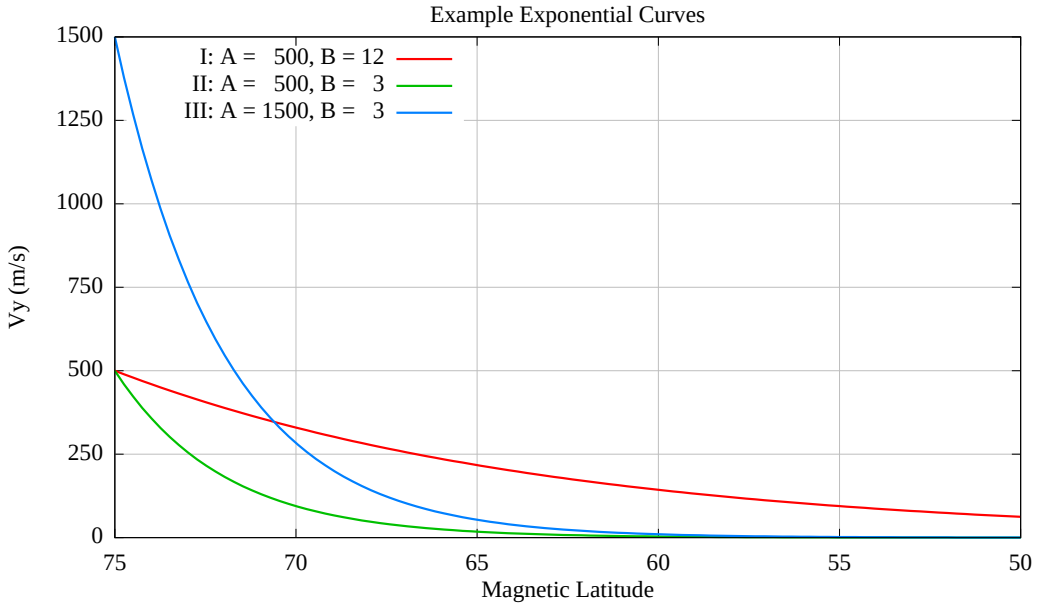

Figure 6.9. Dawnside exponential curves using different A and B parameters. The Roman numerals correspond to the locations shown in Figure 6.8.

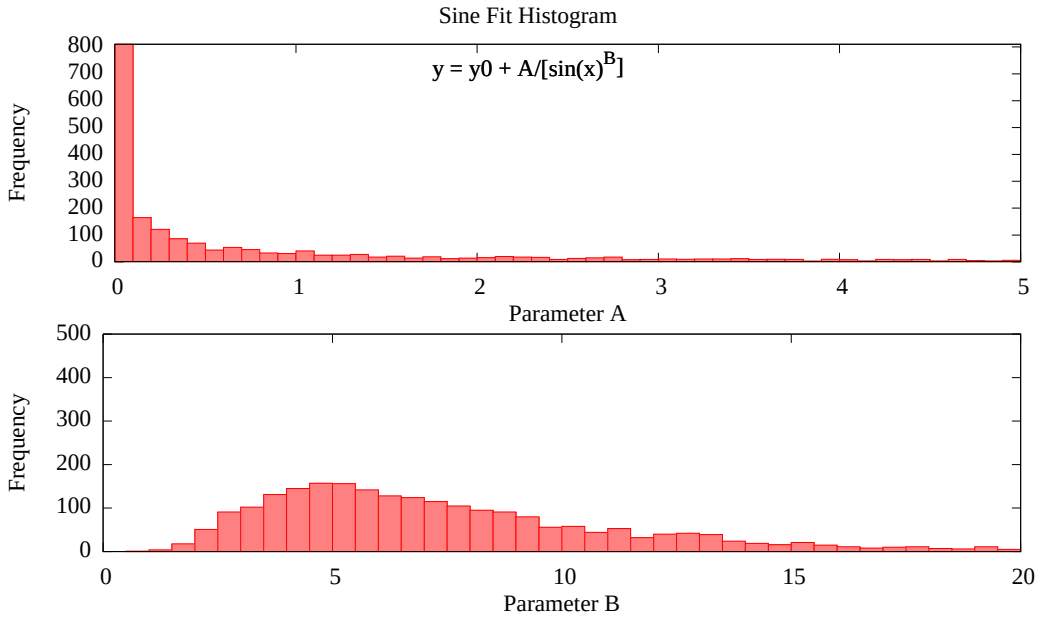

Figure 6.10. Histogram of dawnside sine fit parameters A and B. The function is shown at the top center. Parameter A is in the top panel and B is in the bottom panel.

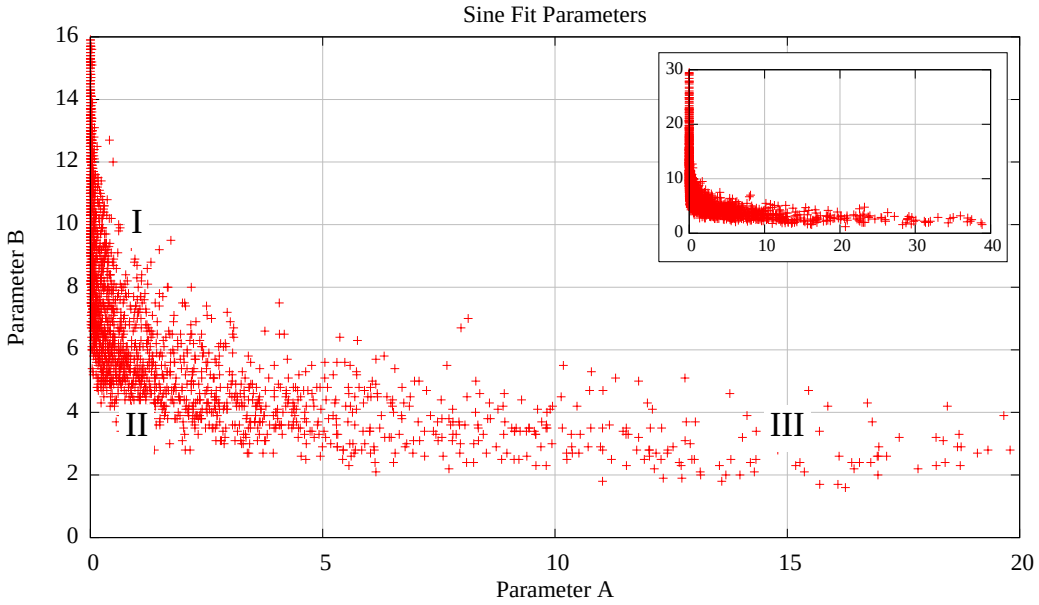

Figure 6.11. Scatterplot of dawnside sine fit parameters A and B. The inset shows the full range of values for A and B, while the main plot shows the region with the largest concentration of points. The Roman numerals correspond to the curves shown in Figure 6.12.

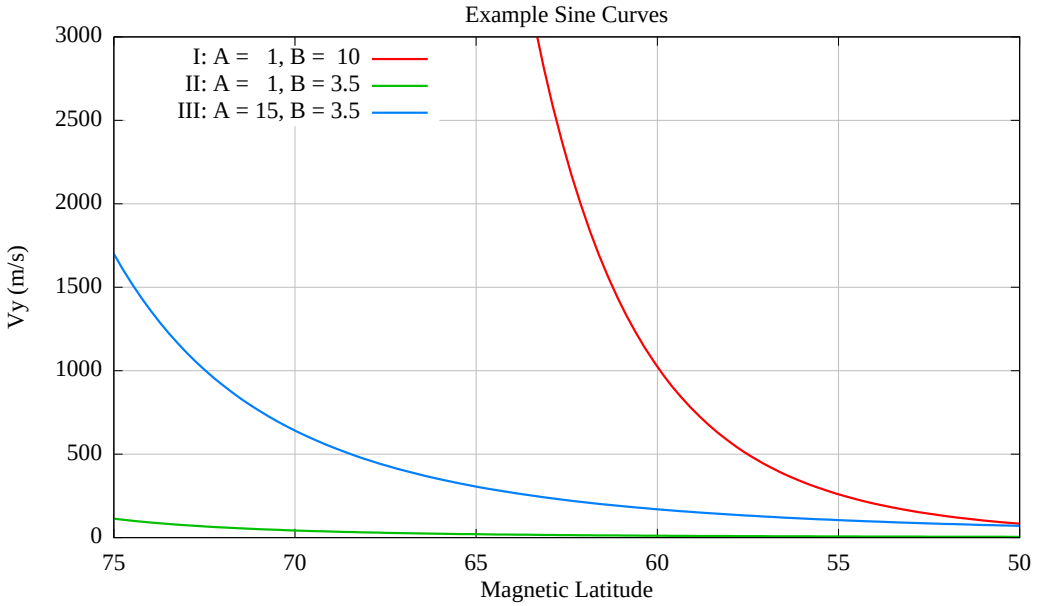

Figure 6.12. Dawnside sine curves using different A and B parameters. The Roman numerals correspond to the locations shown in Figure 6.11.

Also of interest is how parameters A and B change with Kp. Figure 6.13 shows parameter A versus Kp for the exponential fit (top) and the sine fit (bottom). Neither set of data has a clear trend. For $1.0 \leq \text{Kp} \leq 3.3$, the exponential fit mean and median of A are mostly unchanged. For $\text{Kp} < 1.0$, the spread in the data increases significantly and the mean and median rise by 500–1000. The mean and median for large Kp are also much higher; however, very few data points exist at these Kp levels. Table 6.2 shows the results for a LLSF of this data. If all Kp values are used, the fit is very poor with $R^2 = 0.05$, but improves to $R^2 = 0.40$ if only $\text{Kp} \leq 4$ are used. The lines produced by these two fits are also significantly different; the line using all Kp values starts near $A = 1000$ and has a positive slope, while the line using $\text{Kp} \leq 4$ starts near $A = 1300$ and has a negative slope.

As in Figures 6.4–6.6, the values for $\text{Kp} < 0.7$ are inconsistent with the rest of the data. To examine how the LLSF was influenced, these values were removed from the dataset and the LLSF was recalculated. The results from this fit are shown in the middle column of Table 6.2. A negative slope is again obtained when only $\text{Kp} \leq 4$ is used, but when all Kp values are used, the slope becomes significantly positive. Not only does the fit line show the best visual agreement with the data, but it also has $R^2 = 0.35$, which is an improvement. Furthermore, the positive slope implies the expected increase in velocities with Kp.

In comparison to the exponential fit values for A, the sine fit A values show a much clearer trend. The deviation at low Kp is not present and so a LLSF to all the data produces a goodness of fit of $R^2 = 0.31$; if only $\text{Kp} \leq 4$ is included, the fit improves to $R^2 = 0.78$. Again, the scarcity of data for the larger Kp values makes the mean and median suspect. The y-intercept and slope for the sine fit trend of A with Kp are also shown in Table 6.2. Although outliers with high A values at low Kp exist, the standard deviation is small and so the outliers do not influence the trend. The trendline in Figure 6.13, starts at $A = 0.30$ and has a slope of $1.79 \times \text{Kp}$ showing an increase in A with Kp for the sine function.

The data for parameter B is significantly different than for parameter A. Whereas the data for A had large standard deviations and a large difference between the mean and the median, the data for parameter B, shown in Figure 6.14, have a much smaller standard

Table 6.2. Dawnside Statistics for A vs. Kp*

		Exponential Fit	Mod Exp Fit	Sine Fit
	Y-Intercept	1323.70	976.93	0.30
Kp ≤ 4	Slope	-139.31	-17.13	1.79
	R^2	0.40	0.02	0.78
	Y-Intercept	1005.89	680.99	1.42
Kp ≤ 9	Slope	44.64	114.90	1.26
	R^2	0.05	0.35	0.31

*A lack of data for Kp > 4 alters the trend and lowers the goodness of fit value for a linear least square fit. The modified exponential fit does not include the lowest two Kp bins in the analysis.

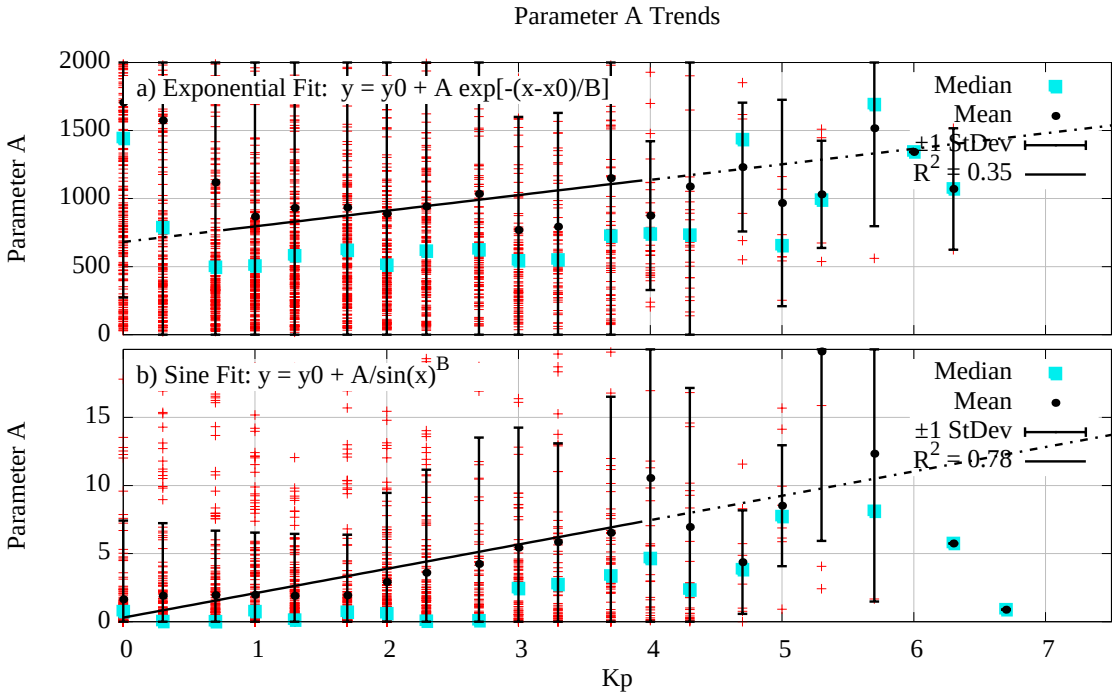

Figure 6.13. Dawnside parameter A versus Kp. Data points are shown as red crosses, and the mean and median are shown as black dots and blue squares, respectively. The standard deviation of the mean is plotted with the vertical black bars, and a LLSF to the mean is shown by the sloping black line. Only the data with Kp ≤ 4 were used to obtain the LLSF.

deviation and nearly identical mean and median for each Kp value resulting in a better LLSF. The same lack of data for Kp $>$ 4 still exists and so the LLSF shown in each plot only used the mean values for Kp $\leq$ 4. Table 6.3 contains the y-intercept and slope for these trendlines. The exponential fit B values increase with Kp, starting near $B = 4$ and increasing by $0.60 \times$ Kp. The goodness of fit is extremely high at $R^2 = 0.91$. The standard deviation of the sine data is slightly larger than the exponential data; however, a clear trend is still apparent. In this case, parameter B decreases with increasing Kp. The LLSF has a goodness of fit value of $R^2 = 0.81$ and decreases y $0.96 \times$ Kp after starting at $B = 9.30$ for Kp = 0.0. A decreasing B value is interesting as it means that for a given latitude and constant A value, the slope of the curve gets flatter with increasing Kp (e.g., red line versus green line in Figure 6.12). This could mean the auroral oval region is being pushed poleward on the dawnside instead of expanding equatorward as the duskside does. However the total picture is not contained in the B value because both A and B have an impact on the slope and magnitude of the sine function.

Another way to examine how the auroral region moves with Kp is to choose a specific gradient and find the latitude at which it occurs. This was done for both the exponential and sine LLSF; the results are shown in Figure 6.15. A velocity gradient ($dV_y/d\theta$) of 20 m/s/deg was chosen and was found to move equatorward with increasing Kp. Both exponential and sine trendlines have goodness of fit values over 0.7 and are both in good agreement with the TDIM and H-M model output shown in the bottom panel of Figure 6.15. However, this finding is in direct contrast to the results from parameter B that implied poleward movement of the auroral region on the dawnside. Although there is a factor of two difference between the duskside and the dawnside ($3.1 \times$ Kp and $1.5 \times$ Kp, respectively), this figure clearly shows as Kp increases, the auroral region moves equatorward. Therefore, it is clear that parameter B alone cannot be used to infer how the curves change with Kp.

Finally, the results on the dawnside are compared to the *Hardy et al.* [1985] statistical auroral oval model. The same type of comparison was done on the duskside. For the dawnside, MLTs of 0500, 0600, 0700, and 0800 correspond to the years 2010, 2009, 2008,

Table 6.3. Dawnside Statistics for B vs. Kp*

		Exponential Fit	Sine Fit
	Y-Intercept	4.08	9.30
Kp $\leq$ 4	Slope	0.60	-0.96
	R^2	0.91	0.81
	Y-Intercept	4.71	8.37
Kp $\leq$ 9	Slope	0.25	-0.46
	R^2	0.20	0.34

*A lack of data for Kp $>$ 4 alters the trend and lowers the goodness of fit value for a linear least square fit.

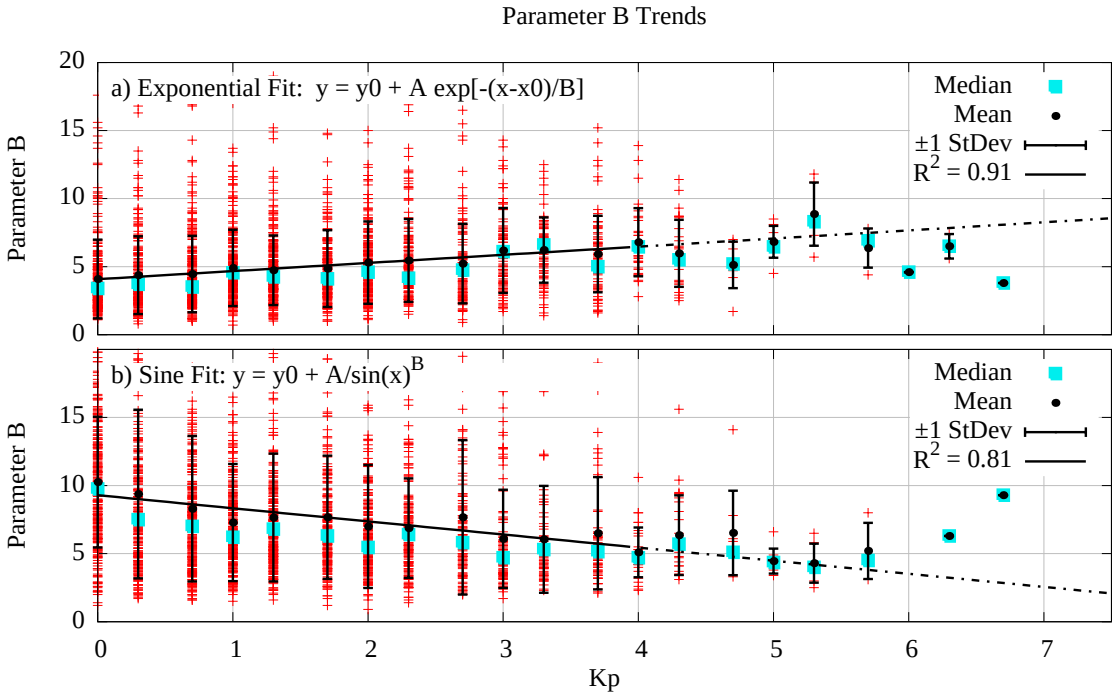

Figure 6.14. Dawnside parameter B versus Kp. Data points are shown as red crosses, and the mean and median are shown as black dots and blue squares, respectively. The standard deviation of the mean is plotted with the vertical black bars, and a LLSF to the mean is shown by the sloping black line. Only the data with Kp $\leq$ 4 were used to obtain the LLSF.

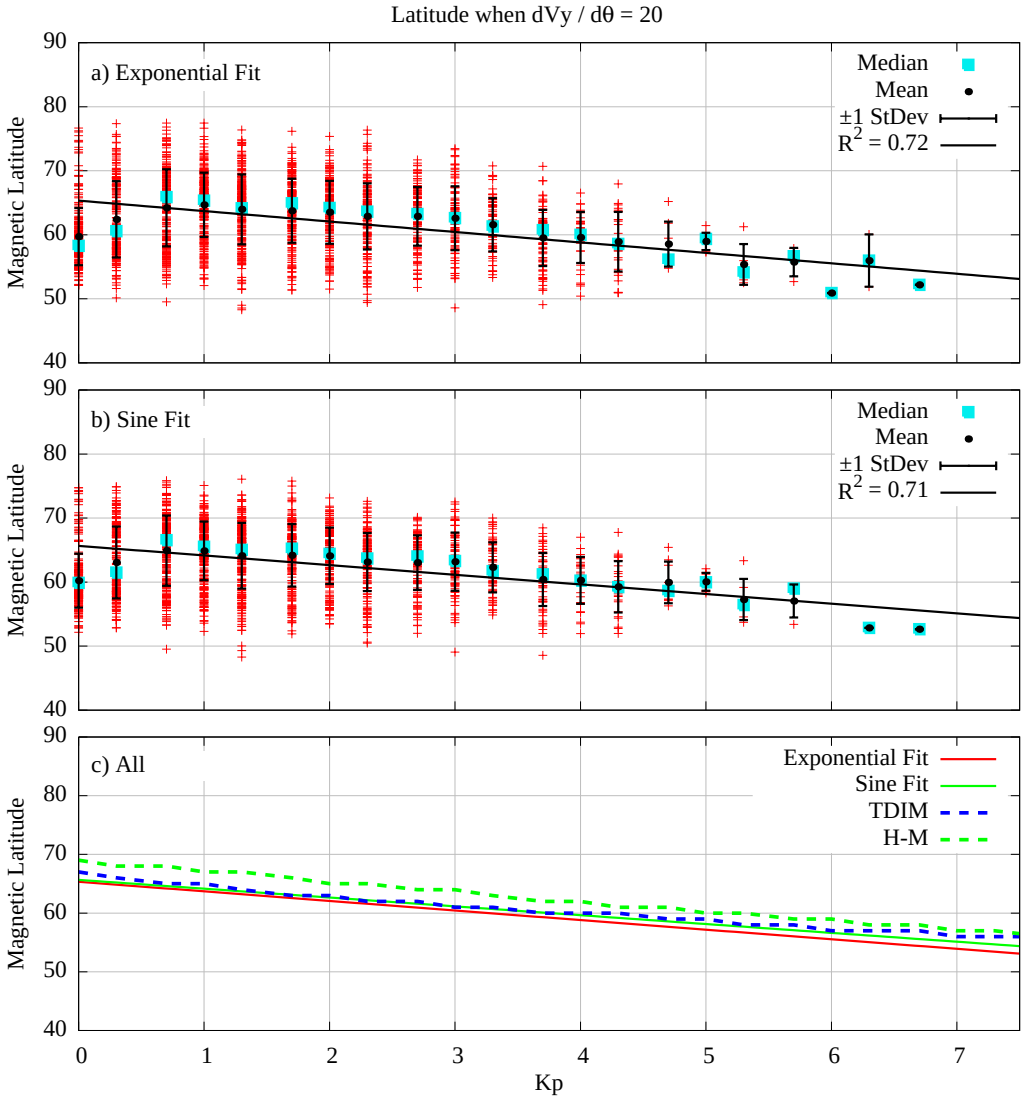

Figure 6.15. Dawnside latitude at which $dVy/d\theta = 20$ m/s/deg versus Kp. Plot setup is similar to Figure 5.8.

and 2007, respectively, due to the precession of the satellite over time. The results are shown in Figure 6.16. The background colors are the energy flux from the *Hardy et al.* [1985] model with warm colors indicating a larger flux. The solid black line is the polar cap radius obtained from data in Chapter 4, the dashed black line is the latitude of the peak velocity, and the red dashed lines are the latitude at which $dV_y/d\theta = 20$ m/s/deg. For all four MLTs, the PCR lines up fairly well with the poleward edge of the region with the largest flux. While the line for the peak latitude is consistent from 0500–0700 MLT, the location changes in the 0800 MLT plot. The results in the 0800 MLT plot are more consistent with the results seen on the duskside, whereas the location of the peak latitude in the 0500–0700 MLT plots seem to indicate the peak energy flux into the ionosphere is equatorward of the maximum velocity; i.e., the location of the auroral oval indicated by the data and the model are not consistent. The main cause of this inconsistency is the latitude of the peak velocity changes very little with latitude. Instead, the lines for the threshold gradient are consistent with the equatorward boundary for the region of large fluxes. These two results indicate the region of the largest energy flux is spread out across the entire fall-off region on the dawnside.

6.4. Summary

This chapter examined the fall-off region on the dawnside where the exponential and sine functions were used to classify the velocity profile obtained from the DMSP data. A LLSF algorithm was used to determine the best fit line for each orbit. The Gaussian function was not used as it produced poorer results on the duskside than the other two functions. For the majority of the study, only 2008–2010 data were used; however, in the final figure, the 2007 data were used to obtain information for the 0800 MLT. Additionally, only orbits with an $R^2 > 0.80$ were used in the analysis. Overall, the sine function performed marginally better than the exponential function on the dawnside. This is evident in the lack of a Kp trend for parameter A for the exponential function. Using the median values for parameters A and B, it was found that, in general, the orbits can be fit with an exponential function

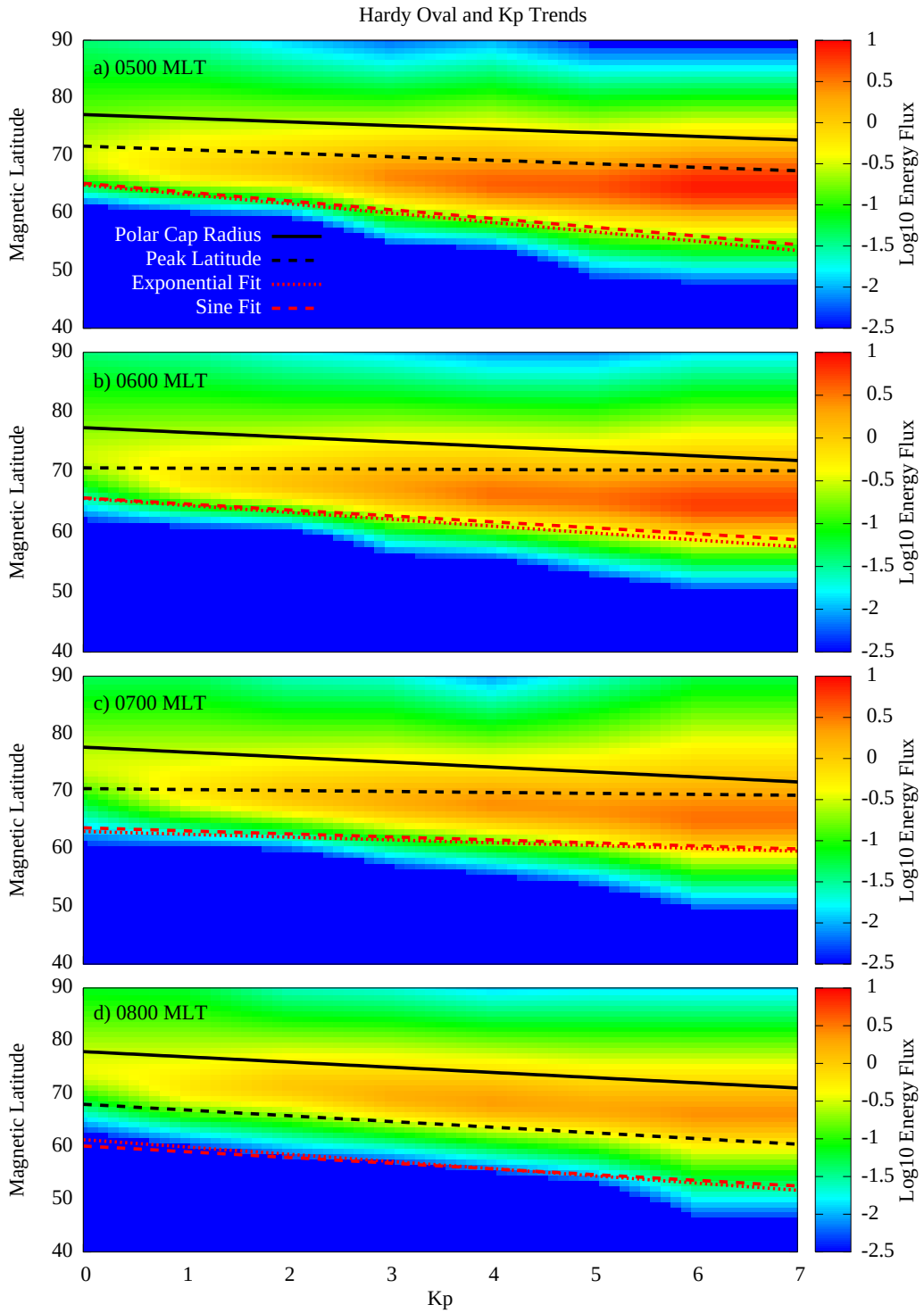

Figure 6.16. Dawnside *Hardy et al.* [1985] auroral oval and Kp trends for four MLTs. Kp trends are for the polar cap radius (solid black line), the peak latitude (dashed black line), and the latitude of the threshold gradient for each functional fit (red dashed lines). The background is the log of the energy flux obtained from the *Hardy et al.* [1985] auroral oval model. Each panel is for the MLT indicated in the top left corner.

using

$$y = 624 \times \exp\left[\frac{-(x - x_0)}{4.3}\right], \tag{6.3}$$

or with a sine function using

$$y = \frac{0.38}{\sin(x)^{6.6}}. \tag{6.4}$$

The relationships derived for use in an empirical model driven by the Kp index are questionable. For quiet geomagnetic conditions (Kp < 4), the two functions are given by the following sets of equations:

$$\begin{aligned}
\text{Exponential Fit: } y &= A \times \exp\left[\frac{-(x - x_0)}{B}\right], && (6.5)\\
A &= 680.99 + 114.90 \times \text{Kp}, && (6.6)\\
B &= 4.08 + 0.60 \times \text{Kp}. && (6.7)\\
\text{Sine Fit: } y &= \frac{A}{\sin(x)^B}, && (6.8)\\
A &= 0.30 + 1.79 \times \text{Kp}, && (6.9)\\
B &= 9.30 - 0.96 \times \text{Kp}. && (6.10)
\end{aligned}$$

CHAPTER 7
CONCLUSIONS AND FUTURE WORK

7.1. Conclusions

This research focused on the high-latitude convection pattern and specifically on the fall-off of the midlatitude velocities. DMSP ion drift data obtained during the 2007–2010 solar minimum was used for the analysis. Because only solar minimum conditions were used, these results may not hold for high Kp. The data was first smoothed and calibrated in an attempt to remove instrumentation errors. The two main problems with the data included errors caused by regions with a large fraction of H^+ ions and by inaccuracies in the satellite attitude specification. Removing these errors required calibrating the velocities so both the dusk and dawn sectors went to zero at low latitudes. This calibration effectively increased the dawnside velocities twice as much as the duskside velocities, and as such, only served to equalize the magnitude of the dusk and dawn velocities.

The first portion of this research focused on determining convection patterns by averaging all data binned by solar and geomagnetic conditions. This process resulted in surprisingly coherent two-cell convection patterns, but the convection patterns lacked evidence of a multi-cell pattern with sunward flow in the polar cap for B_z northward. In the dusk–dawn cross sections, asymmetries associated with positive B_y found in the empirical model output are much larger and more pronounced than any asymmetry in the data, and the *Weimer* [2005] auroral region velocities are up to four times larger than the data. In general, it was found the dusk–dawn cross sections are best represented by the *Heppner and Maynard* [1987] model output. The most important result found is the averaged patterns produced a succinct relationship between the polar cap radius and the geomagnetic index. Not only is there a clear dependence on Kp that is larger than what is currently being used, but the initial radius for Kp= 0.0 is also much smaller than expected.

After the averaged convection patterns were examined, the dusk and dawn fall-off region V_y velocity component for each individual orbit was fit to different functions. An exponential, a sine, and a Gaussian were used on the duskside, but only the exponential

and the sine functions were used on the dawnside because the best fits on the duskside were obtained with the exponential and sine functions. Only 30% of the orbits were used in the analysis because the rest had fits with $R^2 < 0.8$. The remaining 70% of the orbits did not fit the assumption of a smooth fall-off, which is evidence that capturing the real structure of the convection pattern is still an issue.

The sine fits showed their primary difference in parameter A with twice as many orbits having $A \leq 0.1$ on the dawnside as the duskside, which can be seen in a comparison of Figures 5.12 and 6.10. The trends, however, were the same in both sectors with A increasing with Kp for both the exponential and sine functions. On the dawnside, the exponential fit data for the two lowest Kp values was inconsistent with the rest of the data; although this anomaly was assumed to be caused by orbits external to the convection pattern, further investigation is warranted.

From Figures 5.9 and 6.7 it can be seen the difference for the exponential fits is primarily in parameter B with a mean of 6.5 on the duskside, which is nearly twice as large as the mean of 3.5 on the dawnside. Parameter B also exhibited opposite trends in the dusk and dawn sectors for both the exponential and sine functions. The dusk sector trend seemed to indicate a steepening of the gradient with an increase in Kp, while the dawn sector trend supported curves that were flatter at higher Kp values.

Although the trends for B were not as expected on the dawn side, it is understood that B alone cannot describe the curve. The curves in Figure 7.1 are obtained when the trends for A, B, the latitude of the peak velocity, and the peak velocity are combined for both the exponential and sine functions. As expected, the duskside (left) show lower magnitudes and flatter curves for Kp = 0.0 than for Kp = 4.0. Additionally, the latitude of the peak moves equatorward with increasing Kp. The exponential dawnside curves show the same trend as the duskside, but with smaller changes in the steepness of the curve and equatorward movement of the peak (8.5° on the duskside and 2.2° on the dawnside). The magnitude of the peak doubles from Kp = 1.0 to Kp = 4.0 on both the dusk and dawn curves. The dawnside curves for the sine function do not show as clear of a picture. The movement

equatorward with higher Kp is not evident although the magnitude of the peak velocity more than doubles. One trend still clear for the sine function is the dawnside changes are much smaller than the duskside.

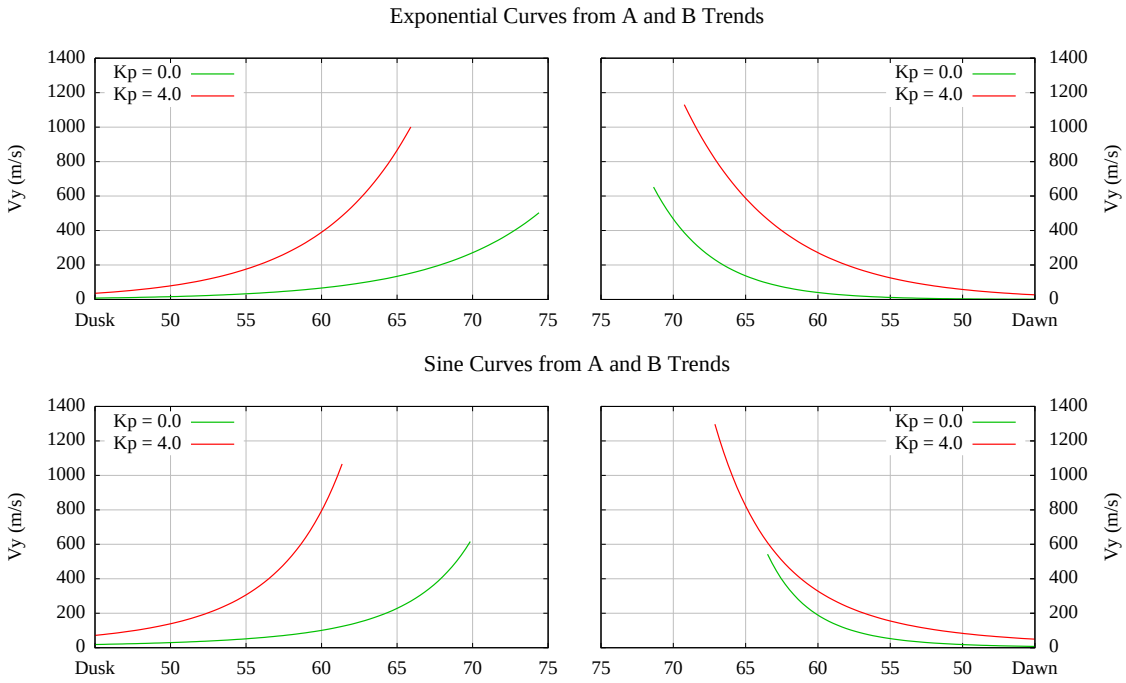

Figure 7.1. Dusk and dawn curves using A and B Kp trends. The top plots show curves for the exponential function and the bottom plots show the sine function. The green line is for Kp = 0.0 and the red line is for Kp = 4.0

The Kp trends obtained for the polar cap radius, peak latitude, and equatorward boundary of the auroral oval all show a consistent pattern of equatorward motion that is twice as large on the duskside than on the dawnside. The polar cap radius is the most similar in both sectors increasing by 4° on the duskside and by 3° on the dawnside. The largest difference is seen in the latitude of the peak velocity, which drops by 15° from Kp = 0.0 to Kp = 7.0 on the duskside, but only 4° on the dawnside. Finally, the equatorward boundary of the auroral region, represented by the latitude at which $dV_y/d\theta = 20$ m/s/deg, moves equatorward by 22° on the duskside and exactly half that, 11°, on the dawnside. The exact values are shown in Table 7.1 and a schematic of the boundary movement is shown in

Figure 7.2. The green lines represent Kp = 0.0 and the red lines Kp = 7.0. The polar cap radius is shown by the solid lines, the peak latitude by the dashed lines, and the equatorward boundary of the auroral oval by the dotted lines. The equatorward motion on the dayside is much smaller than the expansion on the nightside resulting in an inhomogeneous expansion of the polar region and auroral oval. The auroral oval is known to be the most dynamic in the evening sector because the strongest particle precipitation occurs there, however many empirical models use a symmetric expansion of the polar region, which is very different from the results shown here.

7.2. Future Work

This research has set the stage for much additional work. First, expanding the temporal coverage of the data, especially to periods of higher solar activity, could extend the results to higher levels of Kp. This would be particularly useful for the polar cap radius function. Although the use of data from more DMSP satellites would increase both the spatial and temporal coverage in the dawn–dusk sector, it would not expand coverage to the noon–midnight sectors because the DMSP satellites do not fly in a noon–midnight orientation.

Another area of research could involve correlating these results to other solar and geomagnetic indices. While the Kp index was used almost exclusively for this dissertation based on the desire to link convection pattern parameters to ionospheric model drivers, improvements in modeling techniques mean more information is being used to drive and couple these models. Some possible parameters and indices include the solar wind speed and density, the Auroral Electrojet (AE) index, the polar cap (PC) index, and perhaps a closer examination of the Dst index.

During the course of this research, it was noted various methods used to obtain these results could be improved upon or modified. One of these methods was the hand fitting of circles to the polar cap. Instead of doing this by hand, a least square fit of the roots to either a circle or an ellipse may provide an even more consistent result. An additional way to improve this work is to use a different version of the sine function instead of using the form introduced by *Volland* [1978] and to force the function to its maximum at the latitude

Table 7.1. Boundary Kp Trend Statistics*

	Polar Cap Radius Dusk / Dawn	Peak Latitude Dusk / Dawn	$dV_y/d\theta = 20$ m/s/deg Dusk / Dawn
Kp = 0.0	12.2 / 12.5	74.6 / 71.4	67.8 / 65.5
Kp = 4.0	16.6 / 15.7	66.2 / 69.3	55.4 / 59.2
Kp = 7.0	19.9 / 18.1	59.9 / 67.6	46.0 / 54.5

*Values obtained using equations for LLSF trendlines.

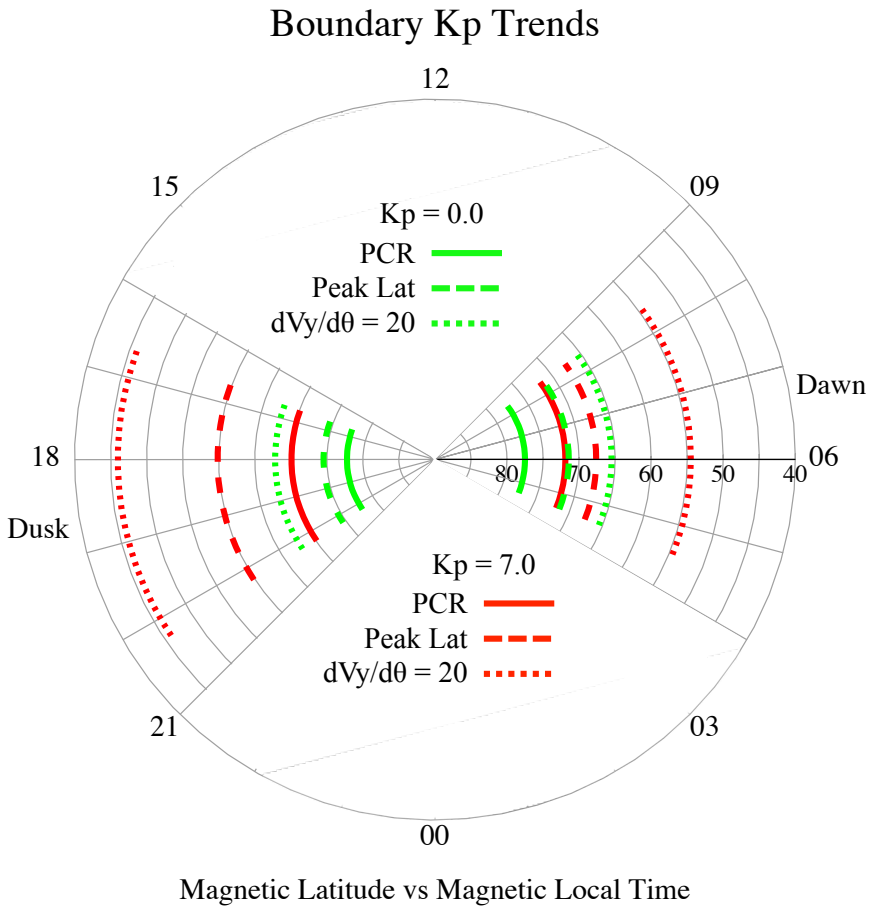

Figure 7.2. Boundary Kp trends. The trends are derived from the averaged convection patterns and functional fits. The green lines are for Kp = 0.0, and the red lines are for Kp = 7.0. The solid lines indicate the polar cap radius, the dashed lines are the latitude of the peak velocity, and the dotted lines show the equatorward boundary of the fall-off region (i.e., $dV_y/d\theta = 20$ m/s/deg).

of the peak velocity. Finally, it was noted many of the orbits from winter months in 2007 presented an interesting signature that may not be caused solely by the presence of large amounts of the hydrogen ion. Further investigation into these orbits is warranted.

An important piece of future work for this dissertation is the verification of these results against other data sets. Coincident data is available from SuperDARN, the Poker Flats and Millstone Hill ISR, and from various other satellite platforms, which should be used to verify both the polar cap radius relationship and the functional fits. Ultimately, the results from this research should be used in an ionospheric model to determine both the sensitivity of the model to these parameters and the overall changes induced by these results. In fact, this work has already been started using the USU TDIM.

REFERENCES

Aggson, T. L., and J. P. Heppner (1964), A proposal for electric field measurements on the Gravity-Gradient ATS-A satellite, NASA-Goddard Space Flight Center, Greenbelt, Maryland.

Alcayde, D., G. Caudal, and J. Fontanari (1986), Convection electric fields and electrostatic potential over $61^\circ < \Lambda < 72^\circ$ invariant latitude observed with the European Incoherent Scatter Facility: 1. Initial results, *J. Geophys. Res.*, *91*(A1), 233–247, doi: 10.1029/JA091iA01p00233.

Bekerat, H. A., R. W. Schunk, and L. Scherliess (2003), Evaluation of statistical convection patterns for real-time ionospheric specifications and forecasts, *J. Geophys. Res.*, *103*(A12), 1413, doi:10.1029/2003JA009945.

Bekerat, H. A., R. W. Schunk, L. Scherliess, and A. Ridley (2005), Comparison of satellite ion drift velocities with AMIE deduced convection patterns, *J. Atmos. Sol. Terr. Phys.*, *67*, 1463–1479, doi:10.1016/j.jastp.2005.08.013.

Berg, W., M. Sapiano, J. Horsman, and C. Kummerow (2013), Improved geolocation and earth incidence angle information for a fundamental climate data record of the ssm/i sensors, *Geoscience and Remote Sensing, IEEE Transactions on*, *51*(3), 1504–1513, doi: 10.1109/TGRS.2012.2199761.

Burden, R. L., and J. D. Faires (2005), *Numerical Analysis*, eighth ed., Thomson Higher Education, Belmont, Calif.

Cousins, E. D. P., and S. G. Shepherd (2010), A dynamical model of high-latitude convection derived from SuperDARN plasma drift measurements, *J. Geophys. Res.*, *115*(A12329), doi:10.1029/2010JA016017.

Cowley, S. W. H., and M. Lockwood (1992), Excitation and decay of solar wind-driven flows in the magnetosphere-ionosphere system, *Ann. Geophys.*, *10*, 103–115.

Dolezalek, H. (1964), Study of atmospheric electric tracing of high-altitude irregularities, AFCRL-678, Bedford, Mass.

Fejer, B. G. (2003), Solar wind-magnetosphere effects in the middle and low latitude ionosphere, in *Proceedings of the International Symposium on Auroral Phenomena and Solar-Terrestrial Relations*, pp. 91–103, Space Res. Inst., Russian Acad. of Sci., Moscow, Russia.

Foster, J. C., J. M. Holt, and R. G. Musgrove (1986), Ionosphere convection associated with discrete levels of particle precipitation, *Geophys. Res. Lett.*, *13*, 656–659.

Friis-Christensen, E., Y. Kamide, A. D. Richmond, and S. Matsushita (1985), Interplanetary magnetic field control of high-latitude electric fields and currents determined from Greenland Magnetometer Data, *J. Geophys. Res.*, *90*(A2), 1325–1338, doi: 10.1029/JA090iA02p01325.

Grocott, A., S. E. Milan, S. M. Imber, M. Lester, and T. K. Yeoman (2012), A quantitative deconstruction of the morphology of high-latitude ionospheric convection, *J. Geophys. Res.*, *117*(A05317), doi:10.1029/2012JA017580.

Hagen, J. B., and P. Y.-S. Hsu (1974), The structure of the protonosphere above arecibo, *J. Geophys. Res.*, *79*(28), 4269–4275, doi:10.1029/JA079i028p04269.

Hairston, M. R., and R. A. Heelis (1990), Model of the high-latitude ionospheric convection pattern during southward interplanetary magnetic field using DE 2 data, *J. Geophys. Res.*, *95*(A3), 2333–2343.

Hairston, M. R., and R. A. Heelis (1993), High-latitude electric field studies using DMSP data, *Tech. Rep. ADA265032*, University of Texas at Dallas, Center for Space Sciences, Richardson, Tex.

Hairston, M. R., and R. A. Heelis (1995), Response time of the polar ionospheric convection pattern to changes in the north-south direction of the imf, *Geophys. Res. Lett.*, *22*(5), 631–634, doi:10.1029/94GL03385.

Hairston, M. R., W. R. Coley, and R. A. Heelis (2010), Mapping the duskside topside ionosphere with CINDI and DMSP, *J. Geophys. Res.*, *115*(A08324), doi:10.1029/2009JA015051.

Hanson, W. B., and R. A. Heelis (1975), Techniques for measuring bulk gas-motions from satellites, *Space Sci. Instrum.*, *1*, 493–524.

Hanson, W. B., S. Sanatani, D. R. Zucarro, and T. W. Flowerday (1970), Plasma measurements with the retarding potential analyzer on OGO 6, *J. Geophys. Res.*, *75*, 5483–5501.

Hanson, W. B., R. A. Heelis, R. A. Power, C. R. Lippincott, D. R. Zuccaro, B. J. Holt, L. H. Harmon, and S. Sanatani (1981), The retarding potential analyzer for Dynamics Explorer-B, *Space Sci. Instrum.*, *5*, 503–510.

Hanson, W. B., W. R. Coley, R. A. Heelis, N. C. Maynard, and T. L. Aggson (1993), A comparison of in situ measurements of E and -V x B from Dynamics Explorer 2, *J. Geophys. Res.*, *98*(A12), 21,501–21,516, doi:10.1029/93JA01422.

Hardy, D. A., M. S. Gussenhoven, and E. Holeman (1985), A statistical model of auroral electron precipitation, *J. Geophys. Res.*, *90*(A5), 4229–4248, doi:10.1029/JA090iA05p04229.

Hargreaves, J. K. (1992), *The solar-terrestrial environment*, Cambridge University Press, Cambridge, U.K.

Heelis, R. A., and W. B. Hanson (2013), *Measurements of Thermal Ion Drift Velocity and Temperature Using Planar Sensors*, pp. 61–71, American Geophysical Union, doi:10.1029/GM102p0061.

Heelis, R. A., J. K. Lowell, and R. W. Spiro (1982), A model of the high-latitude ionospheric convection pattern, *J. Geophys. Res.*, *87*, 6339–6345.

Heinselman, C. J., and M. J. Nicolls (2008), A bayesian approach to electric field and E-region neutral wind estimation with the Poker Flat Advanced Modular Incoherent Scatter Radar, *Radio Sci.*, *43*(RS5013), doi:10.1029/2007RS003805.

Heppner, J. P. (1972), Polar cap electric field distributions related to the interplanetary magnetic field direction, *J. Geophys. Res.*, *77*, 4877.

Heppner, J. P. (1973), High-latitude electric fields and the modulations related to interplanetary magnetic field parameters, *Radio Sci.*, *8*, 933.

Heppner, J. P. (1977), Empirical models of high-latitude electric fields, *J. Geophys. Res.*, *82*, 1115–1125.

Heppner, J. P., and N. C. Maynard (1987), Empirical high-latitude electric field models, *J. Geophys. Res.*, *92*, 4467–4489.

Holt, J. M., R. H. Wand, J. V. Evans, and W. L. Oliver (1987), Empirical models for plasma convection at high latitudes, *J. Geophys. Res.*, *92*, 203–212.

Hysell, D. L., G. Michhue, M. J. Nicolls, C. J. Heinselman, and M. F. Larsen (2009), Assessing auroral electric field variance with coherent and incoherent scatter radar, *J. Atmos. Sol. Terr. Phys.*, *71*(6), 697–707, doi:10.1016/j.jastp.2008.10.013.

Kamide, Y., et al. (1982), Global distribution of ionospheric and field-aligned currents during substorms as determined from six IMS meridian chains of magnetometers: Initial results, *J. Geophys. Res.*, *87*(A10), 8228–8240, doi:10.1029/JA087iA10p08228.

Kavadas, A., and D. W. Johnson (1964), Electron densities and electric fields in the aurora, in *Space Research*, vol. IV, p. 365, North-Holland Publ. Co., Amsterdam, the Netherlands.

Kelley, M. C. (1989), *The Earth's Ionosphere Plasma Physics and Electrodynamics*, Academic Press, San Diego, Calif.

Klenzing, J. H., G. D. Earle, and R. A. Heelis (2008), Errors in ram velocity and temperature measurements inferred from satellite-borne retarding potential analyzers, *Physics of Plasmas*, *15*(6), 062905, doi:10.1063/1.2936270.

Knudsen, W. C. (1966), Evaluation and demonstration of the use of retarding potential analyzers for measuring several ionospheric quantities, *J. Geophys. Res.*, *71*(19).

Lester, M. (2013), The Super Dual Auroral Radar Network (SuperDARN): An overview of its development and science, *Adv. Polar Sci.*, *24*(1), 1–11, doi:10.3724/SP.J.1085.2013.00001.

Lyemori, T., and D. Rao (1996), Decay of the dst field of geomagnetic disturbance after substorm onset and its implication to storm-substorm relation, *Ann. Geophys.*, *14*(6), 608–618, doi:10.1007/s00585-996-0608-3.

Lyon, J., J. Fedder, , and C. Mobarry (2004), The Lyon–Fedder–Mobarry (LFM) global MHD magnetospheric simulation code, *J. Atmos. Sol. Terr. Phys.*, *66*, 1333–1350.

Papitashvili, V. O., and F. J. Rich (2002), High-latitude ionospheric convection models derived from defense meteorological satellite program ion drift observations and parameterized by the interplanetary magnetic field strength and direction, *J. Geophys. Res.*, *107*(A8), SIA 17–1–SIA 17–13, doi:10.1029/2001JA000264.

Papitashvili, V. O., B. A. Belov, D. S. Faermark, Y. I. Feldstein, S. A. Golyshev, L. I. Gromova, and A. E. Levitin (1994), Electric potential patterns in the northern and southern polar regions parameterized by the interplanetary magnetic field, *J. Geophys. Res.*, *99*(A7), 13,251–13,262, doi:10.1029/94JA00822.

Pettigrew, E. D., S. G. Shepherd, and J. M. Ruohoniemi (2010), Climatological patterns of high-latitude convection in the Northern and Southern hemispheres: Dipole tilt dependencies and interhemispheric comparisons, *J. Geophys. Res.*, *115*(A07305), doi:10.1029/2009JA014956.

Peymirat, C., and D. Fontaine (1997), Polar cap convection patterns inferred from EISCAT observations, *Ann. Geophys.*, *15*, 403–411.

Pfaff, R., et al. (2010), Observations of DC electric fields in the low-latitude ionosphere and their variations with local time, longitude, and plasma density during extreme solar minimum, *J. Geophys. Res.*, *115*(A12324), doi:10.1029/2010JA016023.

Powell, K., P. Roe, T. Linde, T. Gombosi, and D. De Zeeuw (1999), A solution-adaptive upwind scheme for ideal magnetohydrodynamics, *J. Comput. Phys.*, *154*, 284–309.

Prölss, G. W. (2004), *Physics of the Earth's Space Environment: An Introduction*, second ed., Springer, Berlin, Germany.

Raeder, J., D. Larson, W. Li, E. Kepko, and T. Fuller-Rowell (2008), OpenGGCM simulations for the THEMIS mission, *Space Sci. Rev.*, *141*(1-4), 535–555, doi:10.1007/s11214-008-9421-5.

Rich, F. J., and M. Hairston (1994), Large-scale convection patterns observed by DMSP, *J. Geophys. Res.*, *99*(A3), 3827–3844, doi:10.1029/93JA03296.

Rich, F. J., and N. C. Maynard (1989), Consequences of using simple analytical functions for the high-latitude convection electric field, *J. Geophys. Res.*, *94*(A4), 3687–3701.

Richmond, A. D. (1992), Assimilative mapping of ionospheric electrodynamics, *Adv. Space Res.*, *12*(6), (6)59–(6)68.

Richmond, A. D., and Y. Kamide (1988), Mapping electrodynamic features of the high-latitude ionosphere from localized observations: Technique, *J. Geophys. Res.*, *93*(A6), 5741–5759, doi:10.1029/JA093iA06p05741.

Schunk, R. W., and A. F. Nagy (2009), *Ionospheres: Physics, Plasma Physics, and Chemistry*, second ed., Cambridge University Press, Cambridge, U.K.

Schunk, R. W., et al. (2004), Global Assimilation of Ionospheric Measurements (GAIM), *Radio Sci.*, *39*.

Senior, C., and M. Blanc (1984), On the control of magnetospheric convection by the spatial distribution of ionospheric conductivities, *J. Geophys. Res.*, *89*(A1), 261–284, doi:10.1029/JA089iA01p00261.

Sojka, J., W. Raitt, and R. Schunk (1979), Effect of displaced geomagnetic and geographic poles on high-latitude plasma convection and ionospheric depletions, *J. Geophys. Res.*, *84*(A10), 5943–5951, doi:10.1029/JA084iA10p05943.

Sojka, J. J., C. E. Rasmussen, and R. W. Schunk (1986), An interplanetary magnetic field dependent model of the ionospheric convection electric field, *J. Geophys. Res.*, *91*(A10), 11,281–11,290, doi:10.1029/JA091iA10p11281.

Tascione, T. F. (1994), *Introduction to the Space Environment*, second ed., Krieger Publishing Company, Malabar, Florida.

Toffoletto, F., S. Sazykin, R. Spiro, and R. Wolf (2003), Inner magnetospheric modeling with the rice convection model, *Space Sci. Rev.*, *107*, 175–196.

Toth, G., et al. (2005), Space weather modeling framework: a new tool for the space science community, *J. Geophys. Res.*, *110*, doi:10.1029/2005JA011126.

Volland, H. (1975), Models of the global electric fields within the magnetosphere, *Ann. Geophys.*, *31*, 159–173.

Volland, H. (1978), A model of the magnetospheric electric convection field, *J. Geophys. Res.*, *83*, 2695–2699.

Weimer, D. R. (1995), Models of high-latitude electric potentials derived with a least error fit of spherical harmonic coefficients, *J. Geophys. Res.*, *100*(A10), 19,595–19,607, doi: 10.1029/95JA01755.

Weimer, D. R. (1996), A flexible, IMF dependent model of high-latitude electric potentials have "space weather" applications, *Geophys. Res. Lett.*, *23*(18), 2549–2552.

Weimer, D. R. (2001), An improved model of ionospheric electric potentials including substorm perturbations and application to the Geospace Environment Modeling November 24, 1996, event, *J. Geophys. Res.*, *106*(A1), 407–416.

Weimer, D. R. (2005), Improved ionospheric electrodynamic models and application to calculating joule heating rates, *J. Geophys. Res.*, *110*(A5), doi:10.1029/2004JA010884.

Whipple, E. C. (1959), Exploration of the upper atmosphere with the help of the third Soviet sputnik (ion trap results), *Proc. IRE*, *47*, 2023–2024.

Wygant, J. R., et al. (2013), The electric field and waves instruments on the radiation belt storm probes mission, *Space Sci. Rev.*, *179*, 183–220, doi:10.1007/s11214-013-0013-7.

Xiong, C., and H. Lühr (2014), An empirical model of the auroral oval derived from CHAMP field-aligned current signatures - Part 1, *Ann. Geophys.*, *32*, 623–631, doi: 10.5194/angeo-32-623-2014.

APPENDICES

APPENDIX A
GOVERNING PROCESSES IN THE IONOSPHERE

A.1. Neutral Atmosphere

The major neutrals in the ionosphere are molecular nitrogen (N_2), molecular oxygen (O_2), and atomic oxygen (O), with minor concentrations of argon (Ar), helium (He), and hydrogen (H). The concentrations of each of these species varies with height and can be approximated using a hydrostatic equilibrium solution. Hydrostatic equilibrium occurs when the forces due to pressure and gravity are in balance. Where this balance occurs, the density of a species as a function of altitude (z) is given as

$$N_s(z) = N_s(z_0) \exp\left[-\frac{z - z_0}{H_s}(z)\right], \tag{A.1}$$

where N_s is the number density, z_0 is a reference altitude, and H_s is the scale height for the species, s, given by

$$H_s(z) = \frac{k_b\, T_s(z)}{m_s\, g(z)}, \tag{A.2}$$

where k_b is Boltzmann's constant, T_s is the temperature, m_s is the mass, and g is gravity. In this approximation, the concentration of the species falls off primarily as a function of mass. Therefore, the concentrations of N_2 and O_2 decrease more rapidly with height than does the concentration of O. Figure A.1 shows the vertical variation up to $1000km$ of the neutral concentrations during solar maximum using this assumption. The relative abundance of each neutral compared with the other neutrals is important when calculating the production and loss of ions.

A.2. Production and Loss

Photoionization is the primary production mechanism for creating ion-electron pairs in the low to midlatitude ionosphere. This ionization results from the absorption by neutrals of solar extreme ultraviolet and X-ray radiation. Production due to photoionization depends on the incoming solar flux, the optical depth, the neutral concentrations, and the ionization

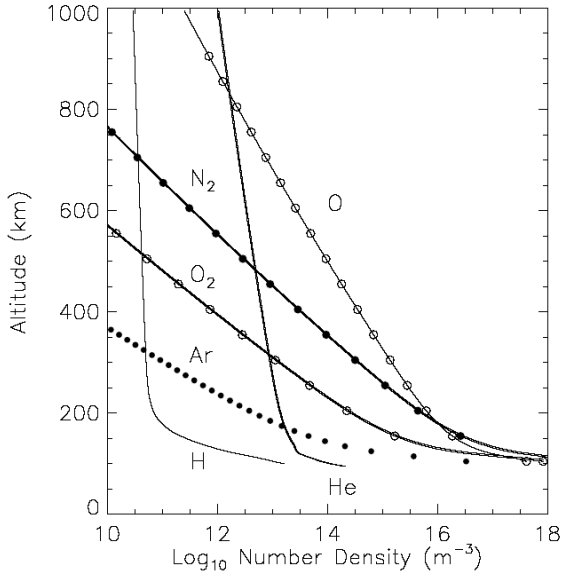

Figure A.1. Major and minor neutral concentrations. Densities are computed by MSIS and represent solar maximum conditions as a function of altitude. Heavier ion concentrations decrease with altitude faster than the light ions.

cross section. Each of these factors may also depend on species, altitude (z), wavelength (λ), or zenith angle (χ); for a particular species, s, the photoionization rate is given as

$$P_s(z,\chi) = N_s(z) \int_0^{\lambda_{si}} I_\infty(\lambda) \exp\left[-\tau(z,\chi,\lambda)\right] \sigma_s^i(\lambda)\, d\lambda, \tag{A.3}$$

where

$$I_\infty(\lambda) \quad \text{is the solar flux at the top of the atmosphere,} \tag{A.4}$$

$$N_s(z) \quad \text{is the number density,} \tag{A.5}$$

$$\tau(z,\chi,\lambda) \quad \text{is the optical depth,} \tag{A.6}$$

$$\sigma_s^i(\lambda) \quad \text{is the ionization cross section,} \tag{A.7}$$

$$\lambda_{si} \quad \text{is the threshold wavelength for ionization.} \tag{A.8}$$

Also contributing to ion production are chemical reactions, secondary electron production, and impact ionization.

The primary ion loss mechanisms in the ionosphere are chemical reactions. The major loss reactions include ion-ion recombination, radiative recombination, dissociative recombination, ion-atom interchange, and associative detachment. An example of each reaction is given below.

$$\text{Ion-ion Recombination:} \quad O_2^+ + O_2^- \longrightarrow O_2 + O_2. \tag{A.9}$$

$$\text{Radiative Recombination:} \quad O^+ + e^- n \longrightarrow O + hv. \tag{A.10}$$

$$\text{Dissociative Recombination:} \quad N_2^+ + e^- \longrightarrow N + N. \tag{A.11}$$

$$\text{Ion-atom Interchange:} \quad O^+ + H \longrightarrow O + H^+. \tag{A.12}$$

$$\text{Associative Detachment:} \quad O^- + O \longrightarrow O_2 + e^-. \tag{A.13}$$

Production and loss due to chemical reactions are dependent on the rate of the particular reaction and on the concentrations of the reactants. For a reaction such as

$$O^+ + N_2 \xrightarrow{k} N_2^+ + O, \tag{A.14}$$

the production rate of N_2^+ (and the loss rate of O^+) is given as

$$P(N_2^+) = L(O^+) = k\left[O^+\right]\left[N_2\right], \tag{A.15}$$

where k is the reaction rate constant for the specific reaction and $[O^+]$ and $[N_2]$ denote the species' concentration. The production and loss rate for each chemical reaction is the term used in the continuity equation (Equation 2.1). The reaction rate constant, k, is dependent on the temperature of each species in addition to the activation energy of the reaction, which can be described as the minimum energy needed to form the new species [*Schunk and Nagy*, 2009]. The reaction rate constant is determined by the equation

$$k_{st} = 2d^2\sqrt{\frac{2\pi k_b}{\mu_{st}}}\sqrt{T_{st}}\exp\left(-\frac{E_a}{k_b T_{st}}\right), \tag{A.16}$$

where the subscripts denote each species in the reaction, d describes the cross section, k_b is Boltzmann's constant, μ_{st} and T_{st} are the reduced mass and temperature, respectively, and E_a is the activation energy. This reaction constant varies by orders of magnitude for the different reaction types listed above, which means some processes will dominate over others. For example, radiative recombination reaction rate constants are on the order of 10^{-12}, while dissociative recombination reaction rate constants are on the order of 10^{-7} [*Schunk and Nagy*, 2009].

In the D region, high neutral concentrations lead to complex chemical reactions. One of these reactions, electron attachment, creates the only significant population of negative ions in the ionosphere. Deep penetration of short wavelength X-ray and EUV radiation also contributes to the complexity of the D region.

The relatively high neutral concentrations in the E region lead to the following chemical reaction production mechanisms for NO^+:

$$N_2^+ + O \longrightarrow NO^+ + N, \tag{A.17}$$

$$O_2^+ + NO \longrightarrow NO^+ + O_2, \tag{A.18}$$

$$O_2^+ + N_2 \longrightarrow NO^+ + NO. \tag{A.19}$$

Ion-atom interchange is relatively fast compared to dissociative recombination in this region resulting in low concentrations of O^+ and leaving the molecular ions (N_2^+, O_2^+, and NO^+) as the major ions. In the F_1 region, O^+ becomes an important ion due to the higher neutral atomic oxygen concentrations at F_1 altitudes. The reaction rate constants determine the loss mechanisms in these regions. Radiative recombination is slow and unimportant, whereas dissociative recombination occurs 10^5 times faster [*Hargreaves*, 1992]. The primary dissociative recombination reactions in the E and F_1 regions are

$$O_2^+ + e^- \longrightarrow O + O, \tag{A.20}$$

$$N_2^+ + e^- \longrightarrow N + N, \tag{A.21}$$

$$NO^+ + e^- \quad \longrightarrow \quad N + O. \tag{A.22}$$

The F_2 region has the same production and loss processes as the E and F_1 regions; however, at and above F_2 region altitudes, plasma transport is significant and determines the density structure. While the F_2 region is controlled by all three processes, the topside ionosphere is controlled by transport alone.

A.3. Transport

The movement of plasma within the ionosphere is described by the full momentum equation, which is given as

$$\rho_s \frac{D_s \vec{u}_s}{Dt} = -\nabla p_s - \nabla \cdot \tau_s + \rho_s \vec{G} + n_s q_s \left[\vec{E} + \vec{u}_s \times \vec{B}\right] + \sum_t \rho_s \nu_{st} \left(\vec{u}_t - \vec{u}_s\right). \tag{A.23}$$

In this equation, the subscripts denote the species, s, and the target, t, ρ_s is the mass density, D_s/Dt is the convective derivative, p_s is the pressure, k_b is Boltzmann's constant, τ_s is the stress, and ν_{st} is the collision frequency. In obtaining Equation A.23, thermal diffusion, Coriolis force, and centripetal force were all assumed to be negligible. After also making the diffusion approximation (steady state and subsonic) Equation A.23 reduces to

$$\nabla p_s + \nabla \cdot \tau_s - \rho_s \vec{G} - n_s q_s \left[\vec{E} + \vec{u}_s \times \vec{B}\right] = \sum_t \rho_s \nu_{st} \left(\vec{u}_t - \vec{u}_s\right). \tag{A.24}$$

Further simplification of the momentum equation is accomplished by considering two separate cases. Diffusion along and perpendicular to the magnetic field will be examined separately. The overall plasma motion is a combination of both solutions.

For diffusion along the magnetic field, the plasma is confined to orbit the magnetic field lines. In this situation the electrons and the major ion species move together and charge neutrality ($n_e = n_i$), and zero current ($n_e \vec{u}_e = n_i \vec{u}_i$) conditions prevail. This ambipolar diffusion behavior is a result of the polarization electric field that develops due to the slight charge separation of the electrons and ions due to their different masses. With this ambipolar diffusion approximation and the previously mentioned assumptions, the ion and

electron momentum equations along the magnetic field are given as

$$\nabla_{||} p_i + (\nabla \cdot \tau_i)_{||} - \rho_i \vec{G}_{||} - n_i e \vec{E}_{||} = \rho_i \nu_{ie} \left(\vec{u}_e - \vec{u}_i\right)_{||} + \rho_i \nu_{in} \left(\vec{u}_n - \vec{u}_i\right)_{||}, \quad \text{(A.25)}$$

$$\nabla_{||} p_e + (\nabla \cdot \tau_e)_{||} - \rho_e \vec{G}_{||} + n_e e \vec{E}_{||} = \rho_e \nu_{ei} \left(\vec{u}_i - \vec{u}_e\right)_{||} + \rho_e \nu_{en} \left(\vec{u}_n - \vec{u}_e\right)_{||}, \quad \text{(A.26)}$$

where $\vec{E}_{||}$ is the polarization electric field. Adding these equations together and solving for the ion velocity gives the ambipolar diffusion equation

$$\vec{u}_{i||} = -D_a \left[\frac{1}{n_i} \nabla_{||} n_i + \frac{1}{T_p} \nabla_{||} T_p - \frac{m_i \vec{G}_{||}}{2 k_b T_p} + \frac{(\nabla \cdot \tau_i)_{||}}{2 n_i k_b T_p} - \frac{m_i}{2 k_b T_p} \nu_{in} \vec{u}_{n||} \right], \quad \text{(A.27)}$$

where terms containing the electron mass (m_e) were neglected and the ideal gas law was used, and where the ambipolar diffusion coefficient (D_a) and plasma temperature (T_p) are given by

$$D_a = \frac{2 k_b T_p}{m_i \nu_{in}}, \quad \text{(A.28)}$$

$$T_p = \frac{T_e + T_i}{2}. \quad \text{(A.29)}$$

Equation A.27 shows that ions move along the magnetic field with the neutral wind subject to temperature gradients, density gradients, gravity, and stress forces.

For diffusion across the magnetic field, the stress term in Equation A.24 is also assumed to be negligible giving

$$\nabla p_s - \rho_s \vec{G} - n_s q_s \left[\vec{E}_{\perp} + \vec{u}_s \times \vec{B} \right] = \rho_s \nu_{sn} \left(\vec{u}_n - \vec{u}_s\right), \quad \text{(A.30)}$$

where $\vec{E}_{\perp}$ is an applied electric field, the subscript, s, denotes either an electron or ion, and the electron-ion collisions are neglected because the momentum transfer is small [*Schunk and Nagy*, 2009]. Transforming Equation A.30 to a reference frame moving with the neutral wind ($\vec{u}_s \rightarrow \vec{u}_s^{'} + \vec{u}_n$) simplifies the solution and introduces an effective electric field given

by $\vec{E}_{\perp}^{'} = \vec{E}_{\perp} + \vec{u}_n \times \vec{B}$. Equation A.30 then becomes

$$\nabla p_s - \rho_s \vec{G} - n_s q_s \left[\vec{E}_{\perp}^{'} + \vec{u}_{s\perp}^{'} \times \vec{B} \right] = -\rho_s \nu_{sn} \vec{u}_{s\perp}^{'}. \tag{A.31}$$

Solving for $\vec{u}_{s\perp}^{'}$ gives

$$\vec{u}_{s\perp}^{'} - \frac{q_s}{m_s \nu_{sn}} \left(\vec{u}_{s\perp}^{'} \times \vec{B} \right) = \frac{-1}{n_s m_s \nu_{sn}} \nabla_{\perp} p_s + \frac{1}{\nu_{sn}} \vec{G}_{\perp} + \frac{q_s}{m_s \nu_{sn}} \vec{E}_{\perp}^{'}. \tag{A.32}$$

Equation A.32 is simplified as

$$\vec{u}_{s\perp}^{'} - K \left(\vec{u}_{s\perp}^{'} \times \hat{b} \right) = \frac{-D_s}{p_s} \nabla_{\perp} p_s + \frac{1}{\nu_{sn}} \vec{G}_{\perp} + \mu_s \vec{E}_{\perp}^{'} \tag{A.33}$$

using the following relations:

$$\begin{aligned} p_s &= n_s k_b T_s, & \mu_s &= \frac{q_s}{m_s \nu_{sn}}, \\ \omega_{cs} &= \frac{q_s B}{m_s}, & \hat{b} &= \frac{\vec{B}}{B}, \\ D_s &= \frac{k_b T_s}{m_s \nu_{sn}}, & K &= \frac{\omega_{cs}}{\nu_{sn}}. \end{aligned}$$

Because $\vec{u}_{s\perp}^{'}$ is perpendicular to the magnetic field, it can have two orientations. Consider a coordinate system at the equator where the magnetic field $\vec{B}$ is pointed north in the $\hat{b}$ direction. Then the components of $\vec{u}_{s\perp}^{'}$ can be in the downward ($\hat{i}$) direction or the horizontal eastward ($-\hat{j}$) direction. Separating $\vec{u}_{s\perp}^{'}$ in Equation A.33 into these components and simplifying gives

$$\vec{u}_{s\perp_D}^{'} \hat{i} - \vec{u}_{s\perp_H}^{'} \hat{j} + K \vec{u}_{s\perp_D}^{'} \hat{j} + K \vec{u}_{s\perp_H}^{'} \hat{i} = \frac{-D_s}{p_s} \nabla_{\perp_D} p_s \hat{i} + \frac{1}{\nu_{sn}} \vec{G}_{\perp_D} \hat{i} + \mu_s \vec{E}_{\perp_D}^{'} \hat{i}, \tag{A.34}$$

where the variations of the density gradient, gravity, and electric field are small in the horizontal direction and can be neglected. Equating all the terms in the $\hat{i}$ direction and all

the terms in the $\hat{j}$ direction, we can write

$$\vec{u}_{s\perp_D}^{'} + K\vec{u}_{s\perp_H}^{'} = \frac{-D_s}{p_s}\nabla_\perp p_s + \frac{1}{\nu_{sn}}\vec{G}_\perp + \mu_s\vec{E}_\perp^{'}, \tag{A.35}$$

$$\vec{u}_{s\perp_H}^{'} = K\vec{u}_{s\perp_D}^{'}. \tag{A.36}$$

Substituting $\vec{u}_{s\perp_H}^{'}$ from Equation A.36 into Equation A.35 and simplifying gives

$$\vec{u}_{s\perp_D}^{'} = \frac{1}{1+K^2}\left[\frac{-D_s}{p_s}\nabla_\perp p_s + \frac{1}{\nu_{sn}}\vec{G}_\perp + \mu_s\vec{E}_\perp^{'}\right]. \tag{A.37}$$

Equation A.37 describes the vertical drift that is perpendicular to the magnetic field, but parallel to the force causing the drift. For $\vec{G}_\perp = \vec{E}_\perp^{'} = 0$ in an unmagnetized case ($K = 0$), Equation A.37 reduces to Fick's Law, which states the particle flux is proportional to the density gradient. Substitution of Fick's Law into the continuity equation results in the classical diffusion equation [*Schunk and Nagy*, 2009].

The horizontal drift is obtained by substituting Equation A.37 for $\vec{u}_{s\perp_D}^{'}$ back into Equation A.36 and simplifying, which results in

$$\vec{u}_{s\perp_H}^{'} = \frac{1}{1+1/K^2}\left[\vec{u}_P + \vec{u}_G + \vec{u}_E\right], \tag{A.38}$$

where

$$\vec{u}_P = \frac{-1}{n_s q_s}\frac{\left(\nabla_\perp p_s \times \vec{B}\right)}{B^2} \quad \text{is the gradient drift,} \tag{A.39}$$

$$\vec{u}_G = \frac{m_s}{q_s}\frac{\left(\vec{G}_\perp \times \vec{B}\right)}{B^2} \quad \text{is the gravitational drift,} \tag{A.40}$$

$$\vec{u}_E = \frac{\left(\vec{E}_\perp^{'} \times \vec{B}\right)}{B^2} \quad \text{is the electrodynamic drift.} \tag{A.41}$$

These three drifts are perpendicular to both the magnetic field and the force (pressure gradient, gravity, or the electric field) causing the drift. Electrons and ions drift across the magnetic field in opposite directions in the presence of pressure gradients and gravity, but

they drift together in the presence of a perpendicular electric field. Typically the pressure gradient and gravitational drifts are small and the electrodynamic drift dominates. Since $\vec{u}_{s\perp}^{\,\prime} = \vec{u}_{s\perp_D}^{\,\prime} + \vec{u}_{s\perp_H}^{\,\prime}$, the total plasma drift across the magnetic field is

$$\vec{u}_{s\perp}^{\,\prime} = \frac{1}{1+K^2}\left[\frac{-D_s}{p_s}\nabla_\perp p_s + \frac{1}{\nu_{sn}}\vec{G}_\perp + \mu_s \vec{E}_\perp^{\,\prime}\right] + \frac{1}{1+\frac{1}{K^2}}\left[\vec{u}_P + \vec{u}_G + \vec{u}_E\right]. \tag{A.42}$$

When collisions are negligible $K \to \infty$ and the first term of Equation A.42 drops out leaving only the motion perpendicular to both the magnetic field and the force. This approximation is valid at high altitudes. In locations where $K \to 0$, the second term drops out leaving only the motion perpendicular to the magnetic field, but parallel to the force. This situation occurs at low altitudes where the magnetic field strength is small compared to the collision frequency. At intermediate locations where neither approximation is valid, the plasma motion will be a combination of these motions and will move perpendicular to the magnetic field and at an angle to the force causing the motion [*Kelley*, 1989].

APPENDIX B

COPYRIGHT PERMISSIONS

Seven figures in this dissertation required copyright permissions from their respective sources. The permission requests were submitted as outlined in the Publication Guide for Graduate Students. The following figures are copies of the copyright licenses.

JOHN WILEY AND SONS LICENSE TERMS AND CONDITIONS

Jun 30, 2015

This Agreement between Janelle Jenniges ("You") and John Wiley and Sons ("John Wiley and Sons") consists of your license details and the terms and conditions provided by John Wiley and Sons and Copyright Clearance Center.

License Number	3658950620171
License date	Jun 30, 2015
Licensed Content Publisher	John Wiley and Sons
Licensed Content Publication	Journal of Geophysical Research
Licensed Content Title	The structure of the protonosphere above Arecibo
Licensed Content Author	Jon B. Hagen,Peter You-Sen Hsu
Licensed Content Date	Oct 1, 1974
Pages	7
Type of use	Dissertation/Thesis
Requestor type	University/Academic
Format	Print and electronic
Portion	Figure/table
Number of figures/tables	2
Original Wiley figure/table number(s)	Figure 4, Figure 5
Will you be translating?	No
Title of your thesis / dissertation	A Study of the Dayside High-Latitude Ionospheric Electrodynamics During Extended Solar Minimum
Expected completion date	Aug 2015
Expected size (number of pages)	180
Requestor Location	Janelle Jenniges 2612 N 230 E LOGAN, UT 84341 United States Attn: Janelle Jenniges
Billing Type	Invoice
Billing Address	Janelle Jenniges 2612 N 230 E LOGAN, UT 84341 United States Attn: Janelle Jenniges
Total	0.00 USD

Figure B.1. Copyright permission received for *Hagen and Hsu* [1974]. Permission is for use of Figure 2.1.

JOHN WILEY AND SONS LICENSE TERMS AND CONDITIONS

Jul 08, 2015

This Agreement between Janelle Jenniges ("You") and John Wiley and Sons ("John Wiley and Sons") consists of your license details and the terms and conditions provided by John Wiley and Sons and Copyright Clearance Center.

License Number	3664340379764
License date	Jul 08, 2015
Licensed Content Publisher	John Wiley and Sons
Licensed Content Publication	Wiley oBooks
Licensed Content Title	Measurements of Thermal Ion Drift Velocity and Temperature Using Planar Sensors
Licensed Content Author	R. A. Heelis,W. B. Hanson
Licensed Content Date	Mar 18, 2013
Pages	11
Type of use	Dissertation/Thesis
Requestor type	University/Academic
Format	Print and electronic
Portion	Figure/table
Number of figures/tables	3
Original Wiley figure/table number(s)	Figure 2, Figure 3, and Figure 4.
Will you be translating?	No
Title of your thesis / dissertation	A Study of the Dayside High-Latitude Ionospheric Electrodynamics During Extended Solar Minimum
Expected completion date	Aug 2015
Expected size (number of pages)	180
Requestor Location	Janelle Jenniges 2612 N 230 E LOGAN, UT 84341 United States Attn: Janelle Jenniges
Billing Type	Invoice
Billing Address	Janelle Jenniges 2612 N 230 E LOGAN, UT 84341 United States Attn: Janelle Jenniges
Total	0.00 USD

Figure B.2. Copyright permission received for *Heelis and Hanson* [2013]. Permission is for use of Figures 2.8, 2.9, and 2.10.

JOHN WILEY AND SONS LICENSE TERMS AND CONDITIONS

Jun 30, 2015

This Agreement between Janelle Jenniges ("You") and John Wiley and Sons ("John Wiley and Sons") consists of your license details and the terms and conditions provided by John Wiley and Sons and Copyright Clearance Center.

License Number	3658930137061
License date	Jun 30, 2015
Licensed Content Publisher	John Wiley and Sons
Licensed Content Publication	Journal of Geophysical Research: Space Physics
Licensed Content Title	Empirical high-latitude electric field models
Licensed Content Author	J. P. Heppner,N. C. Maynard
Licensed Content Date	May 1, 1987
Pages	23
Type of use	Dissertation/Thesis
Requestor type	University/Academic
Format	Print and electronic
Portion	Figure/table
Number of figures/tables	3
Original Wiley figure/table number(s)	Figure 1, Figure 2, and Figure 3.
Will you be translating?	No
Title of your thesis / dissertation	A Study of the Dayside High-Latitude Ionospheric Electrodynamics During Extended Solar Minimum
Expected completion date	Aug 2015
Expected size (number of pages)	180
Requestor Location	Janelle Jenniges 2612 N 230 E LOGAN, UT 84341 United States Attn: Janelle Jenniges
Billing Type	Invoice
Billing Address	Janelle Jenniges 2612 N 230 E LOGAN, UT 84341 United States Attn: Janelle Jenniges
Total	0.00 USD

Figure B.3. Copyright permission received for *Heppner and Maynard* [1987]. Permission is for use of Figure 2.14.

JOHN WILEY AND SONS LICENSE TERMS AND CONDITIONS

Jun 30, 2015

This Agreement between Janelle Jenniges ("You") and John Wiley and Sons ("John Wiley and Sons") consists of your license details and the terms and conditions provided by John Wiley and Sons and Copyright Clearance Center.

License Number	3658951175347
License date	Jun 30, 2015
Licensed Content Publisher	John Wiley and Sons
Licensed Content Publication	Journal of Geophysical Research: Space Physics
Licensed Content Title	Effect of displaced geomagnetic and geographic poles on high-latitude plasma convection and ionospheric depletions
Licensed Content Author	J.J. Sojka,W.J. Raitt,R.W. Schunk
Licensed Content Date	Oct 1, 1979
Pages	9
Type of use	Dissertation/Thesis
Requestor type	University/Academic
Format	Print and electronic
Portion	Figure/table
Number of figures/tables	1
Original Wiley figure/table number(s)	Figure 3
Will you be translating?	No
Title of your thesis / dissertation	A Study of the Dayside High-Latitude Ionospheric Electrodynamics During Extended Solar Minimum
Expected completion date	Aug 2015
Expected size (number of pages)	180
Requestor Location	Janelle Jenniges 2612 N 230 E LOGAN, UT 84341 United States Attn: Janelle Jenniges
Billing Type	Invoice
Billing Address	Janelle Jenniges 2612 N 230 E LOGAN, UT 84341 United States Attn: Janelle Jenniges
Total	0.00 USD

Figure B.4. Copyright permission received for *Sojka et al.* [1979]. Permission is for use of Figure 2.6.

JOHN WILEY AND SONS LICENSE TERMS AND CONDITIONS

Jun 30, 2015

This Agreement between Janelle Jenniges ("You") and John Wiley and Sons ("John Wiley and Sons") consists of your license details and the terms and conditions provided by John Wiley and Sons and Copyright Clearance Center.

License Number	3658921244343
License date	Jun 30, 2015
Licensed Content Publisher	John Wiley and Sons
Licensed Content Publication	Journal of Geophysical Research: Space Physics
Licensed Content Title	Models of high-latitude electric potentials derived with a least error fit of spherical harmonic coefficients
Licensed Content Author	None
Licensed Content Date	Oct 1, 1995
Pages	13
Type of use	Dissertation/Thesis
Requestor type	University/Academic
Format	Print and electronic
Portion	Figure/table
Number of figures/tables	5
Original Wiley figure/table number(s)	Figure 5. Contour graph of electric potential for BT>7.25 nT.
Will you be translating?	No
Title of your thesis / dissertation	A Study of the Dayside High-Latitude Ionospheric Electrodynamics During Extended Solar Minimum
Expected completion date	Aug 2015
Expected size (number of pages)	180
Requestor Location	Janelle Jenniges 2612 N 230 E LOGAN, UT 84341 United States Attn: Janelle Jenniges
Billing Type	Invoice
Billing Address	Janelle Jenniges 2612 N 230 E LOGAN, UT 84341 United States Attn: Janelle Jenniges
Total	0.00 USD

Figure B.5. Copyright permission received for *Weimer* [1995]. Permission is for use of Figure 2.15.

VITA

Janelle V. Jenniges
(May 2015)

EDUCATION:

Ph.D. in Physics, Utah State University, Logan, Utah (expected 2015)
Squadron Officer School Correspondance Program, Air University (2012)
M.S. in Applied Physics, Air Force Institute of Technology, Wright-Patterson Air Force Base, Ohio (2011)
Tropical Weather Analysis and Forecasting, Air Education and Training Command (2009)
M.B.A., University of Phoenix, Phoenix, Arizona (2009)
Weather Officer Course, Air Education and Training Command (2006)
Air and Space Basic Course, Air University (2006)
B.S. in Meteorology-Climatology, University of Nebraska, Lincoln, Nebraska (2005)

EXPERIENCE:

Space Weather Flight Commander, Air Force Weather Agency, Offutt Air Force Base, Nebraska (2011–2012)
Weather Operations Officer, 17th Air Force, U.S. Air Forces Africa, Ramstein Air Base, Germany (2008–2009)
Executive Officer, 603d Support Group, Ramstein Air Base, Germany (2008)
Assistant Flight Commander, 21st Operational Weather Squadron, Sembach Air Base, Germany (2006–2008)

AWARDS & HONORS:

Golden Key National Honor Society (2015)
Air Force Commendation Medal, First Oak Leak Cluster (2012)
Space Weather Company Grade Officer of the Year, Air Force Weather Agency (2011)
Distinguished Graduate, Air Force Institute of Technology (2011)
Tau Beta Pi National Honor Society (2010)
Air Force Achievement Medal (2009)
Air Force Commendation Medal (2008)
Distinguished Graduate, Weather Officer Course (2006)
Distinguished Graduate, Air Force Reserve Officer Training Corp (2005)
Phi Beta Kappa National Honor Society (2005)
Cadet of the Year, United States Air Force (2005)

PUBLICATIONS & PRESENTATIONS:

Jenniges, J. V., J. J. Sojka, R. A. Heelis, and M. David (2015), Approximating Midlatitude Fall-off Velocity Profiles in the Dawn and Dusk Sectors of the High-Latitude Convection Pattern, *Poster presented at the Coupling, Energetics and Dynamics of Atmospheric Regions (CEDAR) Workshop*, Seattle, WA.

Jenniges, J. V., J. J. Sojka, and R. A. Heelis (2014), Evaluating Midlatitude Fall-off Dependencies of the High Latitude Convection Pattern, *Poster presented at the American Geophysical Union Fall Meeting*, San Francisco, CA.

Jenniges, J. V. (2011), Sensitivity Analysis of Empirical Parameters in the Ionosphere-Plasmasphere Model, *Master's Thesis*, Air Force Institute of Technology, Wright-Patterson Air Force Base, OH.

Jenniges, J. V., A. O. Acebal, L. Gardner, R. W. Schunk, and L. Zhu (2010), Uncertainty Associated with Modeling the Global Ionosphere, *Poster presented at the American Geophysical Union Fall Meeting*, San Francisco, CA.